Bio-Inspired Photonic Surfaces by Enhanced Two-Photon Lithography

Dissertation

zur Erlangung des Grades
des Doktors der Ingenieurwissenschaften
der Naturwissenschaftlich-Technischen Fakultät
der Universität des Saarlandes

von
Julia Purtov

Angefertigt am INM – Leibniz Institut für Neue Materialien
Schaltbare Oberflächen / Optische Materialien

Saarbrücken,
Januar 2021

Tag des Kolloquiums:	8. Juli 2021
Dekan:	Prof. Dr. Jörn Eric Walter
Berichterstatter:	Prof. Dr. Eduard Arzt Prof. Dr.-Ing. Frank Mücklich
Akad. Mitglied:	Dr. Oliver Janka
Vorsitz:	Prof. Dr. Tobias Kraus

Danksagung

Die vorliegende Dissertation ist am INM – Leibniz-Institut für Neue Materialien in Saarbrücken unter der Leitung von Prof. Dr. Eduard Arzt in den Forschungsgruppen Schaltbare Oberflächen und Optische Materialien entstanden. Einen entscheidenden Beitrag lieferte auch der Forschungsaufenthalt an der University of Cambridge in Cambridge, England, in der Forschungsgruppe Bioinspired Photonics unter der Leitung von Prof. Dr. Silvia Vignolini.

Als erstes möchte ich mich bei meinem Doktorvater Prof. Dr. Eduard Arzt für die Ermöglichung dieser Dissertation, die durchgehende Unterstützung und den Glauben an eine erfolgreiche Abgabe bedanken.

Ebenfalls möchte ich herzlichst meinen Gruppenleitern Dr. Elmar Kroner und Dr. Peter de Oliveira danken, die mich immer in meinem Vorhaben und meinen Ideen unterstütz haben und somit mir die Freiheiten gegeben haben, meinen eigenen Weg zu gehen.

Einen ganz besonderen Dank und ein großes Lob möchte ich meinem Betreuer Dr. Peter Rogin aussprechen. Mit seinen fachlichen Ratschlägen, dem Verfassen des Simulationsprogramms für die Berechnung der Intensitätsverteilung im Fokusbereich des Lithographiesystems, dem Zurverfügungstellen eines Programms für die Kurvenanpassung im Rahmen der Divergenz-charakterisierung, den guten Ideen, sowie den wertvollen und ausführlichen Diskussionen hat er die Arbeit, so wie sie jetzt vorliegt, erst möglich gemacht. Er stand mir immer mit einem offenen Ohr zu Seite und ist von mir nicht nur als Betreuer, sondern auch als Freund sehr geschätzt. Es war mir eine Ehre, mit diesem Menschen zusammenzuarbeiten und von ihm zu lernen.

Weiterhin möchte ich Dr. René Hensel für seine stetige Unterstützung, die wichtigen Diskussionen und Korrekturen danken. Ihm verdanke ich ein besseres Verständnis für das Erstellen und Bearbeiten von Publikationen.

Ein großer Dank geht auch an Prof. Dr. Silvia Vignolini, die es mir ermöglicht hat, einen Teil meiner Experimente in ihrer Arbeitsgruppe durchzuführen. Ohne diese einmalige Chance wären einige wichtige Charakterisierungen nicht möglich gewesen.

Ich danke ebenfalls der ganzen Gruppe der Bioinspired Photonics, die mich herzlich aufgenommen hat und von der ich viel lernen durfte. Ganz besonders möchte ich hier Dr. Villads Egede Johansen danken, der mit seinen Simulationen der optischen Eigenschaften meiner strukturierten Oberflächen und der Expertise in der Konoskopie und Spektroskopie einen großen Beitrag für die Qualität dieser Arbeit geleistet hat.

Einen großen Dank richte ich auch an meine Kollegen Bruno Schäfer, Jennifer Atchison und Mareike Frensemeier, die ihre Erfahrungen und Zeit für die Ellipsometriemessungen, den Versuchsaufbau für die spektroskopischen Messungen und Diskussionen opferten. Zusätzlich möchte ich mich insbesondere bei meinen Hilfswissenschaftlern und Praktikanten Katja Groß, Reza Hosseinabadi und Lisa Becker bedanken, die mir eine große Hilfe bei der Aufnahme der Daten waren.

Ein besonderer Dank geht auch an Dr. Andreas Verch, einem guten Wissenschaftler, Freund und am Ende Ehemann für seine stetige Unterstützung, die zahlreichen wissenschaftlichen Diskussionen und Korrekturen.

Zu guter Letzt möchte ich auch meiner Tochter danken, die mir das Niederschreiben dieser Arbeit in den letzten Wochen nicht immer leichter gemacht hatte, und mir dabei dennoch so viele schöne Augenblicke schenkte.

Die Zeit meiner Doktorarbeit war mitunter die schönste, erfahrungsreichste und prägendste Zeit meines Lebens, dafür möchte ich mich an dieser Stelle auch bei meinen Freunden und Kollegen bedanken.

Content

Abstract

2D and 3D photonic crystals active in the visible wave range are highly interesting for applications, such as waveguiding elements, sensors, or counterfeiting features. However, the tuneable production of such crystals with the current processes is challenging. Two-photon lithography (TPL), which is mainly used to manufacture microstructures, offers this versatility but currently suffers from insufficient structure resolution and mechanical stability for sub-micrometre structures.

In the course of this work several novel approaches including an improved development and standing wave enhanced two-photon lithography are presented. These approaches improve the structure resolution and quality, and thus, allow stable features sizes down to 120 nm in horizontal and 45 nm in vertical direction. The new capabilities were used to fabricate distinct photonic crystals inspired by the 2D-pillar grating found on the moth eye and the 3D ‘Christmas tree’-like structures covering the wings of the *Morpho*-butterflies. Resulting structures were analysed in detail regarding their sizes and optical properties, showing highly effective diffraction, promising anti-reflection properties, and outstanding angle independent iridescence. The experimental work is supported by correlated simulations investigating the optical properties, structures sizes, and the influences of different experimental parameter settings relevant for the fabrication.

Kurzzusammenfassung

2D und 3D photonische Kristalle, die mit sichtbarem Licht interagieren, finden zunehmend Verwendung in Wellenleitelementen, bei Sensoren oder Sicherheitsmerkmalen. Jedoch ist die Herstellung solcher Kristalle mit den derzeitigen Methoden herausfordernd und komplex. Eine vielversprechende Technik wäre die Zweiphotonenlithografie, die gegenwärtig für die flexible Herstellung von Mikrostrukturen eingesetzt wird. Für die Fertigung von photonischen Kristallen, die hochqualitative Strukturen im Nanometerbereich voraussetzen, besitzt diese Technik jedoch keine ausreichende Strukturauflösung.

In dieser Arbeit werden neue Verfahren wie ein verbesserter Entwicklungsprozess oder die Zweiphotonenlithograpie mit integrierter stehender Welle präsentiert. Diese Methoden erlauben die Herstellung von Submikrometerstrukturen mit einem Limit von 120 nm in horizontaler und 45°nm in vertikaler Richtung. Diese verbesserte Auflösung wurde genutzt, um zwei natürliche photonische Kristalle, die 2D optischen Gitter der Mottenaugen und die geschichteten 3D Strukturen der *Morpho*-Schmetterlinge, künstlich nachzuahmen. Die Untersuchung der optischen Eigenschaften dieser Strukturen zeigten hocheffektive Beugungs- und vielversprechende Antireflexeigenschaften sowie eine herausragende, winkelunabhängige Strukturfarbe. Die experimentelle Arbeit wurde durch Simulationen wie die der optischen Eigenschaften, der erwarteten Strukturgrößen und der Einflüsse von Prozessparametern auf die Herstellung unterstützt.

Abbreviations and Symbols

Chemicals

DETC	7-diethylamino-3-thenoylcoumarin
EtOH	Ethanol
H_2O	Water
IPA	Isopropanol
N_2	Nitrogen
OPPEA	Polyethylene glycol o-phenylphenyl ether acrylate
PGMEA	Propylene glycol methyl ether acetate
PETA	Pentaerythritoltriacrylate

Methods

ETD	Everhart-Thornley-detector
SEM	Scanning electron microscopy
STL	Stereolithography
SWE-TPL	Standing wave enhanced two-photon lithography
TPL	Two-photon polymerisation

General

1, 2, 3D	One, two, three dimensional
CAD	Computer aided design
IR	Infrared
RT	Room temperature
UV	Ultraviolet
VIS	Visible

Units

fs	Femtosecond
h	Hour
µA	Microampere
µl	Microlitre
µm	Micrometre
MHz	Megahertz
mA	Milliampere

min	Minute
mm	Millimetre
ms	Millisecond
mW	Milliwatt
nm	Nanometre
s	Second
rpm	Revolutions per minute

Physical Parameters

d	Diameter
E	Electric field
h	Height
k	Extinction coefficient
N	Number
n	Refractive index
NA	Numerical aperture
P	Dipole density
R	Reflectivity
r	Radius
V	Voltage
θ_{div}	Beam divergence angle
θ_{hdiv}	Half beam divergence angle
θ_i	Light incidence angle
θ_r	Light reflection angle
θ_c	Wetting contact angle
λ	Wavelength
w	Waist size of the beam within the focus
w_z	Beam width at a position z
φ	Phase

TPL-Parameters

CM	Continuous Exposure
SS	Scan Speed
PM	Pulsed Exposure
ET	Exposure Time

PD	Point Distance
LP	Laser Power
ST	Settling Time
FI	Find Interface
LN	Layer Number
LD	Layer Distance
LD	Line Distance

Chapter 1. Introduction

The phenomenon of light has fascinated many famous researchers such as Hooke[1], Newton[2], Lord Rayleigh[3], or Einstein. In the last four hundred years it was discovered that various mechanisms are responsible for the colour appearance of objects illuminated by light. Some mechanisms are decisively dependent on the chemical properties of the irradiated material, such as in the cases of dyes and pigments, where certain wavelengths of light are absorbed in the electronic band structure of the materials. Other colour giving mechanisms are mainly based on structural effects, such as the iridescent colouration of some animals or plants[4-12]. In this case, the colour is caused by the interaction of particular wavelengths with periodical arrangements of different structural features, whereby the affected wavelengths are strongly dependent on the structural dimensions and their periodicity[4,13]. Such periodical arrangements are referred to as photonic structures or photonic crystals, and are grouped into three categories, 1-, 2-, or 3-dimensional photonic crystals; depending on the number of dimensions (D), in which the periodicity extends[5,14]. Some of the most prominent examples occurring in nature are presented in **Figure 1-1**. The 1D-photonic crystals of beetles or the *Pollia* plant comprise periodical multilayers with thicknesses of several hundreds of nanometres (**Figure 1-1a**), which induce a strong reflection due to the alternation of low and high refractive index materials[10,11]. 2D photonic crystals can be found on peacock feathers or on the eyes of moths (**Figure 1-1b**), where the former shows rainbow-like diffraction due to a periodical arrangement of barbules[12], and the latter anti-reflective properties due to closely packed nanopillars[15,16]. Examples of 3D-periodic structures in nature are few, but they exist as ordered colloidal spheres in opals[17,18], or in the freestanding, layered structures on the wings of *Morpho*-butterflies[19] (**Figure 1-1c**).

In recent years, the investigation of photonic crystals and the attempts to reproduce them artificially attracted increasing scientific and commercial interest, as studies revealed fascinating ways of controlling the propagation of light due to the presence of the so-called photonic band gap[13,20-24]. The photonic band gap is similar to the electronic band gap and defines the wavelengths or frequencies which cannot propagate through a photonic crystal. One- and two-dimensional photonic crystals have already found their way into many applications. 1D-photonic crystals, for instance, are used as dielectric mirrors in laser and semiconductor industry; two-dimensional crystals show good performances in waveguides and as diffractive elements and are therefore applied as photonic crystal fibres or optical sensors. 3D-photonic crystals, though, have not been used commercially so far, as their fabrication is very complex and prone to defects[25-27]. Conceivable application fields, however, are manifold. 3D-photonic crystals could be used for selective light scattering, in holograms, as decorative elements, as focussing elements, or as counterfeiting features[28,29].

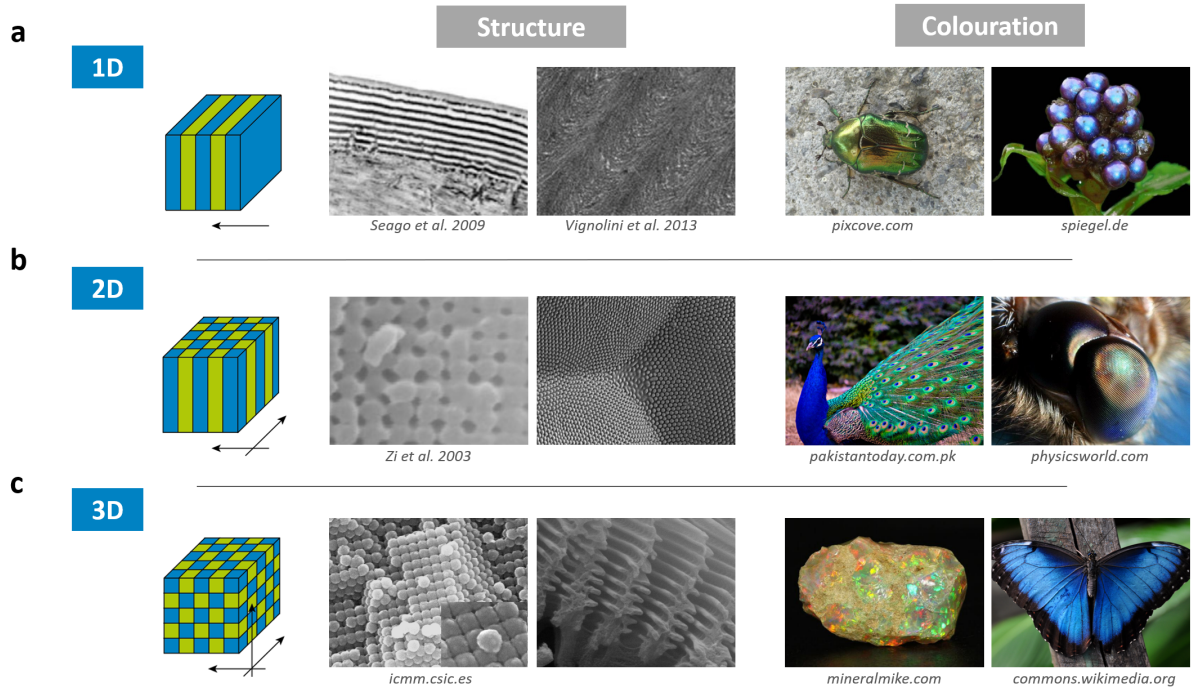

Figure 1-1. Examples of different photonic crystals in nature

The structure and coloration of natural photonic crystals presented in dependence on their classification: 1D-crystals of beetles and the pollia fruit, 2D-crystals of the peacock and the moth-eye, and 3D-crystals of the opal and *Morpho*-butterflies.

Modified photonic crystals e.g., those with deliberately placed defects or irregularities can be utilized to guide light with an only slight loss of energy[30-33], while photonic crystals with tailored disorder or randomness could improve the performance of solar cells and future laser generations[34-44]. A very famous natural blueprint of such a disordered crystal is that found on the wings of the *Morpho* butterfly[45,46]. Here, structural elements with a strict vertical periodicity of air and chitin are integrated into a hierarchical system with small deviations from perfect periodicity on the different structural levels[19,45]. The result is an exceptionally angle-independent, blue reflection[47], and thus, a spatially very consistent photonic band gap.

From a practical and commercial perspective, all applications of 3D-photonic crystals mentioned above can only be realised when the manufacturing meets the demanding requirements. These includes flexible and precise tuning of the photonic band gap, low defect rates, as well as fast, simple, and cost-efficient production. Currently utilised methods, such as the self-assembly of spheres or selective etching of multilayer systems, were successfully used to manufacture 3D-crystals[25,26,48,49], but struggle with significant disadvantages: a high number of complex process steps, high defect rates, and the tricky implementation of deliberate irregularities.

A solution could be a currently rising method referred to as two-photon lithography (TPL), direct laser writing, or similar terms[50-58]. This method allows a very precise fabrication of complex 3D-structures

on the micrometre scale and requires only one lithography step without using structuring masks[50,57,59-62]. While the relevance and capabilities to structure 3D photonic crystals by TPL were shown for infra-red light[63,64], the manufacturing of 3D-crystals that interact with visible light has not been successful so far.

To enable the fabrication of bio-inspired photonic structures as those displayed in **Figure 1-1** several challenges in TPL-fabrication have to be solved: the still high susceptibility of manufactured nano-structures to defect formation, e.g., structural collapse or deformation[65], as well as the relatively low vertical and lateral structuring resolution of approximately 600 x 200 nm of the most two-photon lithography systems[21]. These topics are addressed by the work described in Chapter 5, Chapter 6 and Chapter 8 of this thesis. The new findings are then used to manufacture two bio-inspired photonic surfaces which are presented in Chapter 7 and Chapter 9: i) the 2D optical pillar grating of the moth eye providing anti-reflection properties and ii) the 3D-structure of the *Morpho*-butterfly wing with its slightly disordered air-material layering and angle-independent blue reflection. Further relevant content is addressed in Chapter 2, Chapter 3, and Chapter 4, where a short introduction into light and its interactions with matter, the current State of the Art, and an overview of the used Materials and Methods are given. The thesis closes by showing possible future research directions in Chapter 10 and a final overall conclusion in Chapter 11.

1.1. References

1. Hooke R. *Micrographia: Or Some Physiological Descriptions of Minute Bodies Made by Magnifying Glasses, with Observations and Inquiries Thereupon*. Dover Publications, 2003.
2. Newton I, Innys W. *Opticks:: Or, A Treatise of the Reflections, Refractions, Inflections and Colours of Light*. William Innys at the West-End of St. Paul's., 1730.
3. Rayleigh L. On the Reflection of Light from a Regularly Stratified Medium. *Proceedings of the Royal Society of London Series A, Containing Papers of a Mathematical and Physical Character* 1917, **93**(655)**:** 565-577.
4. Parker AR. The diversity and implications of animal structural colours. *The Journal of Experimental Biology* 1998, **201**(16)**:** 2343-2347.
5. Ingram AL, Parker AR. A review of the diversity and evolution of photonic structures in butterflies, incorporating the work of John Huxley (The Natural History Museum, London from 1961 to 1990). *Philosophical Transactions of the Royal Society B: Biological Sciences* 2008, **363**(1502)**:** 2465-2480.
6. Cooper K, Hanlon R, Budelmann B. Physiological color change in squid iridophores. *Cell Tissue Res* 1990, **259**(1)**:** 15-24.
7. Kinoshita S, Yoshioka S. Structural Colors in Nature: The Role of Regularity and Irregularity in the Structure. *ChemPhysChem* 2005, **6**(8)**:** 1442-1459.
8. Mason CW. Structural Colors in Insects. II. *The Journal of Physical Chemistry* 1926, **31**(3)**:** 321-354.
9. Mouchet SR, Van Hooijdonk E, Welch VL, Louette P, Colomer J-F, Su B-L, *et al.* Liquid-induced colour change in a beetle: the concept of a photonic cell. *Scientific Reports* 2016, **6:** 19322.

10. Seago AE, Brady P, Vigneron J-P, Schultz TD. Gold bugs and beyond: a review of iridescence and structural colour mechanisms in beetles (Coleoptera). *Journal of The Royal Society Interface* 2009, **6**(Suppl 2)**:** S165-S184.
11. Vignolini S, Rudall PJ, Rowland AV, Reed A, Moyroud E, Faden RB, *et al.* Pointillist structural color in Pollia fruit. *Proceedings of the National Academy of Sciences of the United States of America* 2012, **109**(39)**:** 15712-15715.
12. Zi J, Yu X, Li Y, Hu X, Xu C, Wang X, *et al.* Coloration strategies in peacock feathers. *Proc Natl Acad Sci* 2003, **100**(22)**:** 12576-12578.
13. Kinoshita S, Yoshioka S, Miyazaki J. Physics of structural colors. *Reports on Progress in Physics* 2008, **71**(7)**:** 076401.
14. Yablonovitch E. Inhibited Spontaneous Emission in Solid-State Physics and Electronics. *Physical Review Letters* 1987, **58**(20)**:** 2059-2062.
15. Stavenga DG, Foletti S, Palasantzas G, Arikawa K. Light on the moth-eye corneal nipple array of butterflies. *Proceedings of the Royal Society B: Biological Sciences* 2006, **273**(1587)**:** 661-667.
16. Bernhard CG, Gemne G, Sällström J. Comparative ultrastructure of corneal surface topography in insects with aspects on phylogenesis and function. *Z Vergl Physiol* 1970, **67**(1)**:** 1-25.
17. Jones JB, Sanders JV, Segnit ER. Structure of Opal. *Nature* 1964, **204**(4962)**:** 990-991.
18. Gaillou Es, Fritsch E, Aguilar-Reyes B, Rondeau B, Post J, Barreau A, *et al.* Common gem opal: An investigation of micro- to nano-structure. *Am Mineral* 2008, **93**(11-12)**:** 1865-1873.
19. Ghiradella H. Structure of Iridescent Lepidopteran Scales: Variations on Several Themes. *Annals of the Entomological Society of America* 1984, **77**(6)**:** 637-645.
20. Parker AR, Townley HE. Biomimetics of photonic nanostructures. *Nat Nano* 2007, **2**(6)**:** 347-353.
21. Fischer J, Wegener M. Three-dimensional optical laser lithography beyond the diffraction limit. *Laser & Photonics Reviews* 2013, **7**(1)**:** 22-44.
22. Yablonovitch E. Photonic band-gap structures. *J Opt Soc Am B* 1993, **10**(2)**:** 283-295.
23. Joannopoulos JD, Villeneuve PR, Fan S. Photonic crystals: putting a new twist on light. *Nature* 1997, **386**(6621)**:** 143-149.
24. Kim S, Mitropoulos AN, Spitzberg JD, Tao H, Kaplan DL, Omenetto FG. Silk inverse opals. *Nat Photon* 2012, **6**(12)**:** 818-823.
25. Vogel N, Retsch M, Fustin C-A, del Campo A, Jonas U. Advances in Colloidal Assembly: The Design of Structure and Hierarchy in Two and Three Dimensions. *Chemical Reviews* 2015, **115**(13)**:** 6265-6311.
26. Stefik M, Guldin S, Vignolini S, Wiesner U, Steiner U. Block copolymer self-assembly for nanophotonics. *Chemical Society Reviews* 2015, **44**(15)**:** 5076-5091.
27. Watanabe K, Hoshino T, Kanda K, Haruyama Y, Matsui S. Brilliant Blue Observation from a Morpho -Butterfly-Scale Quasi-Structure. *Japanese Journal of Applied Physics* 2005, **44**(1L)**:** L48.
28. Lin SY, Fleming JG, Hetherington DL, Smith BK, Biswas R, Ho KM, *et al.* A three-dimensional photonic crystal operating at infrared wavelengths. *Nature* 1998, **394**(6690)**:** 251-253.
29. Rockstuhl C, Fahr S, Bittkau K, Beckers T, Carius R, Haug FJ, *et al.* Comparison and optimization of randomly textured surfaces in thin-film solar cells. *Opt Express* 2010, **18**(S3)**:** A335-A342.
30. John S. Why trap light? *Nat Mater* 2012, **11**(12)**:** 997-999.
31. Qi M, Lidorikis E, Rakich PT, Johnson SG, Joannopoulos JD, Ippen EP, *et al.* A three-dimensional optical photonic crystal with designed point defects. *Nature* 2004, **429**(6991)**:** 538-542.
32. Bayindir M, Temelkuran B, Ozbay E. Tight-Binding Description of the Coupled Defect Modes in Three-Dimensional Photonic Crystals. *Physical Review Letters* 2000, **84**(10)**:** 2140-2143.
33. Noda S, Chutinan A, Imada M. Trapping and emission of photons by a single defect in a photonic bandgap structure. *Nature* 2000, **407**(6804)**:** 608-610.
34. Vasco JP, Hughes S. Statistics of Anderson-localized modes in disordered photonic crystal slab waveguides. *Physical Review B* 2017, **95**(22)**:** 224202.

35. Wagner MR, Graczykowski B, Reparaz JS, El Sachat A, Sledzinska M, Alzina F, *et al.* Two-Dimensional Phononic Crystals: Disorder Matters. *Nano Letters* 2016, **16**(9)**:** 5661-5668.
36. Gorkunov MV, Gredeskul SA, Shadrivov IV, Kivshar YS. Effect of microscopic disorder on magnetic properties of metamaterials. *Physical Review E* 2006, **73**(5)**:** 056605.
37. Wiersma DS. Disordered photonics. *Nat Photon* 2013, **7**(3)**:** 188-196.
38. Wiersma DS. The physics and applications of random lasers. *Nature Physics* 2008, **4:** 359.
39. Kelzenberg MD, Boettcher SW, Petykiewicz JA, Turner-Evans DB, Putnam MC, Warren EL, *et al.* Enhanced absorption and carrier collection in Si wire arrays for photovoltaic applications. *Nat Mater* 2010, **9:** 239.
40. Vardeny ZV, Nahata A, Agrawal A. Optics of photonic quasicrystals. *Nat Photon* 2013, **7:** 177.
41. Xu Y, Chiu J, Miao L, He H, Alpichshev Z, Kapitulnik A, *et al.* Disorder enabled band structure engineering of a topological insulator surface. *Nature Communications* 2017, **8:** 14081.
42. Potyrailo RA, Ghiradella H, Vertiatchikh A, Dovidenko K, Cournoyer JR, Olson E. Morpho butterfly wing scales demonstrate highly selective vapour response. *Nat Photon* 2007, **1**(2)**:** 123-128.
43. Potyrailo RA, Bonam RK, Hartley JG, Starkey TA, Vukusic P, Vasudev M, *et al.* Towards outperforming conventional sensor arrays with fabricated individual photonic vapour sensors inspired by Morpho butterflies. *Nat Commun* 2015, **6**.
44. Li Q, Zeng Q, Shi L, Zhang X, Zhang K-Q. Bio-inspired sensors based on photonic structures of Morpho butterfly wings: a review. *Journal of Materials Chemistry C* 2016, **4**(9)**:** 1752-1763.
45. Kinoshita S, Yoshioka S, Kawagoe K. Mechanisms of structural colour in the Morpho butterfly: cooperation of regularity and irregularity in an iridescent scale. *Proceedings of the Royal Society B: Biological Sciences* 2002, **269**(1499)**:** 1417-1421.
46. Saito A, Yonezawa M, Murase J, Juodkazis S, Mizeikis V, Akai-Kasaya M, *et al.* Numerical Analysis on the Optical Role of Nano-Randomness on the Morpho Butterfly's Scale. *Journal of Nanoscience and Nanotechnology* 2011, **11**(4)**:** 2785-2792.
47. Vukusic P, Sambles JR, Lawrence CR, Wootton RJ. Quantified interference and diffraction in single Morpho butterfly scales. *Proceedings of the Royal Society B: Biological Sciences* 1999, **266**(1427)**:** 1403-1403.
48. Song B, Johansen VE, Sigmund O, Shin JH. Reproducing the hierarchy of disorder for Morpho-inspired, broad-angle color reflection. *Scientific Reports* 2017, **7:** 46023.
49. Saito A, Yoshioka S-y, Kinoshita S. Reproduction of the Morpho butterfly's blue: arbitration of contradicting factors. 2004; 2004. p. 188-194.
50. Alberto P, Raymond CYA, Heungsoo K, Nicholas AC, Scott AM. Laser 3D micro-manufacturing. *Journal of Physics D: Applied Physics* 2016, **49**(22)**:** 223001.
51. Kasko AM, Wong DY. Two-photon lithography in the future of cell-based therapeutics and regenerative medicine: a review of techniques for hydrogel patterning and controlled release. *Future Medicinal Chemistry* 2010, **2**(11)**:** 1669-1680.
52. Truby RL, Lewis JA. Printing soft matter in three dimensions. *Nature* 2016, **540**(7633)**:** 371-378.
53. Wu S, Serbin J, Gu M. Two-photon polymerisation for three-dimensional micro-fabrication. *Journal of Photochemistry and Photobiology A: Chemistry* 2006, **181**(1)**:** 1-11.
54. Gissibl T, Thiele S, Herkommer A, Giessen H. Two-photon direct laser writing of ultracompact multi-lens objectives. *Nat Photon* 2016, **10**(8)**:** 554-560.
55. Park SH, Yang DY, Lee KS. Two-photon stereolithography for realizing ultraprecise three-dimensional nano/microdevices. *Laser & Photonics Reviews* 2009, **3**(1-2)**:** 1-11.
56. Nishiyama H, Hirata Y. Femtosecond Laser Nonlinear Lithography. In: Wang M (ed). *Lithography*. InTech: Rijeka, 2010, p Ch. 04.
57. Maruo S, Fourkas JT. Recent progress in multiphoton microfabrication. *Laser & Photonics Reviews* 2008, **2**(1-2)**:** 100-111.
58. Koch J, Fadeeva E, Engelbrecht M, Ruffert C, Gatzen HH, Ostendorf A, *et al.* Maskless nonlinear lithography with femtosecond laser pulses. *Appl Phys A* 2006, **82**(1)**:** 23-26.
59. Bhattacharjee N, Urrios A, Kang S, Folch A. The upcoming 3D-printing revolution in microfluidics. *Lab Chip* 2016, **16**(10)**:** 1720-1742.

60. Hohmann JK, Renner M, Waller EH, von Freymann G. Three-Dimensional μ-Printing: An Enabling Technology. *Adv Opt Mater* 2015, **3**(11)**:** 1488-1507.
61. Thiel M, Fischer J, von Freymann G, Wegener M. Direct laser writing of three-dimensional submicron structures using a continuous-wave laser at 532 nm. *Appl Phys Lett* 2010, **97**(22)**:** 221102.
62. LaFratta CN, Fourkas JT, Baldacchini T, Farrer RA. Multiphoton Fabrication. *Angewandte Chemie International Edition* 2007, **46**(33)**:** 6238-6258.
63. von Freymann G, Ledermann A, Thiel M, Staude I, Essig S, Busch K, *et al.* Three-Dimensional Nanostructures for Photonics. *Adv Funct Mater* 2010, **20**(7)**:** 1038-1052.
64. Deubel M, von Freymann G, Wegener M, Pereira S, Busch K, Soukoulis CM. Direct laser writing of three-dimensional photonic-crystal templates for telecommunications. *Nat Mater* 2004, **3**(7)**:** 444-447.
65. LaFratta C, Baldacchini T. Two-Photon Polymerization Metrology: Characterization Methods of Mechanisms and Microstructures. *Micromachines* 2017, **8**(4)**:** 101.

Chapter 2. Fundamentals

This part of the thesis will focus on the theoretical aspects necessary to understand natural photonic crystals and the working principle of two-photon lithography. It will also provide the background knowledge for a novel principle exploited in this thesis, i.e., standing wave enhanced two-photon lithography.

2.1. Wave Theory

2.1.1. *Electromagnetic Waves*

What we call light is a specific radiation which is perceivable by the human eye. Light displays a dual nature, i.e., it shows behaviour associated either with electromagnetic waves following Maxwell's equations or with particles called photons. Electromagnetic waves, in general, are described by transverse waves consisting of two fields oriented perpendicular to each other, the electric field $\vec{E}$ and a magnetic field $\vec{B}$. The simplest description of an electromagnetic wave is that of a harmonic wave that exhibits a constant periodicity in space and time (**Figure 2-1a**).

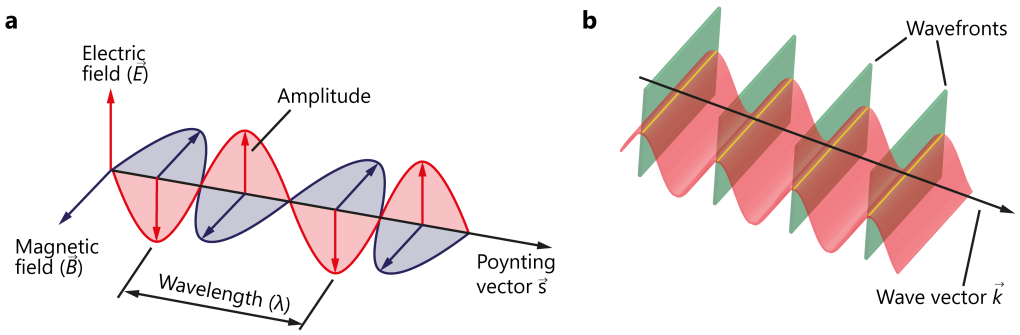

Figure 2-1. Electromagnetic waves

(a) Schematic of the simplest type of an electromagnetic wave, a harmonic wave, which is defined by a sine function with a wavelength λ or alternatively frequency f, and the amplitude A. The electric component is indicated in red, the magnetic component in blue; (b) Schematic of the spatial propagation of an electromagnetic wave indicated by wavefronts and the Poynting vector $\vec{S}$ also called wave vector $\vec{k}$.

In the case of a harmonic wave, the periodicity follows a sine function, where the distance between the adjacent maxima defines the wavelength λ. The propagation direction of spreading waves is expressed by the Poynting vector $\vec{S}$, whose direction is perpendicular to the wave fronts (**Figure 2-1b**). This vector $\vec{S}$ of a wave is generally described by:

$$\vec{S} = \vec{E} \times \vec{H} \qquad (1)$$

where the auxiliary field $\vec{H}$ depends on the magnetic field $\vec{B}$, the vacuum permeability μ_0 and the permeability μ of the medium:

$$\vec{H} = \frac{\vec{B}}{\mu_0 \mu} \tag{2}$$

The intensity I of a wave represents the transferred power per unit area and is defined by the magnitude of $\vec{S}$ averaged over time. I is proportional to the square of the amplitude A of the wave:

$$I \sim A^2 \tag{3}$$

Since the influence of the magnetic auxiliary field is negligible at optical frequencies, wave functions are often represented only by the electric component $\vec{E}$ of the wave. The electric field $\vec{E}$ at a particular location $\vec{x}$ and time t of a harmonic wave is given by:

$$\vec{E}(x,t) = \vec{A_0} \sin \vec{k} \, (\vec{x} - \vec{v}t) \tag{4}$$

where v is the propagation speed of the wave and $\vec{k}$ is the wave vector[1]. In most cases, the vector $\vec{k}$ is equivalent to the Poynting vector $\vec{S}$ described above and is therefore often used as a substitute. Differences between the two vectors are found only in birefringent materials. The wavenumber k is the absolute value of $\vec{k}$ and is defined as:

$$k = |\vec{k}| = \left|\frac{2\pi}{\lambda}\right| \tag{5}$$

The usage of $\vec{k}$ has the advantage that the value of the sine function becomes dimensionless and therefore can be solved in a straightforward manner without any further mathematical assumptions.

The velocity of a wave can be either expressed by the relation between λ and the period τ, the time a wave needs to propagate by one wavelength λ, or by the number of wavelengths occurring during a certain time period, called the frequency f of a wave. The relations are given with:

$$v = \frac{\lambda}{\tau} = \lambda f \tag{6}$$

One harmonic oscillation of an electromagnetic wave following a sine function can be descriptively depicted by means of a unit circle as done in **Figure 2-2**. The following relations are obtained assuming that one oscillation, i.e., one wavelength λ, corresponds to a circle with a circumference of 2π and a full rotation of 360°:

$$\lambda \equiv 2\pi \equiv 360° \tag{7}$$

Each angle ϕ of the circle defines a position on the sine curve. At 0, π, 2π (equivalent to 0°, 180°, and 360°) the projection to the y-axis is 0, while at $\pi/2$, $3\pi/2$ (equivalent to 90° and 270°) the maximum

and minimum values of 1 and -1 are reached. A measure of how fast this rotation is performed is called the angular velocity ω, which relates to the velocity v of a wave defined by equation (6):

$$\boldsymbol{\omega = 2\pi f = \frac{2\pi}{\tau} \equiv \frac{\lambda}{\tau} = v} \tag{8}$$

Using v and Planck's constant h, the energy E transported by a photon of a particular wavelength λ can be calculated according to:

$$\boldsymbol{E = hf = \frac{h\omega}{\lambda}} \tag{9}$$

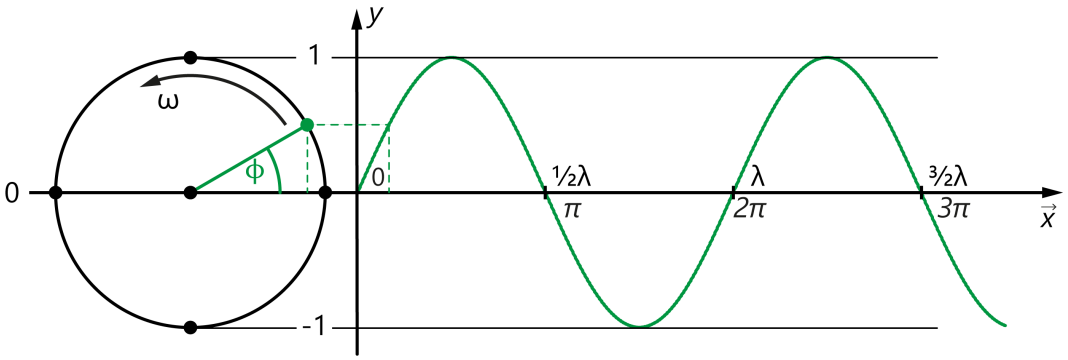

Figure 2-2. Visualisation of a harmonic oscillation by a unit circle

The sine function of a harmonic wave can be visualised by a rotation of a unit circle, where each angle ϕ is assigned to values of the function. Characteristic angles are 90° and 270° as well as 180° and 0°/360°. The former corresponds to the extrema, while the latter defines intersections with the x-axis and are therefore 0. ω defines the angular velocity, i.e., the rotation velocity along the circle, and thus, the velocity of the wave.

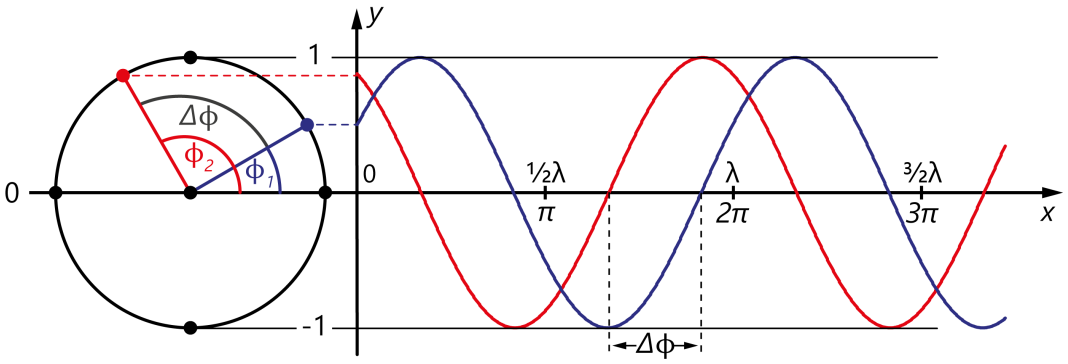

Figure 2-3. Phases and phase shifts of waves

Two harmonic waves corresponding to the phases ϕ = 1/6π (blue) and ϕ = 2/3π (red). The phase of both waves is shifted by $\Delta\phi = \pi/2$.

The angle ϕ denotes to the phase of a wave and defines the state at a particular time t. An example of two waves differing in the phase angles, ϕ = 1/6π (blue) and ϕ = 2/3π (red), is shown in **Figure 2-3**. The difference between two phase angles, and thus, the lateral and temporal displacement of two waves is called phase shift $\Delta\phi$. ϕ can be calculated by:

$$\boldsymbol{\phi = (\vec{k}\vec{x} - \vec{\omega}t)} \tag{10}$$

2.1.2. *Superposition of Waves*

Typically, every theoretical problem in optics can be sufficiently solved by assuming a superposition of harmonic waves. Mathematically, two or more overlaying waves can be described by the superposition principle, which states that, if $\vec{E}_1$ and $\vec{E}_2$ were separate solutions of a particular wave equation, ($\vec{E}_1$ + $\vec{E}_2$) would also solve this equation. Physically this means that waves situated at a particular place at a particular time form a new wave, whose function is expressed by the sum of the individual waves involved. This means that the amplitude A of the resulting wave is calculated by the addition of the amplitudes of the superimposing waves. If these waves have the same frequency and a constant phase difference, they are called coherent waves and can form temporally and spatially constant interference.

Two extreme cases of possible superpositions, called fully constructive and fully destructive interference, are illustrated in **Figure 2-4a,b**. In the case of fully constructive interference (**Figure 2-4a**), the two initial waves are in phase, that is, that both, the maxima and minima amplitudes of both harmonic waves, are entirely overlapping. As a result, the two amplitudes add up to form a resulting wave of higher amplitude. In the case of fully destructive interference (**Figure 2-4b**), the waves are maximally out of phase, i.e., they have a phase shift of 180° (π or $\lambda/2$), resulting in a cancelation of the waves.

Standing waves are a special case of superimposed waves, which are formed by two waves traveling in opposite directions. This can be implemented e.g., by shining coherent light onto a reflective surface, which enforces a constant phase relation between the incident and the reflected wave. **Figure 2-4c** displays a standing wave at different points in time. The standing wave is caused by interference of the incident (in red) and a reflected wave (in blue). The reflection occurs at the interface illustrated at the left-hand side and is accompanied by a 180° phase shift of the phase. The result of the superposition of these two waves is presented in green. As the wavelengths of the incident and the reflected wave are identical, the resulting wave has the same wavelength, too. Two types of points of the resulting wave are of particular significance: i) so called nodes, which occur at multiples of $\lambda/2$ from the reflecting surface. Here, the amplitude is always 0; ii) antinodes occur between the nodes and are shifted by $\lambda/4$ with respect to the nodes. Here the amplitude reaches their extrema.

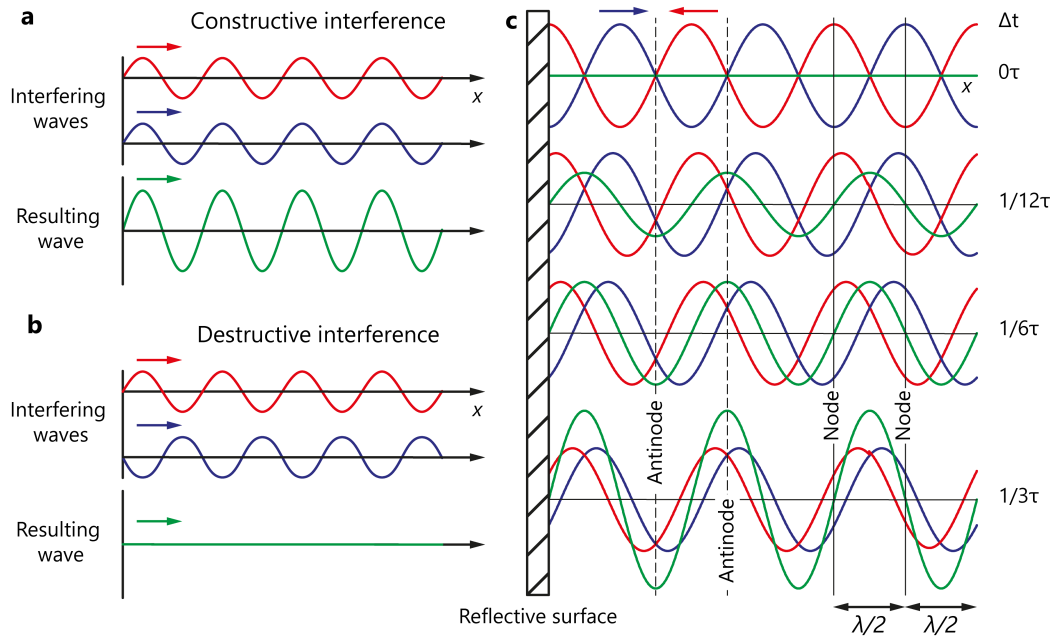

Figure 2-4. Constructive and destructive interference

(a) Fully constructive interference and (b) fully destructive interference shown for two harmonic waves perfectly in phase ($\Delta\phi = 0$) and out of phase ($\Delta\phi = \pi$), respectively. In the first case, the resultant wave exhibits higher amplitudes, in the second case a full cancelation of amplitudes occurs. (c) Schematic visualisation of standing waves (resulting from two identical waves traveling in opposite directions, the incident and reflected wave) in dependence on the phase at the reflective surface.

2.2. Coloured Light

2.2.1. *The Visible Spectrum*

Among the electromagnetic waves, the visible range is associated with wavelengths of 380 - 780 nm, each corresponding to a particular colour starting from violet at the shortest wavelength, ranging over blue, green, and yellow to red at the longest wavelength as illustrated in **Figure 2-5**. The colour impression we experience by looking into the sun is the superposition of all these waves resulting in a single appearance - white. If no waves of the visible spectrum enter our eyes, we experience black.

Although we see white when we look into the sun, not all wavelengths are needed to evoke a white appearance to our eye. White can be experienced by a superposition of so-called complementary colours or opposite colours, e.g., blue and yellow, or by a superposition of three basic colours, e.g., red (R), green (G), and blue (B). The latter is called RGB-palette and is widely used to generate different colours in computer or television screens, where red, green and blue light emitting elements form one shining spot, a pixel, of the screen. By adjusting the illumination of these elements independently the colour of the pixel can be changed. The sum of all pixels of a screen creates the image. This image can be varied by a readjustment of the illumination and the fractions of the red, green and blue waves.

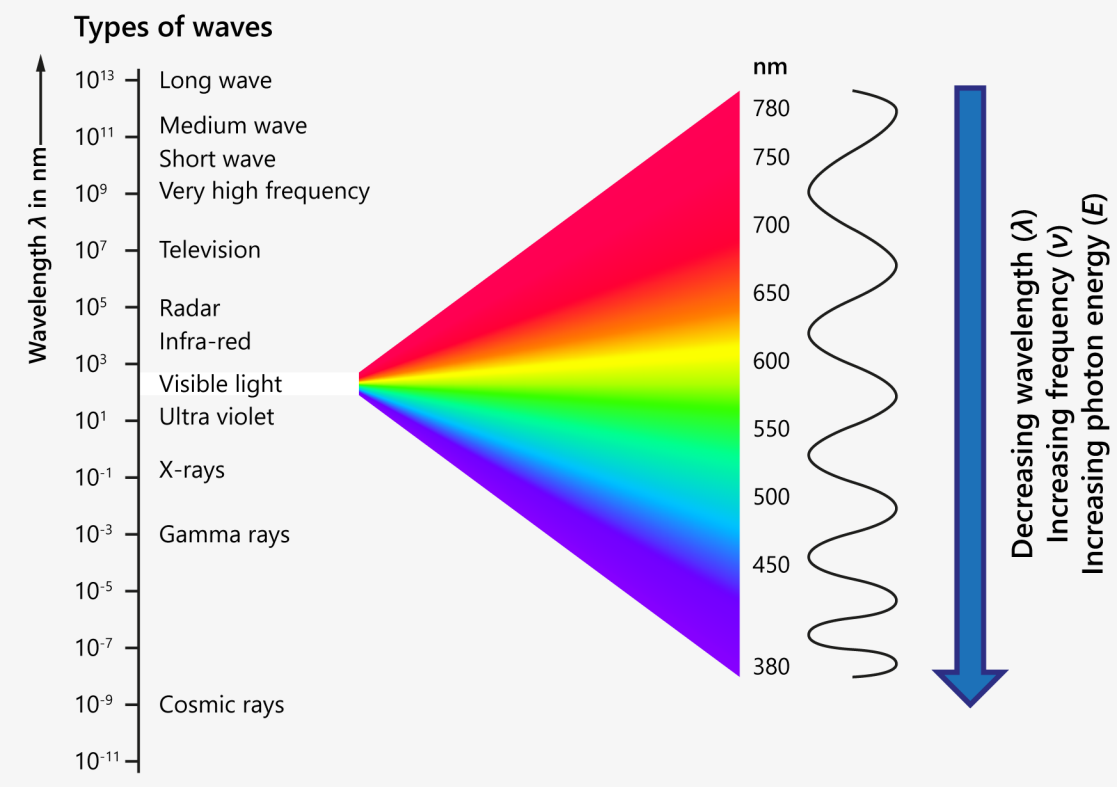

Figure 2-5. Electromagnetic spectrum

Diagram showing the classification of electromagnetic waves depending on their wavelength with a focus on the visible spectrum.

The described visible range of electromagnetic waves is adjacent to wavelengths not detectable by our eyes. Light having wavelengths longer than red light is called infra-red (IR) radiation, whereas waves having shorter wavelengths than violet are called ultraviolet (UV) radiation. There are further types of electromagnetic waves, as X-rays or microwaves, but they are irrelevant for this work and will not be described further.

2.2.2. *Optical Appearance of Surfaces*

A surface which equally reflects every individual wavelength of the visible spectrum appears white and shiny. A matt white is obtained if such a surface additionally scatters the light without a preferred direction. If all wavelengths are partly absorbed to the same extent, a grey appearance is obtained, which becomes darker with increasing light absorption. Black surfaces absorb almost 100% of the light. Colour is introduced if the absorption differs for the different wavelengths. As a result, some wavelengths are less intense in the reflected spectrum, which appears as colour to our eyes. A small example: if white light shines on a surface absorbing light with a wavelength of 500 nm, green light is absorbed and not reflected. Consequently, the reflected light is composed mostly of blue and red wavelengths. The surface appears purple.

Besides absorption, the effect of colouration can also be caused by periodic material systems, which provide a preferential transmission, diffraction, or reflection of certain wavelengths. These colours are called structural colours and are typically iridescent and angle dependent in appearance. This contrasts with a surface coloured by absorption, where the colouration is not affected by the angle and direction of observation. Besides light and observation conditions, the appearance of a structural coloured surface is further dependent on the material, the size and the particular shape of the periodic elements.

2.3. Light Interaction with Structural Elements

2.3.1. *Diffraction and the Fresnel-Huygens-Principle*

The pioneer in diffraction research was the Italian physicist Francesco Grimaldi (1618-1663)[2], who stated that diffraction occurs always if waves are hindered in their propagation[1]. Diffraction involves phase shifts and changes in the direction of the wave propagation as well as a characteristic superposition of different waves, which is largely determined by the diffracting objects. A couple of years later the Dutch mathematician and physicist Christiaan Huygens (1629-1695) published the first explanation for the diffraction phenomenon, nowadays known as Huygens principle[3]. According to Huygens each spot of a primary wave at a time t_1 can be the source of a new, spherical elementary wave, as shown in **Figure 2-6a**. This wave propagates with the same frequency and velocity as the initial wave and the sum of these waves determines the form of the resulting wave at any subsequent time t_2. Fresnel improved this principle by adding interference to Huygen's assumptions[4]. In 1802 Young provided the experimental proof by his single and double-slit experiments[1]. The experimental set-up of the latter is shown in **Figure 2-6b**. This experiment involved a light beam, which was directed on two subsequent barriers possessing one and two slits, respectively. The first barrier served as means to obtain a coherent light beam, which then illuminated the slits of the second barrier behind. The resulting light pattern, displayed by a screen mounted at a small distance behind the second barrier, revealed a periodical alternation of bright and dark areas, which correlated with the maxima and minima of interfering waves. The pattern exhibited one main maximum, which is surrounded by less strong local maxima, which again were surrounded by less intense maxima and so on. If this pattern is compared to the pattern resulting from a single slit experiment (**Figure 2-7b**), it becomes obvious that the intensities of the maxima follow the distribution of the single slit diffraction.

From the geometrical dependence of the experiment, displayed in **Figure 2-7a** Young concluded that the geometrical relation of diffraction can be expressed by:

$$\sin^{-1}\frac{\Delta s}{a} = \tan^{-1}\frac{x}{d} \qquad (11)$$

where Δs is the difference in the length of the optical path between the new emerging elementary waves, a the distance between the two slits, x the location of the light incidence on the screen and d the distance between the slits and the screen. Therefore, the period Δx between two maxima or two minima is approximately given by:

$$\Delta x \approx \lambda \frac{d}{a} \tag{12}$$

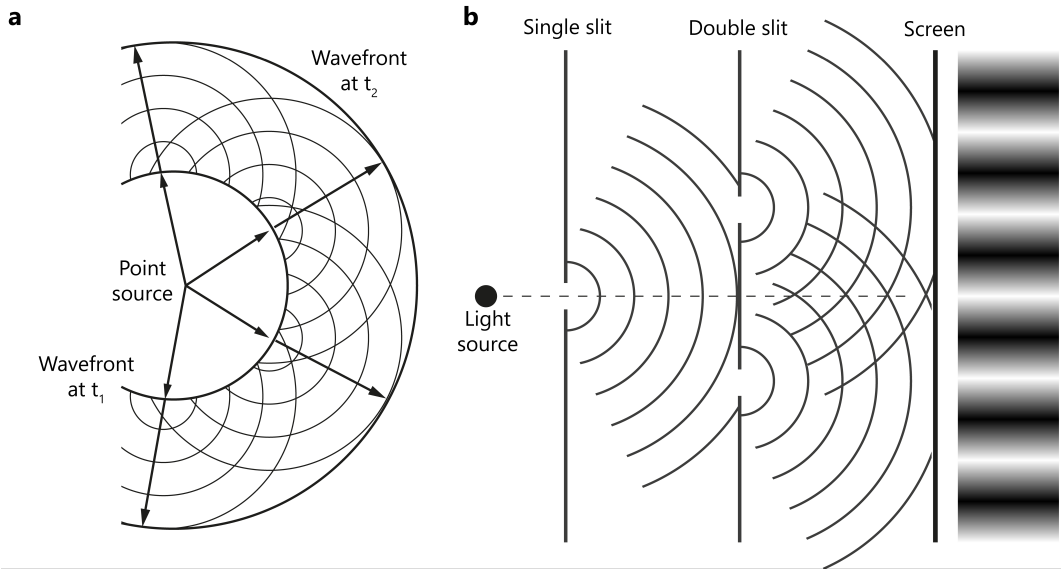

Figure 2-6. Huygens-Fresnel-Principle and Young's double slit experiment

(a) Huygens-principle of elementary waves, where a primary wave at a time t_1 can be expressed by multiple elementary waves, which again form a coherent wave at a time t_2; (b) Schematic of Young's double slit experiment showing the wave character of light due to occurring interference phenomena.

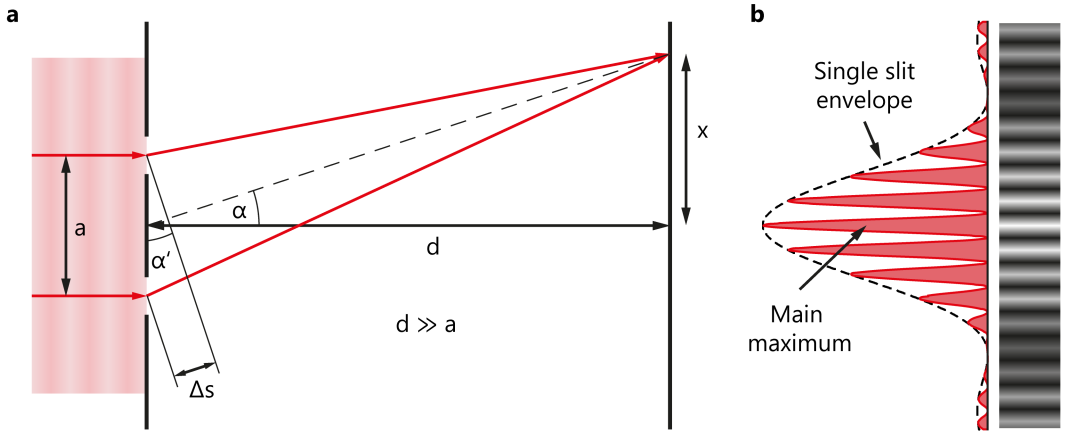

Figure 2-7. Geometry and profile example of diffraction at a double slit

(a) Geometrical dependence of diffraction shown for a double slit experiment; a: distance between the slits, α: angle with respect to the normal, d: distance to the screen, Δs: difference in path distance, x: position on the screen. (b) a possible intensity profile resulting from diffraction at a double slit, which follows the diffraction envelope of a single slit (dashed lines).

2.3.2. *Diffraction at Periodical Structures*

More comprehensive descriptions of diffraction at periodic structures were formulated by William Lawrence Bragg and Max von Laue. The latter describes diffraction using wave vectors and reciprocal lattice vectors, while the former depicts diffraction in a simple geometrical way. For simplicity and as it is sufficient in the context of this thesis, only the Bragg's Law will be discussed in more detail at this point.

The geometrical conditions described by the Bragg's law are illustrated in **Figure 2-8a**. Two parallel beams with identical wavelength and phase are assumed to be scattered at two different planes of a periodical structure with the structure distance d. In this particular case, the angle of incidence θ_i corresponds to the angle of diffraction θ_m resulting in $\theta = \theta_i = \theta_m$. This is often referred to as theta-2-theta configuration. In this case, one beam is scattered directly at the first plane while the second beam propagates to the second plane and is scattered there. The additional traveling distance $2\Delta x$ is called path difference (indicated in blue), and can be calculated using d and θ:

$$\boldsymbol{\Delta x = d \sin \theta} \tag{13}$$

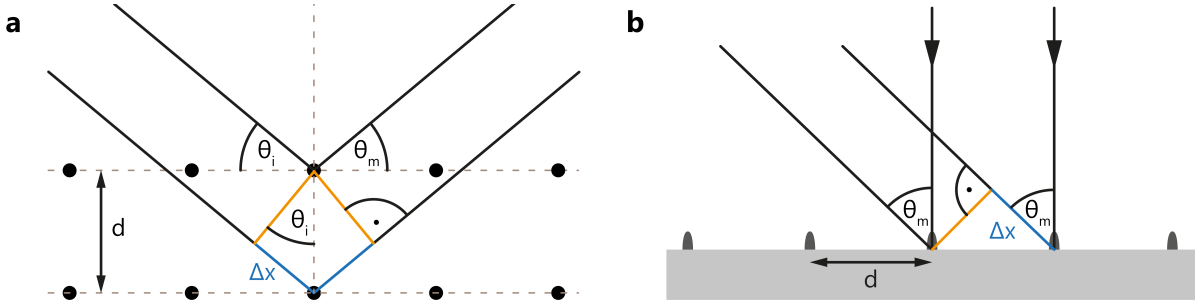

Figure 2-8. Diffraction at periodic structures

(a) Diffraction of waves, when the angle of incidence θ_i corresponds to the angle of diffraction θ_m; here, the path difference results in $2\Delta x$. (b) Diffraction of waves in case of a perpendicular light incidence; here, the path difference is Δx. Both path differences, depicted in blue, depend on the distance d between the structures.

As constructive interference occurs only if two waves are in phase (see also Chapter 2.1.2), two scattered waves can only interfere constructively, when the path difference equals multiples of the incident wavelength:

$$\boldsymbol{2\Delta x = m\lambda} \tag{14}$$

By combining the two equations (13) and (14), Bragg's equation is obtained:

$$\boldsymbol{m\lambda = 2d \sin \theta} \tag{15}$$

From this equation it becomes evident that the angle θ changes for each wavelength λ in a periodic system with constant structure distance d. This relation is indeed the reason why photonic crystals exhibit a characteristic rainbow iridescence with changing viewing angles.

The equation changes slightly, when the angle of incidence is perpendicular to the plane of the periodical elements (**Figure 2-8b**), e.g., in the case of a top illumination on a structured surface as found in microscopy. In this situation, the incident beams have the same path lengths, and the path difference is determined by Δx only. This results in the following equation, also known as grid equation:

$$\boldsymbol{m\lambda = d \sin \theta_m} \tag{16}$$

If the waves, though, have an incident angle θ_i different from 0° with respect to the surface normal an additional path difference Δx_i of the incident wave must be considered. This leads to the quite general equation:

$$\boldsymbol{d\,(\sin \theta_m + \sin \theta_i) = m\lambda} \tag{17}$$

or solved for the scattering angle:

$$\boldsymbol{\theta_m = \sin^{-1}\left(\frac{m\lambda}{d} - \sin \theta_i\right)} \tag{18}$$

An example for a diffracted wave containing several wavelengths is displayed by **Figure 2-9a**. Here, a violet wave is formed by a superposition of a shorter wavelength λ_{blue} and a longer wavelength λ_{red}. This wave is diffracted at a periodical grid perpendicular to the propagation direction of the waves. As the solution of the equation (16) for the 0$^{\text{th}}$ order (m = 0) results for both wavelengths, λ_{blue} and λ_{red} in a scattering angle of 0°, the wave vectors of the blue and red interfering waves do not change and the 0$^{\text{th}}$ order appears violet.

At higher diffraction orders (m = 1;2;3…) this changes. Here, the solutions of the equation (16) always result in $\theta_{blue}, \theta_{red} \neq 0°$ and $\theta_{blue} < \theta_{red}$. This is expressed by a splitting of the blue wave and the red wave at higher orders, where the diffracted blue light will be located always closer towards the zero order than the red. From the same evaluation it can be concluded that the difference between the two diffraction angles $\Delta\theta_{red}$ and $\Delta\theta_{blue}$ increases with the diffraction order ($\Delta\theta_{m1} < \Delta\theta_{m2} < \Delta\theta_{m3} \ldots$) leading to a broadening of the spectrum. The described behaviour can be observed in the examples of real diffraction patterns shown in **Figure 2-9b**, where a diffraction of a monochromatic wave from a green laser source is compared with a corresponding diffraction pattern from a white light source containing the entire wavelengths spectrum. This comparison clearly shows the occurrence of different diffraction orders explained beforehand and the difference in diffraction of different wavelengths.

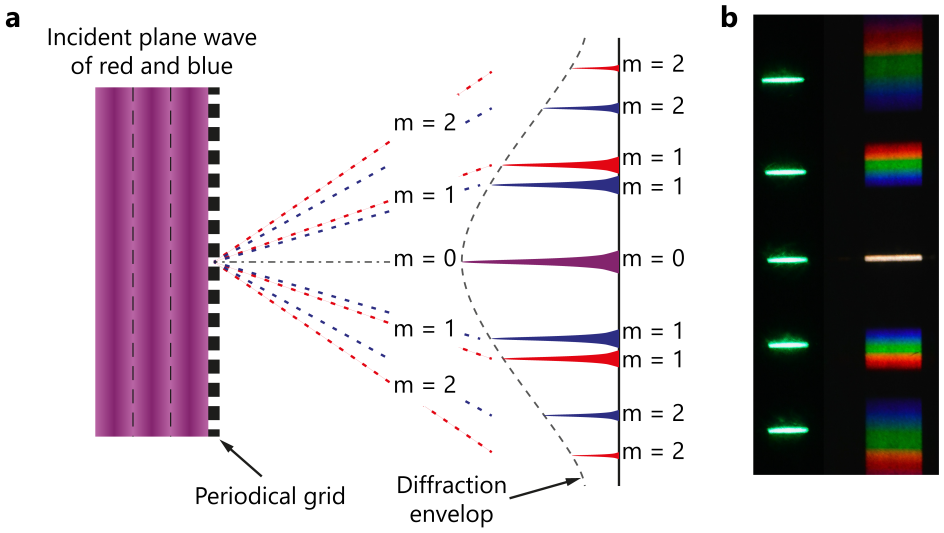

Figure 2-9. Diffraction of superposed waves at periodical grids

(a) Diffraction of a superposed, plane wave of a blue and red wavelength at a periodical grid (b) Comparison of a diffraction spectra of a monochromatic light exhibiting only one wavelength and a spectrum obtained with white light (image provided by Peter Rogin).

2.3.3. *Refractive Index, an Important Optical Constant*

When a wave propagates through media and not through vacuum, its electromagnetic field interacts with the electric charge distribution of the respective medium, resulting in a change of the phase velocity, and thus, the wavelength λ of the wave. The parameter that characterises this change is the dimensionless absolute refractive index n:

$$\boldsymbol{n = \frac{v_0}{v_M} = \frac{\lambda_0}{\lambda_M}} \tag{19}$$

where v_0 and v_M are the phase velocities and λ_0 and λ_M the wavelengths of the wave in vacuum and in the medium, respectively. The frequency f is not affected. The refractive index ratio of two materials exhibiting different refractive indices is called relative refractive index, which plays an important role in the propagation of light at interfaces between two materials, as explained in the next chapter.

2.3.4. *Refraction, Reflection and Transmission at Optical Interfaces*

When light experiences a change in refractive index, various optical phenomena occur simultaneously. These phenomena include refraction, absorption, transmission, as well as specular reflection and diffuse scattering (**Figure 2-10a**). Following the principle of conservation of energy, the relation between the incident beam I on one side and the specular reflection R, scattering S, and refraction RE, which is the sum of the absorption A and transmission T, on the other side can be expressed as follows:

$$\boldsymbol{R + S + RE = R + S + A + T = I} \tag{20}$$

All of them except diffuse scattering, which refers mainly to non-directional light interactions, are direction dependent phenomena following specific geometrical laws. The geometrical relations are indicated in **Figure 2-10b**, where a monochromatic beam with a wave vector $\vec{k}_i$ is considered to fall on a flat interface between two homogeneous media (with the refractive indices $n_1 < n_2$) with an incidence angle θ_i.

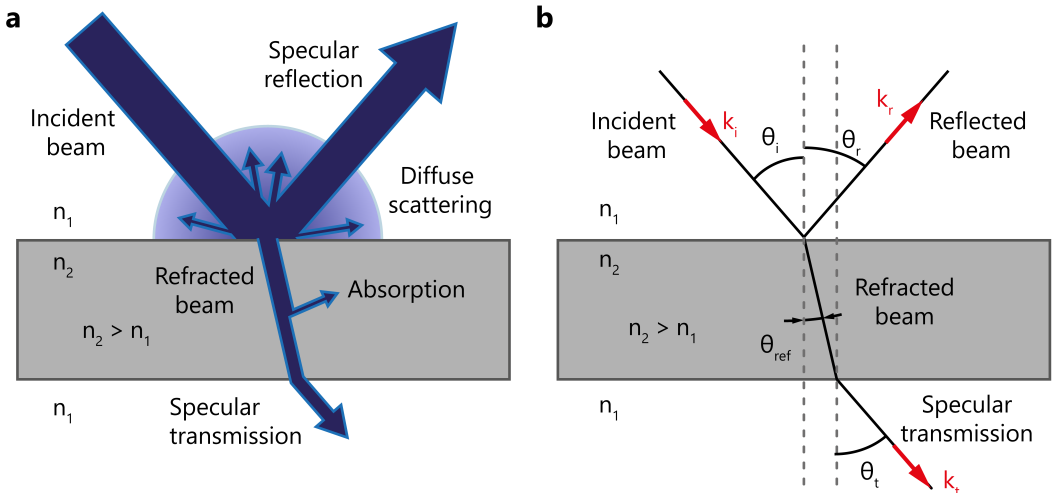

Figure 2-10. Light interactions at flat interfaces

(a) Light interactions occurring at interfaces between two media: refraction, transmission, absorption, spectral reflection and diffuse scattering. (b) Schematic of the geometrical relations. $\vec{k}_i$: wave vector of the incident wave; $\vec{k}_r$: wave vector of the reflected wave; $\vec{k}_{ref}$: wave vector of the refracted wave; $\vec{k}_t$: wave vector of the transmitted wave; θ_i: incidence angle; θ_r: reflection angle; θ_{ref}: refraction angle; θ_t: transmitted angle; n_1, n_2: refractive indices of the media. The propagation of light in both schemes assumes $n_1 < n_2$ and a perfectly flat interface.

Specular reflected light constitutes the fraction of light which is reflected back into the originating medium at a reflection angle θ_r following the law of reflection:

$$\boldsymbol{\theta_r = \theta_i} \tag{21}$$

If the refractive index n_2 is higher than that of the initial medium n_1, the phase of the reflected wave will change by 180°. If not, typically no phase change will occur.

Refracted light constitutes the fraction which enters the medium. In this case, differences in refractive indices do not affect the phase but the propagation direction of the wave. This is described by the Snell's law:

$$\boldsymbol{n_1 \sin \theta_i = n_2 \sin \theta_{ref}} \tag{22}$$

where θ_{ref} is the angle of refraction, n_1,and n_2 are the refractive indices of the different media, and θ_i the angle of incidence. Here, two principle situations can be distinguished: the transition of light from an optically less dense material into a denser medium, i.e. $n_1 < n_2$ (first interface in **Figure 2-10b**), and the transition of light from an optically dense material into a less dense medium, i.e. $n_1 > n_2$ (second

interface **Figure 2-10b**). In the former case, the angle θ_{ref} becomes smaller regarding the normal of the interface (dashed lines in **Figure 2-10b**), while it increases in the latter case. As light transmitted through a material undergoes two equivalent, but opposite refraction events, the directions of the initial and the transmitted light are identical with $\theta_i = \theta_t$.

Fresnel's equations, which are based on Maxwell's equations, allow the prediction of the refracted or reflected light intensity in a given situation. The reflectivity is usually given for two conditions: p-polarised R_p and s-polarised R_s light, where the oscillation of the wave is oriented parallel to the plane of incidence in the former and in perpendicular direction in the latter condition. R_p and R_s can be calculated for non-magnetic materials as follows:

$$\boldsymbol{R_p} = \left|\frac{\boldsymbol{n_1 \cos \theta_i - n_2 \cos \theta_r}}{\boldsymbol{n_1 \cos \theta_i + n_2 \cos \theta_r}}\right|^{\boldsymbol{2}} \tag{23}$$

$$\boldsymbol{R_s} = \left|\frac{\boldsymbol{n_1 \cos \theta_r - n_2 \cos \theta_i}}{\boldsymbol{n_1 \cos \theta_r + n_2 \cos \theta_i}}\right|^{\boldsymbol{2}} \tag{24}$$

For the special case of normal incidence with $\theta_i = \theta_r = 0°$, where s- and p-polarised light are equivalent, the calculation of reflectivity can be simplified to:

$$\boldsymbol{R_{ps}} = \left|\frac{\boldsymbol{n_1 - n_2}}{\boldsymbol{n_1 + n_2}}\right|^{\boldsymbol{2}} \tag{25}$$

From this equation it becomes obvious that the amount of reflected light increases with an increasing difference in the refractive indices. For smaller differences, however, the amount of reflected light is decreased, and consequently, the transmission has to increase according to equation (20), assuming that the medium is not fully absorptive with $A = 0$.

2.3.5. *Reflection at Single Films and in Multi-Thin Film Systems*

The usage of thin-film systems, which utilise the aforementioned effects of reflection and refraction, is of significant relevance in a wide spectrum of technical applications. Depending on the type of stacking and the materials, a multi-layer film can either provide distinct and strong reflection, e.g., in the case of dielectric mirrors, or decrease the reflection to a minimum as found in anti-reflection coatings. The difference in behaviour is mainly dependent on two factors: the optical properties of the materials used and the film thicknesses and periodicities of these materials. A reflective coating can be realised, for example, by alternating layers of two materials with thicknesses of λ/4, where one material exhibits a high and the other a low refractive index.

This can be best rationalised by examining the simplest case of only one film on a substrate in air, as is illustrated in **Figure 2-11a**. This film has two interfaces, one between air and the film material (n_1, n_2)

and another between the film and the subjacent substrate (n_2, n_3). The relation between the refractive indices is considered to be $n_1 < n_2$ and $n_3 < n_2$.

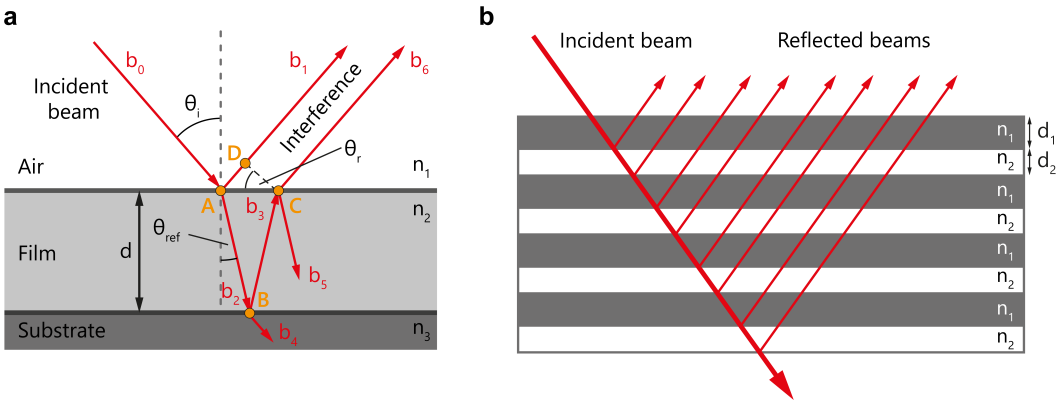

Figure 2-11. Thin film interference at one and multiple thin films

(a) Geometry of a single film interference with $n_1 < n_2 > n_3$: refractive indices of air, film material and substrate, respectively, d: thickness of the film, Θ_i: angle of incidence, Θ_r: angle of reflection, Θ_{ref}: the angle of refraction, b_0: initial beam, b_1: directly reflected beam at the interface n_1, n_2, b_2: refracted beam entering the film, b_3: beam reflected at interface n_2, n_3, b_4: beam entering the substrate, b_5: beam reflected at interface n_2, n_1, b_6: beam entering the air. (b) Multi thin-film interference with the thicknesses d_1,d_2 and refractive indices n_1, n_2, this graphic is simplified the sense that only reflection is presented at the individual layers.

As discussed in greater detail in Chapter 2.3.4, a beam b_0 with an incident angle Θ_i is partly reflected (beam b_1) with Θ_r (according to equation (21)) and partly refracted (beam b_2) with Θ_{ref} (according to equation (22)) at the first interface n_1, n_2. The phase of b_1 is shifted by 180° with respect to the incident beam b_0 due to the condition $n_1 < n_2$. The refracted beam b_2 propagates further through the material to the second interface n_2, n_3 and is again partly reflected (beam b_3) and refracted (beam b_4). In this situation, the phase does not shift during reflection, as $n_2 > n_3$. At the interface n_1, n_2, b_3 is again divided into two beams, b_5 and b_6. While b_5 is once more guided into the material, b_6 is refracted and exits the medium under the same propagation direction as beam b_1. Beams b_6 and b_1 can now interfere. The type of interference can be predicted by considering the optical path difference OPD in relation to the wavelength. Using the geometrical relations indicated in **Figure 2-11a** the OPD can be determined as follows:

$$\boldsymbol{OPD = n_2(\overline{AB} + \overline{BC}) - n_1(\overline{AD})} \tag{26}$$

With Snell's law (22) this equation can be transformed to:

$$\boldsymbol{OPD = 2n_2 d \cos \theta_{ref}} \tag{27}$$

where d is the film thickness, n_2 the refractive index of the film material, and θ_{ref} the angle of the refracted beam b_2. From the equation (27) it becomes evident that the OPD is affected by the thickness of the film, the angle of refraction Θ_{ref}, and thus the incidence angle Θ_i, as well as the refractive index of the used material.

For the example above, one phase shift of 180° must be considered due to the conditions $n_1 < n_2$ and $n_3 < n_2$. As a result, constructive interference will occur only if $OPD = m\lambda - \lambda/2$ where m is a positive integer. If $OPD = m\lambda$, the reflected waves will cancel each other leading to destructive interference. These conditions permute, if phase shifts occur at both interfaces ($n_1 > n_2 > n_3$) or at neither interface ($n_1 < n_2 < n_3$). The effect of the interfering waves can be enhanced by applying not only one film but stacking multiple film layers of at least two different materials (**Figure 2-11b**). If the layer thicknesses are chosen correctly interference of a certain wavelength will occurs not only between beam b_1 and b_6, but all beams reflected by all layer interfaces. By this means, surfaces either highly reflective or anti-reflective for particular wavelengths and angles can be manufactured only by changing the layer thicknesses.

2.3.6. *Surfaces with continuously changing refractive indices*

As explained above, anti-reflection properties of surfaces can be achieved by destructive interference, however, the effect is limited due to the strong dependence on the wavelength and incidence angle. To obtain a broadband anti-reflection, therefore, a different type of a multi-thin film system has to be used. In contrast to the multi-thin films introduced above, where optically dense and less dense media were alternated, films with incrementally increasing refractive indices can be used. By only slowly increasing the refractive index between adjacent layers the reflectivity at the single interfaces can be kept small, as can be deduced from equations (23) and (24). Instead of being reflected, the light is refracted towards the substrate. This is illustrated in **Figure 2-12a**. The brightness of the blue indicates the optical density, the darker the denser. In **Figure 2-12b** the same changes of the refractive index are plotted in dependence on the penetration depth z. In an ideal situation, the reflective index continuously increases as depicted in the last illustration in each row in **Figure 2-12**.

A similarly continuous increase of refractive index of a surface is found in nature on the eyes of moths, although this effect is not obtained by changing the materials properties at the eye's surface but the structure. This approach will be explained in more detail in Chapter 3.2.

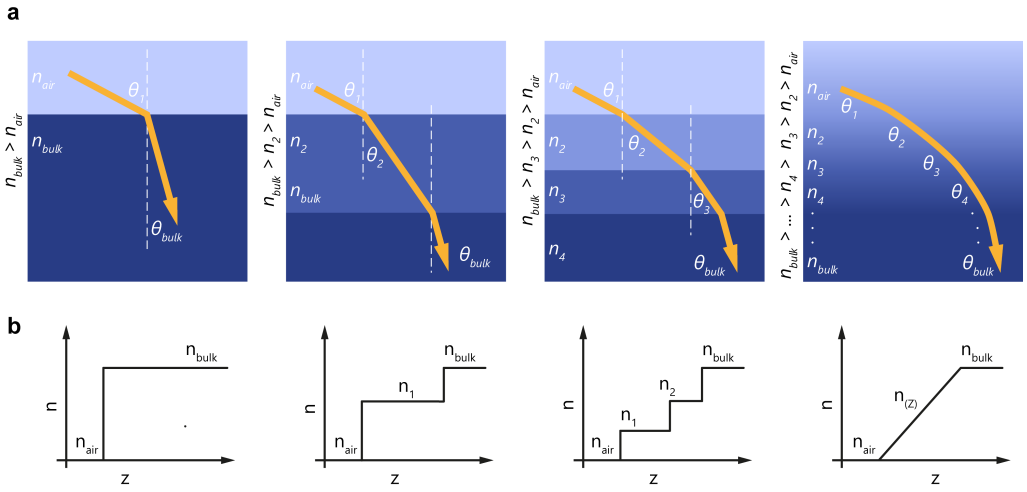

Figure 2-12. Light propagation with increasing refractive indices

(a) Refraction of an angular incident beam at different refraction index systems; (b) the correlated refractive index changes in dependence on the penetration depth *z*.

2.4. References

1. Hecht E. *Optics*. Addison-Wesley, 2002.
2. Hall AR. Beyond the Fringe: Diffraction as Seen by Grimaldi, Fabri, Hooke and Newton. *Notes and Records of the Royal Society of London* 1990, **44**(1)**:** 13-23.
3. Huygens C. *Treatise on Light*. tredition, 2012.
4. Fresnel AJ. *Mémoire sur la diffraction de la lumière*. De l'Imprimerie de Feugueray, rue du Cloitre Saint-Benoit, no. 4, 1819.

Chapter 3. State of the Art

As stated in the introduction, this thesis is about the fabrication of bio-inspired optical structures by means of two-photon lithography. To give an overview of the current state of the art, this chapter will point to recent literature about the two biological model surfaces, the optical grating on the moth's eye and the 'Christmas tree' structures on the butterfly's wing, as well as the recent progress of fabricating these artificially.

3.1. Photonic Structures in Nature

Nature evolved surfaces which are covered by complex structures in order to generate various functional effects[1-4], such as adhesion[5-7], self-cleaning[8-11], or light manipulation[12-17]. The latter includes photonic crystals, i.e., periodic sub-micrometre structures that lead to outstanding iridescent colourations[12,14,18-21]. These colours do not originate from interactions on the atomic level, but are based on the interaction of light with structural features, which cause refraction, reflection, diffraction, and scattering[14,15]. For example, multi-layer systems are the origin of the metallic shine of some beetles and fish[22-24], colloidal arrangements give colour to peacock feathers[25,26], and the 'Christmas tree-like' 3D photonic crystals of the *Morpho*-butterflies cause their famous iridescent blue[27-34]. In contrast to these examples of structural colouration, the photonic structures covering the moth eye or the cicada wings were shown to provide an entirely opposite effect: anti-reflection[17,35-39].

3.2. Anti-Reflection Surfaces of the Moth's Eye

Over one hundred years ago, the German biologist Sigmund Exner was the first scientist to investigate the optical properties of the compound eyes in insects. In his fundamental work he examined the morphology of single subunits of the compound eyes of insects, called ommatidias[40]. Thereupon, it took over forty years for his work to be continued by Bernhard and William. With new arriving observation methods, such as scanning electron microscopy (SEM), the two scientists discovered that the eye of the corneal surface of the moth *Prodenia eridiana* is covered by 200 nm high pillars packed in a hexagonal pattern with a distance of 200 nm from centre to centre[41]. They also performed the first spectrophotometric characterisations and concluded that the pillars decrease the reflection at the surface and correspondingly increase transmission. In this regard, these pillars act as an anti-reflection coating, which, from a theoretical point of view, provides the optimal conditions for a highly effective anti-reflective effect based on a gradually changing index of refraction[38]. Own micrographs of a moth eye possessing such a pattern are displayed in **Figure 3-1**. Further SEM investigations on different moth species revealed that the pillar heights and widths are not fixed to 200 nm, but can vary between a few

nanometres and 230 nm, and 180 to 240 nm, respectively[36]. In the same study, the authors showed by means of simulations that the optimal anti-reflective effect would be achieved by paraboloidally shaped pillars with 250 nm heights and a pillar to pillar spacing of 200 nm.

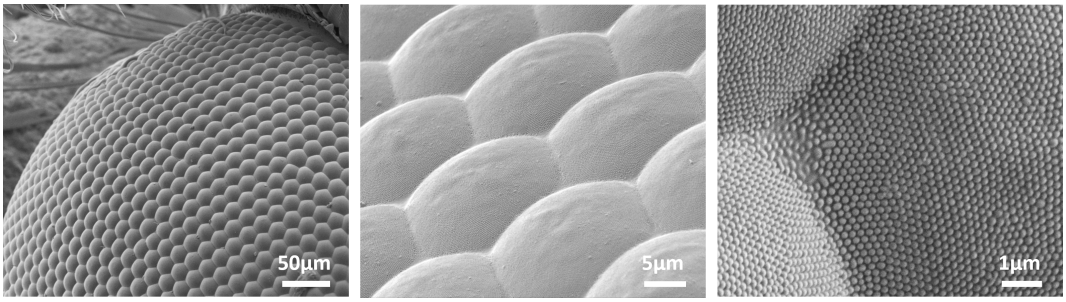

Figure 3-1. Anti-reflective moth-eye structures

SEM-micrographs showing the moth's eye at different magnifications.

The principle of a gradual index of refraction is illustrated in **Figure 3-2**. On a plane surface (**Figure 3-2a,b**), the relative refractive index $n_{air/bulk}$ between air (n_{air} = 1) and an exemplarily, structuring material (e.g. n_{bulk} = 1.5) is substantial and a reflectivity of R = 0.04 is expected according to the Fresnel equation (23) (see Chapter 2.3.3 commenting on the refractive index of materials and Chapter 2.3.4 for the calculation of the reflectivity using Fresnel equations). Now, two principal cases are possible: the wavelength of the light is either shorter than the feature sizes and spacings, or it is longer. If the wavelength is shorter, the wave registers either the refractive index of the bulk material or that of the air between the pillars. This causes typical optical effects, such as diffraction or scattering (see also Chapter 2.3.2 describing the diffraction of light at periodic structures).

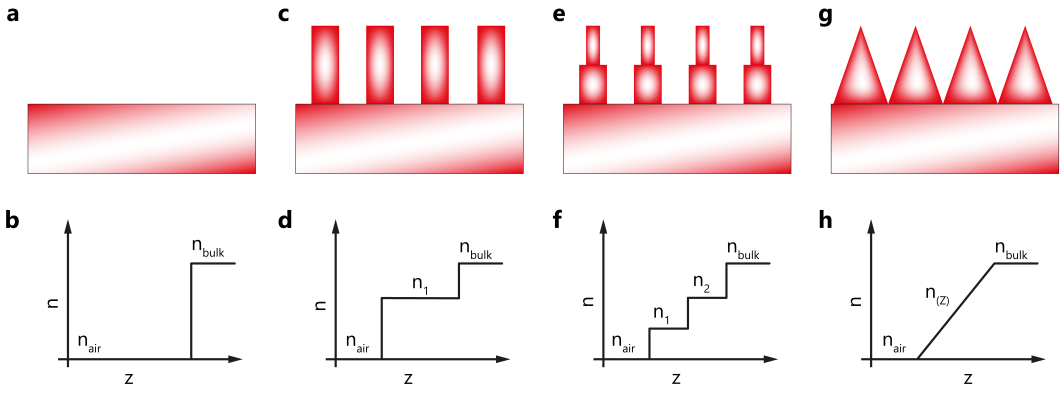

Figure 3-2. Refractive index distribution at structured surfaces

Four examples of surface topographies leading to different relative effective refractive index profiles in the transitional zone between pure air and full bulk material: (a,b) plane surface, (c,d) one pillar layer, (e,f) two hierarchical pillar layers, (g,h) pyramids. Diagrams represent gradient index of refraction as a function of depth along the z-direction, where a strong difference in n corresponds to strong reflection. With increasing 'steps' reflection decreases. (Modified image from Huang et al.[42])

If the wavelength, though, is longer than the periodicity of the surface structures, waves register both media, air and bulk material simultaneously. The resulting effective refractive index at a specific position now depends on the volume ratio between the two media. On a structured surface with only one type of pillars (**Figure 3-2c,d**), the light would perceive a change in the refractive index at two points: the tips of the pillars (e.g. $n_{air/tips}$ = 0.2) and at the transition to the bulk ($n_{tips/bulk}$ = 0.3). If the overall reflectivity is now calculated by the sum of the individual reflectivities, a value of R = 0.02 is obtained, which is lower than the R = 0.04 obtained on the plane surface. On a surface with two hierarchical pillar layers (**Figure 3-2e,f**), the light would perceive three planes: the tips, the second layer, and the bulk interface, which again leads to a lower overall reflectivity. One extreme case is presented by the last example (**Figure 3-2g,h**), where the surface is covered by pyramids instead of pillars. At such surfaces, the ratio between air and bulk material, and thus the effective refractive index, changes continuously at every vertical position. Such a continuously changing refractive index leads to a virtually infinite number of refraction events and as a result to strongly minimized Fresnel reflection.

The strategy to reduce reflectivity by using topography instead of a stack of thin films with increasing refractive index towards the substrate (see Chapter 2.3.5 for a detailed description) has the advantage that only one material is needed to obtain a strong anti-reflective effect. This reduces the fabrication costs for particular applications, and is therefore of interest in commercial coatings.

3.3. Structural Coloration of the Morpho-Butterfly

Butterflies of the *Morpho* family are famous for their iridescent blue colour of their wings, which arises from scales covered by periodically arranged, sub-micrometre sized ridges[34,43,44]. **Figure 3-3** displays a wing of such a structurally coloured butterfly at different magnifications. The iridescent wing is covered by many scales, arranged typically in rows and possessing slightly different tilt angles with respect to the subjacent layer. These scales are curved in shape and carry long ridges from their anchoring point to their tips. If such a scale is broken and the cross-section is examined, incredibly complex structures come to light. These structures are often called ‘Christmas trees’, as they possess a periodical layering of air and material which becomes narrower to the top. Each layer, which is also called lamella, is made of chitin with a refractive index of 1.55[45] separated by air (refractive index of 1). As a consequence, a thin-film like interference occurs between the individual layers of the structures for light with wavelengths in the blue region[27,29,46] (see Chapter 2.3.5 about the origin of multi-thin film interference). Red and green light is guided into the structure and absorbed by pigments, more precisely melanins[47]. Moreover, the lower lamina of scales was reported to act as thin reflector, and therefore, also plays an important role in the blue colouration of the wing[48].

In contrast to most photonic crystals such as those of the peacock feathers or beetles, which tend to change their colour if observed from different viewing angles[49,2,25], the intense blue of the *Morpho* butterfly wing stands out by its angle- and rotation-independent colouration[33,46,50]. While, on macroscopic level, the colour appears uniformly blue, Kinoshita and co-authors reported that the optical response of the photonic crystal on the scale level changes with the viewing angle[50]. Here, a strong blue reflection perpendicular to the ridges was reported in contrast to an abrupt decrease in reflectivity in the parallel direction. This anisotropy is barely observable on macroscopic scale due to the presence of additional hierarchical layers of macroscopic features. This includes e.g. cover scales that act as selective optical diffusors[51], scales of different orientations[31], and a horizontal displacement of the lamellas with respect to those on neighbouring ridges[46]. Both, the misalignment of scales and the displacement of ridges, introduce a global disorder reported to be crucial for the extraordinary performance of the *Morpho*-butterfly[32,33].

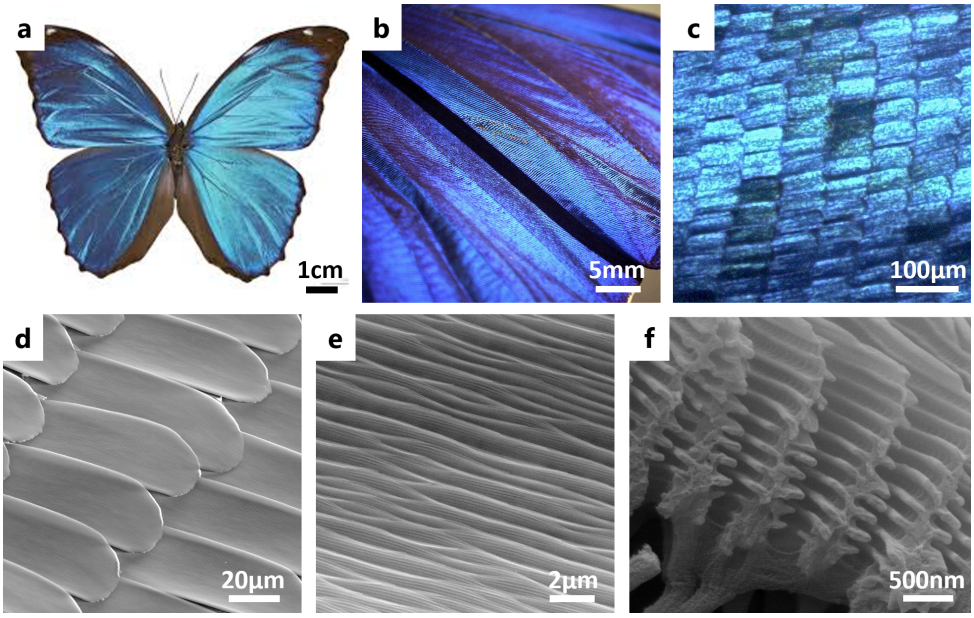

Figure 3-3. Structural coloration of the *Morpho*-butterfly

Photographs of (a) a Morpho-butterfly and (b) its wing. (c) Microscopy reveals multiple iridescent scales, which under the SEM show (d) curved shapes and possess (e) long ridges on their surfaces. (f) In cross-section theses ridges reveal so called ‘Christmas three’ structures. The scale bars are 1 cm, 5 mm, 100 µm, 20 µm, 2 µm, and 500 nm, respectively.

3.4. Bio-Inspired Moth Eye and Butterfly-like Surfaces

The relevance of structures creating anti-reflective or colour effects has been emphasised in many publications for a broad range of research areas[52], including wave control devices[53], laser optics[54], light collection, anti-reflective coatings[55], light trapping[56], holographic lithography[52], data management[57], and sensor applications[58].

The first artificial surface imitating the moth-eye was produced by Clapham & Hutley by means of dual-beam lithography[59]. This publication set off an avalanche of investigations focussing on the fabrication of biomimetic anti-reflective surfaces[42,60-86]. A selection of resulting artificial anti-reflective surfaces realised with different techniques is presented in **Figure 3-4**. The most frequently used approach is to first structure a photoresists on a substrate by laser interference lithography (LIL)[59,65,66,69,78,87], electron beam lithography[67], or imprint lithography[62], and then conduct reactive ion etching (RIE). Another, also widely used method is to apply colloidal particles by dip or spin coating, which likewise act as masks during the subsequent etching process[61,74,76,83-85]. Depending on the size of the spheres and the etching protocol, diverse periodical structures can be fabricated[85]. A very promising result was achieved by structuring silicon via an electron cyclotron resonance (ECR) plasma and oblique-angle deposition[71] leading to very fine structures with high aspect ratios and outstanding anti-reflective properties[60]. Besides finding novel approaches to fabricate moth-like structures, a lot of effort has been spent on templating[63,72,77,86] and the fabrication of these structures from different materials, such as gallium antimonide[75] or ZnO[73].

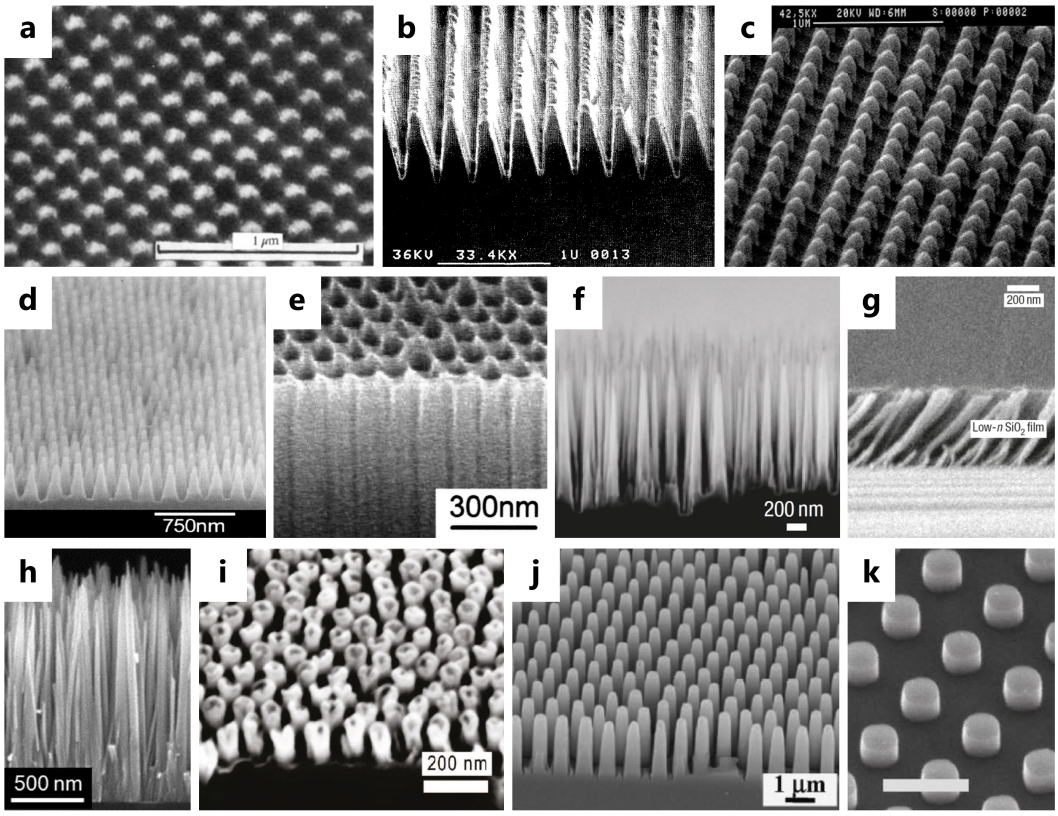

Figure 3-4. Artificially fabricated moth-eye inspired structures

(a) Laser interference lithography[59]; (b,c) laser interference mask and reactive ion etching on quartz[87] and silicon[66]; (d) Electron beam lithography and reactive ion etching[67]; (e) Porous aluminium mask and reactive ion etching[70]; (f) Electron cyclotron resonance plasma etching[60], (g) TiO_2 and SiO_2 low refractive index layers via oblique angle deposition[71]; (h) low temperature solution growth of ZnO[73]; (i) Gold particles mask and reactive ion etching[74], (j) reactive ion etching and soft-lithography as replication[76], (k) Substrate conformal imprint lithography[62].

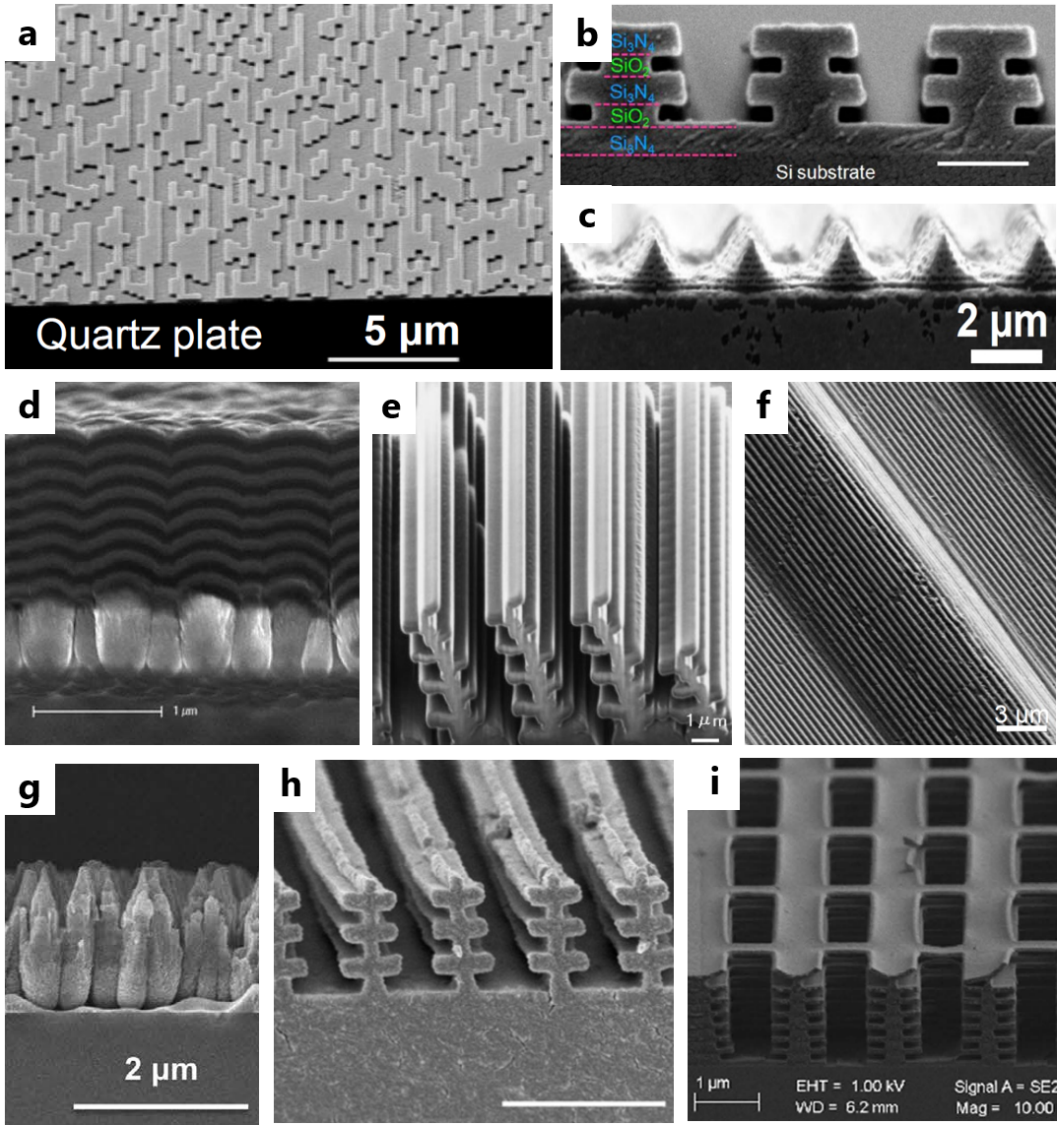

Figure 3-5. Artificially fabricated butterfly inspired structures

(a) Moulding from a pre-structured wafer via nano-casting lithography plus a seven step electron beam deposition[88], (b) 5 step chemical vapour deposition, Deep-UV-lithography and anisotropic RIE; (c) LIL on reflective substrates [89]; (d) heterogeneous colloidal particle supported etching, Cr-absorption layer and a 16 step sputter deposition of multi-thin films[90] (e) focused ion beam patterning[91]; (f) hot embossing of shape memory polymers[92]; (g) structures fabricated equally to those in (d) but with a subsequent etching of the multi-thin film[93]; (h,i) electron beam lithography and etching similar to (b) combined with alternate PMMA/LOR development/dissolution[94,95].

Similar efforts as for mimicking the pillar structures of the moth eyes have been put into the fabrication of *Morpho*-butterfly inspired structures[88-92,94-111] as well as into gaining an understanding of the constant blue colouration[112-114]. Although the physical principle is well understood[28,30,112], the direct imitation of the layered surface structures covering the butterfly wing remains still a challenge, as this topography is much more difficult to realise than the moth eye structures. Among other things, the biggest challenge is the creation of a nanometre range layering of air and quasi-transparent sheets by using only one structuring material. A summary of the various strategies that have been tried to fabricate butterfly-

inspired photonic structures is presented in **Figure 3-5**. Among others, multi-layer deposition, focused ion beam patterning[91], LIL on reflective substrates[89] and hot embossing of shape memory polymers[92] were applied. The most promising results, however, were achieved by multilayer systems containing disorder and an additional absorption layer[96,99], which have been proposed by Saito and co-workers[88,96,97]. In related studies, disorder was introduced by structuring the final multi-layer film via etching[95,100,101,107], by applying multi layers on various pre-structured substrates[88,97,98], or a combination of both approaches[93].

However, such structures have a critical drawback: they are very difficult to make, as numerous techniques have to be combined, such as wet and gas phase film deposition, multiple lithographic structuring and etching steps as well as moulding procedures.

3.5. Microstructuring by Two-Photon Lithography

In the last fifteen years the micro-fabrication by two-photon lithography (TPL) was widely adopted as a universal tool for complex 3D-structuring[115-118]; some examples are illustrated in **Figure 3-6.** Applications range from structuring metallic and ceramic metamaterials[119,120], via photonic crystals[121-126] to directly printed lens systems[127] and polarizers[128]. Studies engaging in 3D-TPL-manufactured structures also include scaffolding for investigations of the heart cell contraction[129-131], innovative drug delivery systems by means of magnetic helical micromachines[132], biomimetic adhesive structures of geckos[133], or the hydrophobic plant surface of *Salvinia molesta*[134].

As two-photon lithography evolved rather rapidly to a widely used tool in various unrelated fields, the same technique is described by a number of different terms making the comparison of results challenging. While the term two-photon is often exchanged by multi-photon, the second term lithography can be replaced by polymerisation or fabrication[130,135,136]. Various combinations like multi-photon fabrication or two-photon polymerisation are also broadly used. Additionally, intermediate terms such as stereo can be added[137,138]. Recently, completely different names, such as direct laser writing (DLW)[131,133,139] or direct laser printing[140], became quite popular originating from the current trend in the macroscopic 3D-fabrication, also known as rapid prototyping. In the further course of the thesis, the term two-photon lithography is going to be used.

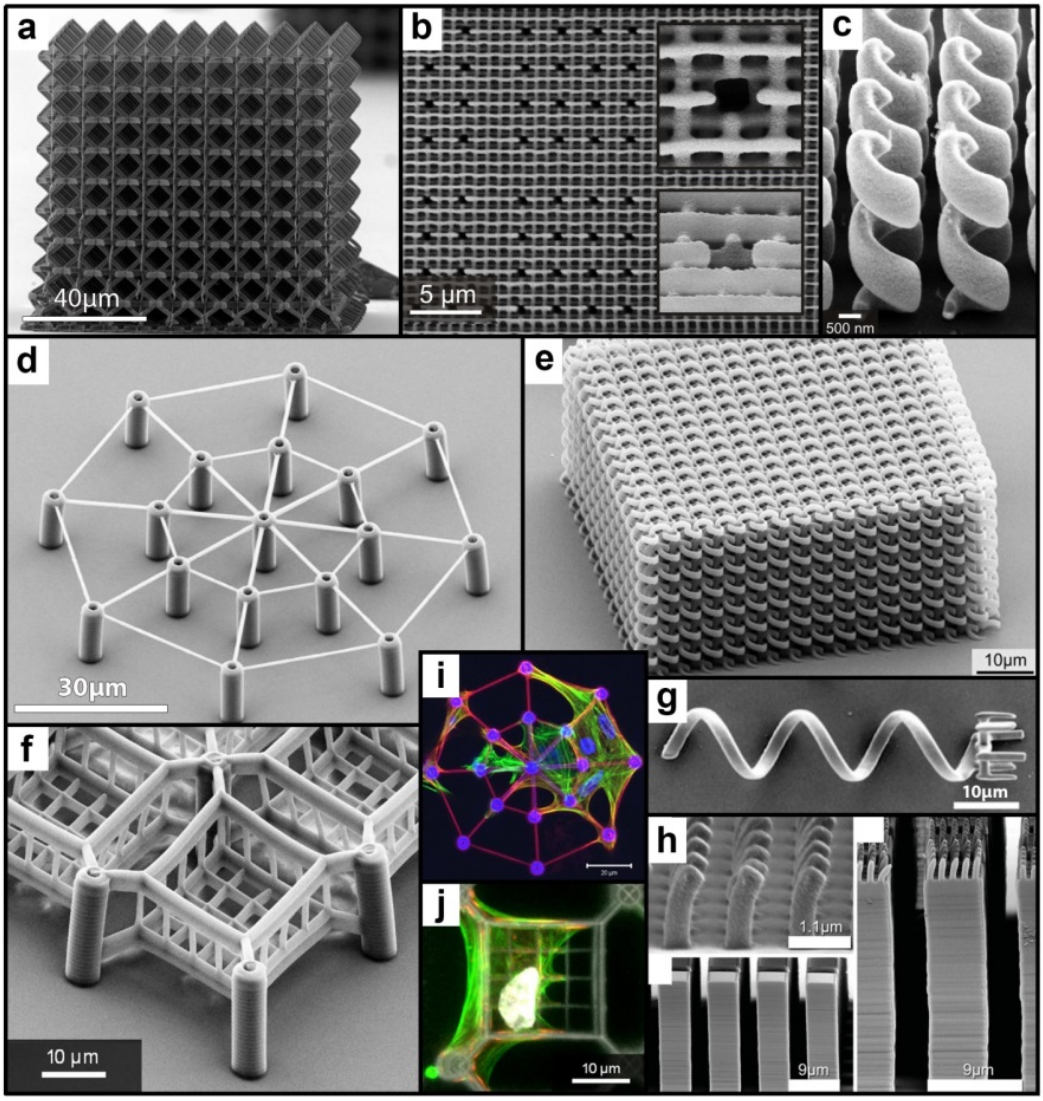

Figure 3-6. Examples of directly fabricated structures via two-photon lithography

(a) Ultralight micro-lattices for thermal insulation[120]; (b) Defect endowed 3D-photonic crystal[121]; (c) Gold helix structures after etching of written polymer matrix[128]; (d) Pattern for measuring contraction forces of heart cells[129]; (e) Bi-chiral dielectric 3D-photonic crystal[141]; (f) defined 3D-scaffold for single cell culturing [132,142]; (g) swimming magnetic helical micromachine for drug delivery[132]; (h) artificial hierarchical gecko structures providing enhanced adhesion[133]; and (d,i) as well (f,j) 3D-scaffolds for different cell experiments.

The principal approach of two-photon lithography (TPL) is very similar to a typical lithography process. It comprises a patterning of photo-sensitive materials via light exposure, a development step to remove redundant material, and a final sample drying. The main difference is that in common lithography the curing of the material takes place in the entire exposed volume, while in two-photon lithography only material in the focus of the structuring beam is cured. As illustrated in **Figure 3-7**, the difference in polymerised volume can be visualised by a fluorescence reaction initiated by either a UV-photon or a two-photon reaction with infra-red light[135]. In the case of UV-irradiation, the energy of one photon is higher or equivalent to the energy needed to start the fluorescence reaction. Fluorescent molecules in the entire beam path light up in blue. In IR-light, almost no reaction occurs and the beam path remains

invisible. However, in the very focus of the beam (indicated by the white arrow), where the density of photons is highest, a molecule can be excited simultaneously by two photons. This excitation is comparable to an excitation with one UV-photon, as an equivalent amount of energy is transferred, and thus, also leads to fluorescence.

Figure 3-7. Difference between one and two-photon reaction

The photograph shows the fluorescence excitation (originating from objective on the left) by a one-photon process using UV light, and (originating from the objective on the right) the two-photon process using IR light. While the excitation occurs over the complete light path in the medium in UV-light, the fluorescence caused by IR appears only in the focus of the beam (indicated by the white arrow). The reason is depicted by the adjacent graphs: while the energy E_{UV} of one single UV-photon is sufficient to excite one fluorescent molecule from the ground state S_0 to the exited state S_1 and cause fluorescence, the energy E_{IR} of one IR-photon is not enough to excite the molecule to state S_1 needed for fluorescence. Only by a simultaneous excitation by two IR-photons, which probability is highest in the focus of the beam, fluorescence can be observed (the photograph was taken from www.spectra-physics.com).

By using such a multi-absorption effect, the effectively exposed volume in TPL can be restricted to the focal region. The resulting polymerised volume element is called voxel, in analogy to the picture element typically referred to as pixel. By moving either the voxel or the substrate deterministically in all x,y,z-directions, whole structures can be built within a suitable photo-active material, as shown in **Figure 3-6**.

As for microscopes, the horizontal resolution limit a_{xy} of a two-photon system is dictated by the Abbe condition:

$$a_{xy} \geq \frac{\lambda}{2n\,sin\alpha} =: \frac{\lambda}{2NA} \tag{28}$$

where λ is wavelength of the laser beam, α the half opening angle of the objective, n the refractive index of the propagating medium, and NA the numerical aperture. When aiming for 3D structures, however, also the vertical resolution limit a_z has to be considered, which can be determined by an extended Abbe condition proposed by Fischer et al.[143]:

$$a_z \geq \frac{\lambda}{n - \sqrt{n^2 - (NA)^2}} \tag{29}$$

If both equations, (28) and (29), are solved using common values of a TPL system, such as a wavelength of λ = 780 nm, a numerical aperture of the objective NA = 1.4, and a refractive index of the photo-active material n = 1.5, the horizontal and vertical resolution results in 546 nm and 811 nm, respectively.

Besides the optical resolution, the voxel dimension is strongly influenced by the laser intensity, the reaction kinetics and mass transport processes[144]. Typically, radical chain reactions are used to multiply the effect of one two-photon event, which are then terminated by oxygen usually present in the photoresists[144]. The light intensity needed to create a stable network that is maintained after the development process is denoted as polymerisation threshold of a material. It is important to distinguish between the optical resolution of a TPL system, the minimal voxel or feature size, and the writing resolution. The first describes the ability of an imaging system to resolve two radiating points. This quantity is mainly determined by the wavelength of the light source, the numerical aperture of the objective, and the optical properties of the medium between the objective and the resolved sample, e.g., air or a photoresist. The so-called writing resolution, in contrast, denotes the ellipsoidal volume of polymerised material remaining after the development. This quantity depends on the optical resolution of the TPL-system described above[145], but also on the physico-chemical characteristics of the photo-active material[146-148], the laser parameters[143,146,149], as well as the exposure doses[150]. Typically, voxel sizes of ca. 200 nm x 600 nm (value was taken from the TPL-device manual) can be obtained, which is below Abbe's resolution limit. Here, the writing resolution describes the minimal distance between two features at which both are perceived as separated. As voxels or lines tend to merge when they are placed too closely, a minimal feature size facilitates, but does not automatically ensure an improvement in writing resolution.

3.6. References

1. Favret EA. *Functional Properties of Bio-inspired Surfaces: Characterization and Technological Applications*. World Scientific, 2009.
2. Gorb SN. *Functional Surfaces in Biology: Little structures with big effects*, vol. 1. Springer Science & Business Media, 2009.
3. Fratzl P, Weinkamer R. Nature's hierarchical materials. *Progress in Materials Science* 2007, **52**(8)**:** 1263-1334.
4. Meyers MA, Chen P-Y, Lin AY-M, Seki Y. Biological materials: Structure and mechanical properties. *Progress in Materials Science* 2008, **53**(1)**:** 1-206.
5. Autumn K, Gravish N. Gecko adhesion: evolutionary nanotechnology. *Philosophical Transactions of the Royal Society A: Mathematical, Physical and Engineering Sciences* 2008, **366**(1870)**:** 1575.
6. Autumn K, Dittmore A, Santos D, Spenko M, Cutkosky M. Frictional adhesion: a new angle on gecko attachment. *Journal of Experimental Biology* 2006, **209**(18)**:** 3569-3579.
7. Arzt E, Gorb S, Spolenak R. From micro to nano contacts in biological attachment devices. *Proc Natl Acad Sci* 2003, **100**(19)**:** 10603-10606.
8. Darmanin T, Guittard F. Superhydrophobic and superoleophobic properties in nature. *Materials Today* 2015, **18**(5)**:** 273-285.

9. Liu X, Liang Y, Zhou F, Liu W. Extreme wettability and tunable adhesion: biomimicking beyond nature? *Soft Matter* 2012, **8**(7)**:** 2070-2086.
10. Koch K, Bhushan B, Barthlott W. Diversity of structure, morphology and wetting of plant surfaces. *Soft Matter* 2008, **4**(10)**:** 1943-1963.
11. Peisker H, Gorb SN. Always on the bright side of life: anti-adhesive properties of insect ommatidia grating. *The Journal of Experimental Biology* 2010, **213**(20)**:** 3457-3462.
12. Mäthger LM, Denton EJ, Marshall NJ, Hanlon RT. Mechanisms and behavioural functions of structural coloration in cephalopods. *Journal of The Royal Society Interface* 2009, **6**(Suppl 2)**:** S149-S163.
13. Ingram AL, Parker AR. A review of the diversity and evolution of photonic structures in butterflies, incorporating the work of John Huxley (The Natural History Museum, London from 1961 to 1990). *Philosophical Transactions of the Royal Society B: Biological Sciences* 2008, **363**(1502)**:** 2465-2480.
14. Vukusic P, Sambles JR. Photonic structures in biology. *Nature* 2003, **424**(6950)**:** 852-855.
15. Parker AR. The diversity and implications of animal structural colours. *The Journal of Experimental Biology* 1998, **201**(16)**:** 2343-2347.
16. Parker AR, Hegedus Z, Watts RA. Solar–absorber antireflector on the eye of an Eocene fly (45 Ma). *Proceedings of the Royal Society of London Series B: Biological Sciences* 1998, **265**(1398)**:** 811-815.
17. Stavenga DG, Arikawa K. Evolution of color and vision of butterflies. *Arthropod Structure & Development* 2006, **35**(4)**:** 307-318.
18. Joannopoulos JD, Villeneuve PR, Fan S. Photonic crystals: putting a new twist on light. *Nature* 1997, **386**(6621)**:** 143-149.
19. Welch VL, Vigneron JP. Beyond butterflies—the diversity of biological photonic crystals. *Opt Quant Electron* 2007, **39**(4-6)**:** 295-303.
20. Kinoshita S, Yoshioka S. Structural Colors in Nature: The Role of Regularity and Irregularity in the Structure. *ChemPhysChem* 2005, **6**(8)**:** 1442-1459.
21. Biró LP, Kertész K, Vértesy Z, Márk GI, Bálint Z, Lousse V, *et al.* Living photonic crystals: Butterfly scales — Nanostructure and optical properties. *Materials Science and Engineering: C* 2007, **27**(5-8)**:** 941-946.
22. Fabricant SA, Kemp DJ, Krajíček J, Bosáková Z, Herberstein ME. Mechanisms of Color Production in a Highly Variable Shield-Back Stinkbug, Tectocoris diopthalmus (Heteroptera: Scutelleridae), and Why It Matters. *PLoS ONE* 2013, **8**(5)**:** e64082.
23. Jordan TM, Partridge JC, Roberts NW. Non-polarizing broadband multilayer reflectors in fish. *Nat Photon* 2012, **6**(11)**:** 759-763.
24. Seago AE, Brady P, Vigneron J-P, Schultz TD. Gold bugs and beyond: a review of iridescence and structural colour mechanisms in beetles (Coleoptera). *Journal of The Royal Society Interface* 2009, **6**(Suppl 2)**:** S165-S184.
25. Zi J, Yu X, Li Y, Hu X, Xu C, Wang X, *et al.* Coloration strategies in peacock feathers. *Proc Natl Acad Sci* 2003, **100**(22)**:** 12576-12578.
26. Yoshioka S, Kinoshita S. Effect of macroscopic structure in iridescent color of the peacock feathers. *FORMA-TOKYO-* 2002, **17**(2)**:** 169-181.
27. Berthier S, Charron E, Boulenguez J. Morphological structure and optical properties of the wings of Morphidae. *Insect Science* 2006, **13**(2)**:** 145-158.
28. Ghiradella H. Structure and development of iridescent butterfly scales: Lattices and laminae. *Journal of Morphology* 1989, **202**(1)**:** 69-88.
29. Ghiradella H. Light and color on the wing: structural colors in butterflies and moths. *Appl Opt* 1991, **30**(24)**:** 3492-3500.
30. Ghiradella H. Structure of butterfly scales: Patterning in an insect cuticle. *Microsc Res Tech* 1994, **27**(5)**:** 429-438.
31. Ghiradella H, Aneshansley D, Eisner T, Silberglied RE, Hinton HE. Ultraviolet reflection of a male butterfly: interference color caused by thin-layer elaboration of wing scales. *Science* 1972, **178**(4066)**:** 1214-1217.
32. Kambe M, Zhu D, Kinoshita S. Origin of Retroreflection from a Wing of the Morpho Butterfly. *Journal of the Physical Society of Japan* 2011, **80**(5)**:** 054801.

33. Kinoshita S, Yoshioka S, Kawagoe K. Mechanisms of structural colour in the Morpho butterfly: cooperation of regularity and irregularity in an iridescent scale. *Proceedings of the Royal Society B: Biological Sciences* 2002, **269**(1499)**:** 1417-1421.
34. Ghiradella H. Structure of Iridescent Lepidopteran Scales: Variations on Several Themes. *Annals of the Entomological Society of America* 1984, **77**(6)**:** 637-645.
35. Bernhard CG, Gemne G, Sällström J. Comparative ultrastructure of corneal surface topography in insects with aspects on phylogenesis and function. *Z Vergl Physiol* 1970, **67**(1)**:** 1-25.
36. Stavenga DG, Foletti S, Palasantzas G, Arikawa K. Light on the moth-eye corneal nipple array of butterflies. *Proceedings of the Royal Society B: Biological Sciences* 2006, **273**(1587)**:** 661-667.
37. Chattopadhyay S, Huang Y, Jen Y-J, Ganguly A, Chen K, Chen L. Anti-reflecting and photonic nanostructures. *Materials Science and Engineering: R: Reports* 2010, **69**(1)**:** 1-35.
38. Bernhard CG, Miller WH, Móller AR. Function of the Corneal Nipples in the Compound Eyes of Insects. *Acta Physiologica Scandinavica* 1963, **58**(4)**:** 381-382.
39. Han ZW, Wang Z, Feng XM, Li B, Mu ZZ, Zhang JQ, *et al.* Antireflective surface inspired from biology: A review. *Biosurface and Biotribology* 2016, **2**(4)**:** 137-150.
40. Exner S. *The Physiology of the Compound Eyes of Insects and Crustaceans*. Springer-Verlag Berlin Heidelberg, 1989.
41. Bernhard CG, Miller WH. A Corneal Nipple Pattern in Insect Compound Eyes. *Acta Physiologica Scandinavica* 1962, **56**(3-4)**:** 385-386.
42. Huang YF, Chattopadhyay S. Nanostructure surface design for broadband and angle-independent antireflection. *Journal of Nanophotonics* 2013, **7**(1)**:** 073594-073594.
43. Mason CW. Structural Colors in Insects. II. *The Journal of Physical Chemistry* 1926, **31**(3)**:** 321-354.
44. Wright WD. The Rays are Not Coloured. *Nature* 1963, **198**(4887)**:** 1239-1244.
45. Vukusic P, Sambles JR, Lawrence CR, Wootton RJ. Quantified interference and diffraction in single Morpho butterfly scales. *Proceedings of the Royal Society B: Biological Sciences* 1999, **266**(1427)**:** 1403-1403.
46. Tabata H, Kumazawa K, Funakawa M, Takimoto J-i, Akimoto M. Microstructures and Optical Properties of Scales of Butterfly Wings. *OPT REV* 1996, **3**(2)**:** 139-145.
47. Stavenga DG, Leertouwer HL, Wilts BD. Coloration principles of nymphaline butterflies – thin films, melanin, ommochromes and wing scale stacking. *The Journal of Experimental Biology* 2014, **217**(12)**:** 2171-2180.
48. Giraldo M, Stavenga D. Brilliant iridescence of Morpho butterfly wing scales is due to both a thin film lower lamina and a multilayered upper lamina. *J Comp Physiol A* 2016, **202**(5)**:** 381-388.
49. Mason CW. Structural Colors in Feathers. II. *The Journal of Physical Chemistry* 1922, **27**(5)**:** 401-448.
50. Kinoshita S, Yoshioka S, Miyazaki J. Physics of structural colors. *Reports on Progress in Physics* 2008, **71**(7)**:** 076401.
51. Yoshioka S, Kinoshita S. Wavelength–selective and anisotropic light–diffusing scale on the wing of the Morpho butterfly. *Proceedings of the Royal Society of London B: Biological Sciences* 2004, **271**(1539)**:** 581-587.
52. Campbell M, Sharp DN, Harrison MT, Denning RG, Turberfield AJ. Fabrication of photonic crystals for the visible spectrum by holographic lithography. *Nature* 2000, **404**(6773)**:** 53-56.
53. Akahane Y, Asano T, Song B-S, Noda S. High-Q photonic nanocavity in a two-dimensional photonic crystal. *Nature* 2003, **425**(6961)**:** 944-947.
54. Russell P. Photonic Crystal Fibers. *Science* 2003, **299**(5605)**:** 358-362.
55. Li Y, Fullager DB, Angelbello E, Childers D, Boreman G, Hofmann T. Broadband near-infrared antireflection coatings fabricated by three-dimensional direct laser writing. *Opt Lett* 2018, **43**(2)**:** 239-242.
56. Baomin W, Kevin PC, Paul WL. Engineering inverse woodpile and woodpile photonic crystal solar cells for light trapping. *Nanotechnology* 2016, **27**(22)**:** 225404.

57. Blanco A, Chomski E, Grabtchak S, Ibisate M, John S, Leonard SW, *et al.* Large-scale synthesis of a silicon photonic crystal with a complete three-dimensional bandgap near 1.5 micrometres. *Nature* 2000, **405**(6785)**:** 437-440.
58. Potyrailo RA, Ghiradella H, Vertiatchikh A, Dovidenko K, Cournoyer JR, Olson E. Morpho butterfly wing scales demonstrate highly selective vapour response. *Nat Photon* 2007, **1**(2)**:** 123-128.
59. Clapham PB, Hutley MC. Reduction of Lens Reflexion by the Moth Eye Principle. *Nature* 1973, **244**(5414)**:** 281-282.
60. Huang Y-F, Chattopadhyay S, Jen Y-J, Peng C-Y, Liu T-A, Hsu Y-K, *et al.* Improved broadband and quasi-omnidirectional anti-reflection properties with biomimetic silicon nanostructures. *Nat Nano* 2007, **2**(12)**:** 770-774.
61. Sun C-H, Jiang P, Jiang B. Broadband moth-eye antireflection coatings on silicon. *Appl Phys Lett* 2008, **92**(6)**:** -.
62. Spinelli P, Verschuuren MA, Polman A. Broadband omnidirectional antireflection coating based on subwavelength surface Mie resonators. *Nat Commun* 2012, **3:** 692.
63. Hong S-H, Bae B-J, Han K-S, Hong E-J, Lee H, Choi K-W. Imprinted moth-eye antireflection patterns on glass substrate. *Electronic Materials Letters* 2009, **5**(1)**:** 39-42.
64. Hartman NF, Gaylord TK. Antireflection gold surface-relief gratings: experimental characteristics. *Appl Opt* 1988, **27**(17)**:** 3738-3743.
65. Motamedi M, Southwell WH, Gunning WJ. Antireflection surfaces in silicon using binary optics technology. *Appl Opt* 1992, **31**(22)**:** 4371-4376.
66. Lalanne P, Morris GM. Antireflection behavior of silicon subwavelength periodic structures for visible light. *Nanotechnology* 1997, **8**(2)**:** 53.
67. Kanamori Y, Sasaki M, Hane K. Broadband antireflection gratings fabricated upon silicon substrates. *Opt Lett* 1999, **24**(20)**:** 1422-1424.
68. Walheim S, Schäffer E, Mlynek J, Steiner U. Nanophase-separated polymer films as high-performance antireflection coatings. *Science* 1999, **283**(5401)**:** 520-522.
69. Hadobás K, Kirsch S, Carl A, Acet M, Wassermann EF. Reflection properties of nanostructure-arrayed silicon surfaces. *Nanotechnology* 2000, **11**(3)**:** 161.
70. Kanamori Y, Hane K, Sai H, Yugami H. 100 nm period silicon antireflection structures fabricated using a porous alumina membrane mask. *Appl Phys Lett* 2001, **78**(2)**:** 142-143.
71. Xi JQ, Schubert MF, Kim JK, Schubert EF, Chen M, Lin S-Y, *et al.* Optical thin-film materials with low refractive index for broadband elimination of Fresnel reflection. *Nat Photon* 2007, **1**(3)**:** 176-179.
72. Jingyun H, Xudong W, Zhong Lin W. Bio-inspired fabrication of antireflection nanostructures by replicating fly eyes. *Nanotechnology* 2008, **19**(2)**:** 025602.
73. Lee Y-J, Ruby DS, Peters DW, McKenzie BB, Hsu JW. ZnO nanostructures as efficient antireflection layers in solar cells. *Nano letters* 2008, **8**(5)**:** 1501-1505.
74. Lohmüller T, Helgert M, Sundermann M, Brunner R, Spatz JP. Biomimetic Interfaces for High-Performance Optics in the Deep-UV Light Range. *Nano Letters* 2008, **8**(5)**:** 1429-1433.
75. Min W-L, Betancourt AP, Jiang P, Jiang B. Bioinspired broadband antireflection coatings on GaSb. *Appl Phys Lett* 2008, **92**(14)**:** -.
76. Min W-L, Jiang B, Jiang P. Bioinspired Self-Cleaning Antireflection Coatings. *Adv Mater* 2008, **20**(20)**:** 3914-3918.
77. Bae B-J, Hong S-H, Hong E-J, Lee H, Jung G-y. Fabrication of Moth-Eye Structure on Glass by Ultraviolet Imprinting Process with Polymer Template. *Japanese Journal of Applied Physics* 2009, **48**(1R)**:** 010207.
78. Song YM, Jang SJ, Yu JS, Lee YT. Bioinspired Parabola Subwavelength Structures for Improved Broadband Antireflection. *Small* 2010, **6**(9)**:** 984-987.
79. Yamada N, Ijiro T, Okamoto E, Hayashi K, Masuda H. Characterization of antireflection moth-eye film on crystalline silicon photovoltaic module. *Opt Express* 2011, **19**(S2)**:** A118-A125.
80. Lee KM, Wang DH, Koerner H, Vaia RA, Tan L-S, White TJ. Enhancement of Photogenerated Mechanical Force in Azobenzene-Functionalized Polyimides. *Angewandte Chemie* 2012, **124**(17)**:** 4193-4197.

81. Kuang P, Eyderman S, Hsieh M-L, Post A, John S, Lin S-Y. Achieving an Accurate Surface Profile of a Photonic Crystal for Near-Unity Solar Absorption in a Super Thin-Film Architecture. *ACS Nano* 2016, **10**(6)**:** 6116-6124.
82. Kowalczyk M, Haberko J, Wasylczyk P. Microstructured gradient-index antireflective coating fabricated on a fiber tip with direct laser writing. *Opt Express* 2014, **22**(10)**:** 12545-12550.
83. Wang Y, Lu N, Xu H, Shi G, Xu M, Lin X, *et al.* Biomimetic corrugated silicon nanocone arrays for self-cleaning antireflection coatings. *Nano Res* 2010, **3**(7)**:** 520-527.
84. Ji S, Park J, Lim H. Improved antireflection properties of moth eye mimicking nanopillars on transparent glass: flat antireflection and color tuning. *Nanoscale* 2012, **4**(15)**:** 4603-4610.
85. Lora Gonzalez F, Chan L, Berry A, Morse DE, Gordon MJ. Simple colloidal lithography method to fabricate large-area moth-eye antireflective structures on Si, Ge, and GaAs for IR applications. *J Vac Sci Technol B* 2014, **32**(5)**:** -.
86. Ko D-H, Tumbleston JR, Henderson KJ, Euliss LE, DeSimone JM, Lopez R, *et al.* Biomimetic microlens array with antireflective "moth-eye" surface. *Soft Matter* 2011, **7**(14)**:** 6404-6407.
87. Enger RC, Case SK. Optical elements with ultrahigh spatial-frequency surface corrugations. *Appl Opt* 1983, **22**(20)**:** 3220-3228.
88. Saito A, Miyamura Y, Nakajima M, Ishikawa Y, Sogo K, Kuwahara Y, *et al.* Reproduction of the Morpho blue by nanocasting lithographya). *Journal of Vacuum Science & Technology B* 2006, **24**(6)**:** 3248-3251.
89. Siddique RH, Hünig R, Faisal A, Lemmer U, Hölscher H. Fabrication of hierarchical photonic nanostructures inspired by Morpho butterflies utilizing laser interference lithography. *Opt Mater Express* 2015, **5**(5)**:** 996-1005.
90. Chung K, Shin JH. Range and stability of structural colors generated by Morpho-inspired color reflectors. *J Opt Soc Am A* 2013, **30**(5)**:** 962-968.
91. Watanabe K, Hoshino T, Kanda K, Haruyama Y, Matsui S. Brilliant Blue Observation from a Morpho -Butterfly-Scale Quasi-Structure. *Japanese Journal of Applied Physics* 2005, **44**(1L)**:** L48.
92. Schneider N, Zeiger C, Kolew A, Schneider M, Leuthold J, Hölscher H, *et al.* Nanothermoforming of hierarchical optical components utilizing shape memory polymers as active molds. *Opt Mater Express* 2014, **4**(9)**:** 1895-1902.
93. Song B, Johansen VE, Sigmund O, Shin JH. Reproducing the hierarchy of disorder for Morpho-inspired, broad-angle color reflection. *Scientific Reports* 2017, **7:** 46023.
94. Cary AT, Yulan F, Anne-Martine J, Eugenii UD, Rene L. Reproduction and optical analysis of Morpho -inspired polymeric nanostructures. *Journal of Optics* 2016, **18**(6)**:** 065105.
95. Zhang S, Chen Y. Nanofabrication and coloration study of artificial Morpho butterfly wings with aligned lamellae layers. *Scientific Reports* 2015, **5:** 16637.
96. Saito A, Yoshioka S-y, Kinoshita S. Reproduction of the Morpho butterfly's blue: arbitration of contradicting factors. 2004; 2004. p. 188-194.
97. Saito A, Miyamura Y, Ishikawa Y, Murase J, Akai-Kasaya M, Kuwahara Y. Reproduction, mass production, and control of the Morpho butterfly's blue. 2009; 2009. p. 720506-720506-720509.
98. Saito A, Murase J, Yonezawa M, Watanabe H, Shibuya T, Sasaki M, *et al.* High-throughput reproduction of the Morpho butterfly's specific high contrast blue. 2012; 2012. p. 83390C-83390C-83310.
99. Chung K, Yu S, Heo C-J, Shim JW, Yang S-M, Han MG, *et al.* Flexible, Angle-Independent, Structural Color Reflectors Inspired by Morpho Butterfly Wings. *Adv Mater* 2012, **24**(18)**:** 2375-2379.
100. Chen Y, Gu J, Zhu S, Fan T, Zhang D, Guo Q. Iridescent large-area ZrO2 photonic crystals using butterfly as templates. *Appl Phys Lett* 2009, **94**(5)**:** 053901.
101. Chen Y, Zang X, Gu J, Zhu S, Su H, Zhang D, *et al.* ZnO single butterfly wing scales: synthesis and spatial optical anisotropy. *Journal of Materials Chemistry* 2011, **21**(17)**:** 6140-6143.
102. Keiichiro W, Takayuki H, Kazuhiro K, Yuichi H, Shinji M. Brilliant Blue Observation from a Morpho -Butterfly-Scale Quasi-Structure. *Japanese Journal of Applied Physics* 2005, **44**(1L)**:** L48.

103. Wang Z, Di Z, Tongxiang F, Jian D, Jiajun G, Qixin G, *et al.* Biomimetic zinc oxide replica with structural color using butterfly (Ideopsis similis) wings as templates. *Bioinspiration & Biomimetics* 2006, **1**(3)**:** 89.
104. Gaillot DP, Deparis O, Welch V, Wagner BK, Vigneron JP, Summers CJ. Composite organic-inorganic butterfly scales: Production of photonic structures with atomic layer deposition. *Physical Review E* 2008, **78**(3)**:** 031922.
105. Kolle M, Salgard-Cunha PM, Scherer MRJ, Huang F, Vukusic P, Mahajan S, *et al.* Mimicking the colourful wing scale structure of the Papilio blumei butterfly. *Nat Nano* 2010, **5**(7)**:** 511-515.
106. Liu F, Liu Y, Huang L, Hu X, Dong B, Shi W, *et al.* Replication of homologous optical and hydrophobic features by templating wings of butterflies Morpho menelaus. *Optics Communications* 2011, **284**(9)**:** 2376-2381.
107. Aryal M, Ko D-H, Tumbleston JR, Gadisa A, Samulski ET, Lopez R. Large area nanofabrication of butterfly wing and three dimensional ultrastructures. *Journal of Vacuum Science & Technology B* 2012, **30**(6)**:** 061802.
108. Han Z, Niu S, Yang M, Zhang J, Yin W, Ren L. An ingenious replica templated from the light trapping structure in butterfly wing scales. *Nanoscale* 2013, **5**(18)**:** 8500-8506.
109. Song B, Eom SC, Shin JH. Disorder and broad-angle iridescence from Morpho-inspired structures. *Opt Express* 2014, **22**(16)**:** 19386-19400.
110. Gu J, Zhang W, Su H, Fan T, Zhu S, Liu Q, *et al.* Morphology Genetic Materials Templated from Natural Species. *Adv Mater* 2015, **27**(3)**:** 464-478.
111. Parker AR, Townley HE. Making photonic structures via cell culture: Morpho butterfly scales. *Bioinspired, Biomimetic and Nanobiomaterials* 2015, **4**(1)**:** 68-72.
112. Gralak B, Tayeb G, Enoch S. Morpho butterflies wings color modeled with lamellar grating theory. *Opt Express* 2001, **9**(11)**:** 567-578.
113. Banerjee S, Cole JB, Yatagai T. Colour characterization of a Morpho butterfly wing-scale using a high accuracy nonstandard finite-difference time-domain method. *Micron* 2007, **38**(2)**:** 97-103.
114. Siddique RH, Diewald S, Leuthold J, Hölscher H. Theoretical and experimental analysis of the structural pattern responsible for the iridescence of Morpho butterflies. *Opt Express* 2013, **21**(12)**:** 14351-14361.
115. Farsari M, Chichkov BN. Materials processing: Two-photon fabrication. *Nat Photon* 2009, **3**(8)**:** 450-452.
116. Hohmann JK, Renner M, Waller EH, von Freymann G. Three-Dimensional μ-Printing: An Enabling Technology. *Adv Opt Mater* 2015, **3**(11)**:** 1488-1507.
117. Geissler M, Xia Y. Patterning: Principles and Some New Developments. *Adv Mater* 2004, **16**(15)**:** 1249-1269.
118. Alberto P, Raymond CYA, Heungsoo K, Nicholas AC, Scott AM. Laser 3D micro-manufacturing. *Journal of Physics D: Applied Physics* 2016, **49**(22)**:** 223001.
119. Zheng X, Smith W, Jackson J, Moran B, Cui H, Chen D, *et al.* Multiscale metallic metamaterials. *Nat Mater* 2016, **15**(10)**:** 1100-1106.
120. Meza LR, Das S, Greer JR. Strong, lightweight, and recoverable three-dimensional ceramic nanolattices. *Science* 2014, **345**(6202)**:** 1322-1326.
121. von Freymann G, Ledermann A, Thiel M, Staude I, Essig S, Busch K, *et al.* Three-Dimensional Nanostructures for Photonics. *Adv Funct Mater* 2010, **20**(7)**:** 1038-1052.
122. Deubel M, von Freymann G, Wegener M, Pereira S, Busch K, Soukoulis CM. Direct laser writing of three-dimensional photonic-crystal templates for telecommunications. *Nat Mater* 2004, **3**(7)**:** 444-447.
123. Deubel M, Wegener M, Linden S, von Freymann G, John S. 3D-2D-3D photonic crystal heterostructures fabricated by direct laser writing. *Opt Lett* 2006, **31**(6)**:** 805-807.
124. Thiel M, Fischer J, von Freymann G, Wegener M. Direct laser writing of three-dimensional submicron structures using a continuous-wave laser at 532 nm. *Appl Phys Lett* 2010, **97**(22)**:** 221102.
125. Rybin M, Shishkin I, Samusev K, Belov P, Kivshar Y, Kiyan R, *et al.* Band Structure of Photonic Crystals Fabricated by Two-Photon Polymerization. *Crystals* 2015, **5**(1)**:** 61.

126. Qu J, Kadic M, Naber A, Wegener M. Micro-Structured Two-Component 3D Metamaterials with Negative Thermal-Expansion Coefficient from Positive Constituents. *Scientific Reports* 2017, **7:** 40643.
127. Thiele S, Arzenbacher K, Gissibl T, Giessen H, Herkommer AM. 3D-printed eagle eye: Compound microlens system for foveated imaging. *Science Adv* 2017, **3**(2).
128. Gansel JK, Thiel M, Rill MS, Decker M, Bade K, Saile V, *et al.* Gold Helix Photonic Metamaterial as Broadband Circular Polarizer. *Science* 2009, **325**(5947)**:** 1513-1515.
129. Klein F, Striebel T, Fischer J, Jiang Z, Franz CM, von Freymann G, *et al.* Elastic Fully Three-dimensional Microstructure Scaffolds for Cell Force Measurements. *Adv Mater* 2010, **22**(8)**:** 868-871.
130. Marino A, Filippeschi C, Mattoli V, Mazzolai B, Ciofani G. Biomimicry at the nanoscale: current research and perspectives of two-photon polymerization. *Nanoscale* 2015, **7**(7)**:** 2841-2850.
131. Selimis A, Mironov V, Farsari M. Direct laser writing: Principles and materials for scaffold 3D printing. *Microelectron Eng* 2015, **132:** 83-89.
132. Tottori S, Zhang L, Qiu F, Krawczyk KK, Franco-Obregón A, Nelson BJ. Magnetic Helical Micromachines: Fabrication, Controlled Swimming, and Cargo Transport. *Adv Mater* 2012, **24**(6)**:** 811-816.
133. Röhrig M, Thiel M, Worgull M, Hölscher H. 3D Direct Laser Writing of Nano-and Microstructured Hierarchical Gecko-Mimicking Surfaces. *Small* 2012, **8**(19)**:** 3009-3015.
134. Tricinci O, Terencio T, Mazzolai B, Pugno NM, Greco F, Mattoli V. 3D Micropatterned Surface Inspired by Salvinia molesta via Direct Laser Lithography. *ACS Applied Materials & Interfaces* 2015, **7**(46)**:** 25560-25567.
135. LaFratta CN, Fourkas JT, Baldacchini T, Farrer RA. Multiphoton Fabrication. *Angewandte Chemie International Edition* 2007, **46**(33)**:** 6238-6258.
136. Maruo S, Fourkas JT. Recent progress in multiphoton microfabrication. *Laser & Photonics Reviews* 2008, **2**(1-2)**:** 100-111.
137. Jacobs PF, Reid DT, Computer, SME. ASAo. *Rapid Prototyping & Manufacturing: Fundamentals of Stereolithography*. Society of Manufacturing Engineers, 1992.
138. Park SH, Yang DY, Lee KS. Two-photon stereolithography for realizing ultraprecise three-dimensional nano/microdevices. *Laser & Photonics Reviews* 2009, **3**(1-2)**:** 1-11.
139. Zeng H, Martella D, Wasylczyk P, Cerretti G, Lavocat J-CG, Ho C-H, *et al.* High-Resolution 3D Direct Laser Writing for Liquid-Crystalline Elastomer Microstructures. *Adv Mater* 2014, **26**(15)**:** 2319-2322.
140. Hu Y, Lao Z, Cumming BP, Wu D, Li J, Liang H, *et al.* Laser printing hierarchical structures with the aid of controlled capillary-driven self-assembly. *Proc Natl Acad Sci* 2015, **112**(22)**:** 6876-6881.
141. Thiel M, Rill MS, von Freymann G, Wegener M. Three-dimensional bi-chiral photonic crystals. *Adv Mater* 2009, **21**(46)**:** 4680-4682.
142. Greiner AM, Richter B, Bastmeyer M. Micro-engineered 3D scaffolds for cell culture studies. *Macromolecular bioscience* 2012, **12**(10)**:** 1301-1314.
143. Fischer J, Wegener M. Three-dimensional optical laser lithography beyond the diffraction limit. *Laser & Photonics Reviews* 2013, **7**(1)**:** 22-44.
144. Mueller JB, Fischer J, Mayer F, Kadic M, Wegener M. Polymerization Kinetics in Three-Dimensional Direct Laser Writing. *Adv Mater* 2014, **26**(38)**:** 6566-6571.
145. Sun H-B, Maeda M, Takada K, Chon JWM, Gu M, Kawata S. Experimental investigation of single voxels for laser nanofabrication via two-photon photopolymerization. *Appl Phys Lett* 2003, **83**(5)**:** 819-821.
146. Xing J-F, Dong X-Z, Chen W-Q, Duan X-M, Takeyasu N, Tanaka T, *et al.* Improving spatial resolution of two-photon microfabrication by using photoinitiator with high initiating efficiency. *Appl Phys Lett* 2007, **90**(13)**:** 131106.
147. Fischer J, Mueller JB, Quick AS, Kaschke J, Barner-Kowollik C, Wegener M. Exploring the Mechanisms in STED-Enhanced Direct Laser Writing. *Adv Opt Mater* 2015, **3**(2)**:** 221-232.
148. Sun H-B, Takada K, S. Kim M, Lee K-S, Kawata S. *Scaling laws of voxels in two-photon photopolymerization nanofabrication*, vol. 83, 2003.

149. Kawata S, Sun H-B, Tanaka T, Takada K. Finer features for functional microdevices. *Nature* 2001, **412:** 697.
150. Tanaka TS, Hong-Bo; Kawata, Satoshi. Rapid sub-diffraction-limit laser micro/nanoprocessing in a threshold material system. *Appl Phys Lett* 2002, **80**(2)**:** 312-314.

Chapter 4. Materials & Methods

This chapter summarises the materials used and techniques applied in the present work. While the first section addresses the materials used for the substrate preparation and patterning techniques, the second section describes the applied procedures including substrate modifications, structuring, simulations and characterisation approaches.

4.1. Photoresists

Photoresists are photo-active materials in which chemical bonds are either created by light illumination, so called negative tone resists, or destroyed, called positive tone resists. Typically, a photoresist contains two main components: organic molecules carrying reactive groups and a photo initiator, which starts a reaction when exposed to light. Structures presented in this work were built up by two different negative type photoresists, IP-Dip and IP-L 780 (Nanoscribe). Both are composed of low molecular weight methacrylate monomers and thenoylcoumarin as initiator. The product information as well as chemical structures of the components are shown in **Table 4-1** and **Figure 4-1**.

Table 4-1. Photoresists used in two-photon lithography

The data shown corresponds to the general product information provided by the manufacturer. (n, refractive index; IPA, isopropanol; PGMEA, propylene glycol methyl ether acetate)

Features	IP-L 780	IP-Dip
n (780 nm) unexposed	1.48	1.52
Prebake	No	No
Cast process	Drop casting	Drop casting
Exposure	780 nm for 2PP	780 nm for 2PP
Postbake	No	No
Developer	PGMEA/IPA	PGMEA/IPA

IP-L 780 is composed of approximately 95% pentaerythritoltriacrylate (PETA; CAS: 3524-68-3) and 5% 7-diethylamino-3-thenoylcoumarin (DETC; CAS: 77820-11-2). IP-DIP includes two more monomeric compounds, 9,9-Bis[4-(2-acryloyloxyethyloxy) phenylfluorene (CAS: 161182-73-6) and polyethylene glycol o-phenylphenyl ether acrylate (OPPEA, CAS: 72009-86-0). In the case of IP-Dip, no photoinitiator is declared in the data sheets, although a starting molecule is required for a

polymerisation reaction. From differential scanning calorimetry experiments (not shown), it is assumed that the same initiator as in IP-L 780, DETC, is applied as a starter.

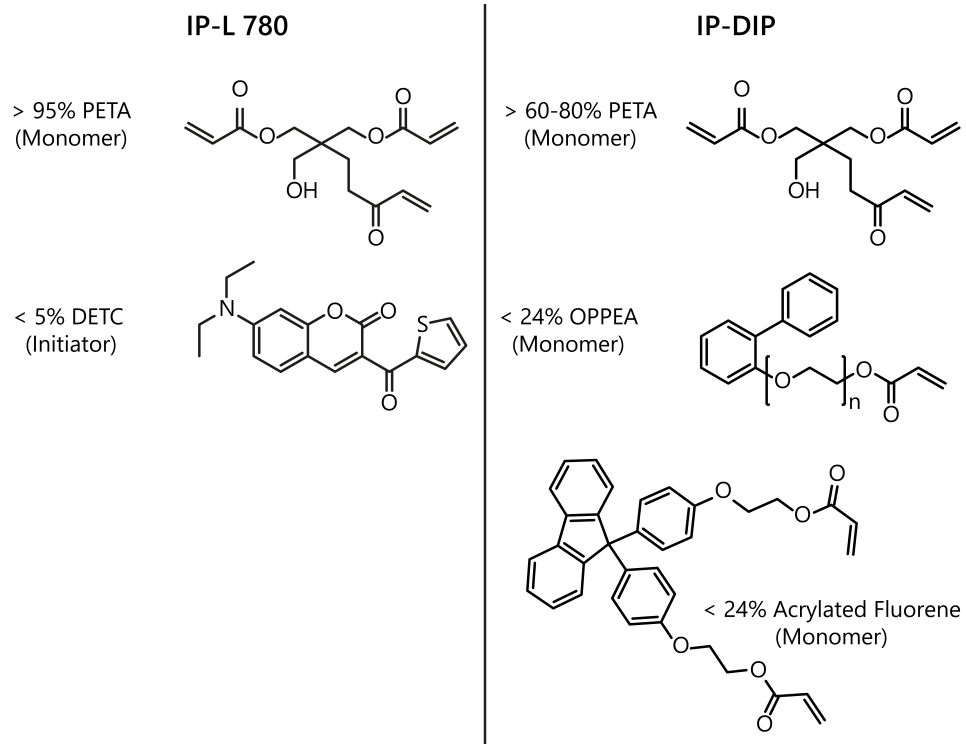

Figure 4-1. Chemical components of photoresists

The data shown corresponds to the material safety data sheets provided by the manufacturer. Acrylated fluorene: 9,9-Bis[4-(2-acryloyloxyethyloxy) phenylfluorene; DETC: 7-diethylamino-3-thenoyl coumarin; OPPEA: polyethylene glycol o-phenylphenyl ether acrylate; PETA: pentaerythritoltriacrylate

4.2. Substrates and Preparation

As substrates for the presented structures, various materials were used: glass coverslips (Menzel-Gläser), fused silica (Nanoscribe), and Silicon wafers (Silicon materials). After cleaning with acetone, isopropanol, ethanol, and water, each for 5 min in an ultra-sonic bath, the substrates were either directly used for two-photon lithography or were further functionalised chemically or covered.

The following substrate modifications were used:

i. Deposition of a gold film on fused silica by using an auto fine coater (JFC-1300, JOEL) for 2 min at 40 mA. The substrate was used as TPL-substrate for the validation experiments described in Chapter 8.

ii. Deposition of an aluminium film on fused silica, to obtain a half opaque and half transmissive substrate. The aluminium deposition was conducted with a sputter coater (TPG 300, Balzers)

equipped with a custom-built sensor, that allows a better control of the resulting thickness. A 100 nm film was applied with a mean sputtering rate of 0.3 nm/s on one half of the substrate while the other was masked by a tape. The substrate was used for the divergence angle characterisation of the TPL-laser beam described in Chapter 4.7.

iii. Substrate functionalisation with (3-Methacryloyloxypropyl) trichlorosilane (Abcr) to enhance the adhesion between TPL-structures and substrate. The procedure is summarised in **Figure 4-2**. After the cleaning steps described above, the surfaces of the substrates were activated with an oxygen plasma for 1 min (ATTO, Diener). Subsequently, the substrates were placed in a desiccator together with 20 µl methacrylated trichlorosilane and held under nitrogen for 1 h. To prevent premature cross-linking of the methacrylate C-C double bonds the silanisation was conducted in complete darkness. It was observed that the performed stick-silanisation caused an unwanted spreading of the photoresist over the edges of the glass substrate. To avoid this, the edges of the glass substrate were masked with parafilm or adhesive tape before the silane treatment. In doing so, a surface energy barrier was created for the photoresist, by maintaining the original surface properties at the edges of the substrate. This mask was removed after the silanisation step. The substrate was used as a substrate for micropillar structures presented in Chapter 5.

Figure 4-2. Stick-silanisation procedure

Substrates were cleaned with acetone, isopropanol, ethanol, and distilled water in an ultrasonic bath. Subsequently, they were activated via plasma (1), masked with tape (2), and placed in a desiccator together with liquid trichlorosilane. After 1 h in vacuum in the dark as well as nitrogen environment at room temperature (RT) the functionalised substrates provides better adhesion to the polymerised photoresist than a substrate without treatment.

4.3. Biological Surfaces

Morpho rethenor butterflies were purchased from Jens Köster (www.butterfly-inc.de). Wings were removed from the butterfly and cut into small pieces of approximately 1 cm^2 or 0.5 cm^2 and then either directly mounted on sample holders or glued on silicon substrates for further investigations.

4.4. Ellipsometry

Ellipsometry was used to determine the refractive index n and the extinction coefficient k in dependence of the wavelength λ for each TPL substrate and photoresists used. Prior to the measurements, the TPL-substrates were cleaned with acetone, isopropanol, ethanol, and water, each for 5 min in an ultra-sonic bath. The photoresists were measured in two conditions: in the unpolymerised state, which is needed for simulations of the expected structure sizes in TPL (used in Chapter 8, Chapter 9), and in the developed state used for the analyses of optical properties of fabricated structures (used in Chapter 6 Chapter 7). Samples of non-cross-linked photoresists for ellipsometry were obtained, by spin coating the material at 3000 rpm (Spin coater Laurell WS 650MZ) on plasma activated fused silica substrates (1 min, oxygen plasma) and then measured directly. To obtained developed samples, the spin coated films were additionally cross-linked by an UV-exposure using an UV-lamp (S1500A, OmniCure) at 350 mW for 300 s in an N_2-atmosphere, and then developed according to the procedure presented in Chapter 5. Ellipsometry data were acquired from three different angles using the Spectroscopic Ellipsometer M-2000 / A-SE (J.A. Woollam Co. Inc.) and fitted by the Cauchy dispersion. The device handling and curve fitting were conducted by Bruno Schäfer. Examples of curves obtained on the different TPL-substrates (silicon, glass, gold, fused silica) and photoresists (IP-DIP, IP-L) are displayed in **Figure 4-3**. The mean refractive indices at λ = 780 nm of each sample, relevant in the course of this thesis, were obtained from three measurements and are summarized in **Table 4-2**.

For simulations supporting a new TPL-fabrication method (mainly discussed in Chapter 8), the reflectivity *R* was calculated according to the simplified Fresnel equation (25). The results for diverse photoresist-substrate-combinations at 780 nm, the laser wavelength of the TPL-system, are shown in **Table 4-2**.

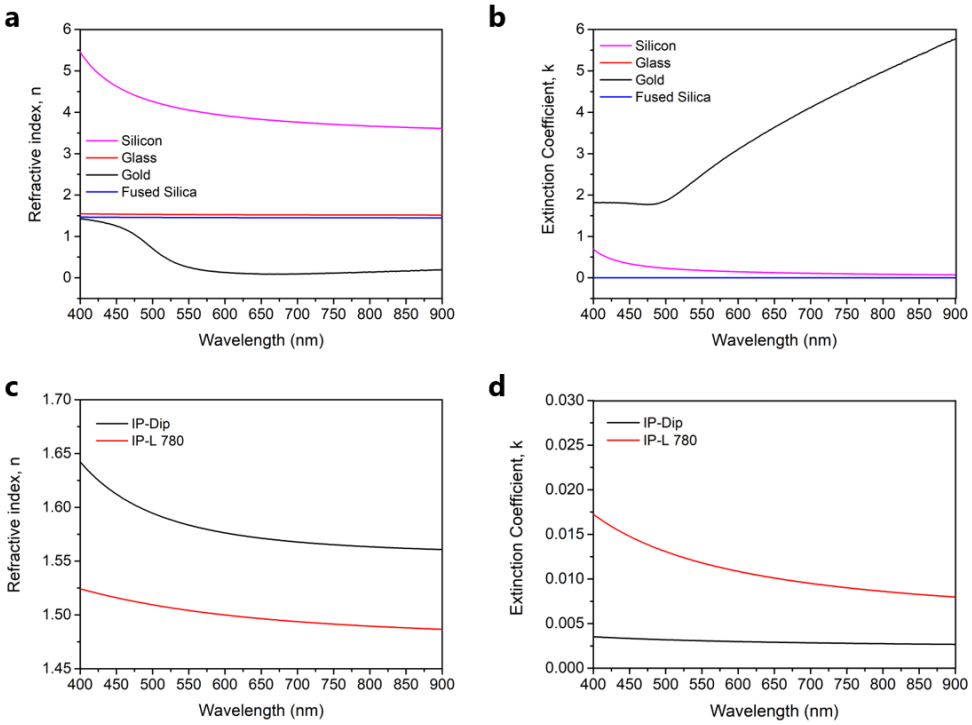

Figure 4-3. Cauchy optical constants of used materials

(a,c) Refractive indices and (b,d) extinction coefficients of (a,b) substrates and (c,d) photoresists determined by fitting of ellipsometry data. (b) At the shown resolution, the curve measured on the glass cover slip is hidden below the curve obtained for fused silica. liq.: non-cross-linked photoresist, dev.: photoresist developed.

Table 4-2. Relevant refractive indices *n* and reflectivities *R* at the photoresist-substrate interface

n_{780}: refractive index at the laser wavelength of the TPL-system used, $R_{IP\text{-}Dip}$: Reflectivity at the interface between IP-Dip photoresist and the different substrates, $R_{IP\text{-}L\ 780}$: Reflectivity at the interface between IP-L 780 photoresist and the different substrates. [1] non-cross-linked photoresist, [2] photoresists after polymerisation, development and additional UV-exposure

Substrate	n_{780}	$R_{IP\text{-}DIP}$	$R_{IP\text{-}L\ 780}$
Gold	0.128	0.7108	0.7054
Fused Silica	1.45	0.0003	0.0001
Glass	1.5157	0.0000	0.0002
Silicon	3.684	0.1767	0.1843
IP-Dip[1]	1.5034	-	-
IP-L[1]	1.4708	-	-
IP-Dip[2]	1.5286	-	-
IP-L[2]	1.4911	-	-

4.5. Contact Angle Characterizations

In Chapter 5, forces acting during the evaporation on small pillar arrays are discussed. The equations used depend on the contact angle between the pillar material and the evaporating liquid, in this case isopropanol. In order to obtain this value, the resist was spin coated for 5 min at 3000 rpm (Spin coater Laurell WS 650MZ) on plasma activated fused silica substrates (1 min, oxygen plasma) and subsequently cross-linked by UV-exposure using a UV-lamp (S1500A, OmniCure) at 350 mW for 300 s in an N_2-atmosphere. Isopropanol drops (97 %, Sigma Alderich) of ca. 3 µl were applied via pipetting and the contact angles were recorded using the contact angle measuring device (OSA 25, Data Physics) set to the sessile drop method. Contact angles were evaluated using ellipse-fitting. Nine measurements on different films on different positions were performed resulting in a contact angle θ_c of 14.6 ± 1.9°. An example of an isopropanol drop on IP-Dip photoresist is shown in **Figure 4-4**.

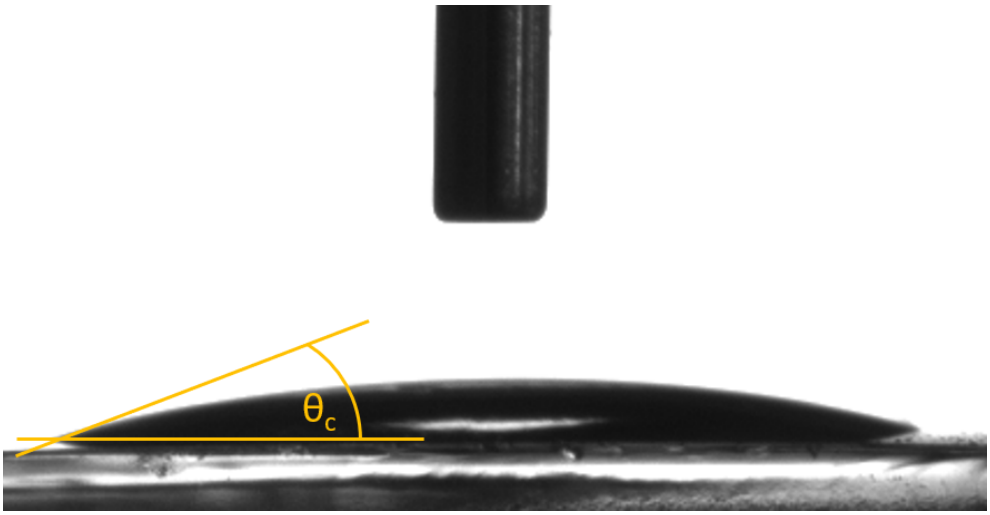

Figure 4-4. Contact angle of isopropanol on IP-Dip photoresist

θ_c: Contact angle of 14.6°.

4.6. Two-Photon Lithography

This chapter gives information about the applied TPL device, important fabrication parameters, approaches to implement structures for fabrication, and the general experimental approach. It does not contain detailed experimental parameters for fabricated TPL structures presented in this thesis. These are reported in the respective experimental parts the 'Results and Discussions' chapters.

4.6.1. *General Device Assembly*

In the present work a two-photon lithography (TPL) printing system controlled by the DeScribe software, both purchased from Nanoscribe, was used. An image of the system is shown in **Figure 4-5**.

The system is installed on an optical breadboard and is equipped with an optic cabinet comprising the optics and the FemtoFiber pro NIR laser (Toptica Photonics AG, laser power range 50 – 150 mW, pulse length of 100 – 200 fs, 780 nm centre wavelength), an inverse optical microscope with autofocus function (Carl Zeiss Axio Observer), a hierarchical positioning system, a computer as well as an electronics rack.

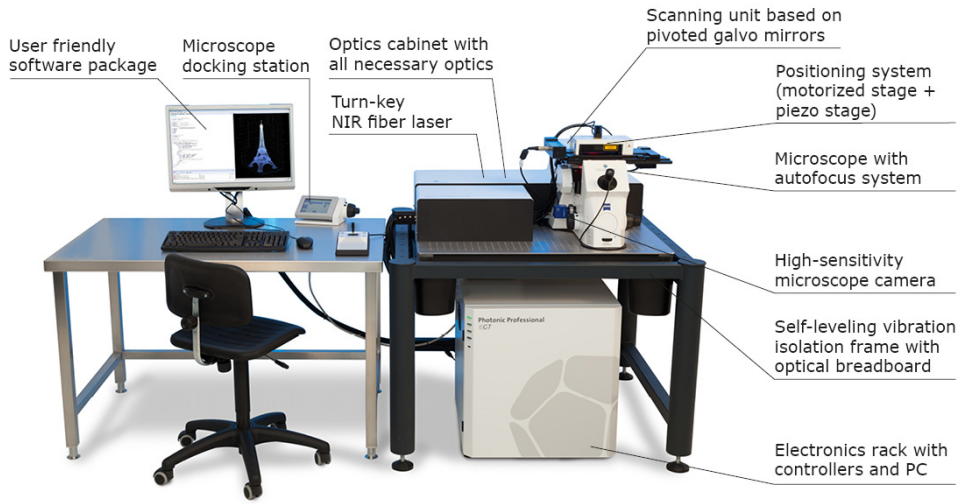

Figure 4-5. Two-photon lithography system

Main components of the two-photon lithography system comprising a microscope, a high pulsed IR-femtosecond laser, a hierarchical positioning system, and a vibration isolation (image was taken from the manufacturer homepage).

4.6.2. *The Positioning System*

The hierarchical positioning system allows a nanometre accurate beam positioning, while providing an accessible writing area of 100x100 mm. The accuracy of several nanometres is given by two deflecting mirrors, also known as mirror galvanometer, where the mirror deflections actuate the laser beam motion. Experience showed that addressing positions beyond an area of 140x140 µm leads to vignetting effects, and thus, loss in structure quality. For this reason, samples were stitched by using accessible piezo elements or the motorised x-y-stage. The piezo movement operates within a range of 300x300x300 µm with a precision of several tens of nanometres. Larger areas had to be stitched with a precision of +/- 200 nm by using the motorised stage.

4.6.3. *Experimental Setups of the TPL System*

The TPL-system allows two principal experimental set-ups, the standard set-up and the dip-in set-up, both illustrated in **Figure 4-6**. In case of the standard configuration, the photoresist is situated on the bottom side of a glass coverslip and the objective is immersed in an oil droplet from the top. In this configuration, the laser beam propagates through oil (Zeiss, $n = 1.518$) as well as the glass substrate ($n = 1.5157$) before it is focused within the photoresist (IP-L 780, $n = 1.4903$) (see Chapter 4.4 for the

refractive index characterisation of substrates and photoresists). The resulting structures do not face the objective.

In case of the dip-in configuration, the objective is immersed directly into the photoresist (IP-Dip, n = 1.50) and the structures are built up on the top side facing the objective. This configuration allows for higher features and offers the opportunity to print on opaque substrates. However, this approach has higher requirements on the photoresist, which limits the variability of applicable materials in this configuration.

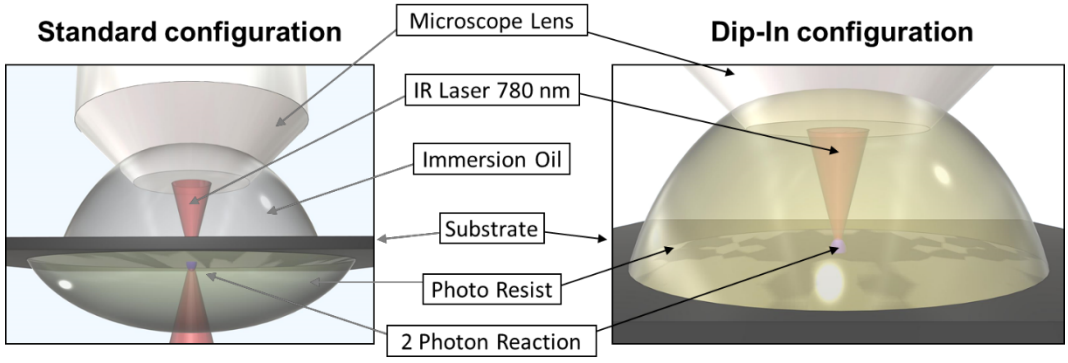

Figure 4-6. The two experimental set-ups of the two-photon lithography system

(a) Standard configuration: objective is immersed in oil and the photoresist is placed on the opposite side of a transparent glass substrate. Structures are printed on the averted side of the substrate; (b) Dip-In configuration: objective is directly immersed into the photoresist. Structures are written at the glass-photoresist interface facing the objective (image provided by Elmar Kroner)

4.6.4. *Maximum Resolution and Minimum Feature Size*

According to the manufacturer data sheet, the lateral resolution of the used system is specified to be ≤ 500 nm, typically 400 nm, when using the galvanometer, and ≤ 500 nm, typically 300 nm, when using the piezo stage only; considering a 63x objective with NA = 1.4 and the application of the IP-DIP photoresist. This results in a lateral feature size of ≤ 200 nm, typically 160 nm, and ≤ 200 nm, typically 150 nm, for the use of the galvanometer and piezo stage, respectively. The vertical resolution is stated to be ≤ 1500 nm; typically 1000 nm for the galvanometer mode and ≤ 1000 nm; typically 800 nm for the piezo stage movement.

4.6.5. *Experimental Procedure*

The typical TPL-experiment consists of the following steps:

i) Calibration of the laser

ii) The preparation of the substrate and mounting into a sample holder

iii) Application of the photoresist
iv) Loading of the sample holder into the TPL-system
v) Adjustment of the objective lens
vi) Loading of the exposure parameters and the structure design
vii) Approaching the target location, typically using the autofocus
viii) Exposure of the photoresist
ix) Unloading of the sample
x) Sample development

4.6.6. *Experimental Exposure Parameters*

In addition to the two printing configurations, the TPL-system provides numerous further parameters and settings. The most important are summarised by **Table 4-3**. In piezo mode, the laser is fixed and the movement of the voxel is performed by a simultaneous (x,y,z) displacement of piezos. In galvo mode, galvanic mirrors are used to scan the laser in the x,y directions and z is set by a piezo. The latter mode is typically used for layer-by-layer fabrications, where an object is built by horizontally stacked slices. After one slice is polymerised, the z-position of the sample is changed by the piezo and the next slice begins.

Furthermore, the used TPL-system provides the capability to change the exposure approach during the beam movement from continuous exposure to pulsed exposure, and vice versa. In the continuous exposure, the material is exposed continuously, while the laser beam is moved. Here, the exposure dose is determined by the scan speed and the laser power of the laser beam. In the pulsed mode, the beam is periodically blanked during the movement resulting in a dotted exposure. This approach is characterised by the laser power, the exposure time per dot, as wells as the distance between two exposed dots, called point distance.

The system also allows a flexible adjustment of the laser power in the range from 0 % to 100 %, where 100 % is equivalent to 50mW. It has to be mentioned, though, that the laser power is measured before the beam enters the objective, which is not equivalent to the power that affects the photoresist in the focal point.

The two last parameters important to mention are the settling time and the find interface setting. The first determines the waiting time between two exposed objects: lines during continuous exposure and points during the pulsed exposure. The latter allows for instance to add a focus offset to the autofocus result moving the z-position of the first voxel into the substrate and thereby improving the attachment of fabricated structures to the substrate. In addition to the standard parameters described, further self-implemented parameters, such as layer number, layer distance, and line distance were used. The parameters and their description are listed in **Table 4-4**.

Table 4-3. Experimental parameters provided by the TPL-system

Abbr.: Abbreviation

Parameter	Abbr.	Unit	Description
Galvo writing mode			x and y-coordinates of the beam are changed by galvanic mirrors, z-positions are approached by piezo movement
Piezo writing mode			All coordinates are approached via piezo movement only
Continuous Exposure	CM		The material is exposed continuously, while the laser beam is moved
Scan Speed	SS	µm/s	Velocity of the laser beam motion during a continuous exposure
Pulsed Exposure	PM		The laser beam is periodically blanked during the movement resulting in a pulsed exposure
Exposure Time	ET	ms	The time the material is irradiated during the pulsed exposure
Point Distance	PD	nm	The distance between to exposed spots during the pulsed exposure movement
Laser Power	LP	mW	Laser power of the beam entering the objective; the parameter does not express the laser power in the focal plane
Settling Time	ST	ms	The waiting time until the next position is exposed
Find Interface	FI	µm	Negative offset of all values ensuring substrate attachment

Table 4-4. Self-implemented experimental parameters

Parameter	Abbr.	Unit	Description
Layer Number	LN		Number of layers exposed to build up a structure
Layer Distance	LD	µm	Offset between two exposed layers
Line Distance	LD	nm	Distance between the two exposed lines

4.6.7. *Structure Design*

As explained in detail in Chapter 3.5, polymerisation of the photoresist is initiated only in the focus point of the IR-laser beam. The smallest polymerised 3D-unit is represented by a voxel, a vertically elongated ellipsoid. By moving this voxel in a coordinate system, a great variety of 3D-structures can

be fabricated. To control the laser parameters and the exact movements of the beam, so called print jobs or motion protocols must be created. These motion protocols are expressed in the General Writing Language (GWL, programming language developed by Nanoscribe) and can be obtained by two approaches, by GWL-programming combined with computer added design (CAD) or by pure GWL-programming.

Microstructures are typically sketched using a CAD–software, for example the Inventor software (Autodesk). From such 3D-sketches, the surface geometry is exported as stereolithography (stl)-file containing only the 3D-envelope of the structure without any representation of colour or texture. This 3D-envelope can then be converted into a motion protocol by means of the DeScribe-software and directly used for fabrication or adjusted manually. The latter becomes necessary if several structures, each represented by a 3D-envelope, are intended to be exposed during the same TPL-fabrication job. The manual adjustment can also be used to define the structure position on the substrate or to tailor the exposure parameters.

For structure sizes in the range of voxels it is more suitable to implement the motion protocol directly using the DeScribe-software. Here, the laser position can be determined precisely in a x,y,z-coordinate system, what provides a high control over the exposed volume. This approach is recommended to be used only by experienced users, as it requires a detailed knowledge of the different coordinate systems of the positioning system as well as commands for hardware control. A wrong programming could cause serious damage to the piezo elements or the objective.

4.6.8. *Development*

Similar to the most common lithography methods, in TPL a subsequent development step has to be performed to remove the unexposed photoresist after the exposure. The typically used procedure comprises development in propylene glycol monomethyl ether acetate (PGMEA) at RT for 20 min, a subsequent rinsing with isopropanol, and air drying. As this typical development procedure was not sufficient for structures presented in this work, an improved method was developed, which is presented in detail in Chapter 5.

4.7. Divergence Angle Characterisation of the Laser Beam Used in TPL

Beam divergence is an angular measure of the increase in beam diameter with respect to the axial position, and as such, an important parameter in the simulation of intensity distributions along the optical axis. The beam divergence angle θ_{div} of the TPL-laser beam was determined by measuring the beam width at various distances from the focal spot using an adapted version of the knife edge method[1]. The

experimental set-up is shown in **Figure 4-7**. For this, the common TPL substrate was modified. The modified substrate consisted of a fused silica slide partially coated with aluminium (see Chapter 4.2 for preparation), on whose backside a BPW34-photodiode was glued. The photodiode was placed exactly at the edge of the aluminium-coating, so that half of the diode was facing the transparent part of the substrate and the other half the coated, thus opaque, part of the substrate (**Figure 4-7a,b**).

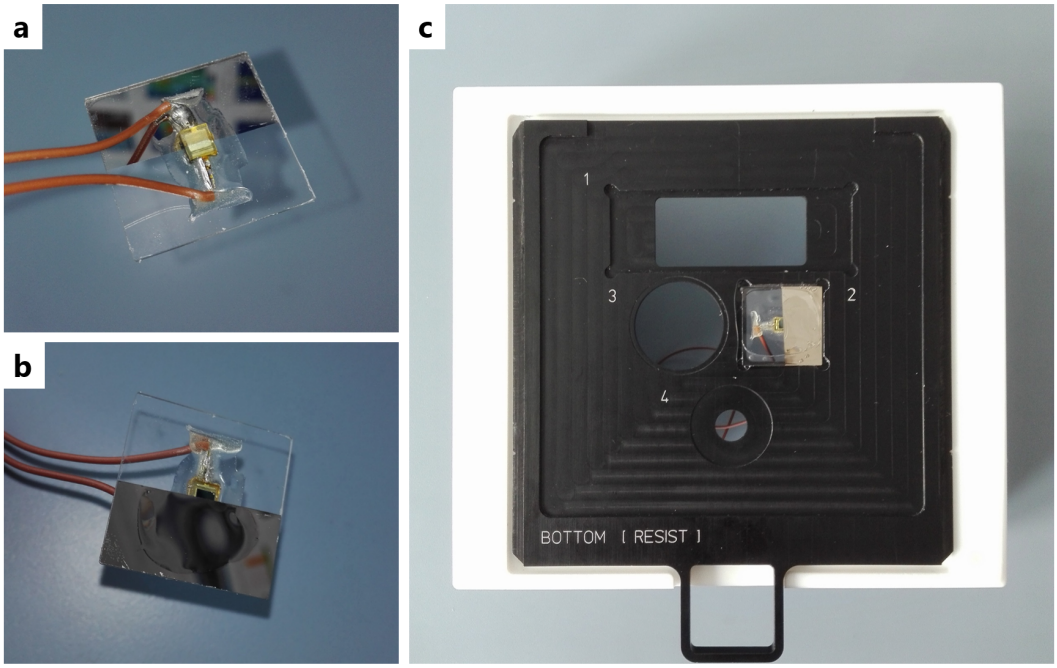

Figure 4-7. Experimental set-up of the TPL-beam shape characterisation

(a) Bottom and (b) top view of the modified TPL substrate composed of a fused silica substrate partly coated by aluminium, and a glued photodiode. (c) The modified substrate mounted into the TPL-holder instead of a commonly used substrate.

The modified substrate was mounted into the TPL-holder and covered by immersion oil (Zeiss, n = 1.51) instead of the commonly applied photoresist (**Figure 4-7a,c**). After placing the holder into the TPL-system the photodiode was connected to an oscilloscope (Pico Scope 2205) and a laptop. The TPL-experiment was designed to expose 200 lines with 20 µm lengths separated by 2 µm (**Figure 4-8a**), where approximately 150 lines were exposed on the transparent substrate and 50 on the opaque substrate (**Figure 4-8b**). Each line was exposed repeatedly for 50 times at the same position with a waiting time of 0.5 ms before the next line exposure. The system was operated at 10 mW laser power and 7000 µm/s beam velocity.

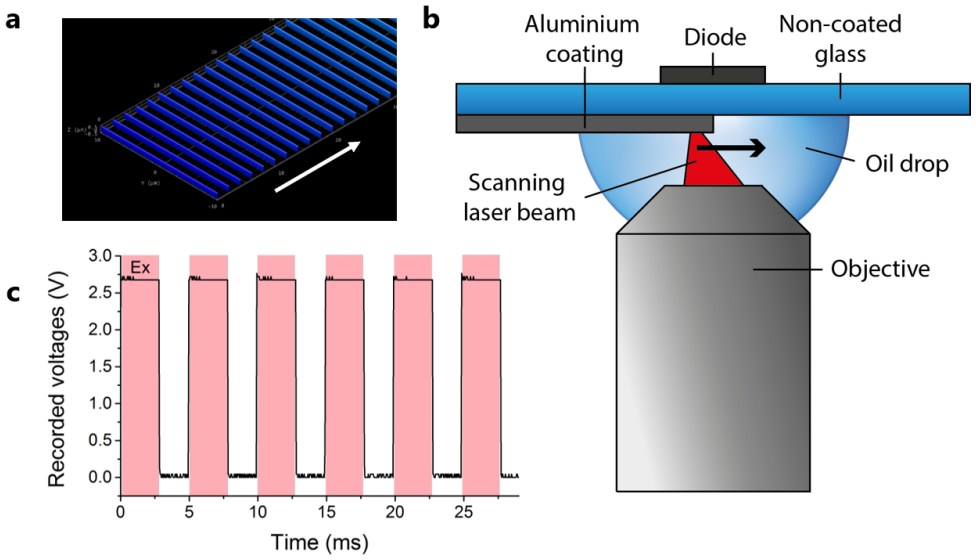

Figure 4-8. Experimental approach of the TPL-beam shape characterisation

(a) Laser movement during the experiment: 200 20 µm lines separated by a 2 µm pitch; (b) experimental set-up; (c) Example of a recorded signal on the transparent half of the substrate. High voltage values correlate to line exposures (ex, red areas).

Diode currents induced by each written line were transformed into voltages using a low-noise current preamplifier with 500 µA/V (SR570, Stanford Research Systems). An example of such a voltage signal is displayed in **Figure 4-8c**. Every red section in the graph corresponds to 50 exposed lines separated by the waiting time of 0.5 ms. The experiment was performed at three different focal planes: 50 µm defocus, 100 µm defocus, and 150 µm defocus (**Figure 4-9a**) and plotted against the displacement of the laser beam (**Figure 4-9b**). The experiment was repeated 3 times at each defocus resulting in 3 experimental sets.

To obtain the beam radii denoted as *a*, *b*, and *c* in **Figure 4-9a**, the curves were fitted against model curves obtained for a beam having a Gaussian intensity distribution with a variable beam radius as a fit parameter (**Figure 4-9b**). The distance between 90% and 50% ($d_{50\text{-}90}$) of the initially measured voltages were extracted from the fitted curves for each defocus. This range corresponds to a beam only slightly mask by the aluminium coating (90%), and the centre of the illuminated area where half of the beam is masked (at the inflection point).

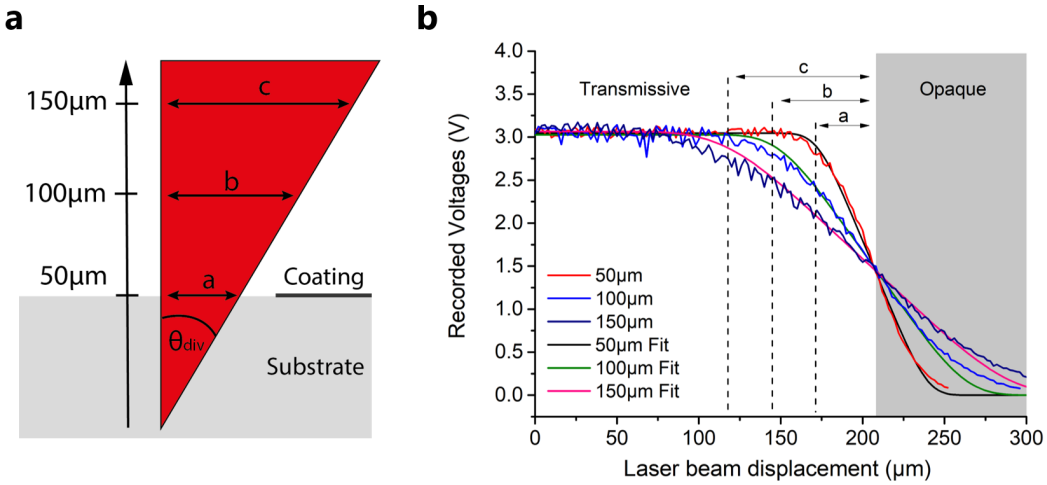

Figure 4-9. Schematic and results of the divergence angle measurements

(a) Schematic of the measured defocus positions; *a*, *b*, *c* denote the beam radii at 50 µm, 100 µm, and 150 µm defocus, respectively; θ_{div} half divergence angle; (b) Smoothed voltage curves and their fits of one experimental set; *a*, *b*, *c* indicate distances between 90% and 50% ($d_{50\text{-}90}$) of the initially measured voltages for the different curves, respectively.

The mean $d_{50\text{-}90}$ values for the different focal planes were plotted against the corresponding defocus and a linear fit was performed to determine the slope $\Delta y/\Delta x$ (**Figure 4-10**). From the resulting $\Delta y/\Delta x$ = 0.61, the half divergence angle θ_{hdiv} can be calculated as follows:

$$\boldsymbol{\theta_{hdiv} = arctan(\Delta y/\Delta x)} \qquad (30)$$

resulting in θ_{hdiv} = 31.38°, and thus, with $\theta_{div} = 2\theta_{hdiv}$ in a beam divergence angle θ_{div} of 62.76°.

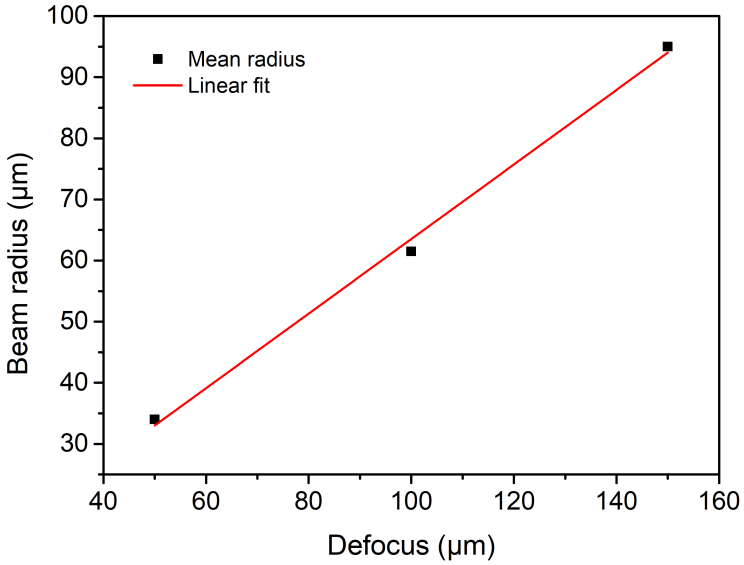

Figure 4-10. Obtained beam radii plotted against the defocus

Each data point represents the mean radius of three measurements.

4.8. Simulations of Intensity Distributions during TPL

This chapter gives a detailed insight into the simulations performed in Chapter 8, where the intensity distributions and dimensions of TPL-structures close to the focal spot of the TPL-system are predicted considering a standing wave formation at a reflective substrate. The simulation program was implemented by Peter Rogin, Leibniz Institute for New Materials, in Object Pascal (Lazarus IDE v. 1.6.).

The simulations were approached in two steps to minimise the calculation time. In the first step, 2D-maps of the electric field distribution over particular field points x_F around the focus were calculated with different divergence angles of the beam α (equivalent to θ_{hdiv} in Chapter 4.7). The used approach is based on the Fresnel-Huygens principle (see Chapter 2.3.1 for the explanation of the Fresnel-Huygens principle) and assumes multiple dipole emitters x_S as light source. The latter was used, as the light distribution of such a source is expected to be comparable with the distribution caused by a focusing objective. In the second step, the 2D-maps provided the input values to evaluate the field distribution, when a reflection plane is introduced at a particular focal plane F causing a standing wave formation between the incoming and reflected wave. Varied parameters per 2D-map were the wavelength λ, the refractive index of the propagating medium n, the substrate reflectivity R, the phase shift during reflection φ_r and the position of the focal plane with regard to the reflective plane F.

4.8.1. *Definition of the Coordinate System and Boundary Conditions*

The characteristic variables of the field distribution, such as field strength and dipole density, are represented by vectors. For the reason of simplicity, the components of these vectors are mathematically treated as complex numbers, where the real part of the complex number determines the physical quantity.

Light waves are always treated as harmonic waves, whose temporal development is systematically excluded according to $V_t(\vec{x}, t) = V(\vec{x}) \cdot e^{-i\omega t}$ for any time-dependent variable V_t. The following considerations always refer to the position dependent part $V(\vec{x})$.

The origin 0/0/0 of the coordinate system was set to the focal point of the laser beam, such that the z-axis corresponds to the axis of the laser beam, and the xy-plane to a cross-section through the focal point. The direction of the laser beam was conceived to originate from positive z-values and to propagate in the direction of negative z-values. The dipoles were arranged in a two-dimensional circular plane parallel to the xy-plane at a height z_S above the calculated field distribution assuming an exit pupil of a microscope objective. Dipole source points x_S and field points x_F were chosen independently and are

therefore described by not related coordinates in the same coordinate system. The respective position vectors are given by:

Field Point: $$\vec{x}_F = \begin{pmatrix} x \\ y \\ z \end{pmatrix}$$

Source Point: $$\vec{x}_S = \begin{pmatrix} u_s \\ v_s \\ z_s \end{pmatrix} \quad (31)$$

4.8.2. *Determination of the Electric Field Maps*

Considering the Fresnel-Huygens principle (explained in detail in Chapter 2.3.1), the electric field $\vec{E}(\vec{x}_F)$ of a point $\vec{x}_F$ located in an electric field below a distribution of dipole source points $\vec{x}_S$ can be calculated by the superposition of all electric fields $\vec{E}$ which depend on the respective positions u and v of the emanating source points within the distribution:

$$\vec{E}(\vec{x}_F) = \iint_{u_s,v_s} \vec{E}\, du_s\, dv_s = \iint_{u_s,v_s} f\left[\vec{P}(\vec{x}_S), \vec{\Delta}\right] du_s\, dv_s \quad (32)$$

where $\vec{E}$ is determined by a function *f* describing the dipole field within an area element $du\ dv$ around the source point at a given distance with the dipole density $\vec{P}(\vec{x}_S)$ and the distance vector between the source and field point $\vec{\Delta} = \left(\vec{x}_M - \vec{x}_Q\right)$. With

$$\rho = \frac{2\pi}{\lambda}\left|\vec{\Delta}\right| \quad (33)$$

where ρ is the distance between the measuring point and source point scaled to the wavelength λ, and the direction vector $\vec{n}$ from the source point to the measuring point normalized to the unit length

$$\vec{n} = \frac{\vec{\Delta}}{\left|\vec{\Delta}\right|} \quad (34)$$

With (33) and (34) $\vec{E}$ can be expressed by:

$$\vec{E} = \left\{ \frac{\left(\vec{n} \times \vec{P}(\vec{x}_S)\right) \times \vec{n}}{\rho} + \left[3 \cdot \vec{n} \cdot \left(\vec{n} \cdot \vec{P}(\vec{x}_S)\right) - \vec{P}(\vec{x}_S)\right] \cdot \left(\rho^{-3} + i \cdot \rho^{-2}\right) \right\} \cdot e^{i\rho} \quad (35)$$

This equation is derived from the expression formulated by Hertz in 1887 describing a field of a dipole radiator, but without the constant pre-factor $\omega^3/4\pi\varepsilon c^3$, which is considered to be 1 in this case, and thus, is not stated in the equation.

To estimate the dipole density $\vec{P}(\vec{x}_S)$ of a point $\vec{x}_S$ three factors has to be considered: the respective dipole amplitude $\left|\vec{P}(r)\right|$, the polarization $\vec{e}_P$, and the phase $\varphi(r)$.

Dipole amplitude: It is assumed that the beam has a Gaussian beam profile in the plane of the circular source distribution, which radius r_{max} results from the set divergence angle α of the beam and the working distance z_S between the focus and the source. With the numerical aperture *NA* of the lens, the refractive index n of the immersion medium for which the numerical aperture is defined, the condition for r_{max} is given b:

$$\boldsymbol{arctan(r_{max}/z_S) = arcsin\left(\frac{NA}{n_{NA}}\right)} \tag{36}$$

The amount of the dipole density $\vec{P}(r)$ of a source point located with a distance r to the z-axis with the maximum value r_{max} and a Gaussian distribution with a width w, whereby r and w are calculated with

$$\boldsymbol{r = \sqrt{u^2 + v^2}} \tag{37}$$

$$\boldsymbol{w = z_S \cdot tan(\alpha)} \tag{38}$$

can therefore be estimated by:

$$\left|\vec{\mathbf{P}}(\mathbf{r})\right| = \mathbf{P_0} \cdot \mathbf{e}^{-(\mathbf{r}/\mathbf{w})^2} \tag{39}$$

Where P_0 is solely a constant scaling factor that is assumed to be 1 for convenience.

Polarisation: The polarisation of an electromagnetic wave is essentially transversal to the direction of the propagation; in this case the xy-plane. The rotation symmetry of a voxel is only given when no direction in the xy-plane is distinguished, and thus, only by circular polarization. This can be represented by a complex polarization vector as follows:

$$\vec{\boldsymbol{e}}_{\boldsymbol{P}} = \frac{\mathbf{1}}{\sqrt{\mathbf{2}}}\begin{pmatrix} \mathbf{1} \\ \pm\boldsymbol{i} \\ \mathbf{0} \end{pmatrix} \tag{40}$$

where the positive and negative signs before the imaginary unit *i* describe right and left circular polarization, respectively. As the direction of the circular polarization is irrelevant for the simulation result, they are treated as equal in the calculations.

When a circular polarization of the beam is assumed, the field distribution becomes rotationally symmetrical with respect to the z-axis, and thus, allows a sufficient description of the field by the calculation of the xz-plane only. Consequently, y = 0 and can be neglected in further considerations.

Phase: A condition for focusing is that the contributions of all dipoles from the source plane arrive at the focal point ($x = y = z = 0$) with the same phase φ^2. Deviations in travel time or distance must therefore be compensated by differences in the phase. The distance $d(r)$ from a source point in the source plane at z_S with a distance r to the z-axis, calculated by equation (37), where

$$\boldsymbol{d(r) = \sqrt{z_S^2 + r^2}} \tag{41}$$

The phase shift on the way from source to the focus point is $2\pi * d/\lambda$. So, this focusing condition is fulfilled by a phase φ of the source of

$$\boldsymbol{\varphi(r) = -\frac{2\pi}{\lambda} \cdot \sqrt{z_S^2 + r^2}} \tag{42}$$

With the dipole amplitude $\left|\vec{P}(r)\right|$, the polarization $\vec{e}_P$, and the phase $\varphi(r)$, driven from equations (39), (40), (42) respectively, the dipole density $\vec{P}(\vec{x}_S)$ can be calculated with:

$$\boldsymbol{\vec{P}(\vec{x}_S) = \left|\vec{P}(r)\right| \cdot \vec{e}_P \cdot e^{i\varphi(r)}} \tag{43}$$

As an estimation of $\vec{E}(\vec{x}_F)$ by the presented integral in (32) is very time-consuming and the computing costs are immense, a statistical Monte-Carlo-experiment was conducted. For this purpose, the xz-plane was divided into discrete pixels (field points) and the following procedure is applied repeatedly:

i. Selection of an arbitrary field point x_F
ii. Random selection of arbitrary u, v-values of the continuous source distribution determining x_S
iii. Calculation of the intensity contribution $\vec{E}$ of the selected source point x_S to the selected field point x_F
iv. Addition of the calculated $\vec{E}$ to previous $\vec{E}$-values at this measuring point.

In the end, the value $\vec{E}$ at each point was divided by the respective number of contributions $N_{\vec{E}}$, which corresponded roughly to $N_{\vec{E}}$ = 100000 per field point. The resolution (interpolation point distance) between the field points of a map was set to 10 nm and run several days to obtain high-resolution simulations. The following values were assumed as constants: a wavelength λ_{map} = 0.5 µm of the beam and the objective parameters with a working distance z_S = 100 µm, a numerical aperture NA = 1.4 (based on the refractive index n_{NA} = 1.5 of an immersion medium).

4.8.3. *Evaluation of the Field Distribution with an Applied Reflective Plane*

In second step of the simulation, the obtained 2D-maps were used to examine the field distribution, when a reflection plane is introduced close to the focus at a particular focal plane F. In this case, the source waves are reflected with a particular reflectivity R, (which, in TPL depends of the refractive index of the photoresist and the refractive index; see ellipsometry measurements in Chapter 4.4 for evaluation), undergo a phase shift φ, and superimpose with other incoming waves leading to a standing wave formation, and thus, to a new electric field distribution $\vec{E}_{ir}(\vec{x}_F)$. Mathematically this can be expressed by:

$$\boldsymbol{\vec{E}_{ir}(\vec{x}_F) = \vec{E}_i(\vec{x}_F) + \vec{E}_r(\vec{x}_F)} \tag{44}$$

where $\vec{E}_i(\vec{x}_F)$ and $\vec{E}_r(\vec{x}_F)$ represent the electric field of the incoming and reflected wave, respectively. The electric field of the incoming wave $\vec{E}_i(\vec{x}_F)$ corresponds to:

$$\boldsymbol{\vec{E}_i(\vec{x}_F) = \vec{E}(\vec{x}_F)\left(f_\lambda \cdot \vec{x}_F - \vec{\delta}\right)} \tag{45}$$

with the displacement vector $\vec{\delta}$

$$\boldsymbol{\vec{\delta} = \begin{pmatrix} 0 \\ 0 \\ z_F \end{pmatrix}} \tag{46}$$

indicating the shift of the focus distance z_F.

The wavelength ratio f_λ between the evaluated wavelength λ_{eval} and the wavelength λ_{map} = 0.5 µm (applied in the calculation of the field maps in step number one) permits to adapt the results to the actual wavelength and refractive index used in the experiments:

$$\boldsymbol{f_\lambda = \frac{\lambda_{map}}{\lambda_{eval}}} \tag{47}$$

Here, λ_{eval} is determined by the new laser wavelength λ_{source} divided by the refractive index of the propagating medium n_m (in the case of the TPL, the wavelength of the laser and the refractive index of the photoresist) as follows:

$$\boldsymbol{\lambda_{eval} = \frac{\lambda_{source}}{n_m}} \tag{48}$$

Taking into account the reflection characteristics a_r of the surface with $a_r° = \sqrt{R}$, the phase shift φ during reflection, and the opposite propagation direction M_z of the reflected wave, which can be expressed mathematically by:

$$\boldsymbol{M_z = \begin{bmatrix} 1 & 0 & 0 \\ 0 & 1 & 0 \\ 0 & 0 & -1 \end{bmatrix}} \tag{49}$$

the field distribution $\vec{E}_r(\vec{x}_F)$ can be calculated the reflected wave similar to $\vec{E}_i(\vec{x}_F)$:

$$\boldsymbol{\vec{E}_r(\vec{x}_M) = M_z \cdot\ a_r \cdot e^{i\varphi} \cdot \vec{E}(\vec{x}_F)\left(f_\lambda \cdot M_z \cdot \vec{x}_F - \vec{\delta}\right)} \tag{50}$$

In the last step, $\vec{E}_r(\vec{x}_F)$ and $\vec{E}_i(\vec{x}_F)$ are used in the following condition, which is based on equation (**3**), to calculate intensity maps of the xz-plane:

$$\boldsymbol{I = \left|\vec{E}_i(\vec{x}_F)\ + \vec{E}_r(\vec{x}_F)\right|^2} \tag{51}$$

The obtained intensities of a the xz-map are scaled to the maximum value and displayed as a coloured image, where the colours depend on the intensity value.

4.9. Scanning Electron Microscopy

Surface topographies fabricated via two-photon polymerisation were examined using scanning electron microscopy (SEM) (Quanta 250 FEG, FEI) equipped with an Everhart-Thornley-detector (ETD) under high vacuum. Samples were cut and fixed with clamps on a metallic sample holder and observed from different perspectives. In order to minimise charge effects a copper tape was applied close to the structures. No coating was applied to maintain the functionality of the samples after examination. In the respective chapters more details are provided in the experimental part.

4.10. Optical Microscopy Imaging

Two optical microscopes (Eclipse LV100ND, Nikon, and Scope.A1 with HAL 100, Zeiss) were used for visual inspection of the fabricated TPL-structures. The optical microscopes were operated either in bright or dark field mode after white balancing with a white sheet of paper. The images were recorded using 5x, 10x, 20x, and 50x air objectives (Nikon, NA = 0.15, 0.3, 0.45, 0.8, respectively).

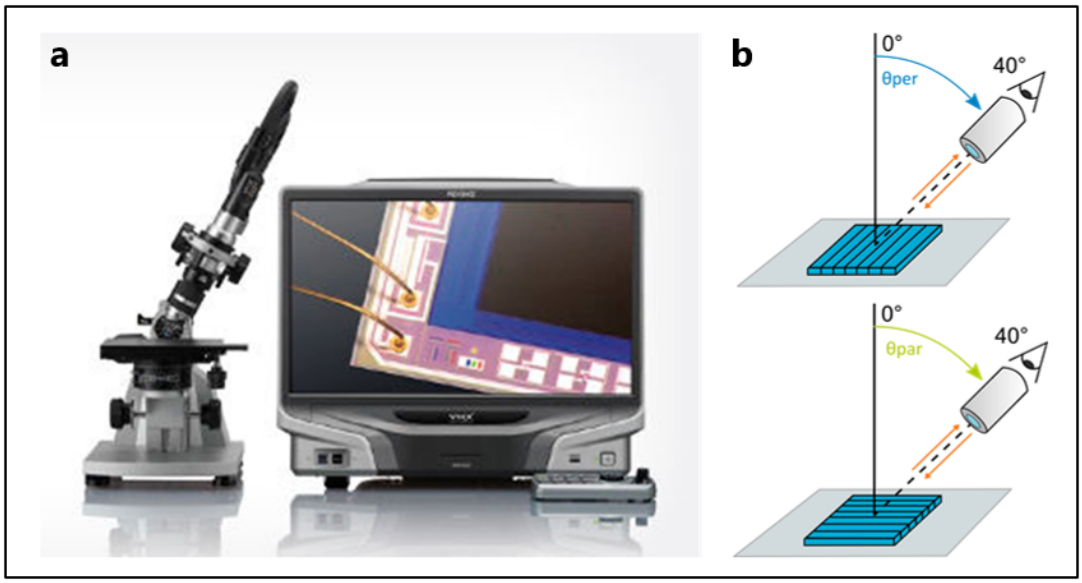

Figure 4-11. Angular resolved optical imaging

Digital microscope with an objective mounted at a rotating holder enables recordings from different angles of view (image was taken from manufacturer homepage). (b). Samples were investigated in two directions: perpendicular and parallel to sample features, which are indicated by lines on the sample.

Angular resolved optical imaging and video recordings were performed with a digital optical microscope (VHX-5000, Keyence) equipped with a tiltable objective holder; displayed in **Figure 4-11**. The tilting was performed manually, and therefore, had only a low accuracy for the adjusted incident and recording angle θ. Two different telecentric zoom objectives, VH-Z20W and VHZ100UW, were used with fully opened aperture. The former was operated with light coming through the objective, the latter with light

arising from circularly arranged diodes around the objective. This results in a bright field and dark field situation, respectively. As for the conventional microscopy, a white sheet of paper was used for white balancing.

Samples were investigated from two directions: perpendicular and parallel to sample features as depicted in **Figure 4-11b.** Videos show the continuous change in viewing angle for both rotations while moving the objective from 0° to 90° tilt. Additionally, images of particular observation angles were made in 10°-step. More details regarding the experiments performed are provided in the respective chapters.

4.11. Spectroscopy

Spectroscopy is a widely used technique to characterise wavelengths reflected, absorbed, or transmitted through a material. A typical spectrometer consists of a collimating mirror, a diffraction grating or prism, a focussing mirror, and a detector. An example of such a spectrometer is given in **Figure 4-12.** In this work, two different spectrometry set-ups were used, one providing angular resolution in backscattering condition, and another that enabled the measurements of very small areas.

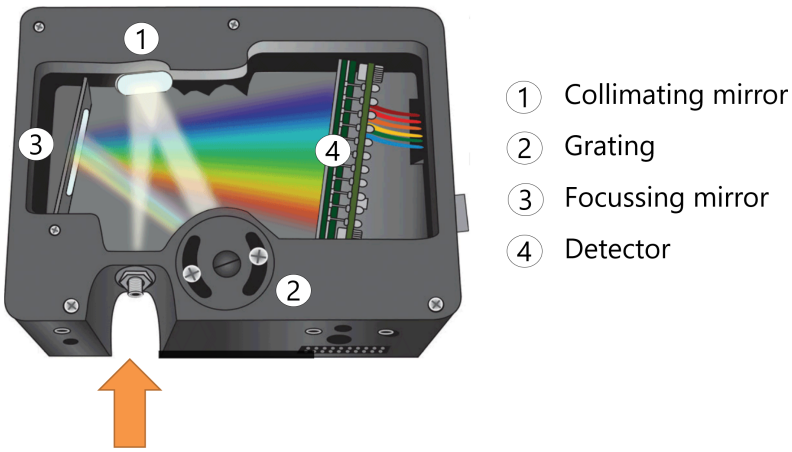

Figure 4-12. Assembly of a typical spectrometer

A typical spectrometer consists of a collimating mirror (1), a diffraction grating or prism (2), a focussing mirror (3), and a detector (4). The image was taken from the Ocean Optics homepage (oceanoptics.com) and modified. The orange arrow indicates the incoming light direction.

4.11.1. *Angular Dependent Spectroscopy*

Reflection spectra at different incident angles were recorded with a self-assembled set-up. This set-up included a commercially available USB 4000 spectrometer (Ocean Optics) with a spectral range from 200 nm to 1000 nm, a 400 µm reflection probe fibre, and a light source with a full irradiation spectrum of 200 – 1000 nm (DH-mini UV-Vis-NIR deuterium-Halogen light source). This spectrometer was combined with a goniometer (parts purchased from Thorlabs). The assembly is shown in **Figure 4-13**.

During investigations samples were attached to the sample holder with double sided adhesive tape. Spectra were recorded with 21-23 ms integration time, a boxcar window width of 5 and were averaged over 5 scans.

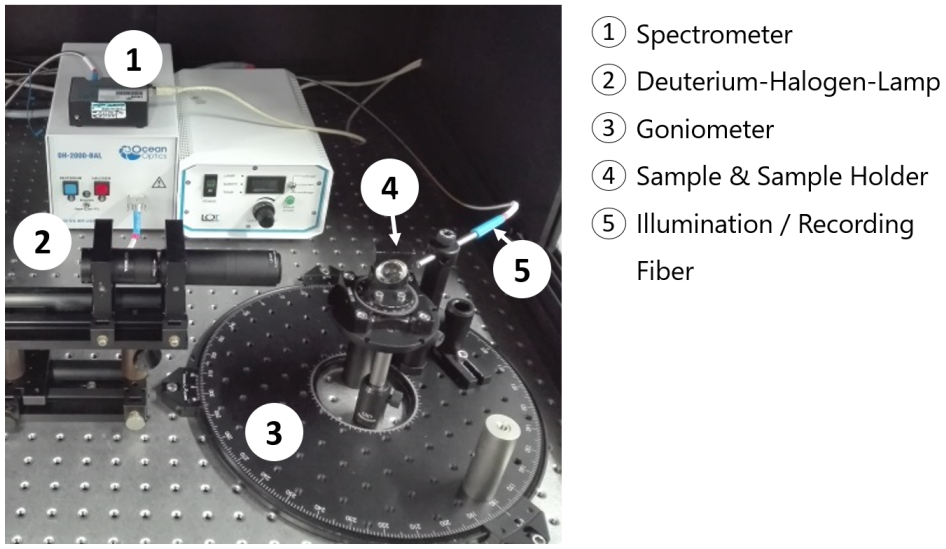

Figure 4-13. Experimental set-up for angle resolved spectroscopy

The experimental set-up for angle resolved spectroscopy consisted of (1) a spectrometer, (2) a light source, (3) a goniometer consisting of two rotatable stages, (4) a sample holder, (5) and a reflection probe fibre. In this set-up the incidence angle is equal to the recording angle.

4.11.2. *Micro-Spectroscopy*

Spectroscopic analyses on areas of only several tens of micrometres were conducted at the University of Cambridge, Cambridge, UK in the group of Bio-inspired Photonics headed by Prof. Vignolini. The experimental set-up consisted of an optical microscope (Scope.A1 with HAL 100, Carl Zeiss) equipped with a spectrometer unit with a spectral range of 400 - 800 nm (AvaSpec-HS2048, Avantes Sens Line), and a 200 µm glass fibre (FC-UV200-2-SR). The device is shown in **Figure 4-14a**. To ensure sufficient focusing and alignment the fibre was fixed in an optical cage providing movements with three degrees of freedom. The light beam of the microscope as well as the spectrometer fibre were aligned before each experiment. For this, the focal spot of the spectrometer fibre was visualised using an additional light source. After the beam was focused on a mirror and brought in overlay with the illuminating light spot, the fibre was coupled into the spectrometer. Spectra were recorded in reflection and transmission mode; the respective beam paths are sketched in **Figure 4-14b**. The microscope was operated with a 10x air objective (Carl Zeiss) with an NA of 0.3 and a maximally closed aperture. This results in opening angles of the incident and recording light cone between approximately 0° and 15°, respectively. Obtained curves were average over 5 recorded spectra and normalised using either a silver mirror or a white diffusor as reference. Integration times of 150 ms and 600 ms were applied for the references, respectively.

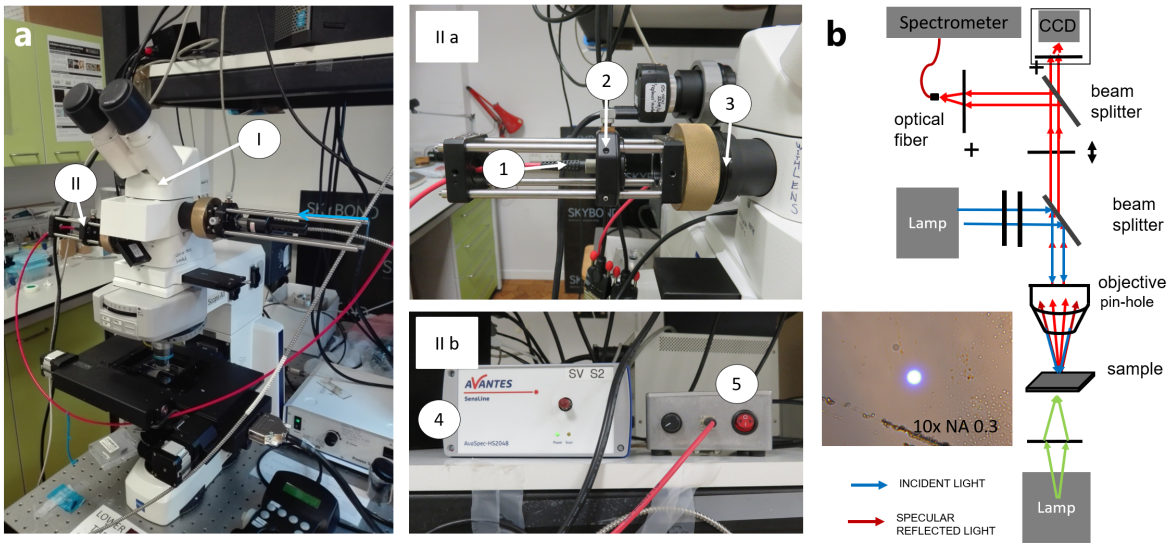

Figure 4-14. Microscopy supported spectroscopy set-up

(a) Optical microscope (I) equipped with a spectroscopy unit (II). (IIa) and (IIb) give a more detailed view of the spectroscopy unit. The spectroscopy unit consisted of a fibre (1) mounted into an optical cage (2) a focussing lens (3), a spectrometer (4) and an additional light source. (b) Optical path of the spectrometry set-up (The sketch was provided by Olimpia Onelli, University of Cambridge). The inserted micrograph shows the field of view during the fibre adjustment.

4.12. Conoscopy

Spatial scattering characterizations at 475 nm were performed using a microscope (Scope.A1 with HAL 100, Zeiss) equipped with a Bertrand lens and an additional laser unit. The application of a Bertrand lens enables a transformation of the distribution of propagation angles directly into a 2D image. In images recorded by conoscopy, the scale bars address angles instead of length units. The laser unit was comprised of a supercontinuum laser (SuperK EXTREME, EXU-6, spectrum 400-2400 nm, variable bandwidth 10-100 nm, 600 mW, Gaussian profile, single mode, 78 MHz, NKT Photonics), a tuneable single line filter (SuperK VARIA, NKT Photonics), and a broadband fibre delivery device (SuperK CONNECT, NKT Photonics) equipped with a photonic fibre (FD7-PM, NKT Photonics).The device was used at the University of Cambridge, Cambridge, UK, in the group of Bio-inspired Photonics headed by Prof. Vignolini and is shown in **Figure 4-15**. The device was aligned before each measurement including the correction of the objective, the adjustment of the aperture position, the focus of the Bertrand lens, the correction of the fibre coupling block, and the orientation of the laser beam in real and k-space. Two air objectives, 10x objective with a NA of 0.3 (Zeiss) and a 100x objective with a NA of 0.95 (Zeiss), were used during the analyses. The imaging, spectra recording, and setting of laser parameters were controlled by a self-implemented MATLAB-script written by Villads Egede Johansen, University of Cambridge.

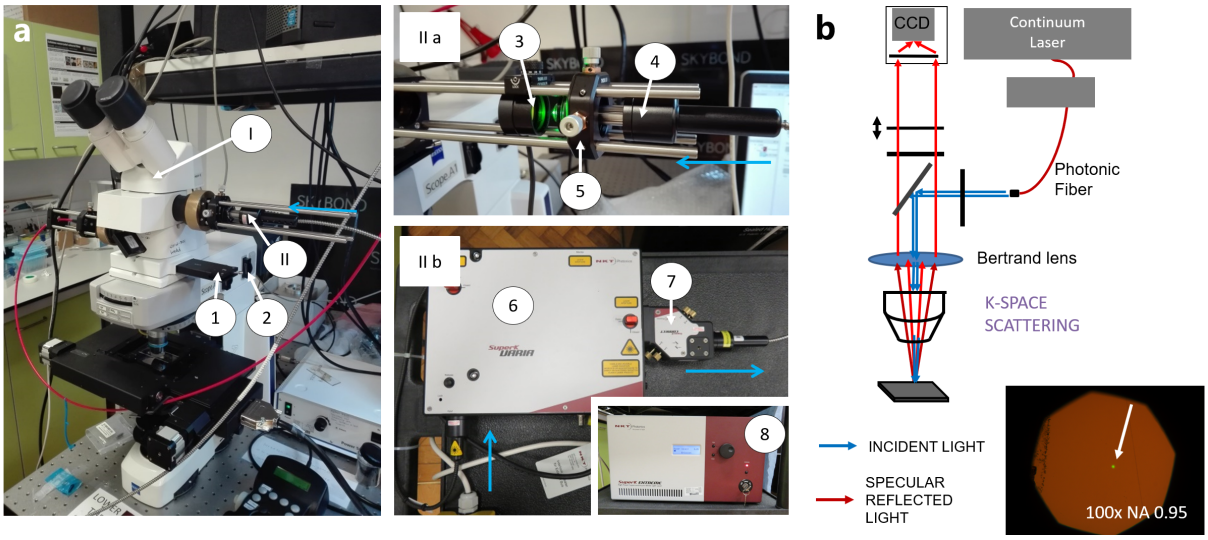

Figure 4-15. Conoscopy set-up

(a) Optical microscope (I) equipped with super continuum laser (II). (IIa) and (IIb) give a more detailed view of the laser unit. Bertrand lens (1), aperture of the microscope (2) optical density filter (3) optical fiber (4), x,y,z dimension alignment tool (5) tuneable single line filter (6), a broadband fiber delivery device (7) and a supercontinuum laser (8). (b) Optical path of the conoscopy set-up (The sketch was provided by Olimpia Onelli, University of Cambridge). The inserted micrograph shows the field of view during the laser adjustment.

4.13. References

1. Suzaki Y, Tachibana A. Measurement of the μm sized radius of Gaussian laser beam using the scanning knife-edge. *Appl Opt* 1975, **14**(12)**:** 2809-2810.
2. Feynman RP, Leighton RB, Sands ML. *The Feynman lectures on physics*. Addison-Wesley Pub. Co.: Reading, Mass., 1963.

Chapter 5. Improved Development Procedure to Enhance the Stability of Structures Created by Two-Photon Lithography

5.1. Abstract

Natural functional surfaces often rely on unique nano- and micropatterns. To mimic such surfaces successfully, patterning techniques are required that enable the fabrication of three-dimensional structures at the nanoscale. It has been reported that two-photon lithography (TPL) is a suitable method for this. However, polymer structures fabricated by TPL often tend to shrink and to collapse during the fabrication process. In particular, delicate structures suffer from their insufficient mechanical stability against capillary forces which mainly arise in the fabrication process during the evaporation of the developer and rinsing liquids. Here, we report a modified development approach, which enables an additional UV-treatment to post cross-link created structures before they are dried. We tested our approach on nanopillar arrays and microscopic pillar structures mimicking the moth-eye and the gecko adhesives, respectively. Our results indicate a significant improvement of the mechanical stability of the polymer structures, resulting in fewer defects and reduced shrinkage of the structures.

Purtov J, Verch A, Rogin P, Hensel R. Improved development procedure to enhance the stability of microstructures created by two-photon polymerisation. Microelectron Eng 2018, 194: 45-50. The article is available under: https://doi.org/10.1016/j.mee.2018.03.009

5.2. Introduction

In the last decade, two-photon polymerisation (TPL) has been established as a versatile tool for the microfabrication of complex, three-dimensional structures[1]. Applications include the fabrication of photonic crystals[2], directly printed lens systems[3], microfluidic devices[4], biological scaffolds[5], and templates for metamaterials[6,7]. In general, TPL relies on similar principles as known for common optical lithography, namely, exposure of an often-negative photoresist and a wet development process followed by the drying of the structures. In contrast to linear lithography, TPL uses a focused, femtosecond-pulsed, near-infrared (NIR) laser allowing spatially controlled two-photon polymerisation[8]. The size of the reaction volume, the so-called voxel, determines the resolution of the system, which is typically in the range of a few hundreds of nanometres[9,10]. By stacking voxels in all dimensions various three-dimensional (3D) structures can be fabricated.

Despite the opportunity to generate high resolution 3D structures, TPL bears several obstacles. One of the biggest challenges is the discrepancy between the dimensions of the designed 3D model and the final polymer structure[11-13]. The reasons for that are defects caused by surface wrinkling, strong and anisotropic shrinkage of the polymer, and the collapse of structural features due to insufficient mechanical stability. In order to at least mitigate these failures, several approaches have been discussed[14-16]. It has been proposed to modify the 3D model to compensate for the expected shrinkage[14], or to add so called shrinkage guides to the original design to achieve isotropic shrinkage[15]. The cross-linking density of the resist, and therefore its mechanical stability, can be improved by longer laser exposure times[16]. This, though, leads inevitably to increased feature sizes. In addition to shrinkage driven effects, capillary forces can cause significant defects, such as deformation or collapse of structures. Capillary forces usually occur during drying, i.e., the evaporation of the rinsing solution during the last process step. In order to reduce capillary forces liquids with low surface tension[17,18], for example hexamethyldisilazane, or critical point drying[19,20] are used. However, these approaches contain several process steps and, therefore, are more time consuming.

In this paper, we report a modified development protocol for TPL to produce nano- and microscopic structures with enhanced mechanical stability, reduced material shrinkage and fewer defects. In the new development procedure, the specimens were kept immersed in developer and rinsing liquids until the structures were mechanically stabilized by an additional ultraviolet (UV) exposure. It is anticipated, that the UV-exposure provides further cross-linking between the reactive sites of the resist molecules, which remained unreacted after the initial laser exposition. As a result, the stability of the structure enhances and becomes more resistant against capillary forces. The new approach is demonstrated on nanopillar arrays as well as microstructures, and is compared to the same motives developed by the conventional procedure without the additional UV-treatment. Created nanopillar arrays were inspired by structures found on the moth's eye[21-23], while the micropillars with mushroom-shaped tips mimicked the adhesive

gecko toes[24,25]. The results obtained demonstrate that an additional cross-linking step during the development enhances the stability of TPL-structures and helps to reduce defects and material shrinkage. By this, the proposed approach offers high potential for a reliable fabrication of high-resolution structures and is easily integrated into existing process schemes.

5.3. Experimental

5.3.1. *Two-Photon Patterning*

Nanopillar structures were defined using the DeScribe-software of the two-photon lithography (TPL) system (Professional GT, Nanoscribe, Germany). These pillars were arranged in 50x50 µm arrays with pitch distances ranging from 280 nm up to 1700 nm. The TPL-device was operated at a constant laser power of 16 mW. In contrast, the 3D-design for gecko-inspired microstructures was created using a computer assisted design (CAD) software (Inventor, Autodesk, USA). All structures were fabricated from a negative photoresist (IP-Dip, Nanoscribe, Germany) on fused silica substrates. For the microstructures, (3-methacryloyloxypropyl) trichlorosilane (Abcr, Germany) was immobilized on the substrates via vapor deposition to enhance the adhesion of the acryl-based resist to the substrate[26]. The structures were generated using the so-called “dip-in mode” where the objective of the TPP-System (63x with NA = 1.4, Zeiss, Germany) is dipped directly into the resist. Exposure parameters were 25 mW and 50.000 µm/s for laser power and scan speed, respectively.

5.3.2. *Development Procedures*

Following the conventional development process (see black route in **Figure 5-1**), the structures were developed by immersion into propylene glycol monomethyl ether acetate (PGMEA, Sigma Aldrich, Germany) for 20 min at room temperature to remove unbound monomeric material. After that, the structures were carefully rinsed using isopropanol (IPA, Sigma Aldrich, Germany) and subsequently dried in air by evaporation.

Following the development proposed in this study (see red route in **Figure 5-1**), after the 20 min of development 70 % of the PGMEA were carefully replaced with isopropanol without exposing the structures to air. This solvent exchange was repeated three times, separated by a residence time of 10 min. In contrast to the conventional method, the specimens were additionally cross-linked using UV-exposure for 300 s (200 W, OmniCure S1500A, igb-tech, Germany), while the samples were still immersed in isopropanol. The UV source had a maximum peak at 365 nm (see **Figure S 5-1** in the Supplementary Information) and an intensity of 51 mW/cm^2. Finally, the samples were removed from the liquid, rinsed with fresh isopropanol, and dried in air.

5.3.3. *Scanning Electron Microscopy*

Scanning electron micrographs of generated TPL-structures were examined at tilt angles of 0°, 40° and 50° in high-vacuum mode using a Quanta 250 FEG (FEI, The Netherlands) equipped with an Everhart-Thornley-detector (ETD). The spot size and the accelerating voltage were set to 2.0 and 2 kV, respectively. Samples were fixed with clamps on a metallic sample holder. A copper tape was placed close to the samples to minimize charging effects. The specimens were not coated with conductive material to maintain their optical properties. The ratios between upright and collapsed pillars were determined by analysing scanning electron micrographs at lower magnification showing entire nanopillar arrays at 0° incident angle. Shrinkage of TPL-structures was evaluated on micropillars by measuring the pillar heights, pillar diameters, the diameter of the disc, and the diameter at the pillar-substrate-interface.

5.3.4. *Optical Properties*

The optical characteristics of the nanopillar arrays were extracted from optical microscopy images recorded with an Eclipse LV100ND (Nikon, Japan) equipped with a 20x colour-corrected objective. The microscope was operated in the bright field mode with a fully opened aperture. Prior to examination, white balance was set using a white sheet of paper.

5.4. Results

The main idea of the new development procedure, as described in section 5.3.2 and as illustrated in **Figure 5-1**, is to provide additional stabilization to the structural features before exposing them to capillary forces. This was exemplified on nanoscopic and microscopic pillar arrays, respectively.

5.4.1. *Nanopillar Arrays*

Two identical specimens were created by TPP comprising a series of 50x50 µm arrays of nanopillar structures with varying pitch distances, p, from 280 to 1700 nm. The pitch distance specifies the distance between adjacent pillars (see **Figure 5-2b**). One specimen was developed according to the conventional, the other according to the improved development strategy introduced in **Figure 5-1**. The structures obtained were investigated using SEM and fractions of upright standing and collapsed pillars were determined. The optical properties of whole arrays were analysed using optical microscopy.

The resulting nanopillar arrays and the fractions of free standing pillars are presented in **Figure 5-2** and **Figure 5-3** The conventionally developed array with $p = 1700$ nm exhibited 54 % upright standing pillars, whereas 46 % of the pillars were collapsed or detached from the substrate during the development (**Figure 5-3**). The pillar heights and diameters (**Figure 5-2**) were 1050 ± 31 nm and

326 ± 8 nm, respectively. Most free ends of the pillar structures were slightly bent. Similar results were obtained for pitch distances of 1560 nm, 1420 nm, and 1270 nm. For smaller pitch distances, the bending of the free ends of the nanopillars was more prominent. At a pitch distance of 1130 nm, structures condensed into aggregates. As a consequence, the fraction of upright pillars drastically dropped to 15 %. With further decreasing pitch, the number of pillars forming aggregates increased. At a pitch distance of 710 nm, all individual pillars were integrated into aggregates and no upright standing pillars were observed. At the smallest pitch distance of 280 nm, the spacing between pillars was smaller than the diameter of the voxels. Hence, the pillar structures laterally overlapped and formed a rough quasi-film without any recognizable pillar structures.

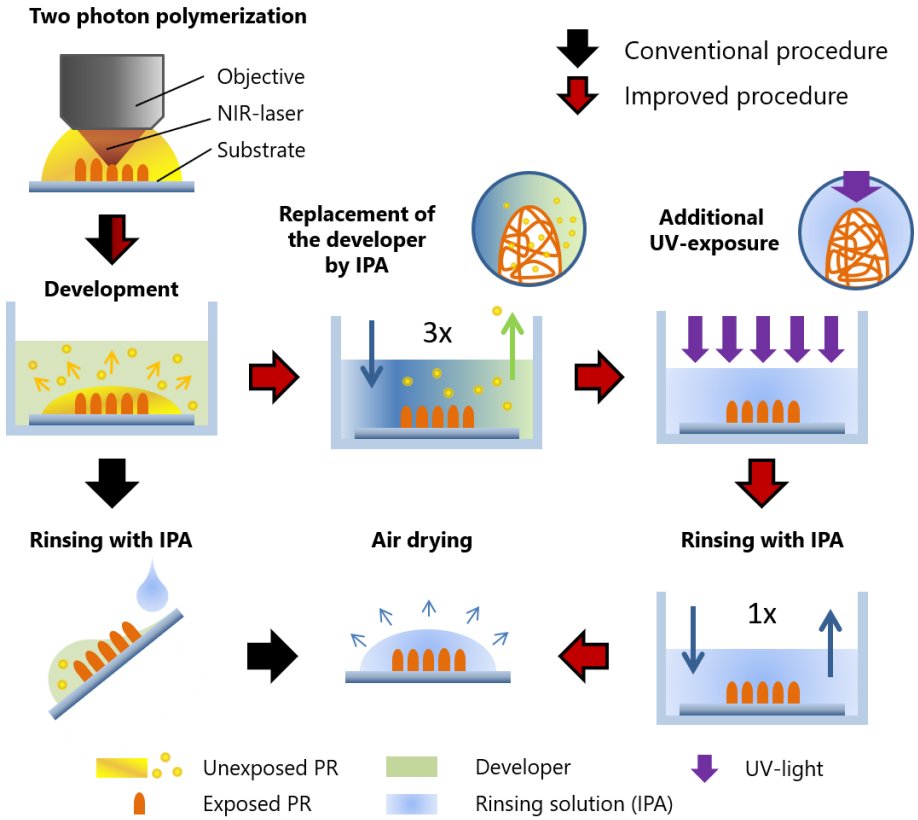

Figure 5-1. Schematic illustration of the conventional and the improved wet development approach

Upon two-photon polymerisation via near-infrared (NIR)-laser exposure, the structures are developed to remove unexposed photoresist (PR). The conventional development (black arrows) includes the development in the developer liquid followed by careful rinsing with isopropanol (IPA) and drying of the specimen. The improved proposed procedure (red arrows) includes gentle replacement of the developer-monomer-mixture with isopropanol, while structures are kept immersed during the whole procedure. Next, the structures are further cross-linked by additional ultraviolet (UV) exposure. Finally, the structures are rinsed and dried in air.

For the nanopillar arrays developed by the improved development procedure, scanning electron micrographs revealed the same pillar sizes as reported for the conventional development above. However, most of the pillars stayed upright and had straight tips (**Figure 5-2d**). 100 % upright standing

pillars without any tip bending were obtained for all pitch distances down to 570 nm (**Figure 5-3**). At a pitch distance of 420 nm, the fraction of upright pillars was still almost 100%, but a slight bending of the structures and pillar agglomeration occurred. Similar to the conventionally created pillar arrays, the structures fused into a rough quasi-film at the smallest pitch distance.

The optical analysis revealed a strong correlation between the homogeneity in the optical appearance of arrays and the fraction of upright pillars. The conventionally developed arrays appeared slightly coloured in regions with upright standing pillars and colourless in regions where pillars were missing or had collapsed (**Figure 5-2b**). In contrast, arrays developed with the improved approach appeared more saturated in colour, particularly for pitch spacings in the range between 570 – 990 nm (**Figure 5-2c**). None of these arrays exhibited colourless areas due to pillar collapses and therefore gave a homogeneous optical impression.

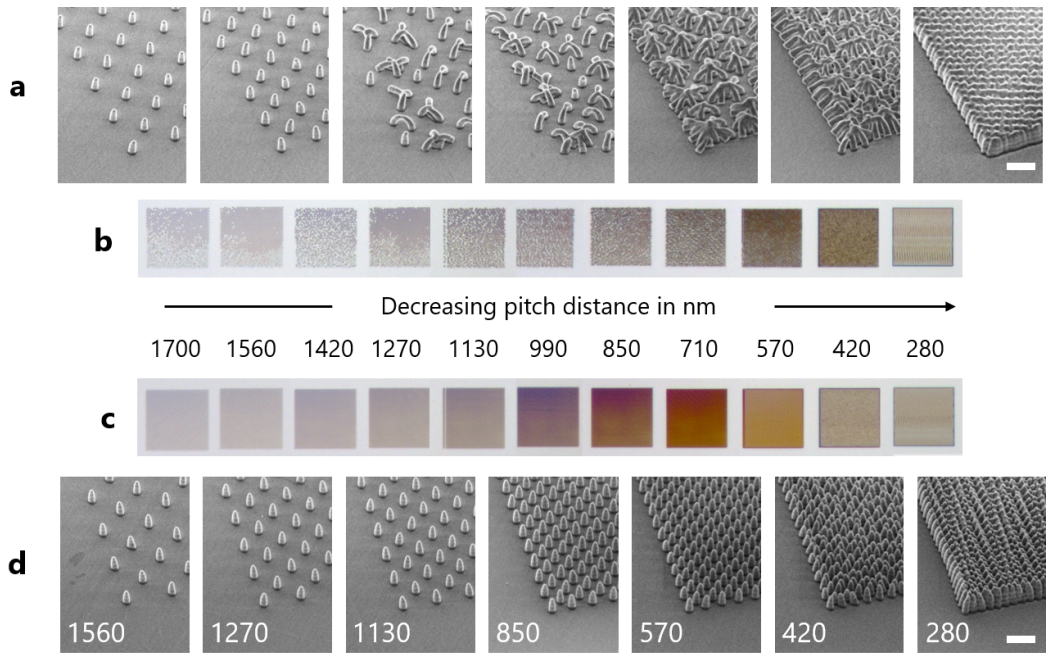

Figure 5-2. Comparison of nanopillar arrays developed by different strategies

Nanopillar arrays with different pitch distances developed (a,b) by the conventional and (c,d) by the improved strategy (a,d) Scanning electron images of pillar arrays at 40° tilt; the scale bar is 2 µm. (b,c) Bright field optical micrographs of 50x50 µm nanopillar arrays on a fused silica substrate.

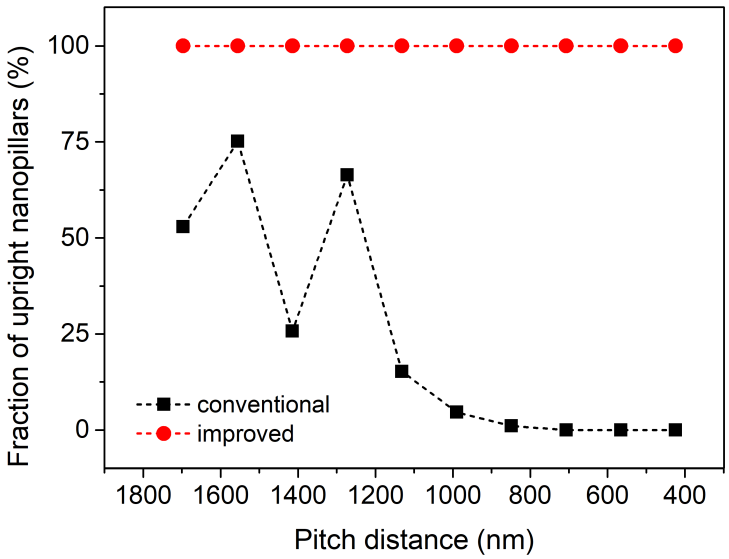

Figure 5-3. Fraction of upright nanopillars as a function of the pitch distance

The fraction of upright nanopillars is the number of upright standing pillars, i.e., pillars showing no collapse or agglomeration, normalized to the total number of pillars per array. Red circles represent the results of arrays developed by the improved development procedure including post UV exposure. Black squares depict the results of arrays developed using the conventional development approach. Dashed lines are intended to guide the eye.

5.4.2. *Microscopic structures*

Microscopic mushroom-shaped pillars were created based on a CAD model. The model used, and the resulting microscopic pillar arrays developed by both, the conventional and the improved development approach are displayed in **Figure 5-4**. The model consisted of a cylindrical pillar with straight side walls and a disc at the free end forming the so-called mushroom tip (**Figure 5-4a**). The conventionally developed structures were strongly deformed and exhibited collapsed parts (**Figure 5-4b**). In contrast, the structures obtained upon the improved approach exhibited straight sidewalls and a smooth top disc, close to the computer model. Only a surface roughness at the sidewalls originating from the writing process (i.e., the vertical stacking of slices) was observed. **Figure 5-5** shows an analysis of the shrinkage by comparing the originally defined dimensions in the 3D CAD-model with the real dimensions determined for fabricated structures. The pillars were designed with a diameter of 24 µm and a height of 39.5 µm. A disc with 30 µm diameter and 0.5 µm thickness represented the mushroom tip. For the conventional development, about 20 % shrinkage in the pillar height and the disc diameter were observed. The pillar diameter shrunk by 26 %. Even at the pillar-substrate interface, 8 % shrinkage was found. For the structures developed with the improved method, an overall shrinkage of about 10 % for the pillar height, pillar diameter, as well as the disc diameter were obtained. The shrinkage at the pillar-substrate interface was negligible.

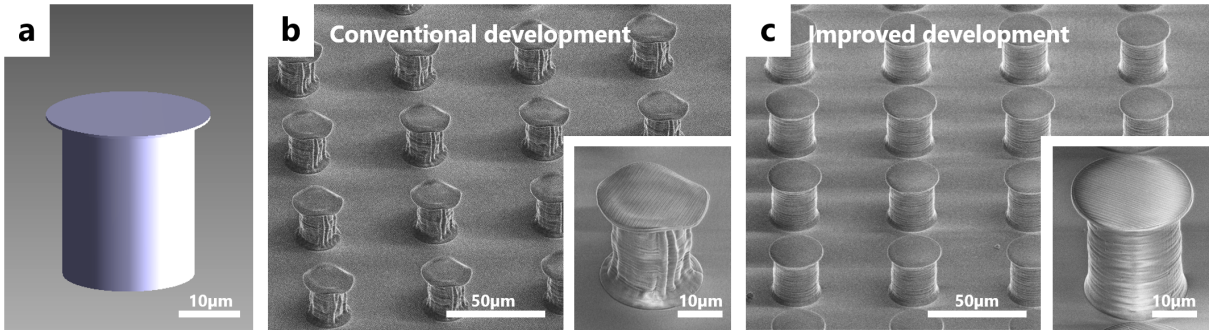

Figure 5-4. Microscopic mushroom-shaped pillars

(a) 3D CAD-model of the mushroom-shaped pillar used for TPL. (b,c) Scanning electron micrographs at 50° tilt of structures developed either via (b) the conventional development or (c) the improved development strategy.

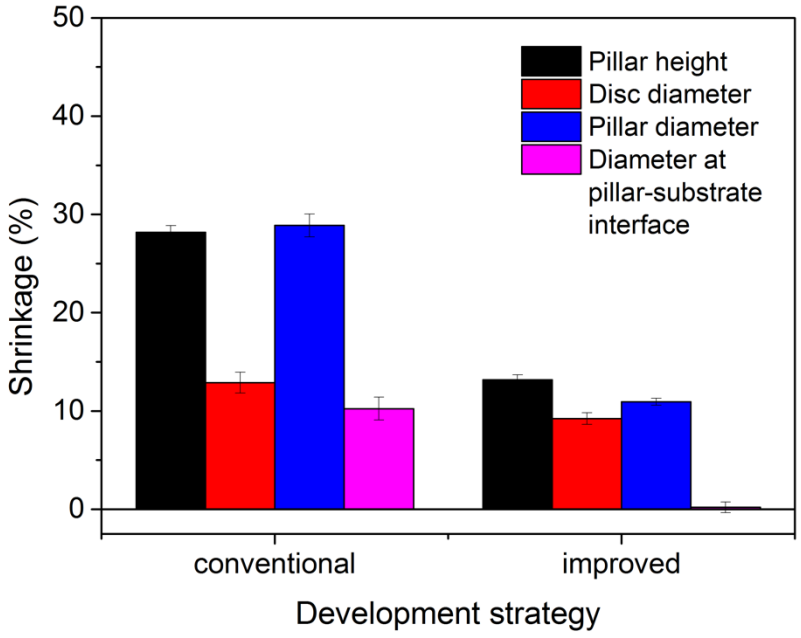

Figure 5-5. Shrinkage of microscopic pillar structures

Pillar characteristics were extracted from SEM-images (n = 5) and compared to the original sizes used in the 3D CAD design.

5.5. Discussion

In this work, we propose a novel development approach for two-photon polymerisation that, in particularly, facilitates the creation of closely packed nanopillar arrays and complexly shaped microscopic structures.

In fact, the collapse of densely packed nanostructures could be prevented down to a pitch distance, p, of 420 nm, whereas conventionally developed pillars collapsed already at the much larger pitch distance of 1130 nm. In general, two different types of pillar collapse can be distinguished: on the one hand the ground collapse, that is pillars detach from the substrate when the spacing between adjacent pillars is larger than the height of the pillars[12], on the other hand the lateral collapse, that is pillars cluster or form agglomerates when the spacing between pillars is smaller than their height[27]. For the structures developed with the conventional method, we observed ground collapse at p =1420 nm and three different degrees of lateral collapse depending on the pitch distance (**Figure 5-6a**): upright pillars with bent tips ($p = 1130$ nm), pairs of attached pillars ($p = 990$ nm) and clusters of more than two pillars ($p < 850$ nm).

The collapse of the nanopillar arrays is most likely induced by capillary forces. These forces act at each individual pillar tip at the three-phase contact line during the drying of the structures (**Figure 5-6b**)[28,29]. The capillary force is given by $F_C = \left(2\pi\gamma r^2/(p-2\delta)\right) cos^2\,\theta$, where γ is the surface tension of the liquid, here isopropanol, r is the radius of the pillars, θ is the receding contact angle, and δ denotes the deflection of the pillar [25]. The term $(p-2\delta)$ reflects the actual spacing between two pillar tips, which dynamically changes when the pillars bend[29]. In the undeformed state, when $\delta = 0$, the force is the higher the denser the array is packed, because F_C scales inversely proportional to p. The capillary force increases with increasing δ and is highest just before two adjacent pillars touch each other. At this point, δ equals approximately $p/2$. An elastic restoring force, F_E, is acting against the described bending induced by the capillary forces and is given by $F_E = 3\pi E r^4\,\delta/4h^3$, where E is Young's modulus and h the height of the pillars[25]. The elastic restoring force increases linearly with δ. If F_E is larger than F_C, the pillars will resist capillary forces and the fraction of upright pillars in the dried array will be high. In contrast, if F_E is smaller than F_C, the pillars will most likely bend and collapse. After the liquid is evaporated completely, mainly van der Waals forces, F_{vdW}, act between attached pillars. Hence, the stability of agglomerates formed by capillarity depends on the force balance between F_E and F_{vdW} [29]. For $F_E > F_{vdW}$, the pillars most likely snap back to a vertical position, but a slight bending of the tips can be maintained due to plastic deformations. For $F_E < F_{vdW}$, the pillars remain in contact at the tips. With decreasing spacing between the pillars, the maximum deflection of the pillars decreases, hence F_E decreases and, therefore, the probability for the formation of agglomerates increases. This is in line with our observations shown in **Figure 5-2**. However, the smallest pitch allowing intact, upright standing

pillar arrays, varied with the development procedure. Most likely, the additional UV-treatment during the improved procedure facilitated an elevated cross-linking density, which is associated with an increased Young's modulus. As the elastic restoring force scales linearly with Young's modulus, the mechanical stability and resistance against capillary forces were enhanced and allowed smaller pitch distances. This assumption is supported by the results obtained on the microscopic structures. Here, an elevated cross-linking density is in line with the reduced deformation and shrinkage found in structures developed by the improved procedure as shown in **Figure 5-4**. Moreover, the homogeneous shrinkage obtained in structures upon post-curing indicates, that this method also reduces cross-linking inhomogeneities initially formed by the sequential laser exposure within the TPL-structures. An increased homogeneity of the polymer network results in less internal stresses within the structures, and therefore, higher agreement with the original 3D model, as was observed.

The improved procedure can also be applied to accelerate the TPL fabrication process. A promising example is the fabrication of so-called core-shell structures. Here, only the shell (contour) of the structure and a few internal features supporting the shape of the shell are exposed and polymerized during the TPL, whereas a significant amount of the unreacted, liquid photoresist remains inside the structure. This approach can enormously speed up the process time, but requires a post UV cross-linking as presented in our paper; otherwise, the structures would suffer even more from shrinkage and capillary forces.

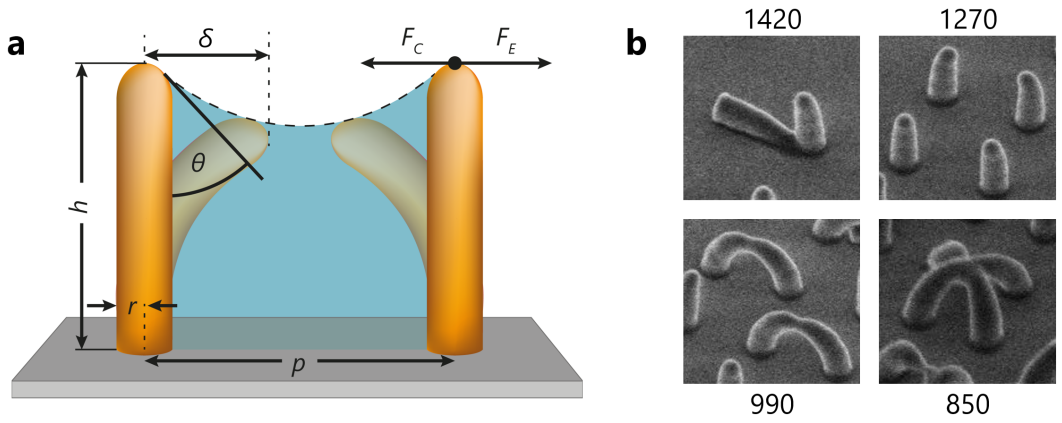

Figure 5-6. Collapse of structures by capillary forces

(a) Schematic illustration of forces acting on pillars during evaporation. The ratio between the capillary force (F_C) and elastic restoring force (F_E) determines the type of collapse. The forces depend mainly on the pillar height, h, radius of the pillars, r, receding contact angle θ, deflection of the pillar, δ, and pitch distance, p. (b) Different types of pillar collapse obtained for commonly developed structures as a function of pitch distance: ground collapse ($p = 1420$ nm), upright pillars with bent tips ($p = 1270$ nm), pairs of attached pillars ($p = 990$ nm) and clusters of more than two pillars ($p \leq 850$ nm).

5.6. Conclusions

A novel development strategy for structures created by two-photon polymerisation was introduced. The proposed approach enables a mechanical stabilization of created structures before they are exposed to capillary forces. The feasibility of the improved method was demonstrated for densely packed nanopillar arrays and complexly shaped microstructures, wherein the following conclusions can be drawn:

(1) The modified development procedure enables an additional UV-exposure before drying and, therefore, before exposing to capillary forces.

(2) A post UV-treatment of reactive groups, which remained unreacted upon the two-photon polymerisation, enhances the cross-linking density, and therefore, the mechanical stability of structures and their resistance against mechanical deformations. Thus, the number of defects and collapsed structures in densely packed arrays can be drastically reduced.

(3) UV cross-linking reduces the polymer shrinkage from 30 to 10 %. In addition, the shrinkage is almost isotropic compared to the anisotropic shrinkage of not post-treated structures.

In summary, optical gratings based on different pillar sizes can be manufactured by varying the laser power in TPL in a single process step on one surface. However, the fabrication of precise optical gratings close to the polymerisation threshold of the photoresist requires a deep understanding of the involved processes.

5.7. Acknowledgements

The authors gratefully acknowledge valuable input by Stefanie Faust; the reported findings about gecko-inspired structures were obtained within her bachelor thesis project. In addition, we thank Reza Hosseinabadi for his help with the TPL-fabrication. R.H. acknowledges partial funding from the European Research Council under the European Union's Seventh Framework Program (FP/2007-2013)/ERC Advanced Grant no. 340929.

5.8. References

1. Farsari M, Chichkov BN. Materials processing: Two-photon fabrication. *Nat Photon* 2009, **3**(8)**:** 450-452.
2. von Freymann G, Ledermann A, Thiel M, Staude I, Essig S, Busch K, *et al.* Three-Dimensional Nanostructures for Photonics. *Adv Funct Mater* 2010, **20**(7)**:** 1038-1052.
3. Thiele S, Arzenbacher K, Gissibl T, Giessen H, Herkommer AM. 3D-printed eagle eye: Compound microlens system for foveated imaging. *Science Adv* 2017, **3**(2).

4. Waheed S, Cabot JM, Macdonald NP, Lewis T, Guijt RM, Paull B, *et al.* 3D printed microfluidic devices: enablers and barriers. *Lab Chip* 2016, **16**(11)**:** 1993-2013.
5. Marino A, Filippeschi C, Mattoli V, Mazzolai B, Ciofani G. Biomimicry at the nanoscale: current research and perspectives of two-photon polymerization. *Nanoscale* 2015, **7**(7)**:** 2841-2850.
6. Zheng X, Smith W, Jackson J, Moran B, Cui H, Chen D, *et al.* Multiscale metallic metamaterials. *Nat Mater* 2016, **15**(10)**:** 1100-1106.
7. Meza LR, Das S, Greer JR. Strong, lightweight, and recoverable three-dimensional ceramic nanolattices. *Science* 2014, **345**(6202)**:** 1322-1326.
8. Hohmann JK, Renner M, Waller EH, von Freymann G. Three-Dimensional μ-Printing: An Enabling Technology. *Adv Opt Mater* 2015, **3**(11)**:** 1488-1507.
9. Mueller JB, Fischer J, Mayer F, Kadic M, Wegener M. Polymerization Kinetics in Three-Dimensional Direct Laser Writing. *Adv Mater* 2014, **26**(38)**:** 6566-6571.
10. Zhou X, Hou Y, Lin J. A review on the processing accuracy of two-photon polymerization. *AIP Adv* 2015, **5**(3)**:** 030701.
11. LaFratta C, Baldacchini T. Two-Photon Polymerization Metrology: Characterization Methods of Mechanisms and Microstructures. *Micromachines* 2017, **8**(4)**:** 101.
12. Roca-Cusachs P, Rico F, Martínez E, Toset J, Farré R, Navajas D. Stability of Microfabricated High Aspect Ratio Structures in Poly(dimethylsiloxane). *Langmuir* 2005, **21**(12)**:** 5542-5548.
13. Takada K, Kaneko K, Li Y-D, Kawata S, Chen Q-D, Sun H-B. Temperature effects on pinpoint photopolymerization and polymerized micronanostructures. *Appl Phys Lett* 2008, **92**(4)**:** 041902.
14. Sun H-B, Suwa T, Takada K, Zaccaria RP, Kim M-S, Lee K-S, *et al.* Shape precompensation in two-photon laser nanowriting of photonic lattices. *Appl Phys Lett* 2004, **85**(17)**:** 3708-3710.
15. Lim TW, Son Y, Yang D-Y, Pham TA, Kim D-P, Yang B-I, *et al.* Net Shape Manufacturing of Three-Dimensional SiCN Ceramic Microstructures Using an Isotropic Shrinkage Method by Introducing Shrinkage Guiders. *Int J Appl Ceram Tec* 2008, **5**(3)**:** 258-264.
16. Park S-H, Kim KH, Lim TW, Yang D-Y, Lee K-S. Investigation of three-dimensional pattern collapse owing to surface tension using an imperfection finite element model. *Microelectron Eng* 2008, **85**(2)**:** 432-439.
17. Bray DF, Bagu J, Koegler P. Comparison of hexamethyldisilazane (HMDS), Peldri II, and critical-point drying methods for scanning electron microscopy of biological specimens. *Microsc Res Tech* 1993, **26**(6)**:** 489-495.
18. Hazrin-Chong NH, Manefield M. An alternative SEM drying method using hexamethyldisilazane (HMDS) for microbial cell attachment studies on sub-bituminous coal. *Journal of Microbiological Methods* 2012, **90**(2)**:** 96-99.
19. Namatsu H, Kurihara K, Nagase M, Iwadate K, Murase K. Dimensional limitations of silicon nanolines resulting from pattern distortion due to surface tension of rinse water. *Appl Phys Lett* 1995, **66**(20)**:** 2655-2657.
20. Namatsu H, Yamazaki K, Kurihara K. Supercritical drying for nanostructure fabrication without pattern collapse. *Microelectron Eng* 1999, **46**(1)**:** 129-132.
21. Clapham PB, Hutley MC. Reduction of Lens Reflexion by the Moth Eye Principle. *Nature* 1973, **244**(5414)**:** 281-282.
22. Wilson SJ, Hutley MC. The Optical Properties of 'Moth Eye' Antireflection Surfaces. *Opt Acta* 1982, **29**(7)**:** 993-1009.
23. Min W-L, Jiang B, Jiang P. Bioinspired Self-Cleaning Antireflection Coatings. *Adv Mater* 2008, **20**(20)**:** 3914-3918.
24. del Campo A, Greiner C, Arzt E. Contact Shape Controls Adhesion of Bioinspired Fibrillar Surfaces. *Langmuir* 2007, **23**(20)**:** 10235-10243.
25. Chandra D, Yang S. Capillary-Force-Induced Clustering of Micropillar Arrays: Is It Caused by Isolated Capillary Bridges or by the Lateral Capillary Meniscus Interaction Force? *Langmuir* 2009, **25**(18)**:** 10430-10434.
26. Finn A, Hensel R, Hagemann F, Kirchner R, Jahn A, Fischer W-J. Geometrical properties of multilayer nano-imprint-lithography molds for optical applications. *Microelectron Eng* 2012, **98**(Supplement C)**:** 284-287.

27. Chandra D, Yang S. Stability of High-Aspect-Ratio Micropillar Arrays against Adhesive and Capillary Forces. *Acc Chem Res* 2010, **43**(8)**:** 1080-1091.
28. Pokroy B, Kang SH, Mahadevan L, Aizenberg J. Self-Organization of a Mesoscale Bristle into Ordered, Hierarchical Helical Assemblies. *Science* 2009, **323**(5911)**:** 237-240.
29. Hu Y, Lao Z, Cumming BP, Wu D, Li J, Liang H, *et al.* Laser printing hierarchical structures with the aid of controlled capillary-driven self-assembly. *Proc Natl Acad Sci* 2015, **112**(22)**:** 6876-6881.

5.9. Supplementary Information

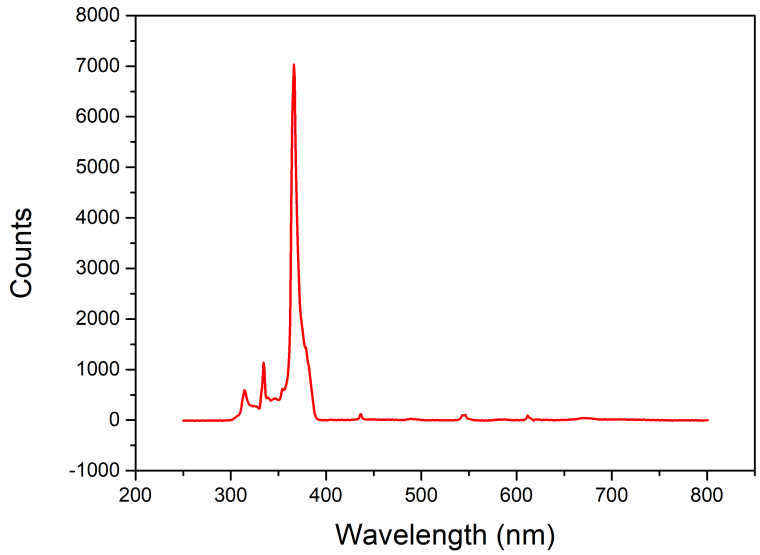

Figure S 5-1. Spectrum of UV-lamp used for the additional cross-linking

Chapter 6. Nanopillar Diffraction Gratings by Two-Photon Lithography

6.1. Abstract

Two-dimensional photonic structures such as nanostructured pillar gratings are useful for various applications including wave coupling, diffraction optics, and security features. Two-photon lithography facilitates the generation of such nanostructured surfaces with high precision and reproducibility. In this work, we report on nanopillar diffraction gratings fabricated by two-photon lithography at various laser powers close to the polymerisation threshold of the photoresist. As a result, defect-free arrays of pillars with diameters down to 184 nm were fabricated. The structure sizes were analysed by scanning electron microscopy and compared to theoretical predictions obtained from Monte Carlo simulations. The optical reflectivities of the nanopillar gratings were analysed by optical microscopy and verified by rigorous coupled-wave simulations.

Purtov J, Rogin P, Verch A, Johansen VE, Hensel R. Nanopillar Diffraction Gratings by Two-Photon Lithography. Nanomaterials 2019, 9: 1495. The article is available under: https:// doi:10.3390/nano9101495

6.2. Introduction

Two-dimensional photonic structures such as periodical pillar gratings are applicable for light coupling devices[1], solar devices[2], sensors[3], encoders[4], holographic structures[5], or security features[6]. The optical characteristics of such gratings are very sensitive to the shape, diameter, and height of the nanostructures, as well as the pitch and periodicity of the array[7-11]. Therefore, these features require strict tolerances to ensure uniformity with virtually no defects within the grating. Simultaneously, there is a desire to enable flexible manufacturing of optical elements, as each application has its own requirements regarding design and feature size. In this context, two-photon lithography (TPL) is a promising candidate for the fabrication of nanostructured gratings with tuneable optical properties.

In recent years, TPL has been established as a suitable technique for the fabrication of complex three-dimensional structures with submicron resolution[12-15]. Its versatility has been demonstrated by various applications ranging from microfluidic devices[16], micropatterned adhesives[17,18], biological and mechano-sensitive scaffolds[19-22], and optical devices, such as lenses[23] and photonic crystals[24,25]. In a typical TPL process, a focused, femtosecond-pulsed, near-infrared laser (λ = 780 nm) exposes a photoresist, that is composed of reactive monomers and a photoinitiator. However, the photoreaction is only initiated when two photons excite the initiator concertedly. As a result, the initiator molecule decomposes into radicals, which induce a cross-linking reaction of the oligomers. Such a two-photon event is very rare, so that the probability of a two-photon excitation, and thus the start of polymerisation, is only given in the focal region where the photon density is highest[15]. The polymerisation reaction is in most cases terminated by oxygen quenching of radicals[26]. The size of the voxel, i.e., the volume element at which the polymerisation occurs, is a function of the beam[15,27,28], the exposure parameters[29,30], and the chemical and physical properties of the photoresist[26,29,31,32]. In order to estimate the lateral voxel size S, Sun et al.[33] empirically derived an equation based on the diffraction limit l_{diff}, a material constant α, the applied laser power E_{re}, and the threshold laser power E_{th} required for the cross-linking reaction:

$$\boldsymbol{S = l_{diff}\alpha\sqrt{\frac{\ln(E_{re}/E_{th})}{4k\ln 2}}} \tag{52}$$

where k equals 1 or 2 for a single or two-photon excitation, respectively. According to equation (52) S decreases with E_{re} and reaches 0 for $E_{re} = E_{th}$. From this it can be concluded that the smallest lateral feature sizes are achieved for laser powers close to the polymerisation threshold of the photoresist. Small feature sizes, however, are highly susceptible to deformations and collapse due to their low mechanical resistance[34-36] (see also Chapter 5). In particular, nanostructures with high aspect ratios and low mechanical stiffness are prone to such defects[37,38].

In the present study, we report on the fabrication of nanopillar diffraction gratings. These are fabricated via TPL and laser energies close to the polymerisation threshold of the photoresist (10–23 mW)

combined with a recently reported, improved development routine[36]. The obtained structures are analysed by scanning electron microscopy. To enable a prediction of the size of the nanopillars for further investigations, numerical simulations based on a Monte Carlo algorithm were performed. The optical properties of the gratings with pillar diameters between 120 and 430 nm and heights ranging from 330 to 1315 nm were corroborated by rigorous coupled-wave analysis (RCWA) simulations.

6.3. Experimental

6.3.1. *Two-Photon Patterning*

Diffraction gratings were fabricated from a negative tone photoresist IP-Dip (Nanoscribe, Eggenstein-Leopoldshafen, Germany) on fused silica substrates using the Professional GT two-photon lithography system (Nanoscribe, Eggenstein-Leopoldshafen, Germany). The system consisted of a 63× objective (NA = 1.4, Carl Zeiss, Oberkochen, Germany) and a femtosecond pulsed IR-laser (λ = 780 nm, 80 MHz laser repetition rate, and 100–200 fs pulse length, TOPTICA Photonics AG, Graefelfing, Germany). The system was operated in 'dip-in' mode, where the objective is immersed into the photoresist. The nanopillars were arranged with a centre-to-centre distance of 1 µm in a square lattice of 50 × 50 µm. Each pillar consisted of four vertically stacked voxels, whose focal points were separated by 300 nm, whereby the lowest voxel was placed 200 nm below the substrate-resist interface to ensure appropriate attachment to the fused silica substrate. The exposure and settling times were set to 0.1 and 2 ms, respectively. All diffraction gratings were fabricated on the same substrate with altered laser powers ranging from 10 to 23 mW for different gratings. To improve the mechanical stability of the nanopillars, the development was performed according to Purtov et al.[36]. Structures were developed for 20 min in PGMEA (Sigma-Aldrich, Steinheim, Germany), after which 70% of the solution was carefully replaced with isopropanol (Sigma-Aldrich, Steinheim, Germany) without exposing the structures to air. Such a solvent exchange was repeated three times, separated by a residence time of 10 min. Subsequently, a UV-post-crosslinking was applied (t = 300 s, λ_{UV} = 365 nm, 350 mW, OmniCure S1500A, igb-tech, Friedelsheim, Germany) before structures were removed from the liquid and air-dried.

6.3.2. *Scanning Electron Microscopy*

Samples were fixed on a metallic sample holder and investigated at tilt angles of 0° and 40° using a Quanta 250 FEG (FEI, Eindhoven, The Netherlands) equipped with an Everhart-Thornley-Detector (ETD) in high-vacuum mode. Copper tape was placed close to the nanostructures to avoid charging, as no conductive coating was applied to preserve the optical properties of the arrays. The spot size and the acceleration voltage were set to 2.0 and 2 kV, respectively. The measured pillar heights in micrographs were corrected for the sample tilt.

6.3.3. *Optical Properties*

The optical reflection characteristics of the pillar arrays were investigated using an optical microscope (Eclipse LV100ND, Nikon, Tokyo, Japan) equipped with a 20× colour-corrected objective (NA = 0.45). The microscope was operated in bright field mode with a fully opened illumination aperture upon a white balance using a white sheet of paper.

6.3.4. *Simulations of Voxel Sizes*

In order to gain a better understanding of the size- and shape-changing effects during the TPL-process, the obtained nanostructures were analysed and compared to theoretical pillar sizes derived from simulations considering the different laser powers applied. Since the Gaussian beam formalism based on the paraxial approximation is not appropriate to describe the tightly focused beam used in the experiment, the electric field distribution around the focal spot had to be determined by numerical integration. This integration was performed using the Huygens' principle, i.e., by assuming the field distribution to be the result of superimposing fields originating from an ensemble of emitting elementary sources. This approach was implemented in a self-written software executing a Monte Carlo algorithm, which is briefly described in the following. A more detailed derivation can be found in Chapter 4.8.

The coordinate system of the simulation was defined with the light incident from the +z-direction. The origin of the coordinate system was set to the focal spot of the focussed beam. The elementary emitters were assumed to be dipole oscillators distributed in a planar arrangement parallel to the x-y focal plane with a normal distance z_0. The plane of the dipole oscillators can be regarded as the exit pupil of the focusing objective with z_0 being the working distance. The phase of the dipoles $\varphi(r)$ as a function of distance r from the z-axis was adjusted to result in a constant phase at the origin of the coordinate system (i.e., the centre of the focal spot), which gives focusing:

$$\boldsymbol{\varphi} = -\frac{\boldsymbol{2\pi}}{\boldsymbol{\lambda}} \cdot \sqrt{\boldsymbol{z_0^2 + r^2}} \tag{53}$$

The amplitude of the dipole strength per unit area $\vec{P}$ followed a Gaussian radial profile, while the polarisation was assumed to be circular in order to result in a rotationally symmetric field distribution around the focal spot. By arbitrarily setting all constant factors to 1, the full description of the radial distribution of the dipole strength is given by:

$$\vec{\boldsymbol{P}}(\boldsymbol{r}) = \boldsymbol{e}^{-(r/w)^2} \cdot \begin{pmatrix} \boldsymbol{1} \\ \boldsymbol{i} \\ \boldsymbol{0} \end{pmatrix} \cdot \boldsymbol{e}^{i\varphi(r)}\boldsymbol{\varphi} \tag{54}$$

The width w of the Gaussian function was calculated from the half divergence angle α, (experimentally determined to be 31.4 degrees by analysing the beam profile as a function of the z-coordinate) and the working distance z_0, as:

$$\boldsymbol{w = z_0 \cdot tan(\alpha)} \tag{55}$$

The distribution described above was then cut-off at a finite maximum radius r_{max} representing the finite opening of the focusing lens, which is defined by:

$$\boldsymbol{arctan(r_{max}/z_0) = arcsin\left(\frac{NA}{n}\right)} \tag{56}$$

where NA is the numerical aperture of the lens and n the refractive index of the medium.

The field distribution near the focal spot was calculated as the superposition of elementary waves emerging from the emitter distribution (equation (54)). To do this, the field in the volume surrounding the focal spot was mapped to a two-dimensional array of pixels addressed by axial and radial coordinates in the x-z-plane, taking advantage of the deliberately introduced rotational symmetry of the source. The resolution of this field map was chosen to be $\lambda/50$, where λ was set to 780 nm/1.52 = 513 nm (the wavelength of the laser divided by the refractive index of the photoresist). The Monte Carlo algorithm repeatedly picked a randomly selected pair of a pixel $\vec{x}_f$ in this map and a point $\vec{x}_s$ in the source distribution in order to calculate the contribution of the source emitter to the selected pixel. The latter was taken to be the field of an elementary dipole equivalent to the emitter strength $\vec{P} = \vec{P}(\vec{x}_s)$. Omitting constant factors, the elementary dipole field is given by:

$$\boldsymbol{\vec{E}(\vec{x}_f) = \left\{\frac{(\vec{n} \times \vec{P}) \times \vec{n}}{R} + \left[3 \cdot \vec{n} \cdot (\vec{n} \cdot \vec{P}) - \vec{P}\right] \cdot \left(R^{-3} + i \cdot R^{-2}\right)\right\} \cdot e^{iR}} \tag{57}$$

where $R = \frac{2\pi}{\lambda}\left|\vec{x}_f - \vec{x}_s\right|$ is the distance between the source and the pixel in the field map scaled by the wavelength, and $\vec{n} = \frac{\vec{x}_f - \vec{x}_s}{|\vec{x}_f - \vec{x}_s|}$ is the normalised vector pointing from the source point to the pixel. All contributions to one pixel originating from different source points (typically 10^5 contributions per pixel) were averaged into one field vector approximating the electrical field with full phase information at the centre of each pixel. The square of the above field vector, $I = \vec{E}^2$, is a relative intensity proportional to the physical intensity; the factor of proportionality arising from all the constants explicitly or implicitly omitted above. To calculate voxel sizes as a function of the laser power, this intensity distribution needs to be correlated to the laser power. We start by expressing the latter as a factor f times the threshold laser power (determined to be 9.3 mW by the analysis of the observed pillar diameters according to equation (52); see **Figure 6-1b**) On the other hand, the above intensity distribution has a maximum I_{max} at the focal spot. At the threshold laser power ($f = 1$), this maximum is equivalent to the polymerisation threshold I_{th}, $I_{max} = I_{th}$. At a higher laser power, the whole intensity distribution is multiplied by f, and polymerisation is initiated wherever the scaled intensity exceeds the threshold. The theoretical height of a voxel is thus determined as the size of the interval in a longitudinal section through the

intensity map where $f \cdot I > I_{th}$. To derive the width of the voxel, the same analysis is applied to the cross-section.

The resulting theoretical voxel sizes were used to calculate the theoretical height h of the pillars as follows:

$$\boldsymbol{h = (a - 1)b + c + d/2} \tag{58}$$

where a = 4 is the number of stacked voxels, b = 300 nm is the vertical centre-to-centre distance between voxels, c = - 200 nm is the centre distance of the first voxel from the substrate interface, and d is the height of an individual voxel obtained from the numerical simulations. The resulting theoretical pillar heights and diameters were further used to calculate the initial aspect ratios of pillars and to estimate the shrinkage by comparing the theoretical with the experimental values (see **Table S 6-1** in the Supplementary Information).

6.3.5. *Simulation of Optical Spectra*

Although no reflection spectra were recorded due to instrumental limitations, an attempt was made to correlate the observed colours with simulated optical spectra. These were calculated from simulated diffraction efficiencies taking into account the different diffraction orders and the finite aperture angle of the microscope objective used. Diffraction was simulated by rigorous coupled-wave analysis (RCWA) using the electromagnetic solver, S4, developed at the Stanford University[39,40]. In these simulations, the pillar shape was approximated as a cylinder with an ellipsoidal tip. The radii of the cylinders r_c were set to the experimentally determined radii of pillars fabricated at different laser powers. The cylinder heights h_c were calculated with $h_c = h_p - h_e$, where h_p was the measured pillar height. The height of the ellipsoidal tip h_e was assigned to half the voxel height evaluated by Monte Carlo simulations described above, as this parameter was hard to determine experimentally. Using this set of parameters, the pillar envelope function can be described as follows:

$$\boldsymbol{y(z)}\begin{cases} \boldsymbol{r_c} & \textbf{for } \boldsymbol{z \le h_c} \\ \boldsymbol{r_c}\sqrt{\boldsymbol{1 - \left(\frac{z - h_c}{h_e}\right)}} & \textbf{for } \boldsymbol{h_c < z \le h_p} \end{cases} \tag{59}$$

where the z-axis is assumed to be normal to the substrate surface, and thus corresponds to the structure expansion in the vertical direction. The pillars were discretised in slices of 10 nm. A periodic boundary condition was applied with a box size of 1 × 1 µm (in accordance with the pillar centre-to-centre distance) as well as an incidence angle of 0°. The refractive index and extinction coefficient of the cured photoresist and the fused silica substrate were taken from ellipsometry measurements (see **Figure S 6-1** in the Supplementary Information).

In experiments, the observed colours originate from reflected light that is diffracted by the grating. Reflection occurred at two different interfaces, i.e., the pillar-substrate interface and the backside of the 1 mm fused silica substrate. Due to the opening angle of the objective with NA = 0.45, only diffraction angles of equal to or below 27° were collected. To quantify the contribution of different diffraction orders to the colouration, an overlap factor OF between the incident light and the light cones of different diffraction orders were numerically calculated using the given geometrical parameters of the fabricated nanostructures and the imaging system (angle of incidence, collection angle). In the case of the 1st diffraction order, OF was found to range from 0.45 at a wavelength of 400 nm to 0.045 at 800 nm. Overlap factors for higher diffraction orders were zero except for negligible values at the shortest wavelengths and, therefore, were not considered in further calculations. The reflection at the pillar-substrate interface was calculated by summing 100 % of the reflectivity values obtained for the 0^{th} diffraction order and the values of the 1^{st} diffraction order multiplied by 4 OF_λ, where 4 is the number of contributing 1^{st} order diffraction cones, and OF_λ the overlap for the respective wavelength. The reflection at the backside of the substrate was calculated in the same way but using transmissive diffraction efficiencies. For each grating, both contributions were added to a final reflection spectrum.

6.4. Results

6.4.1. *Nanopillar Sizes*

Sizes of the nanopillars fabricated with laser powers varying from 10 to 23 mW were obtained from SEM-micrographs (**Figure 6-1a**). The pillar diameters ranged from 120 nm to 430 nm (measured at the bottom of the pillars). The heights of the pillars extended from 330 to 1315 nm. The structures exhibited an almost constant aspect ratio (height over diameter) of about 3 (**Figure 6-1b**). Evaluation of the defect rate revealed high quality of the obtained optical gratings with 100 % upright standing pillars for all gratings with pillar diameters down to 184 nm (**Figure 6-1c**). Gratings fabricated with the lowest laser power of 10 mW and thus, closest to the polymerisation threshold, exhibited 30 % freestanding pillars and 70 % collapsed structures. With a diameter of 120 nm, these pillars were the smallest high aspect ratio pillars fabricated with TPL to our best knowledge so far. The collapse of the pillars is most likely induced by capillary forces during drying upon development and post-curing. These collapses occur when the capillary forces exceed the elastic restoring forces of the pillars[36]. As the latter decrease with pillar diameter, smaller structures tend to collapse more easily. For the sake of completeness and to demonstrate the importance of using a UV-post-curing during development, similar pillar structures were fabricated without the additional UV-exposure, exhibiting much more defects even for larger structures (see **Figure S 6-2** in the Supplementary Information).

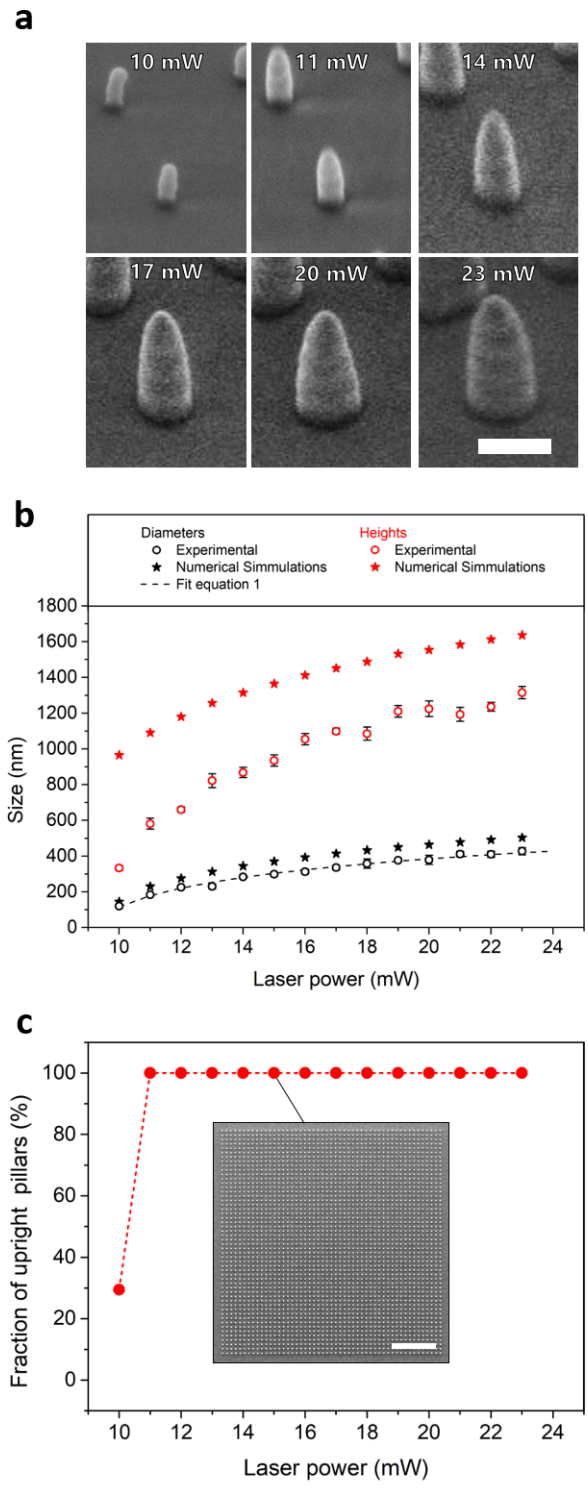

Figure 6-1. Sizes of nanopillars as a function of the applied laser power.

(a) Scanning electron micrographs of nanopillars fabricated with different laser powers. The scale bar is 500 nm. (b) Diameters (black symbols) and heights (red symbols) of the nanopillars obtained from two-photon lithography (open circles) compared to numerical simulations (filled stars). The dashed line shows the fit of the pillar diameters using equation (58) to estimate the threshold laser power of the photoresist. (c) Defect rates of optical gratings expressed as fractions of upright pillars in dependence on the applied laser power. The values were obtained from Scanning Electron Microscopy (SEM)-images as shown for 15 mW in the insert. The scale bar is 10 µm.

6.4.2. *Optical Properties*

Figure 6-2 shows optical micrographs of the nanopillar gratings. The divergence angle of the illuminating light as well as the collection angle of the microscope were both 27°. The optical micrographs revealed a coloured reflection of the gratings, which is based mainly on diffraction and interference effects. Absorption can be neglected due to the low extinction coefficients of all materials involved (**Figure S 6-1** in the Supplementary Information). The colour of the gratings changed with the laser power from slight brownish (11 mW) to blue-green (23 mW). For 10 mW, the surface appeared colourless (**Figure 6-2a**). To quantify the optical appearance of the gratings, the optical micrographs were compared with numerical simulations that provide expected optical spectra for the experimental set-up used (**Figure 6-3**). The simulations were performed for six gratings corresponding to 10 mW (colourless), 11 mW (slightly yellow), 14 mw (brown), 17 mW (blue-brown), 20 mW (blue), and 23 mW (blue-green).

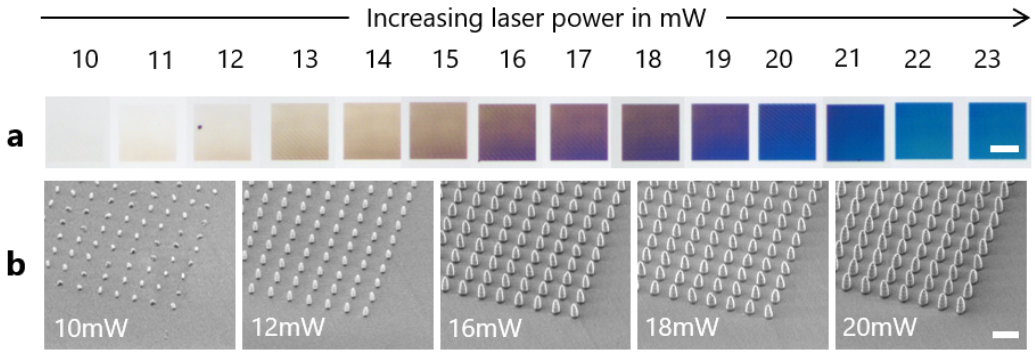

Figure 6-2. Optical appearance of the nanopillar gratings in dependence on the laser power.

(a) Optical micrographs of 50 × 50 µm nanopillar gratings on a fused silica substrate. Scale bar is 25 µm. (b) Scanning electron micrographs showing the corresponding nanopillars. Scale bar is 1 µm.

The obtained spectra did not fully agree with the colours recorded by optical microscopy. Minor deviations can be expected from using diffraction efficiencies for normal incidence to approximate the whole cone of incident light. Moreover, considerable differences could be attributed to variations of the pillar shape. In the fabricated gratings, the shape of the pillars varied between cylinders and cones (compare **Figure 6-1a**), whereas cylindrical pillars with elliptical tips were assumed in the simulations. The shape, though, is important for the choice of an appropriate pillar diameter for simulations. This argument was confirmed by simulations with 20% smaller pillar diameters, which led to a significant blue-shift of the spectra (dashed lines in **Figure 6-3**) and a better correspondence with the colours observed. From this, it is concluded that even small variations in the shape of the pillars dramatically affect the optical appearance of the gratings, and that it is therefore not sufficient to evaluate diameters at the pillars' bases only. This outcome supports our arguments that good understanding of occurring effects, such a shrinkage, surface tension, and related mechanisms, as well as their influence on the

feature shape and sizes are important for a precise prediction of the optical properties of pillar gratings fabricated via TPL.

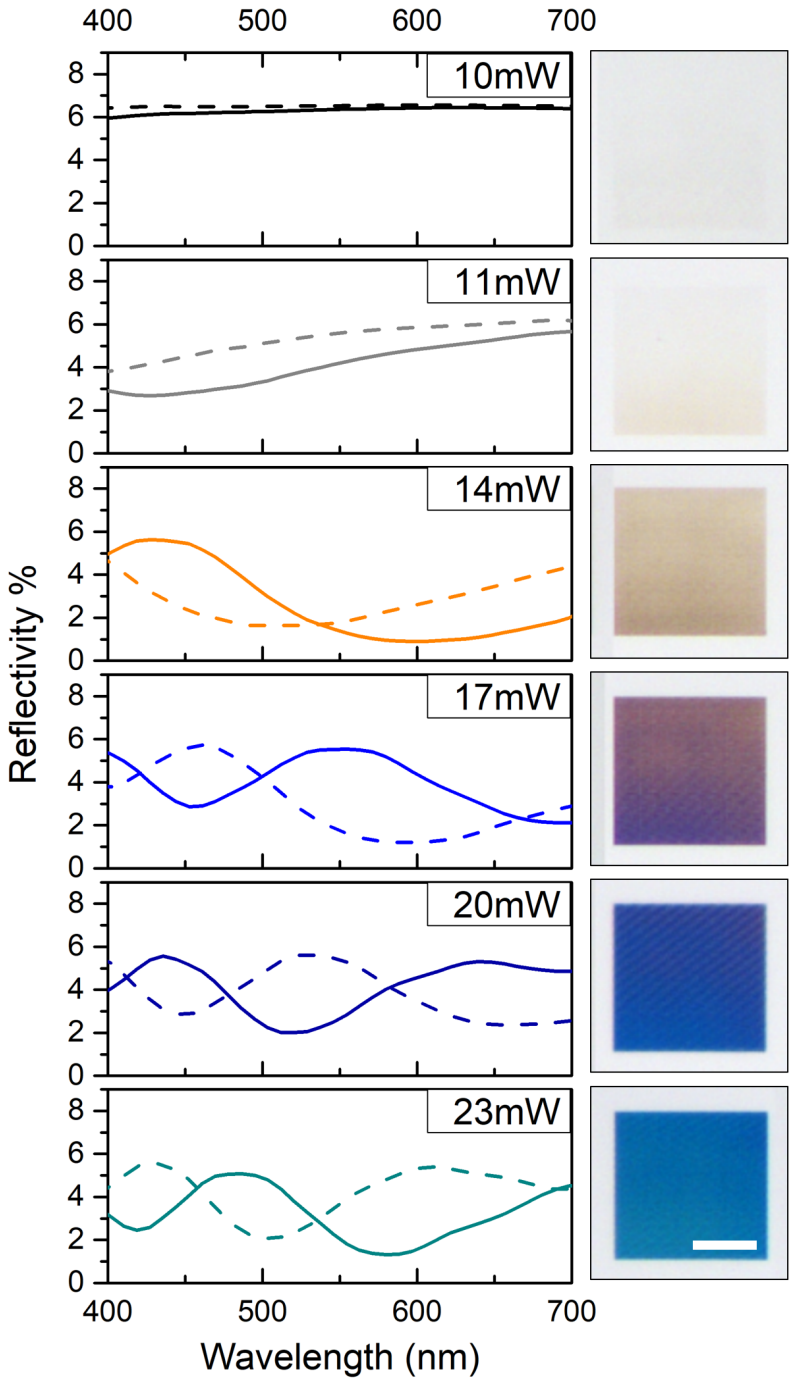

Figure 6-3. Optical properties of the nanopillar gratings.

Reflectivity in dependence on the wavelength obtained from numerical simulations for structure sizes as measured by SEM (solid line) and pillars assuming 20% smaller diameters (dashed line) (left) compared to optical micrographs of nanopillar gratings fabricated with different laser powers (right). The scale bar is 25 µm.

The total reflectivities shown in **Figure 6-3** comprise the reflected diffraction at the pillar-substrate interface as well as the transmissive diffraction of light reflected at the backside of the substrate. As these two are expected to differ strongly in their minima due to variation in the optical path, minima as low as 1% predicted by simulation were surprising. Nevertheless, their presence is confirmed by the intense colours of the gratings. We assume that this could be caused by Mie resonances[42]. This assumption is supported by the strong dependence of the spectra on the pillar diameter. Small pillars obtained at low laser powers interact predominantly with ultraviolet to blue light, leading to a brownish hue. As the pillar size increases with increasing laser power, the resonance shifts towards red wavelengths, resulting in a blueish hue. This variability in colour due to the size and shape of nanopillars gratings allows for efficient diffractive colour filters.

6.5. Conclusions

Optical pillar gratings were successfully fabricated via TPL at different laser powers close to the polymerisation threshold of the photoresist and investigated with respect to their sizes and optical properties using imaging techniques and numerical simulations. The following conclusions can be drawn:

(1) Defect-free nanopillar gratings were fabricated down to pillar diameters of 184 nm and aspect ratios about 3. The smallest pillar diameters achieved were 120 nm, but on imperfect arrays, and therefore would require further optimization in fabrication.

(2) Simulations of the voxel sizes overestimated experimental pillar sizes by 20% in lateral and up to 65% in the vertical direction. This effect can be rationalized by shrinkage that differs due to varying amounts of unreacted oligomers, different overlapping of adjacent voxels, substrate adhesion, and probably surface tension effects.

(3) The nanopillar gratings interfered with visible wavelengths and varied in their optical properties depending on the pillar sizes tuned by TPL. The simulation of the optical spectra confirmed that the colouration originates indeed from the diffraction of reflected light, but also prompts the notion that the size and shape of the nanopillars strongly influence the optical appearance.

In summary, optical gratings based on different pillar sizes can be manufactured by varying the laser power in TPL in a single process step on one surface. However, the fabrication of precise optical gratings close to the polymerisation threshold of the photoresist requires a deep understanding of the involved processes.

6.6. Acknowledgements

The authors thank Reza Hosseinabadi for his help with the TPL-fabrication and the optical imaging. VEJ thanks the European Commission (Marie Curie Fellowship Looking Through Disorder (LODIS), 701455) for financial support. The project was partially funded by the European Research Council under the European Union's Seventh Framework Program (FP/2007-2013)/ERC Advanced Grant no. 340929.

6.7. References

1. Catchpole KR, Green MA. A conceptual model of light coupling by pillar diffraction gratings. *Journal of Applied Physics* 2007, **101**(6)**:** 063105.
2. Chong TK, Wilson J, Mokkapati S, Catchpole KR. Optimal wavelength scale diffraction gratings for light trapping in solar cells. *Journal of Optics* 2012, **14**(2)**:** 024012.
3. Yan H, Huang L, Xu X, Chakravarty S, Tang N, Tian H, *et al.* Unique surface sensing property and enhanced sensitivity in microring resonator biosensors based on subwavelength grating waveguides. *Opt Express* 2016, **24**(26)**:** 29724-29733.
4. Mao X, Zeng L. Design and fabrication of crossed gratings with multiple zero-reference marks for planar encoders. *Meas Sci Technol* 2018, **29**(2)**:** 025204.
5. Kim DY, Tripathy SK, Li L, Kumar J. Laser-induced holographic surface relief gratings on nonlinear optical polymer films. *Appl Phys Lett* 1995, **66**(10)**:** 1166-1168.
6. Gale MT, Knop K, Morf RH. *Zero-order diffractive microstructures for security applications*, vol. 1210. SPIE, 1990.
7. Wang Y, Lu N, Xu H, Shi G, Xu M, Lin X, *et al.* Biomimetic corrugated silicon nanocone arrays for self-cleaning antireflection coatings. *Nano Res* 2010, **3**(7)**:** 520-527.
8. Dewan R, Fischer S, Meyer-Rochow VB, Özdemir Y, Hamraz S, Knipp D. Studying nanostructured nipple arrays of moth eye facets helps to design better thin film solar cells. *Bioinspiration & biomimetics* 2011, **7**(1)**:** 016003.
9. Ji S, Park J, Lim H. Improved antireflection properties of moth eye mimicking nanopillars on transparent glass: flat antireflection and color tuning. *Nanoscale* 2012, **4**(15)**:** 4603-4610.
10. Lora Gonzalez F, Chan L, Berry A, Morse DE, Gordon MJ. Simple colloidal lithography method to fabricate large-area moth-eye antireflective structures on Si, Ge, and GaAs for IR applications. *J Vac Sci Technol B* 2014, **32**(5)**:** -.
11. Chigrin DN, Lavrinenko AV. *Nanopillar coupled periodic waveguides: from basic properties to applications*, vol. 6393. SPIE, 2006.
12. Farsari M, Chichkov BN. Materials processing: Two-photon fabrication. *Nat Photon* 2009, **3**(8)**:** 450-452.
13. Gissibl T, Thiele S, Herkommer A, Giessen H. Two-photon direct laser writing of ultracompact multi-lens objectives. *Nat Photon* 2016, **10**(8)**:** 554-560.
14. Hohmann JK, Renner M, Waller EH, von Freymann G. Three-Dimensional μ-Printing: An Enabling Technology. *Adv Opt Mater* 2015, **3**(11)**:** 1488-1507.
15. Kawata S, Sun H-B, Tanaka T, Takada K. Finer features for functional microdevices. *Nature* 2001, **412:** 697.
16. Waheed S, Cabot JM, Macdonald NP, Lewis T, Guijt RM, Paull B, *et al.* 3D printed microfluidic devices: enablers and barriers. *Lab Chip* 2016, **16**(11)**:** 1993-2013.
17. Fischer SCL, Groß K, Torrents Abad O, Becker MM, Park E, Hensel R, *et al.* Funnel-Shaped Microstructures for Strong Reversible Adhesion. *Adv Mater Interfaces* 2017, **4**(20)**:** 1700292-n/a.
18. Hensel R, Moh K, Arzt E. Engineering Micropatterned Dry Adhesives: From Contact Theory to Handling Applications. *Adv Funct Mater* 2018, **28**(28)**:** 1800865.

19. Marino A, Filippeschi C, Mattoli V, Mazzolai B, Ciofani G. Biomimicry at the nanoscale: current research and perspectives of two-photon polymerization. *Nanoscale* 2015, **7**(7)**:** 2841-2850.
20. Marino A, Ciofani G, Filippeschi C, Pellegrino M, Pellegrini M, Orsini P, *et al.* Two-Photon Polymerization of Sub-micrometric Patterned Surfaces: Investigation of Cell-Substrate Interactions and Improved Differentiation of Neuron-like Cells. *ACS Applied Materials & Interfaces* 2013, **5**(24)**:** 13012-13021.
21. Wolfenson H, Meacci G, Liu S, Stachowiak MR, Iskratsch T, Ghassemi S, *et al.* Tropomyosin controls sarcomere-like contractions for rigidity sensing and suppressing growth on soft matrices. *Nature Cell Biology* 2015, **18:** 33.
22. Klein F, Striebel T, Fischer J, Jiang Z, Franz CM, von Freymann G, *et al.* Elastic Fully Three-dimensional Microstructure Scaffolds for Cell Force Measurements. *Adv Mater* 2010, **22**(8)**:** 868-871.
23. Thiele S, Arzenbacher K, Gissibl T, Giessen H, Herkommer AM. 3D-printed eagle eye: Compound microlens system for foveated imaging. *Science Adv* 2017, **3**(2).
24. von Freymann G, Ledermann A, Thiel M, Staude I, Essig S, Busch K, *et al.* Three-Dimensional Nanostructures for Photonics. *Adv Funct Mater* 2010, **20**(7)**:** 1038-1052.
25. Nawrot M, Zinkiewicz Ł, Włodarczyk B, Wasylczyk P. Transmission phase gratings fabricated with direct laser writing as color filters in the visible. *Opt Express* 2013, **21**(26)**:** 31919-31924.
26. Mueller JB, Fischer J, Mayer F, Kadic M, Wegener M. Polymerization Kinetics in Three-Dimensional Direct Laser Writing. *Adv Mater* 2014, **26**(38)**:** 6566-6571.
27. Sun H-B, Maeda M, Takada K, Chon JWM, Gu M, Kawata S. Experimental investigation of single voxels for laser nanofabrication via two-photon photopolymerization. *Appl Phys Lett* 2003, **83**(5)**:** 819-821.
28. Fischer J, Wegener M. Three-dimensional optical laser lithography beyond the diffraction limit. *Laser & Photonics Reviews* 2013, **7**(1)**:** 22-44.
29. Xing J-F, Dong X-Z, Chen W-Q, Duan X-M, Takeyasu N, Tanaka T, *et al.* Improving spatial resolution of two-photon microfabrication by using photoinitiator with high initiating efficiency. *Appl Phys Lett* 2007, **90**(13)**:** 131106.
30. Tanaka TS, Hong-Bo; Kawata, Satoshi. Rapid sub-diffraction-limit laser micro/nanoprocessing in a threshold material system. *Appl Phys Lett* 2002, **80**(2)**:** 312-314.
31. Fischer J, Mueller JB, Quick AS, Kaschke J, Barner-Kowollik C, Wegener M. Exploring the Mechanisms in STED-Enhanced Direct Laser Writing. *Adv Opt Mater* 2015, **3**(2)**:** 221-232.
32. Sun H-B, Takada K, S. Kim M, Lee K-S, Kawata S. *Scaling laws of voxels in two-photon photopolymerization nanofabrication*, vol. 83, 2003.
33. Sun H-B, Suwa T, Takada K, Zaccaria RP, Kim M-S, Lee K-S, *et al.* Shape precompensation in two-photon laser nanowriting of photonic lattices. *Appl Phys Lett* 2004, **85**(17)**:** 3708-3710.
34. LaFratta C, Baldacchini T. Two-Photon Polymerization Metrology: Characterization Methods of Mechanisms and Microstructures. *Micromachines* 2017, **8**(4)**:** 101.
35. Hu Y, Lao Z, Cumming BP, Wu D, Li J, Liang H, *et al.* Laser printing hierarchical structures with the aid of controlled capillary-driven self-assembly. *Proc Natl Acad Sci* 2015, **112**(22)**:** 6876-6881.
36. Purtov J, Verch A, Rogin P, Hensel R. Improved development procedure to enhance the stability of microstructures created by two-photon polymerization. *Microelectron Eng* 2018, **194:** 45-50.
37. Roca-Cusachs P, Rico F, Martínez E, Toset J, Farré R, Navajas D. Stability of Microfabricated High Aspect Ratio Structures in Poly(dimethylsiloxane). *Langmuir* 2005, **21**(12)**:** 5542-5548.
38. Chandra D, Yang S. Capillary-Force-Induced Clustering of Micropillar Arrays: Is It Caused by Isolated Capillary Bridges or by the Lateral Capillary Meniscus Interaction Force? *Langmuir* 2009, **25**(18)**:** 10430-10434.
39. Liu V, Fan S. S4 : A free electromagnetic solver for layered periodic structures. *Comput Phys Commun* 2012, **183**(10)**:** 2233-2244.
40. Available from: https://web.stanford.edu/group/fan/S4/
41. Lim TW, Son Y, Yang D-Y, Pham TA, Kim D-P, Yang B-I, *et al.* Net Shape Manufacturing of Three-Dimensional SiCN Ceramic Microstructures Using an Isotropic Shrinkage Method by Introducing Shrinkage Guiders. *Int J Appl Ceram Tec* 2008, **5**(3)**:** 258-264.

42. Kuznetsov AI, Miroshnichenko AE, Brongersma ML, Kivshar YS, Luk'yanchuk B. Optically resonant dielectric nanostructures. *Science* 2016, **354**(6314)**:** aag2472.

6.8. Supplementary Information

Table S 6-1 Summary of pillar dimensions as a function of the laser power

Experimental data were obtained from scanning electron micrographs (SEM). Theoretical predictions were calculated using eq. (1) in the main text (Sun et al.) and numerical simulations.

	SEM-investigation			Fit Sun et al.	Numerical Simulations				
Laser Power [mW]	Pillar Diam. [nm]	Pillar Height [nm]	Fraction of upright pillars [%]	Voxel Diam. [nm]	Voxel Diam. [nm]	Voxel Height [nm]	Pillar Height [nm]	Aspect ratio	Shrinkage [%]
10	120 ± 11	333 ± 13	29.45	115	144	531	965	6.69	65.5
11	184 ± 5	581 ± 30	100	178	230	781	1.09	4.74	46.72
12	225 ± 7	660 ± 14	100	221	275	959	1.18	4.29	44.04
13	230 ± 14	822 ± 39	100	254	312	1.113	1.257	4.02	34.58
14	284 ± 7	868 ± 28	100	281	344	1.228	1.314	3.82	33.94
15	298 ± 6	935 ± 31	100	303	370	1.33	1.365	3.69	31.5
16	313 ± 12	1.054 ± 32	100	323	392	1.424	1.412	3.6	25.35
17	336 ± 13	1.099 ± 17	100	341	413	1.502	1.451	3.51	24.26
18	358 ± 25	1.085 ± 36	100	357	433	1.576	1.488	3.44	27.08
19	376 ± 9	1.21 ± 33	100	372	449	1.664	1.532	3.41	21.02
20	379 ± 26	1.224 ± 44	100	385	464	1.708	1.554	3.35	21.24
21	411 ± 17	1.193 ± 39	100	397	478	1.768	1.584	3.31	24.68
22	410 ± 18	1.236 ± 24	100	408	491	1.825	1.613	3.29	23.35
23	427 ± 20	1.315 ± 35	100	419	503	1.873	1.637	3.25	19.65

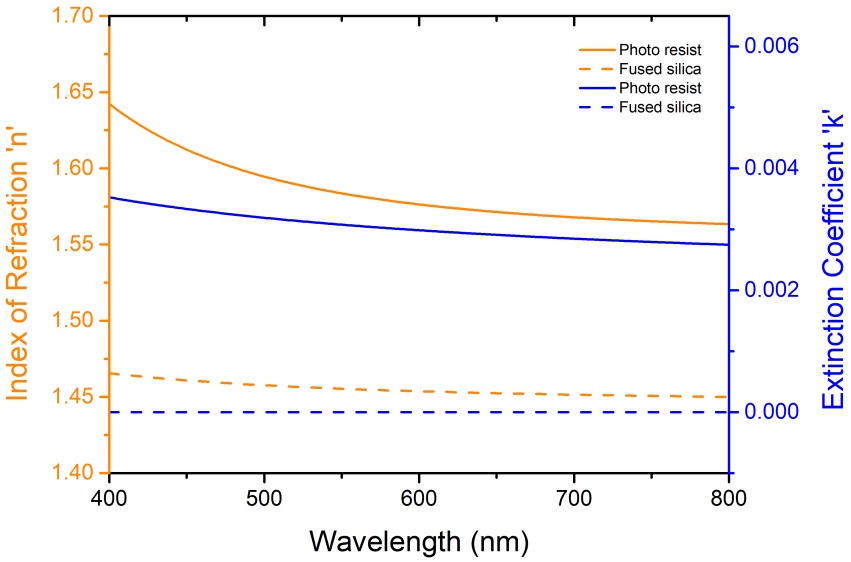

Figure S 6-1. Optical constants of used materials

Refraction index and extinction coefficient depending on the wavelength measured on UV-cured IP-DIP photoresist film (continuous line) and the fused silica substrate (dashed line) by ellipsometry.

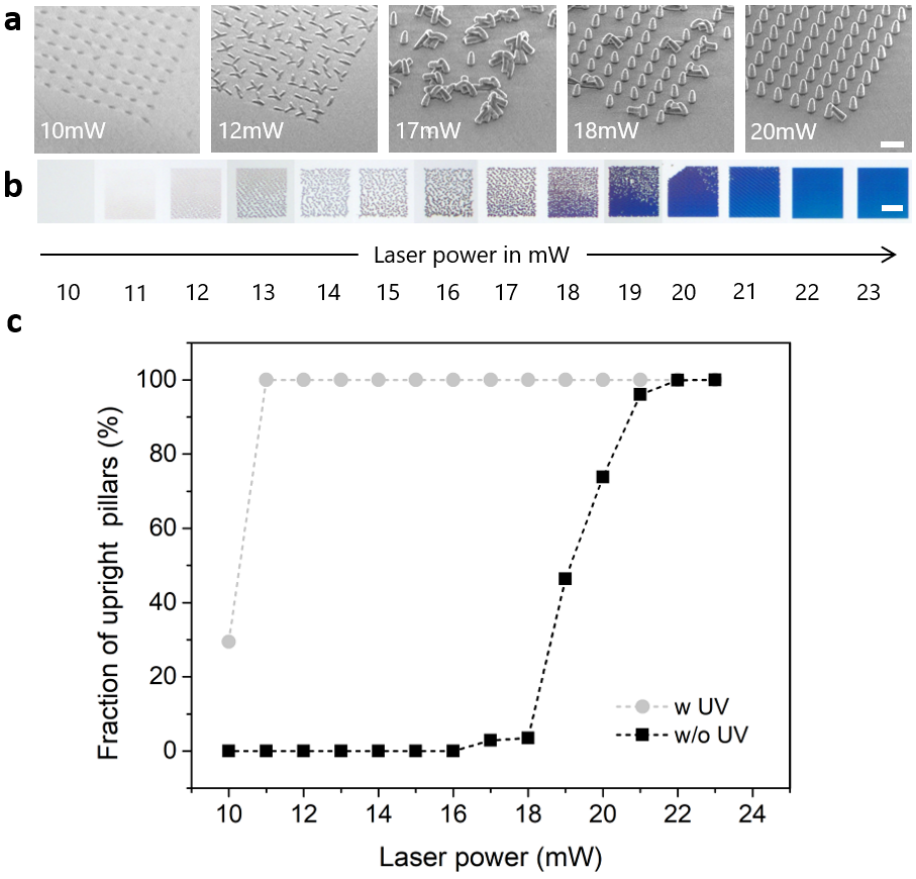

Figure S 6-2. Optical pillar gratings when fabricated without UV-post-curing

(a) SEM-micrographs. Scale bar is 1 µm. (b) Optical micrographs of 50x50 µm nanopillar gratings on a fused silica substrate. Scale bar is 10 µm. (c) Fraction of upright pillars without (black squares) and with additional cross-linking (grey circles). Dotted lines are added to guide the eyes.

Chapter 7. Diffraction and Anti-reflection Gratings for Anti-counterfeiting

7.1. Abstract

Surfaces which can both diffract and anti-reflect visible wavelengths could add a further, very useful component for the design of anti-counterfeiting surfaces. However, the fabrication of such surfaces is challenging, as the most structuring techniques allow for only one type of grating per surface. In this work, we report on the simultaneous fabrication of diffraction gratings in close proximity to anti-reflection gratings by means of two-photon lithography. The fabricated pillar gratings are investigated regarding their structure sizes and optical properties using scanning electron microscopy, optical microscopy, and reflective and transmissive spectroscopy.

7.2. Introduction

Effective optical diffraction gratings affecting visible wavelengths are not only important in many classical application areas of optics, such as lasers, monochromators, or sensors[1], but find also increasing interest in applications regarding optical computing[2,3], and the miniaturisation of optical devices and measurement tools[4]. A similarly strong interest exists for anti-reflection surfaces with gradual refractive indices, as they can be used as anti-reflection coatings on light coupling devices[5,6] or to improve solar cell efficiency[7,8]. For optical security features, though, it would be favourable to combine the optical properties of both, diffractive and anti-reflective elements. This would increase the complexity of the optical response of a security feature, and thus, reduce the risk of its counterfeit[9-12]. A way to achieve this is to combine different types of pillar gratings on one single surface, e.g., one type possessing pillar sizes and distances comparable to the wavelengths of visible light and the other possessing pillars and distances smaller than these wavelengths. In case of the former, light is typically diffracted. The latter, though, shows anti-reflection properties. Here, the light experiences the surface structures as a medium with a continuously changing refractive index, what strongly reduces Fresnel reflection and could even enhance transmission[13-15]. The fabrication of such different gratings on one singe surface, however, is exceedingly difficult to achieve, as methods which provide the structural resolution needed for anti-reflection structures to not very in different types of pillars per processed surface[16-19].

A rather recent alternative method to obtain multiple closely placed structure types is two-photon lithography (TPL), which enables flexible fabrication of complex 3D-structures in even one single exposure process step[20,21]. In a typical TPL process, a highly pulsed infrared laser is focussed onto a photoresist. Only in the very focus of the beam, the photon density is high enough to induce a two-photon process, which activates the photoinitiator, and thus, starts a cross-linking reaction of the photoresist. The smallest achievable volume for polymerisation is a so-called voxel, whose size is determined by the kinetics of the used photoresist[22-25] and the characteristics of the laser beam[22,26-28]. By varying the beam intensity for example, pillar gratings with pillar diameters between 430 nm and 120 nm could be created[21] (see also Chapter 6). It was further shown in the same study, that these size differences had an impact on the observed colour and the simulated reflection spectra of the gratings. A change in colour was also observed by reducing the pillar distance from 1700 to 280 nm within the gratings[20] (see also Chapter 5). The flexibility of TPL to vary both, pillar size and pillar distance, during the lithography process, and thus, to create different pillars in direct neighbourhood, makes this technique a good candidate for the fabrication of surfaces providing diffractive and anti-reflective optical properties.

In the present study, we report on the simultaneous fabrication of diffraction gratings and anti-reflection gratings in close proximity by means of two-photon lithography. Therefore, several gratings with 780 nm and 280 nm structure distance were fabricated with slightly different laser powers and

investigated regarding their optical performance by means of optical microscopy. The gratings yielding the best performances were investigated in more detail by scanning electron microscopy and micro-spectroscopy.

7.3. Experimental

7.3.1. *Two-Photon Patterning*

Pillar gratings with an area of 160 x 160 µm were fabricated on one single glass substrate from a polyacrylated photoresist (IP-L-780, Nanoscribe) by using a commercially available TPL-system (Professional GT Nanoscribe) equipped with a 63x oil objective (NA = 1.4, Carl Zeiss). Each structure was built by a vertical stacking of 4 voxels with a vertical centre-to-centre distance of 300 nm and a negative offset of 200 nm with respect to the substrate surface for the first voxel to ensure substrate adhesion. The pillar structures were distributed in square patterns. In the case of the diffraction grating, the pillar distance was conceived to be d_{710} = 710 nm. In case of the anti-reflection grating, the distance was conceived to be d_{280} = 280 nm. As such close packing of structures could result in a local increase in temperature, and thus, to a size increase of fabricated TPL-features[29], neighbouring pillars were fabricated using a double patterning approach. Therefore, two identical square patterns were exposed in succession with a pillar distance of $d_{exp} = d\sqrt{2}$ with d corresponding to the final pillar distances d_{710} and d_{280}, respectively. The offset Off_{xy} between both square patterns was $d_{exp}/2$ in both, x and y-direction. Laser powers between 13 mW and 17 mW were used to fabricate five arrays with 710 nm pillar distance next to five arrays with 280 nm pillar distance. The exposure time was set to 0.1 ms and the settling time to 2 ms. The development of the structures was performed according to Purtov et al.[20] to prevent pillar collapse.

7.3.2. *Scanning Electron Microscopy*

Resulting TPL structures were examined using a scanning electron microscope (SEM) (Quanta 250 FEG, FEI) equipped with an Everhart-Thornley-detector (ETD) in high vacuum. As no coating was applied to retain the optical properties of the samples, a copper tape was placed close to the fabricated TPL structures to minimise charging effects. The spot size was set to 2.0 and the accelerating voltage to 2 kV. The pillar heights in the micrographs were measured and corrected for the sample tilt of ca. 40°.

7.3.3. *Optical microscopy*

Optical micrographs were taken using a microscope in bright and dark field (Eclipse LV100ND Nikon) equipped with a 10x air objective (NA = 0.3, Nikon). The microscope was operated with a fully opened

aperture, and a white sheet of paper was used for white balance correction. The exposure time was set to 6 ms and 400 ms in bright and dark field, respectively.

7.3.4. *Micro-Spectroscopy*

Spectroscopy data were obtained using a custom-modified optical microscope (Scope.A1, Zeiss) equipped with a spectrometer (AvaSpec-HS2048, Avantes Sens Line), a halogen lamp (HAL 100, Zeiss) and a 200 µm glass fibre (FC-UV200-2-SR, Avantes). The microscope was operated with a 10x air objective (Zeiss) with a NA of 0.3 and an illumination aperture set to minimum. The measurements were conducted in both, reflection and transmission mode. With the rearranged Abbe equation $\alpha = \sin^{-1}(NA/n)$, (equation (28)), NA = 0.3, and n_{air} = 1, the recorded light cone is expected to have a divergence angle of ~17°. Recorded spectroscopy data were averaged over 5 spectra and smoothed using a moving average with a sliding window length of 30 across consecutive data points. A silver mirror served as the reference using an integration time of 150 ms. Recorded reflection and transmission spectra were compared to spectra obtained on an unstructured glass substrate to determine the effect of the surface structuring.

7.4. Results and Discussion

7.4.1. *Optical Properties*

Five 710 nm and five 280 nm gratings were fabricated in close proximity with laser powers between 13 mW and 17 mW. Micrographs obtained on theses gratings in bright and dark field revealed the expected optical behaviours with regard to the pillar distance conceived (**Figure 7-1**). In the bright field images, the 710 nm gratings were strongly coloured with colours varying from yellow at 13mW to violet at 17mW, while gratings with 280 nm distances appeared colourless (**Figure 7-1a**). In the dark field, gratings fabricated with 780 nm distances showed a strong blue-green scattering, whose intensity increased towards higher laser powers (**Figure 7-1b**). In contrast, the 280 nm gratings appeared almost dark with some slight blue scattering mainly at the stitching boarders. The intensity of this scattering seemed to decrease towards greater laser powers.

For both pillar distances, investigations via micro-spectroscopy revealed the most distinct diffraction and anti-reflection effect on gratings fabricated with 17mW. The obtained spectra are displayed in **Figure 7-2**. On the 710 nm grating, normal reflection was strongly reduced to only 10% for wavelengths between 450 nm and 600 nm. For shorter and longer wavelengths, the reflectivity increased to 17% and 40%, respectively, which is in correlation with the violet colour observed by microscopy (cp. **Figure 7-1a**). In transmission, the shape of the curve was narrower with a clear minimum around 500 nm (**Figure 7-2b**). The maximal diffraction efficiency was found to be 95% at 500 nm. On the 280 nm

gratings, the normal reflectivity was reduced strongest at 450 nm, slowly rising to 750 nm with a total variance of 10% over the investigated spectrum. Here, the maximal reflection was found to be 72% for blue wavelengths and 83% for red wavelengths, respectively (**Figure 7-2a**). The transmission, in contrast, was barely affected with a maximum intensity loss of only 2% in the blue range (**Figure 7-2b**).

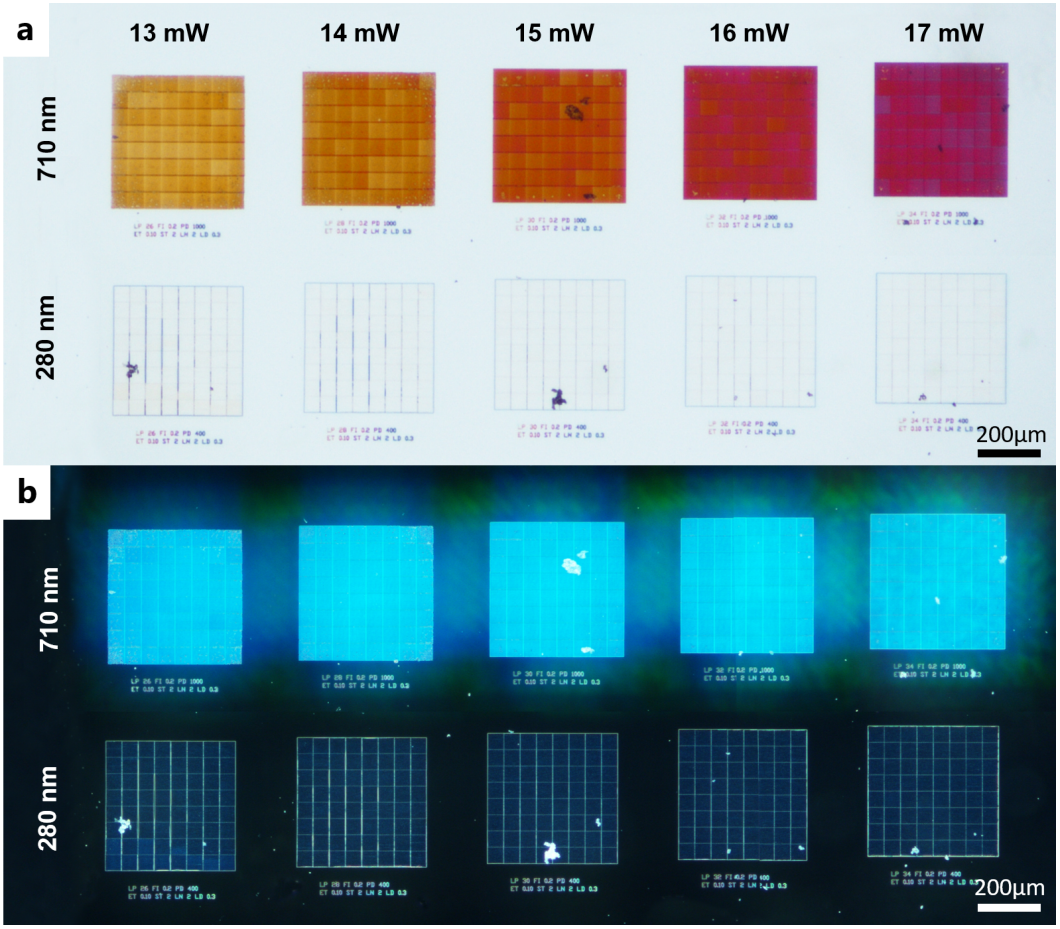

Figure 7-1 Micrographs of TPL gratings in bright and dark field

Bright field (a) and dark field (b) images of pillar arrays with 710 nm and 280 nm pillar distance. The arrays were fabricated at the laser powers between 13 mW and 17 mW as indicated above.

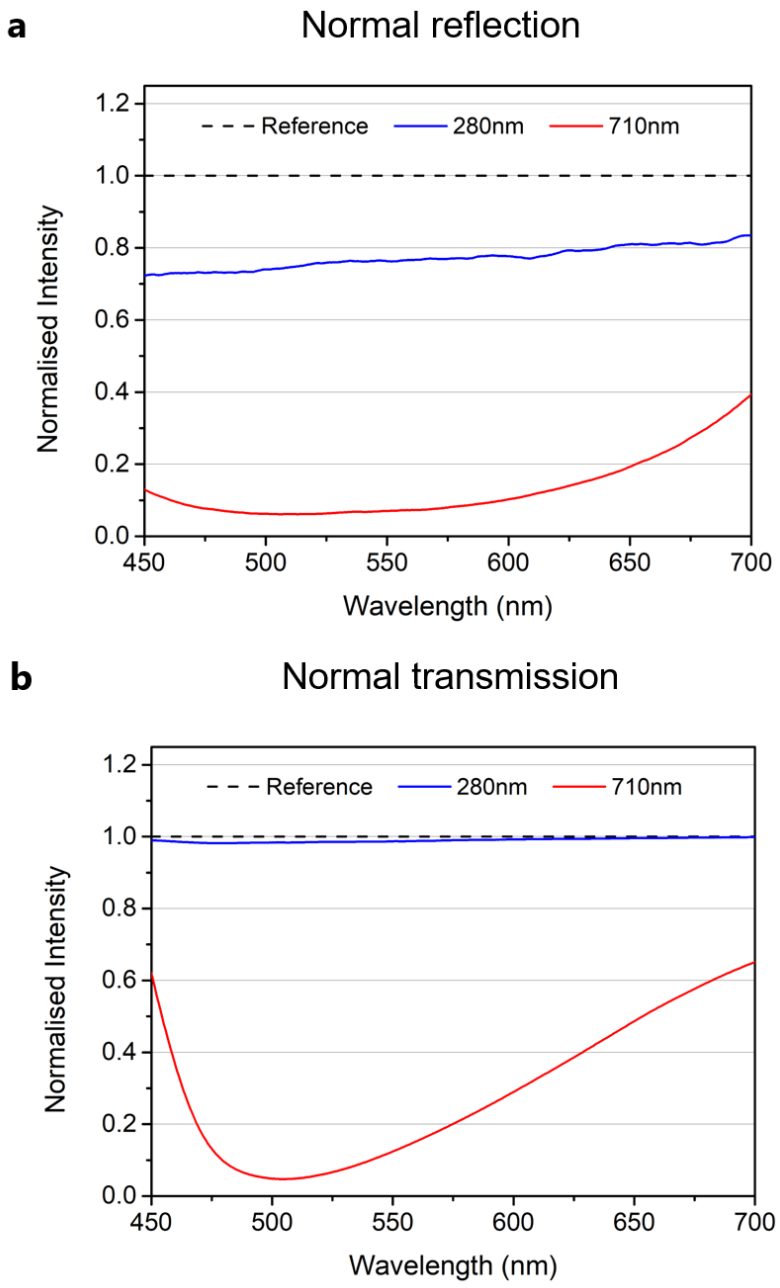

Figure 7-2 Spectroscopy results of gratings with the best performance

(a) Normal reflection and (b) transmission measured on the 710 nm-grating (red line) and the 280 nm-grating (blue line) fabricated with a laser power of 17 mW. The curves are presented in relation to the unstructured glass substrate (black dashed line).

7.4.2. *Topographies of gratings*

Scanning electron microscopy results obtained on pillar gratings fabricated with 17 mW are shown in (**Figure 7-3** and **Figure 7-4**). The pillar distances of both gratings were in agreement with the conceived values of 710 nm and 280 nm. Furthermore, the 710 nm grating itself revealed defect-free and highly ordered distinct pillars with heights of 1010 nm and diameters of 350 nm (**Figure 7-3a-c** and **Figure 7-4a,c**). The pillars on the grating conceived to have 280 nm pillar distance did not appear free-standing

but formed a quasi-film with a maximum thickness of 1110 nm (measured at the edge of the film). This film contained periodic protuberances with a tip distance of 270 - 280 nm and a depth of 200 nm (**Figure 7-3d-e** and **Figure 7-4b,c**). All values are summarised in **Table S 7-1** in the Supplementary Information.

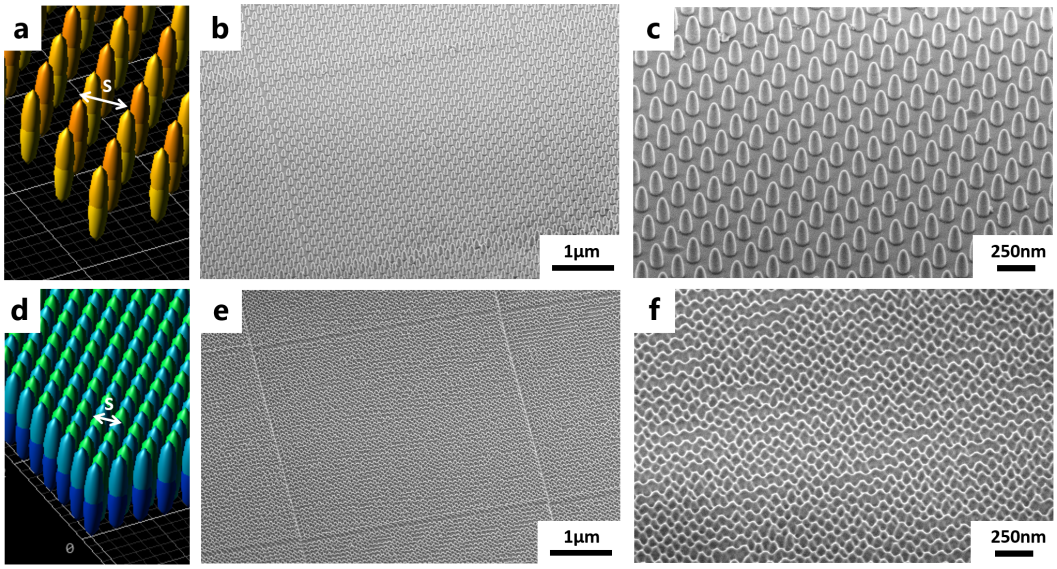

Figure 7-3. Resulting TPL-optical gratings

(a,d) Conceived structure for the TPL fabrication (b-f) SEM-images of fabricated gratings at different magnifications, ~40° tilt. (a-c) 710 nm grating and (d-f) 280 nm grating.

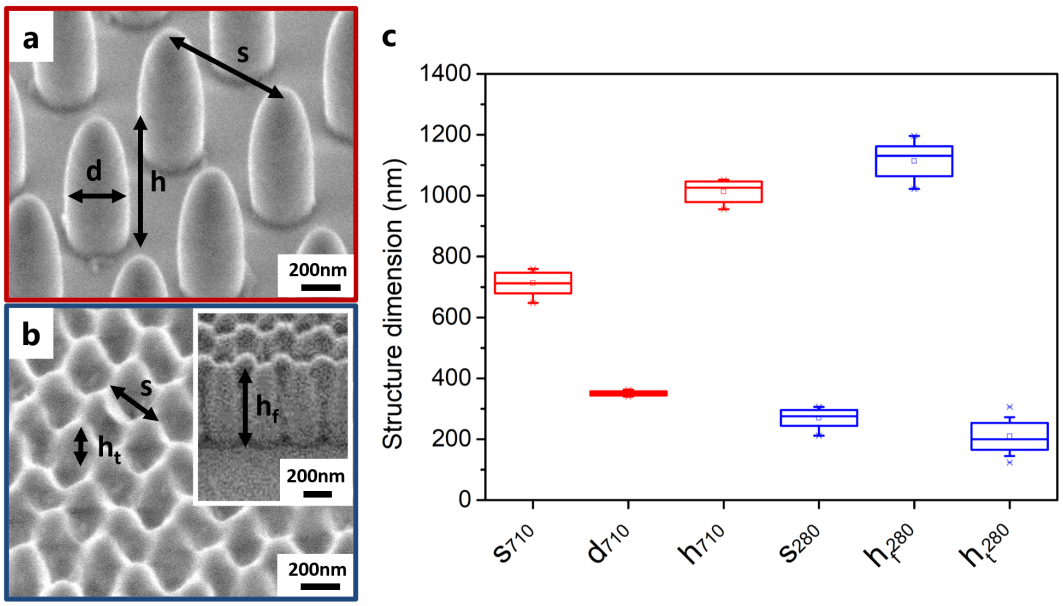

Figure 7-4. Structure sizes of TPL-fabricated optical gratings

(a,b) SEM images at ~40° tilt, black markings indicate the determined geometrical feature characteristics, the inset shows the edge of the 280 nm-grating. (c) Extracted structure dimensions of the 710 nm grating (red) and 280 nm grating (blue); s: spacing; d: diameter, h: pillar height, h_f: height of the quasi-film, h_t: height of protuberances.

7.5. Discussion

Surfaces which can do both, diffract and anti-reflect visible wavelengths, could add a particularly useful component to the design of new anti-counterfeiting markers. In this work it was shown that such a surface was achieved by the TPL fabrication of pillar gratings differing in their pillar distance, in one case having a distance of 710 nm and in the other a distance of 280 nm. The former diffracted light strongly with an efficiency of 95% at 500 nm. This is a high value in comparison to other TPL-fabricated optical gratings presented in earlier studies, where maximal efficiencies 85% or less were reported[30-32]. The efficiency is assumed to benefit from the high uniformity of pillar diameters and pillar heights, a very constant pillar distance (see **Table S** 7-1 in the Supplementary information for detailed values), a high aspect ratio of the pillar structures of almost 3, and a rather high refractive index n around 1.5 of the used photoresist (data are shown in **Figure S 7-1** in the Supplementary Information).

Pillars of the anti-reflective gratings with a distance of 280°nm did not appeared clearly separated but reminded closely the outer surface of the moth's eye, an often-pictured biological example of an anti-reflective surface[33,34]. In the case of the moth, the anti-reflective effect is caused by a delicate and closely packed pillar grating, which provokes a continuously increasing refractive index towards the animal's eye. As a result, light does not face strong differences in the refractive index, which leads to a significant reduction of Fresnel reflection[35-37]. Comparable to the natural blueprint, which is reported to have 200 nm high pillars separated by roughly 200 nm[38,39], the fabricated quasi-film featured periodic protuberances with a depth of 200 nm and a tip distance of 270 - 280 nm. The optical properties of the pillar materials were also found to be similar. With the comparably low extinction coefficient κ and the refractive index n of 1.5 at λ = 500 nm (data are shown in **Figure S 7-1** in the Supplementary Information) the photoresist was close to values reported for the natural chitin of the insect[40]. From that it can be concluded, that the anti-reflective properties of the artificial grating with the pillar distance of 280 nm is most likely evoked by the same effect ascribed to the natural grating - a refractive index gradient.

This assumption is supported by the obtained reflection and transmission spectra, which reveal a broadband reduction of the normal reflection and an almost unaffected transmission. The maximal anti-reflective effect on the coated glass substrate was determined to be at 450 nm with a reduction in reflectivity of 28%. The actual performance of the film, however, is expected to be twice as good than the measured value. This is based on the fact that the structures were fabricated on a thin transparent glass substrate. Therefore, the value recorded by micro-spectroscopy includes not only normal reflection at the structured surface, but also contributions from the backside of the substrate[21]. To estimate the efficiency of the film E_{film}, that is relevant when structures are applied on a thicker glass substrate or a

glass fibre, the reflection at the second interface has to be deducted This can be done by using the following equation:

$$E_{film} = \frac{R_{film}}{R_{glass}} = \frac{\left(\frac{I_{r,total} - I_i R_{glass}}{I_i - I_i R_{glass}}\right)}{R_{glass}} \quad (60)$$

where R_{film} is the actual reflectivity of the quasi-film covered glass surface, R_{glass} the calculated reflectivity of a flat glass/air interface using the Fresnel's equation (25) [41], I_i the incident intensity, and $I_{r,total}$ the detected reflected intensity. With that, a value of $E_{film} = 57\%$ is obtained for light with 500 nm wavelength. Although such an efficiency is not yet sufficient to compete with anti-reflective surfaces structured by other techniques[34,42,43], it is sufficient to provide a significant optical contrast when applied together with diffraction gratings on a surface for anti-counterfeiting applications. This result together with the reportedly good reproducibility of structures are good arguments to use TPL for security feature applications. It has to be pointed out, though, that the structuring via TPL is time intensive and therefore limited in its output. From this perspective it is rather plausibly to use the TPL manufactured surfaces as masters for further processing, such as for micro-imprint techniques[44-46].

In the future, the knowledge acquired here and the high flexibility of TPL to place different features close together could be combined to create highly sophisticated patterns of pillar gratings. The complexity and thus the security level of a TPL produced anti-counterfeiting label, could be increased even more by structuring on non-planar substrates.

7.6. Conclusions

Two optical gratings with pillar distances of 710 nm and 280 nm were fabricated on the same substrate by means of TPL. The grating with the larger pillar distance showed a high diffraction efficiency of up to 95%. The grating with the small pillar distance showed anti-reflective properties causing a decrease in reflectivity by up to 28%.

TPL can be used to fabricate highly efficient optical pillar diffraction gratings and anti-reflective films in close proximity. This makes the surface particularly interesting for an application as master in the fabrication of anti-counterfeiting labels.

(2) The high efficiency of the diffraction grating with 710 nm pillar distance is most probably caused by high uniformity of pillar diameters and pillar heights, a very constant pillar distance, a high aspect ratio of the pillar structures of almost 3, and a rather high refractive index n around 1.5 of the used photoresist.

(3) The fabricated 280 nm pillar grating is comparable to the grating found of the moth's eye. The anti-reflective effect most likely evokes from a refractive index gradient, which reduces the Fresnel reflection.

(4) Further investigations could focus on the increase in complexity by conceiving tailored patterns and on effects of non-flat substrates.

7.7. Acknowledgements

Foremost, I want to thank Silvia Vignolini from the University of Cambridge, UK, for the opportunity to perform the micro-spectroscopy measurements in her laboratory. Further thanks go to Lisa Becker and Bruno Schäfer, both INM, for their contribution to the microscopy imaging and the determination of optical material properties. Moreover, I acknowledge Andreas Verch, Elmar Kroner, and Peter Rogin for helpful discussions and proofreading.

7.8. References

1. Yan H, Huang L, Xu X, Chakravarty S, Tang N, Tian H, *et al.* Unique surface sensing property and enhanced sensitivity in microring resonator biosensors based on subwavelength grating waveguides. *Opt Express* 2016, **24**(26)**:** 29724-29733.
2. Grenier JR, Fernandes LA, Aitchison JS, Marques PVS, Herman PR. Femtosecond laser fabrication of phase-shifted Bragg grating waveguides in fused silica. *Opt Lett* 2012, **37**(12)**:** 2289-2291.
3. Wang Z, Xu X, Fan D, Wang Y, Subbaraman H, Chen RT. Geometrical tuning art for entirely subwavelength grating waveguide based integrated photonics circuits. *Scientific Reports* 2016, **6:** 24106.
4. Li C, Liao C, Wang J, Gan Z, Wang Y. Femtosecond Laser Microprinting of a Polymer Optical Fiber Interferometer for High-Sensitivity Temperature Measurement. *Polymers* 2018, **10**(11)**:** 1192.
5. Catchpole KR, Green MA. A conceptual model of light coupling by pillar diffraction gratings. *Journal of Applied Physics* 2007, **101**(6)**:** 063105.
6. West H, Garcia Y, Rechtman L, Blau M, Marom DM. Subwavelength Nano-Pyramids 3D Printed Directly on Optical Fiber Tip Serving as Anti-Reflection Coating. 2018 International Conference on Optical MEMS and Nanophotonics (OMN); 2018 29 July-2 Aug. 2018; 2018. p. 1-5.
7. Chong TK, Wilson J, Mokkapati S, Catchpole KR. Optimal wavelength scale diffraction gratings for light trapping in solar cells. *Journal of Optics* 2012, **14**(2)**:** 024012.
8. Kuang P, Eyderman S, Hsieh M-L, Post A, John S, Lin S-Y. Achieving an Accurate Surface Profile of a Photonic Crystal for Near-Unity Solar Absorption in a Super Thin-Film Architecture. *ACS Nano* 2016, **10**(6)**:** 6116-6124.
9. Mayer F, Richter S, Hübner P, Jabbour T, Wegener M. 3D Fluorescence-Based Security Features by 3D Laser Lithography. *Advanced Materials Technologies* 2017, **2**(11)**:** 1700212.
10. Bae HJ, Bae S, Park C, Han S, Kim J, Kim LN, *et al.* Biomimetic Microfingerprints for Anti-Counterfeiting Strategies. *Adv Mater* 2015, **27**(12)**:** 2083-2089.
11. Xuan R, Ge J. Photonic Printing through the Orientational Tuning of Photonic Structures and Its Application to Anticounterfeiting Labels. *Langmuir* 2011, **27**(9)**:** 5694-5699.

12. Nam H, Song K, Ha D, Kim T. Inkjet Printing Based Mono-layered Photonic Crystal Patterning for Anti-counterfeiting Structural Colors. *Scientific Reports* 2016, **6**(1)**:** 30885.
13. Deinega A, Valuev I, Potapkin B, Lozovik Y. Minimizing light reflection from dielectric textured surfaces. *J Opt Soc Am A* 2011, **28**(5)**:** 770-777.
14. Bernhard CG, Gemne G, Sällström J. Comparative ultrastructure of corneal surface topography in insects with aspects on phylogenesis and function. *Z Vergl Physiol* 1970, **67**(1)**:** 1-25.
15. Raguin DH, Morris GM. Antireflection structured surfaces for the infrared spectral region. *Appl Opt* 1993, **32**(7)**:** 1154-1167.
16. Song YM, Jang SJ, Yu JS, Lee YT. Bioinspired Parabola Subwavelength Structures for Improved Broadband Antireflection. *Small* 2010, **6**(9)**:** 984-987.
17. Lora Gonzalez F, Chan L, Berry A, Morse DE, Gordon MJ. Simple colloidal lithography method to fabricate large-area moth-eye antireflective structures on Si, Ge, and GaAs for IR applications. *J Vac Sci Technol B* 2014, **32**(5)**:** -.
18. Wang Y, Lu N, Xu H, Shi G, Xu M, Lin X, *et al.* Biomimetic corrugated silicon nanocone arrays for self-cleaning antireflection coatings. *Nano Res* 2010, **3**(7)**:** 520-527.
19. Lalanne P, Morris GM. Antireflection behavior of silicon subwavelength periodic structures for visible light. *Nanotechnology* 1997, **8**(2)**:** 53.
20. Purtov J, Verch A, Rogin P, Hensel R. Improved development procedure to enhance the stability of microstructures created by two-photon polymerization. *Microelectron Eng* 2018, **194:** 45-50.
21. Purtov J, Rogin P, Verch A, Johansen VE, Hensel R. Nanopillar Diffraction Gratings by Two-Photon Lithography. *Nanomaterials* 2019, **9**(10)**:** 1495.
22. Sun H-B, Maeda M, Takada K, Chon JWM, Gu M, Kawata S. Experimental investigation of single voxels for laser nanofabrication via two-photon photopolymerization. *Appl Phys Lett* 2003, **83**(5)**:** 819-821.
23. Fischer J, Wegener M. Three-dimensional optical laser lithography beyond the diffraction limit. *Laser & Photonics Reviews* 2013, **7**(1)**:** 22-44.
24. Kawata S, Sun H-B, Tanaka T, Takada K. Finer features for functional microdevices. *Nature* 2001, **412:** 697.
25. Mueller JB, Fischer J, Mayer F, Kadic M, Wegener M. Polymerization Kinetics in Three-Dimensional Direct Laser Writing. *Adv Mater* 2014, **26**(38)**:** 6566-6571.
26. Xing J-F, Dong X-Z, Chen W-Q, Duan X-M, Takeyasu N, Tanaka T, *et al.* Improving spatial resolution of two-photon microfabrication by using photoinitiator with high initiating efficiency. *Appl Phys Lett* 2007, **90**(13)**:** 131106.
27. Sun H-B, Takada K, S. Kim M, Lee K-S, Kawata S. *Scaling laws of voxels in two-photon photopolymerization nanofabrication*, vol. 83, 2003.
28. Tanaka TS, Hong-Bo; Kawata, Satoshi. Rapid sub-diffraction-limit laser micro/nanoprocessing in a threshold material system. *Appl Phys Lett* 2002, **80**(2)**:** 312-314.
29. Takada K, Kaneko K, Li Y-D, Kawata S, Chen Q-D, Sun H-B. Temperature effects on pinpoint photopolymerization and polymerized micronanostructures. *Appl Phys Lett* 2008, **92**(4)**:** 041902.
30. Guo H, Jiang H, Luo L, Wu C, Guo H, Wang X, *et al.* Two-photon polymerization of gratings by interference of a femtosecond laser pulse. *Chemical Physics Letters* 2003, **374**(3)**:** 381-384.
31. Zhang D, Men L, Chen Q. Femtosecond laser fabricated polymeric grating for spectral tuning. *Journal of Physics Communications* 2018, **2**(9)**:** 095016.
32. Kim DY, Tripathy SK, Li L, Kumar J. Laser-induced holographic surface relief gratings on nonlinear optical polymer films. *Appl Phys Lett* 1995, **66**(10)**:** 1166-1168.
33. Han ZW, Wang Z, Feng XM, Li B, Mu ZZ, Zhang JQ, *et al.* Antireflective surface inspired from biology: A review. *Biosurface and Biotribology* 2016, **2**(4)**:** 137-150.
34. Ko D-H, Tumbleston JR, Henderson KJ, Euliss LE, DeSimone JM, Lopez R, *et al.* Biomimetic microlens array with antireflective "moth-eye" surface. *Soft Matter* 2011, **7**(14)**:** 6404-6407.
35. Bernhard CG, Miller WH, Móller AR. Function of the Corneal Nipples in the Compound Eyes of Insects. *Acta Physiologica Scandinavica* 1963, **58**(4)**:** 381-382.
36. Wilson SJ, Hutley MC. The Optical Properties of 'Moth Eye' Antireflection Surfaces. *Opt Acta* 1982, **29**(7)**:** 993-1009.

37. Dewan R, Fischer S, Meyer-Rochow VB, Özdemir Y, Hamraz S, Knipp D. Studying nanostructured nipple arrays of moth eye facets helps to design better thin film solar cells. *Bioinspiration & biomimetics* 2011, **7**(1)**:** 016003.
38. Bernhard CG, Miller WH. A Corneal Nipple Pattern in Insect Compound Eyes. *Acta Physiologica Scandinavica* 1962, **56**(3-4)**:** 385-386.
39. Stavenga DG, Foletti S, Palasantzas G, Arikawa K. Light on the moth-eye corneal nipple array of butterflies. *Proceedings of the Royal Society B: Biological Sciences* 2006, **273**(1587)**:** 661-667.
40. Leertouwer HL, Wilts BD, Stavenga DG. Refractive index and dispersion of butterfly chitin and bird keratin measured by polarizing interference microscopy. *Opt Express* 2011, **19**(24)**:** 24061-24066.
41. Hecht E. *Optics*. Addison-Wesley, 2002.
42. Min W-L, Jiang B, Jiang P. Bioinspired Self-Cleaning Antireflection Coatings. *Adv Mater* 2008, **20**(20)**:** 3914-3918.
43. Ji S, Park J, Lim H. Improved antireflection properties of moth eye mimicking nanopillars on transparent glass: flat antireflection and color tuning. *Nanoscale* 2012, **4**(15)**:** 4603-4610.
44. Park SH, Yang DY, Lee KS. Two-photon stereolithography for realizing ultraprecise three-dimensional nano/microdevices. *Laser & Photonics Reviews* 2009, **3**(1-2)**:** 1-11.
45. Bae B-J, Hong S-H, Hong E-J, Lee H, Jung G-y. Fabrication of Moth-Eye Structure on Glass by Ultraviolet Imprinting Process with Polymer Template. *Japanese Journal of Applied Physics* 2009, **48**(1R)**:** 010207.
46. Arne S, Helmut S. Fabrication of 3D nanoimprint stamps with continuous reliefs using dose-modulated electron beam lithography and thermal reflow. *Journal of Micromechanics and Microengineering* 2010, **20**(9)**:** 095002.

7.9. Supplementary Information

Table S 7-1. Summary TPL-structure dimensions

s: spacing; d: diameter, h: structure height, h_f: height of the film, h_t: height of pillar top contributing to the nipple-like roughness.

Dimension	Mean (nm)	Deviation (nm)	Minimum (nm)	Median (nm)	Maximum (nm)
s_{710}	713	34	648	712	760
d_{710}	350	7	340	351	362
h_{710}	1012	34	955	1026	1052
s_{280}	270	26	212	276	306
d_{280}	344	23	317	333	390
h_{f280}	1113	49	1022	1130	1196
$h_{t\ 280}$	209	44	124	200	307

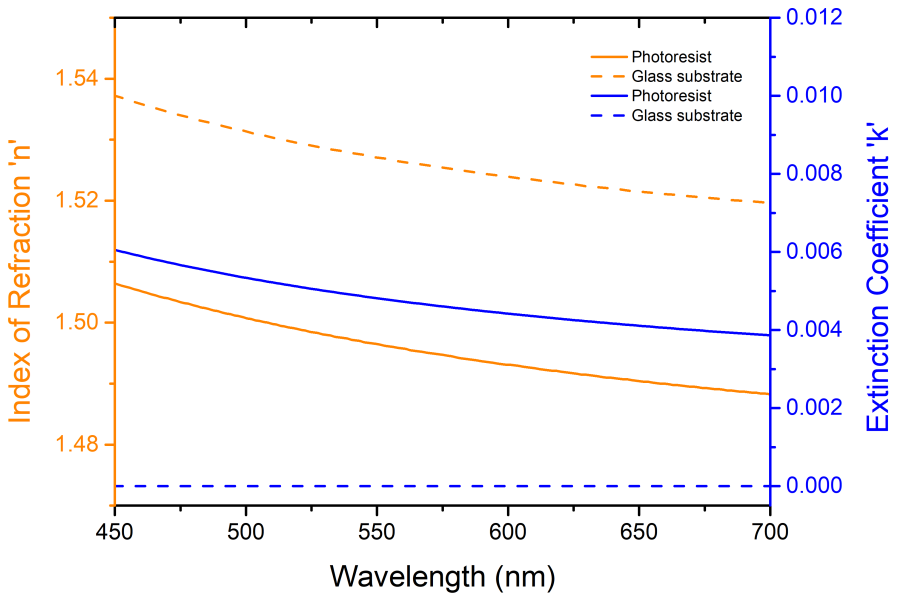

Figure S 7-1. Optical constants of the used phot resist (IP-L 780)

The real part, the index of refraction *n*, and the imaginary part, the extinction coefficient *κ*, of the complex refractive index are given.

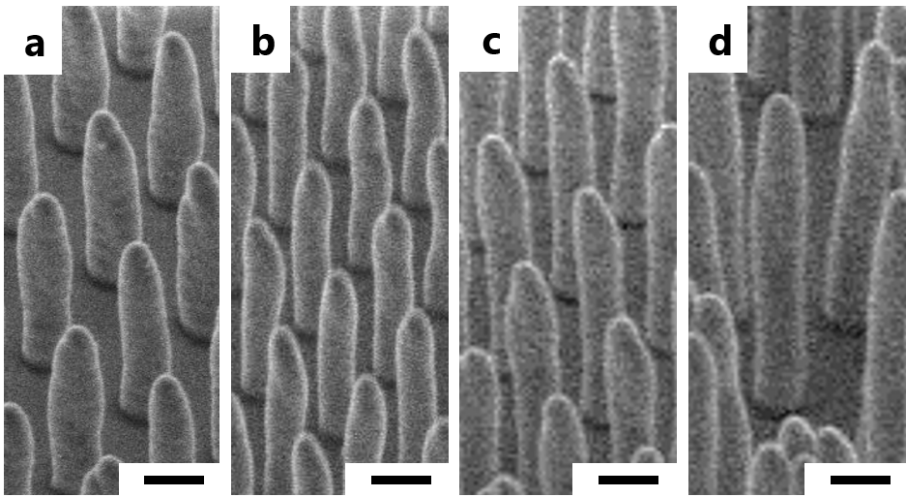

Figure S 7-2. Pillar gratings with variable heights

TPL-pillar gratings with (a) 2300 nm, (b) 2900 nm, (c) 3400 nm, and (d) 4350 nm heights, fabricated on one glass substrate. The scale bars are 500nm.

Chapter 8. 3D Photonic Structures by Standing Wave Enhanced Two-Photon Lithography

8.1. Abstract

Photonic crystals are used in a wide field of applications, for example in lasers, for structural colouration, or in telecommunication. So far only few methods facilitate the fabrication of truly 3D-photonic structures. A promising candidate is two-photon lithography. However, its writing resolution is not sufficient to allow vertical periodicities that interact with visible wavelengths. We report on a novel approach, where the vertical periodicity was decreased by a factor of 3.5 from 800 nm to 230 nm and the feature size by a factor of over 13 from 600 nm to 45 nm. This was achieved by introducing a standing wave pattern into the direct laser writing process by means of a reflective substrate. The approach was depicted in detail by simulations and validated by various experiments. To demonstrate the potential of the standing wave enhanced direct laser writing, multiple submicron and nanostructures are presented.

The content of this chapter was filed as a patent application:

Purtov J, Kroner E, Rogin P, Frensemeier M, Verfahren zur Herstellung von Mikrostrukturen, Anmeldenr. DE102016125690.0 vom 23.12.2016

8.2. Introduction

Photonic structures, in particular photonic crystals, have attracted considerable attention, as they allow an extraordinary control and modulation of light[1-4]. This is a technical demand for a broad range of applications, e.g. in optical communication[4,5] and laser technologies[6]. While two dimensional photonic crystals are already realised in conventional applications such as photonic fibres or light coupling elements[7,8], the reliable fabrication of three dimensional (3D) photonic crystals is still a challenge. Techniques, such as self-assembly of monodispersed particles or block copolymers are promising, but are deficient in a reliable and deterministic control of the structural features[9,10], e.g. the deliberate introduction of defects into a perfect periodicity[11].

A method with the potential to achieve such a deterministic control of structural elements is two-photon polymerisation (TPL), also referred to as direct laser writing (DLW)[12]. TPL describes a bottom-up technique enabling layer-by-layer fabrication of complex structures by moving the focus of a short pulse, high energy laser beam through a monomeric material. By focussing the laser, the intensity of photons increases locally leading to a two-photon reaction of the initiator and subsequent cross-linking of the monomers as soon as a certain intensity threshold is exceeded. The smallest possibly polymerised volume is typically represented by an upright standing ellipsoid called voxel. The size of such a voxel is strongly dependent on the writing conditions, such as the wavelengths of the laser, the numerical aperture of the TPL-system and the photoresist used. Considering the most frequently used conditions, that is, a laser beam in the infra-red with a wavelength of ca. 780 nm, a numerical aperture of 1.4, and a methacrylate based photoresist, a voxel of ca. 200 nm in horizontal (x,y) and 600 nm in vertical (z) direction can be formed.

To obtain smaller voxels, and thus smaller feature sizes, different approaches were proposed in the past. For example, the lateral feature size of periodically arranged structures was reduced down to 120 nm by using an improved development procedure of structures[13]. Furthermore, the application of STED-enhanced two-photon lithography was shown to lead to lines below 65 nm in width[14]. Although these approaches are suitable for structuring photonic crystals in 2D, there are of limited value for structuring crystals in 3D. This is due to the only negligible impact on the structure size in vertical direction.

Based on this motivation, we developed a new approach called standing wave enhanced two-photon lithography (SWE-TPL). SWE-TPL is characterised by the introduction of a standing wave into the common TPL-process to reduce drastically the vertical feature size. The main process parameters of this new approach were determined via simulations and validated experimentally by fabricating arrays of layered pillars. The potential of SWE-TPL is demonstrated by fabricating a selection of structures novel to TPL with this new approach for the first time opening more potential application fields.

8.3. Experimental

8.3.1. *Refractive Indices of Materials Used*

The refractive indices of the used materials used were determined using ellipsometry (Spectroscopic Ellipsometer M-2000 / A-SE (J.A. Woollam Co. Inc.). For that, data were collected from three different incident angles and then fitted using the Cauchy dispersion. A detailed description can be found in Chapter 4.4. The results relevant for this chapter are depicted in **Figure S 8-1**. The values obtained for 780 nm were taken to calculate the reflectivity at the interface between the IP-Dip photoresist and the different substrates according to the equation (25). These results are presented in the Materials and Methods section in **Table 4-2**. The reflectivities were further applied as input parameters to simulate the intensity patterns of structures presented in the validation experiments.

8.3.2. *Beam Divergence Characterization of the Two-Photon Lithography System*

In order to estimate the voxel modulation in vertical direction during SWE-TPL-structuring, the divergence angle of the used laser beam was determined. The procedure is described in detail in Chapter 4.7 and is summarized by **Figure S 8-2**. The divergence angle, θ_{div}, of the TPL-system was calculated to be θ_{div} = 31.4°.

8.3.3. *Simulation of the Field Distribution in the Writing Process*

The modelling was carried out using a program self-written in Free Pascal / Lazarus (described in greater detail in Chapter 4.8). The numerical program allows to superimpose the fields of an incident wave focused to a point at a given distance from a surface, and a reflected wave derived from the incident one by taking into account the position and the reflection properties of the surface. Calculating the field distribution of the incident wave is a non-trivial task, as the Gaussian formalism typically used to describe laser beams is based on a paraxial approximation, which is not appropriate for high divergence angles. Therefore, a more realistic numerical model was used to calculate a field map surrounding the focal region. Both, the incident and the reflected wave amplitudes, were then interpolated at the respective points in this field map.

The calculation of this field map was carried out assuming a continuous distribution of dipole emitters in a plane at some distance z_0 (arbitrarily chosen to be 200 λ) from the focal point. This emitter plane might represent e.g., the exit pupil of a focusing objective. The fields emitted from all dipoles in the emitter plane were then superimposed in the field map according to Huygens' principle.

The amplitude of the emitting dipoles was assumed to depend on the distance r from the axis of symmetry according to a Gaussian function $A(r) = \exp(-r^2/w^2)$, the width w of the latter being

chosen to match a desired angle α of divergence according to $\tan\alpha = w/z_0$. To limit the computational effort, but also to model a well-defined numerical aperture NA, this Gaussian function was truncated at distances exceeding a given limiting radius $r_{max} = z_0 \cdot \tan(\arcsin(NA))$. Focusing was achieved by an appropriate distribution of the phase $\theta(r) = -2\pi\sqrt{r^2 + z_0^2}/\lambda$. In order to ensure rotational symmetry, circular polarization was assumed in all calculations.

Field maps for given angles of divergence and numerical apertures were calculated with a typical resolution of $\lambda/50$ for an (r,z) receiver plane around the focal spot by means of a Monte Carlo type integration, i.e. by randomly selecting pixels in the receiver plane and coordinates in the emitter plane, and summing up all respective contributions for each receiving pixel.

In the next step a reflection plane is introduced close to the focal spot. The incident waves are reflected with a particular reflectivity R, undergo a phase shift φ, and superimpose with other incoming waves yielding a standing wave, and thus, a new electric field distribution. By changing the distance between the reflection plane and the focal spot, field maps for different focal positions with respect to the reflection plane can be calculated.

In order to predict the outcome of the SWE-TPL validation experiments, intensity field maps for the respective focal positions were combined. As additional parameters, the determined divergence of the TPL-system angle of 31.4°, a ~20 % reflectivity of the substrate, a refractive index of 1.50 of the liquid photoresist, and the laser wavelength of 780 nm were used. Please note, that the given intensities differ from the actual intensities by a constant factor and are therefore given in arbitrary units (a.u.).

8.3.4. *Two-Photon Polymerisation and Imaging*

SWE-TPL structures were fabricated from a negative Pentaerythritol triacrylate (PETA) photoresist (IP-Dip, Nanoscribe, Germany) by using the two-photon polymerisation system Professional GT, Nanoscribe, Germany, equipped with a femtosecond pulsed IR-laser (λ = 780 nm, maximum laser output power 140 mW, pulse width 100 fs and repetition rate 80 MHz) and a 63x objective (NA = 1.4, Zeiss, Germany). Note that all laser powers given in this section relate to the temporally averaged output. The TPL system was operated in the so-called “dip-in mode” where the objective is dipped directly into the resist. Upon writing, the structures were developed using a recently proposed development method to increase the structure resistance against capillary forces[13]. Validation structures were fabricated with the following parameters: i) variation of substrate reflectivity: 0.1 ms exposure time, 4 focal positions with 300 nm distance; on fused silica: 16 mW laser power, 600 nm structure to structure distance; on silicon: 20 mW laser power, 800 nm structure to structure distance; on fused silica sputter coated with gold: 16 mW laser power, 1000 nm structure to structure distance; ii) variation of laser power: 0.05 ms exposure time, 4 focal positions with 300 nm distance, 600 nm structure to structure distance. The laser

power was varied from 9 to 20 mW. iii) variation of focal distance: 0.05 ms exposure time, 19 mW laser power, 1000 nm structure to structure distance. The distance of the 4 focal positions was altered from 100 up to 700 nm. The settling time as well as the focal starting position were identical in all experiments with 1 ms and -200 nm, respectively.

Imaging was performed using a scanning electron microscope, FEI Quanta 250 FEG, equipped with an Everhart-Thornley-Detector (ETD) and Low Vacuum Secondary Electron Detector (LVSED) in high and low-vacuum mode. Samples were fixed on a metallic sample holder by clamps and observed at different tilt angles using a spot size of 2.0 and acceleration voltages < 5 kV. Optical micrographs were recorded on a Nikon Eclipse LV100ND optical microscope using a 20x colour-corrected objective lens (Nikon) with a numerical aperture of 0.45. The microscope was set to reflected bright field mode with a fully opened illumination aperture. The white balance was set before each measurement using a white sheet of paper as reference.

8.4. Results and Discussion

8.4.1. *Concept of Standing Wave Enhanced Two-Photon Lithography (SWE-TPL)*

To initiate the polymerisation in classical TPL, two photons have to interact simultaneously with one initiator molecule of the photoresist[15]. Such an event requires a very high photon density. This is typically achieved by using femtosecond near-infrared laser pulses with a peak power in the kilowatt range, and by tightly focussing this pulsed laser beam to form a small focal spot. The volume element, in which the photon density is high enough to trigger the polymerisation reaction, is called voxel and represents the smallest fabrication unit of a classical TPL system. Typically, such a voxel can be approximated by an ellipsoid elongated along the (vertical) beam axis having a height of at least 600 nm and a width of at least 200 nm[16] (**Figure 8-1a**).

Standing wave formation (**Figure 8-1d**) occurring on reflective substrates due to coherent interference of incident and reflected waves is usually avoided in lithography approaches, as it causes ridges in the sidewalls of structures and thus affects the quality of the fabricated surfaces. A thorough understanding of this effect, however, allows the vertical writing resolution of TPL to be significantly improved for periodic structures such as 3D-photonic crystals. In contrast to a system with a parallel illumination of monochromatic light, where the vertical intensity distribution contains strictly periodic anti-nodes with uniform intensities (**Figure 8-1b**), the anti-nodes in the focussed TPL-beam are assumed to vary in their intensities depending on their location with respect to the focal spot (**Figure 8-1c**). This has two consequences: first, the probability of a two-photon effect, and thus, a polymerisation event is increased in the anti-nodes close to the focal spot, and second, these anti-nodes are separated by nodes with intensity minima, preventing polymerisation in this region. By an adequately setting the TPL fabrication

parameters, including the beam parameters, the exposure time, the reflectivity of the substrate, and the optical and chemical properties of the photoresist, the intensity distribution could be modulated in such way that the polymerisation threshold of the photoresist was exceeded only in the anti-node of the focal plane. This improved the resolution and decreased the vertical feature size of periodical TPL-structures without using stimulated emission depletion (STED)[17] by simply applying a reflective substrate to the experimental TPL set-up (**Figure 8-1e**).

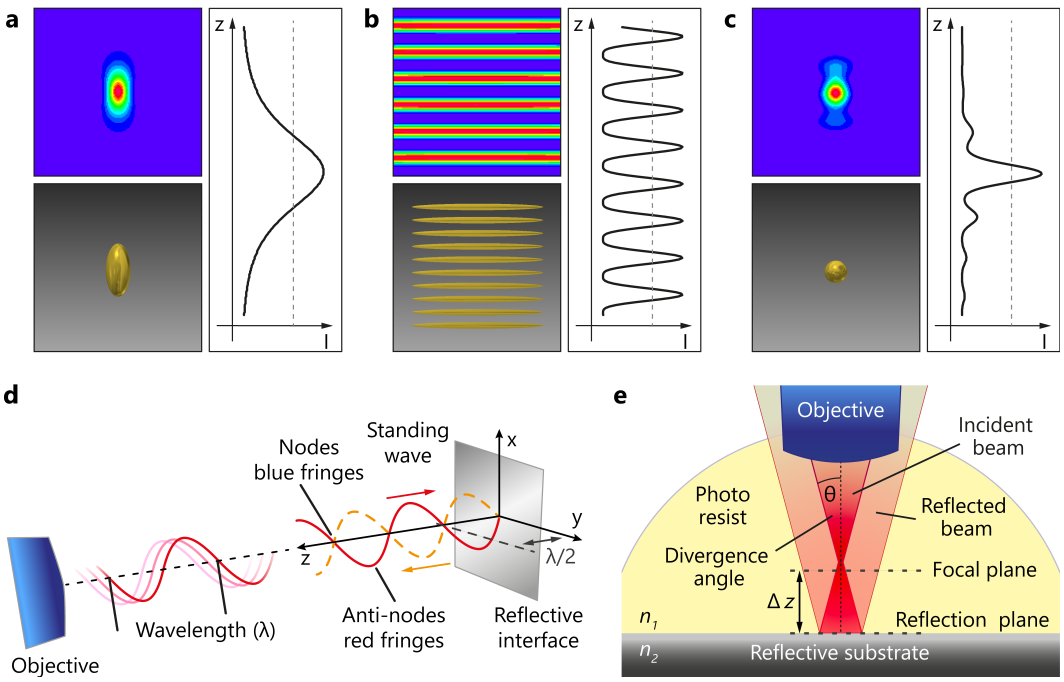

Figure 8-1. Principle of standing wave enhanced two-photon lithography (SWE-TPL)

Two-photon intensity distributions for: (a) a focused beam of a typical TPL system; (b) a parallel beam with an incorporated standing wave, and (c) a focused TPL beam with an incorporated standing wave as used in SWE-TPL. Each image includes a simulation of the expected photon distribution (upper left corner, highest intensities are indicated in red, the lowest in blue), its schematic vertical profile along the optical axis (right plot) with an arbitrary chosen reaction threshold (dashed line), and the anticipated polymerised structure (lower left corner). (d) Schematic of a standing wave pattern along the optical axis caused by a reflective substrate and (e), the experimental set-up for SWE-TPL.

8.4.2. *Simulations on the Influence of Different Experimental Parameters*

The modulation of the photon intensity in the focal plane depends on the reflectivity R of the surface, the divergence angle θ of the beam, and the vertical position of the focal plane F (indicated in **Figure 8-2e**). Numerical simulations of the electric field distribution were performed in order to understand the effects of these parameters in detail. Exemplary results are presented in **Figure 8-2a-c**, with the following parameter sets:

- 2a: Variation of *substrate reflectivity R* (F =2 λ and θ = 30°),
- 2b: Variation of *divergence angle* θ (F =0 and R = 100%), and
- 2c: Variation of *focal distance F* (θ = 30° and R = 100%).

Influence of substrate reflectivity – Simulating a non-reflective substrate resulted in a vertical electric field distribution with the previously described characteristics for standard TPL: a steady intensity distribution with one maximum (**Figure 8-2a**, first row). By increasing the reflectivity to 20 %, this distribution was modulated by a superimposed pattern with local minima and maxima (**Figure 8-2a**, second row). A further increase in the substrate reflectivity led to an enhancement of the highest peak intensity and an increase of the modulation depths between the maxima and minima (**Figure 8-2a**, third row). Thus, the introduction of a reflective surface in TPL enables the splitting of one broad intensity maximum into several smaller maxima, which are clearly separated from each other by substantial minima. It can be concluded that the reflectivity allows vertically stacking of polymerisation sites and determines the modulation depth between maxima und minima.

Influence of divergence angle – To understand the influence of the divergence angle θ on the intensity distribution of the previously described intensity profile, the reflectivity was set to 100% and the focus was chosen to be on the reflective surface whilst varying θ. The results are given in **Figure 8-2b**. In classic beam theory it is expected that a higher θ leads to a smaller depth of focus and a smaller focal area. This causes a higher intensity in the focal spot and a faster drop in intensity with increasing distance in vertical direction. For TPL this would result in a lower vertical size of the voxel. By introducing a reflective surface, this effect was superimposed with the standing wave effect described above. An increasing θ led to an increased intensity in the focal spot and, at the same time, to a faster decay of the intensity maxima with increasing distance from the focal point. For example, increasing the divergence angle from 20° to 40° led to a ~10-fold increase in maximum intensity (**Figure 8-2b** first and third row). At the same time, the intensity ratio between the intensity maximum closest to the focus spot and the next intensity peak was approximately 92% for θ = 20°, while it was only 68% for θ = 40°. If the intensity was adjusted in a way that it was equal in the focal spot for all divergence angles, the number of maxima exceeding a critical threshold value decreased with increasing divergence angle. Thus, small divergence angles led to polymerisation at several adjacent local intensity maxima, while large divergence angles were more suited to polymerise a low number of discs, or even single discs. It can be concluded that the divergence angle allows the number of spots to be controlled at which polymerisation occurs.

Influence of focal plane – The results of simulations varying the focal plane F revealed that the modulation depth also depended on the position of the focal plane with respect to the surface, which was assumed to be fully reflective in this set of simulations (**Figure 8-2c**). For the focal plane set to F = 0, that is, the focal plane coincides with the surface of the reflective surface, a full modulation of

the intensity was found. The envelope of the intensity maxima was four times as high as the intensity in the case without a reflective surface, while the intensity minima were all found to be zero. With increasing distance between focal plane and reflective surface, i.e., $F = 2\lambda$, the intensity at the focal point was significantly lower compared to the peak intensity of the $F = 0$ case. Moreover, the minima did not reach zero anymore and the modulation in intensity became less pronounced. Further increase in the distance to the reflecting surface led to a "smoothing" of the modulation, which may lead to a classical intensity profile if the distance to the reflective surface is large enough. It can be concluded that the distance between focal plane and reflective substrate must be small enough to evoke a suitable standing wave effect.

Other influences of optical parameters - The photon intensity distribution during the TPL process is, in addition to the parameters presented above, also depending on the wavelength λ and the refractive index n of the medium of propagation. Both aspects influence the generic results shown here as scaling factors and have to be considered for a full picture. However, these parameters are not expected to affect the general outcome of the simulation results.

Note that the simple threshold model used above is not fully adequate to describe resulting structures due to kinetic effects of the photoresist. Once initiated, the photo polymerisation requires time and extends over some distance. Furthermore, the dose required to immobilise the formed polymer has to be accumulated over several femtosecond pulses. During this time, diffusion of activated polymer chains is possible, which might lead to deviations between the geometric intensity profile and the resulting polymeric structure geometry. The influence of the intensity distribution in combination with polymerisation kinetics on the resulting structure geometries require a coupled opto-chemical simulation, which is currently not available. However, diffusion and extended polymerisation zones may form 'bridges' between features originating from different local intensity maxima or connect the structure to the substrate, which is otherwise difficult to achieve near the highly reflective surface.

If the reflectivity of substrate is so high that 'bridging' does not occur, it is possible to isolate a feature originating from one single intensity maximum as the smallest possible structural element. Apart from choosing the appropriate focal position, there are two key factors: the divergence angle of the beam and the laser power. As shown in the simulations above, a higher divergence angle will reduce both, the lateral extent of the discs and the number of discs possibly exceeding the polymerisation threshold at a given laser power. The latter is the second key parameter: only if the laser power is chosen such that the peak intensity slightly exceeds the threshold it will it be possible to produce single discs at the position of highest intensity.

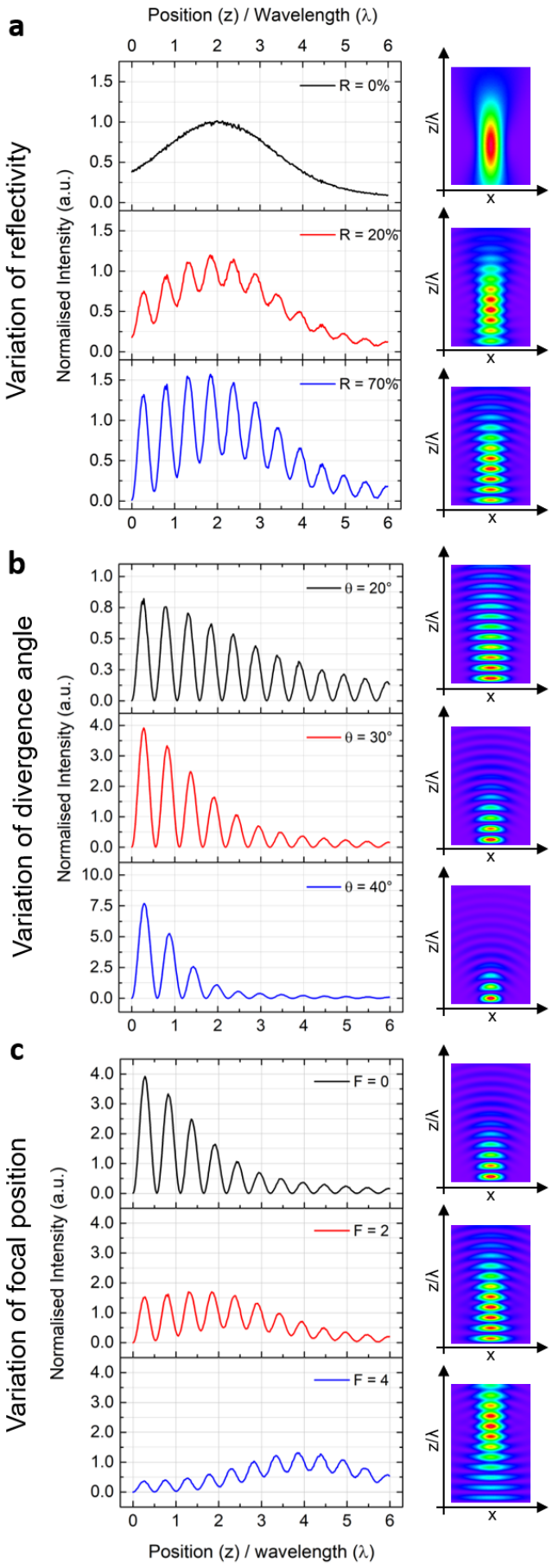

Figure 8-2. Simulation results for the variation of experimental parameters

(a) Variation of substrate reflectivity ($F = 2\lambda$, $\theta = 30°$); (b) variation of divergence angle ($F = 0$, $R = 1$); (c) variation of focal position ($R = 1$, $\theta = 30°$). The graphs on the left-hand side display the intensity distribution along the z-axis of the beam, whereas the corresponding colour-coded two-dimensional intensity maps are shown on the right (red = highest and violet = lowest intensity). The noise apparent in the graphs is a result from the Monte Carlo type approach used for the numerical integration. In a, curves are normalised to the maximum obtained with 0 % reflectivity. Curves shown in b and c as well as 2D-plots are normalised to their maximum, respectively.

8.4.3. *Validation via Structuring Experiments*

Based on the intensity maps shown in **Figure 8-2** and assuming that the photoresist only polymerises if a certain threshold intensity is exceeded, one would expect a voxel being divided into a stack of thin discs separated by roughly half a wavelength in the vertical direction. Above a certain laser energy these discs may be connected, due to radical diffusion as well as due to a less than full modulation. The width of the necks between the discs is then mainly depending on the modulation depth and thus on both the reflectivity and the distance from the interface. By sequentially superimposing these multi-disc voxels at several different focal distances from the interface, it should be possible to create high aspect ratio micropillars exhibiting a periodic variation of the diameter in the vertical direction.

To variety these considerations and to investigate the transferability of the previously discussed approach to real experiments, micropillars were fabricated out of 4 stacked voxels while varying: i) the reflectivity R of substrates: 0 %, 20 % and 70 %; ii) the applied laser power LP, 9-20 mW; and iii) and the distance between adjacent focal planes F: 0.1, 0.5, and 0.7 µm. The results as well as the corresponding simulations are presented in **Figure 8-3.** The complete experimental details can be found in the Materials and Methods section.

The comparison between simulation and SWE-TPL experiments reveals a very good agreement between the expected intensity distributions and the geometrical shapes of the fabricated structures. As expected from simulations, structures fabricated on non-reflective substrates exhibited the typical paraboloidal shape of subjacent stacked voxels (cp. **Figure 8-2a** and **Figure 8-3a,b,** 0%). Fabrication on a reflective substrate, however, yielded pillars showing distinct layers (**Figure 8-3a,b,** 20%,70%), which apparently correspond to the maxima seen in the intensity profiles in **Figure 8-3c**. If the polymerisation threshold of the photoresist is estimated from the best correlation between simulated and observed pillar heights at 0% substrate reflectivity (dashed lines in **Figure 8-3c**), the number of fabricated layers and the number of maxima exceeding this threshold matched also very well in the case of higher reflectivities. This correlation between layers and maxima held true for the validation experiments with varied laser power and focus distance. The simulations also predicted well the discussed 'bridging' between adjacent layers, when the minima were close to the polymerisation threshold, as well as its dependence on the reflectivity. The structure heights and the layer thickness, though, were slightly smaller than expected, probably due to shrinkage during the development process[13]. At R = 20 % experimental pillar structures had a maximum structure size of 1140 nm x 547 nm (pillar height x pillar diameter at the base), 5 layers with an ellipsoidal shape (mean values for all layer heights and diameters: 230 nm x 460 nm with a vertical pitch of 235 nm; measured at the laterally widest position of each layer) and broad bridges connecting adjacent layers (compare **Figure 8-3a-c**, 20%). At R = 70 % pillar structures revealed a structure size of 1120 nm x 620 nm, with 6 layers of flatter but wider ellipsoids (mean values for all layer heights and diameters: 185 nm x 504 nm with a vertical pitch of 225 nm), and narrower bridges

between the layers (compare **Figure 8-3a-c**, 70%). With increasing reflectivity, a higher modulation depth was expected from modulations (**Figure 8-3c**, first image). On the experimental level, such an increase in modulation depth would manifest itself in narrower necks between the layers as well as a flattening of the elliptical shape. Additionally, the diameters of the discs are expected to increase, as the intensity shows increased maxima due to the enhanced reflected fraction of the wave. Both, the increased diameter of layers and the stronger modulations expressed as narrower necks within the structures were found to be more pronounced on the R = 70 % reflective substrate than on the R = 20 % substrate.

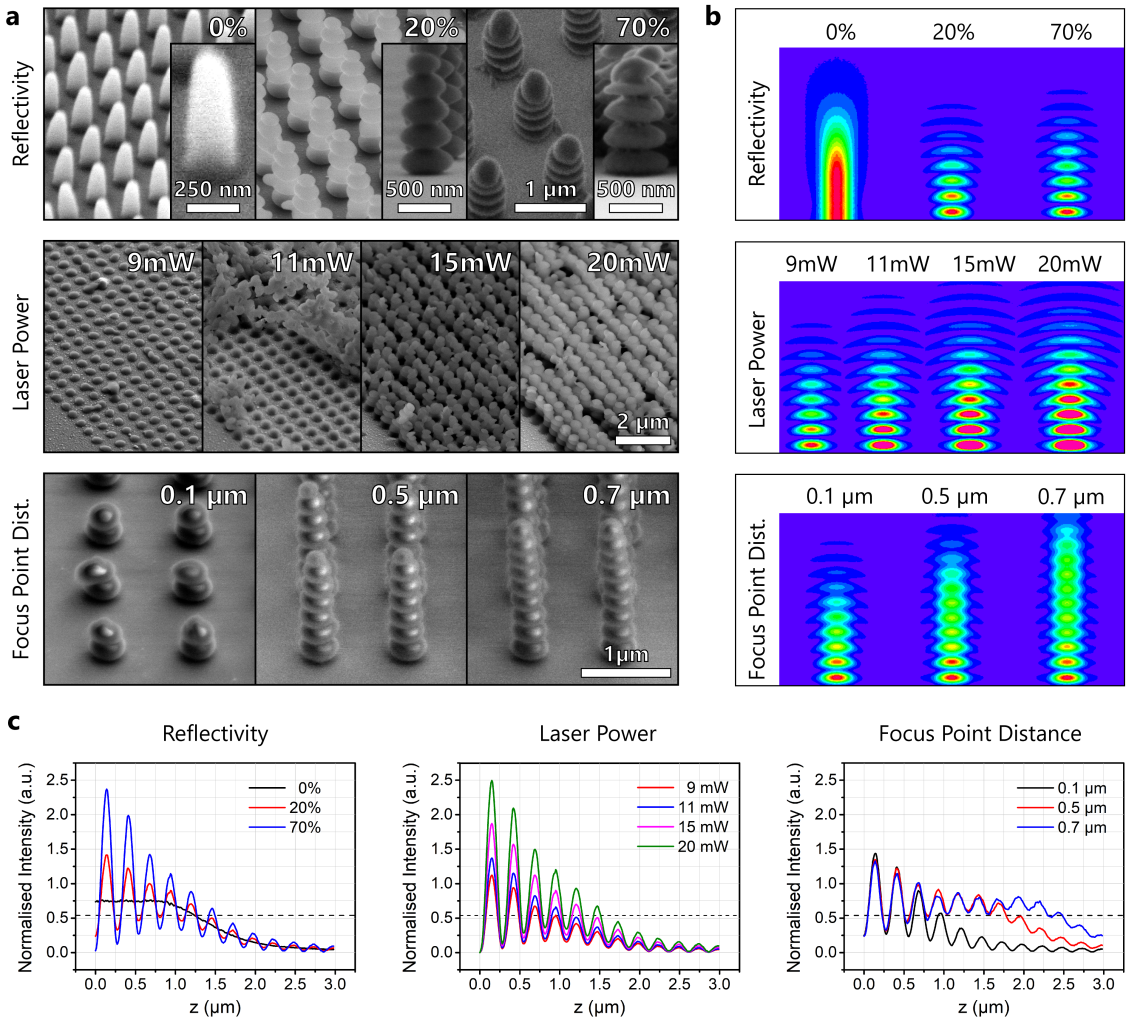

Figure 8-3. Correlation of simulations and TPL-fabricated pillar structures

(a) SEM images, (b) 2D-intensity maps, and (c) intensity profiles along the optical axis of structures fabricated with different substrate reflectivity, laser powers and distances between adjacent focus points (from the top to bottom row in (a) and (b), or from left to right in (c). The dashed lines indicate the assumed polymerisation threshold of the photoresist.

Simulations discussed above evinced that by using a highly reflective substrate together with low laser powers, the connection between adjacent layers should not form effectively. This prediction was confirmed by experiments varying the laser power, where laser powers of 9 mW, 11 mW, 15 mW, and 20 mW were used on a substrate with a reflectivity of R = 70% (cp. **Figure 8-2b** and **Figure 8-3a-c**, laser power). From simulations (**Figure 8-3c**, laser power), the fabricated structures were expected to feature, three, four, five, and six layers depending on the laser power. At 9 mW laser power, this expectation was not confirmed. Instead of three layers, the obtained structures revealed only one layer as well as randomly distributed material. This material is assumed to be the remnants of the upper layers, which were washed off due to a lack of connection between the discs. By increasing the laser power, and thereby the volume with beam intensities above the polymerisation threshold, discs of all layers are expected to extend mainly in lateral size. At 11 mW this primarily led to lateral connections between discs of adjacent pillars at the base and an enhanced accumulation of elliptically shaped photoresist material. At 15 mW, discs revealed a weak vertical connection resulting in structures already resembling the free-standing layered pillars described in the experiment performed with varying reflectivities (**Figure 8-2a**). A few of these pillars comprised of the five layers predicted by simulations. The majority, however, exhibited only four layers with the fifth's layer laterally attached in some cases. Pillars fabricated with 20 mW showed the best agreement to the simulations as they were least defective. At this laser power, far less unconnected discs were found. The structures were consistent to a great extent with the predicted number of 6 layers and showed noticeably the weak connection between the first and the second layer (counted from the substrate's surface) caused by a high modulation depth of the beam intensity profile. At this laser power, already, much less unconnected ellipses were found. For a better layer connectivity on a highly reflective substrate, therefore, the application of higher dwell times, photoresists with higher diffusion coefficient, or higher laser powers, as shown experimentally should be used to facilitate 'bridge' formation.

The results on structures created by changing the distance between different focal planes during exposure, and thereby the maximal focal distance, is in accordance with the previous experiments. The simulations reliably predicted the number of layers written as well as the decrease in modulation depth and amplitude ratio with increasing focal distance (cp. **Figure 8-2c** and **Figure 8-3a-c**, focus point dist.). The reduced modulation depth and amplitude ratio manifested themselves in less distinct 'bridges' and layers towards the structures' tips.

Further experiments, which will not be discussed in detail here, revealed that fine tuning of parameters can lead to a wide diversity of pillar structures differing in diameter, height, or tip shape. This can be achieved for example by altering the laser powers and exposure times (for examples see **Figure S 8-3** in the Supplementary Information). The probably most intriguing result of this study for photonics applications, though, is the excellent predictability of the experimentally obtained number of layers and

the occurrence of ‘bridging’ by simulations. This way, the appearance of photonic structures produced by SWE-TPL can be reliably predicted, which reduces the number of necessary experiments.

8.4.4. *Examples of Novel Structures Enabled by SWE-TPL*

By applying the presented SWE-TPL approach, several extraordinary micro- and nanometre structures were fabricated for the first time by using two-photon lithography. Examples are presented in **Figure 8-4**: a) bio-inspired structures, b) disordered photonic structures, c) highly porous films, and d) novel fence-like structures. The first structure represents ordered ridges mimicking the photonic crystals of a *Morpho*-butterfly[18,19]. Such photonic crystals have already been shown to have a great impact in the fields of photonics, sensing, enhanced Raman spectroscopy and others[20-23]. Pillars with distinct vertical layering but random distribution were chosen as an example for disordered photonic structures, which currently receive much attention in imaging, random lasing and solar energy[24]. Both, the ridges and the pillars, can be tuned in height, thickness, and arrangement and can even be freely combined on one single surface. This enables the design of a great variability of orientation and wavelengths specific optical surfaces, of which examples are shown in **Figure 8-4e** and **Figure 8-4f**. Furthermore, the application of SWE-TPL allows for the fabrication of films containing defined layers of pores (**Figure 8-4c**). Similar films were reported to act as effective sensors or to play an important role in energy applications[25,26].

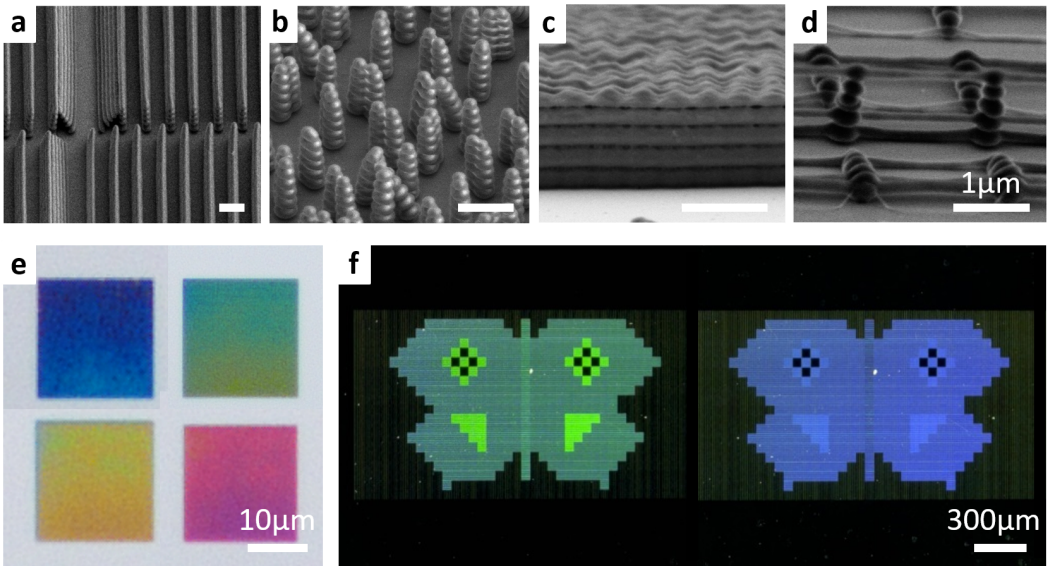

Figure 8-4. Examples of 3D-structures enabled by the means of SWE-TPL

(a-d) SEM images of (a) bio-inspired photonic crystal, (b) disordered photonic surface, (c) porous multi-films, and d, fence-like structures containing multiple polymer bridges spanned over 2 µm and a maximum thickness of 45 nm between two fixing stalks. (e,f) Micrographs illustrating the variability for the tuning possibilities of optical surfaces by for instance changing (e) the parameter setting during the SWE-TPL or (f) the shape design and observation angle of the fabricated structures. Scale bars: (a-d) 1 µm, (e) 10 µm, and (f) 300 µm.

The fence-like structures exhibiting a polymer-air layering, however, are the most delicate and most impressive structure fabricated by the novel SWE-TPL technique (**Figure 8-4d**). This structure was achieved by singling out only those maxima with the highest intensity, as discussed in the simulation section. In the presented example, several planes of free-hanging nanowires were spun between pillars separated by 2 µm. These nanowires exhibited thicknesses as small as 45 nm and were separated by air-gaps down to 200 nm (see also **Figure S 8-4**). Variations of fence-like structures have great applicational potential in 3D-printed wave guiding devices, resonance antennas or topographies used in lasing applications. To our knowledge, such structures are exceptional on this scale and have not been reported so far.

8.5. Conclusion

In this work we proposed a novel approach called standing wave enhanced two-photon lithography (SWE-TPL). SWE-TPL is characterised by the introduction of a standing wave into the common TPL-process by using a reflective substrate. This enables the modulation of the intensity distribution of the typically vertically elongated focal spot, and thus to new possibilities in the fabrication process. The following conclusions can be drawn from the presented experiments and the accompanying simulations:

(1) This approach allows to reduce drastically the feature size in vertical direction by a factor up to 13 without changing the main TPL-system parameters. In this case it was a reduction from 600 nm to 45 nm for a system working with 780 nm. This reduction, though, has potential to be further improved by using smaller laser wavelengths, higher numerical apertures, or an adapted photoresist.

(2) The application of SWE-TPL enables the fabrication of structures, not yet feasible on that scale. One example are fence-like structures with free-hanging nanowires exhibiting a thickness of 45 nm and a length of 2µm. These fence-like were enabled by an improvement in achievable vertical periodicity by a factor of 3.5 from 800 nm to 230 nm.

(3) TPL can be used to fabricate structures, whose vertical layering induces photonic bandgaps in the visible range.

(4) Structures usually challenging to produce due to several complex manufacturing procedures, can be fabricated by SWE-TPL requiring only one fabrication step. This includes layered *Morpho*-butterfly-like structures, disordered materials, layered porous films and surfaces exhibiting diverse photonic structures at the same time.

(5) The tight correlation between simulations and fabricated structures allows for a faster determination of suitable TPL-process parameters for a particular optical structure.

8.6. Acknowledgements

Foremost I want to acknowledge Peter Rogin for developing the simulation program I could use to investigate the intensity profiles during SWE-TPL procedure. I also thank Andreas Verch, Elmar Kroner and Peter Rogin for helpful discussions and proofreading. Furthermore, I want to acknowledge Reza Hosseinabadi for his support with the TPL fabrication and the optical imaging as well as Bruno Schäfer for his help in measuring the refractive indices of the materials and substrates used.

8.7. References

1. Parker AR, Townley HE. Biomimetics of photonic nanostructures. *Nat Nano* 2007, **2**(6)**:** 347-353.
2. Biró LP, Vigneron JP. Photonic nanoarchitectures in butterflies and beetles: valuable sources for bioinspiration. *Laser & Photonics Reviews* 2011, **5**(1)**:** 27-51.
3. Kim S, Mitropoulos AN, Spitzberg JD, Tao H, Kaplan DL, Omenetto FG. Silk inverse opals. *Nat Photon* 2012, **6**(12)**:** 818-823.
4. Joannopoulos JD, Villeneuve PR, Fan S. Photonic crystals: putting a new twist on light. *Nature* 1997, **386**(6621)**:** 143-149.
5. Deubel M, von Freymann G, Wegener M, Pereira S, Busch K, Soukoulis CM. Direct laser writing of three-dimensional photonic-crystal templates for telecommunications. *Nat Mater* 2004, **3**(7)**:** 444-447.
6. Noda S, Chutinan A, Imada M. Trapping and emission of photons by a single defect in a photonic bandgap structure. *Nature* 2000, **407**(6804)**:** 608-610.
7. Knight JC. Photonic crystal fibres. *Nature* 2003, **424**(6950)**:** 847-851.
8. Akahane Y, Asano T, Song B-S, Noda S. High-Q photonic nanocavity in a two-dimensional photonic crystal. *Nature* 2003, **425**(6961)**:** 944-947.
9. Vogel N, Retsch M, Fustin C-A, del Campo A, Jonas U. Advances in Colloidal Assembly: The Design of Structure and Hierarchy in Two and Three Dimensions. *Chemical Reviews* 2015, **115**(13)**:** 6265-6311.
10. Stefik M, Guldin S, Vignolini S, Wiesner U, Steiner U. Block copolymer self-assembly for nanophotonics. *Chemical Society Reviews* 2015, **44**(15)**:** 5076-5091.
11. Deubel M, Wegener M, Linden S, von Freymann G, John S. 3D-2D-3D photonic crystal heterostructures fabricated by direct laser writing. *Opt Lett* 2006, **31**(6)**:** 805-807.
12. von Freymann G, Ledermann A, Thiel M, Staude I, Essig S, Busch K, *et al.* Three-Dimensional Nanostructures for Photonics. *Adv Funct Mater* 2010, **20**(7)**:** 1038-1052.
13. Purtov J, Verch A, Rogin P, Hensel R. Improved development procedure to enhance the stability of microstructures created by two-photon polymerization. *Microelectron Eng* 2018, **194:** 45-50.
14. Fischer J, von Freymann G, Wegener M. The Materials Challenge in Diffraction-Unlimited Direct-Laser-Writing Optical Lithography. *Adv Mater* 2010, **22**(32)**:** 3578-3582.
15. LaFratta CN, Fourkas JT, Baldacchini T, Farrer RA. Multiphoton Fabrication. *Angewandte Chemie International Edition* 2007, **46**(33)**:** 6238-6258.
16. Fischer J, Wegener M. Three-dimensional optical laser lithography beyond the diffraction limit. *Laser & Photonics Reviews* 2013, **7**(1)**:** 22-44.
17. Li L, Gattass RR, Gershgoren E, Hwang H, Fourkas JT. Achieving λ/20 Resolution by One-Color Initiation and Deactivation of Polymerization. *Science* 2009, **324**(5929)**:** 910-913.
18. Ghiradella H. Light and color on the wing: structural colors in butterflies and moths. *Appl Opt* 1991, **30**(24)**:** 3492-3500.
19. Berthier S, Charron E, Boulenguez J. Morphological structure and optical properties of the wings of Morphidae. *Insect Science* 2006, **13**(2)**:** 145-158.

20. Potyrailo RA, Bonam RK, Hartley JG, Starkey TA, Vukusic P, Vasudev M, *et al.* Towards outperforming conventional sensor arrays with fabricated individual photonic vapour sensors inspired by Morpho butterflies. *Nat Commun* 2015, **6**.
21. Zhang W, Gu J, Liu Q, Su H, Fan T, Zhang D. Butterfly effects: novel functional materials inspired from the wings scales. *Physical Chemistry Chemical Physics* 2014, **16(**37**):** 19767-19780.
22. Zhang F, Shen Q, Shi X, Li S, Wang W, Luo Z, *et al.* Infrared Detection Based on Localized Modification of Morpho Butterfly Wings. *Adv Mater* 2015, **27**(6)**:** 1077-1082.
23. Potyrailo RA, Ghiradella H, Vertiatchikh A, Dovidenko K, Cournoyer JR, Olson E. Morpho butterfly wing scales demonstrate highly selective vapour response. *Nat Photon* 2007, **1**(2)**:** 123-128.
24. Wiersma DS. Disordered photonics. *Nat Photon* 2013, **7**(3)**:** 188-196.
25. Wang Y, Wang X, Yi G, Xu Y, Zhou L, Wei Y. Synthesis of layered hierarchical porous SnO2 for enhancing gas sensing performance. *J Porous Mater* 2016, **23**(6)**:** 1459-1466.
26. Hur K, Hennig RG, Wiesner U. Exploring Periodic Bicontinuous Cubic Network Structures with Complete Phononic Bandgaps. *The Journal of Physical Chemistry C* 2017, **121**(40)**:** 22347-22352.

8.8. Supplementary Information

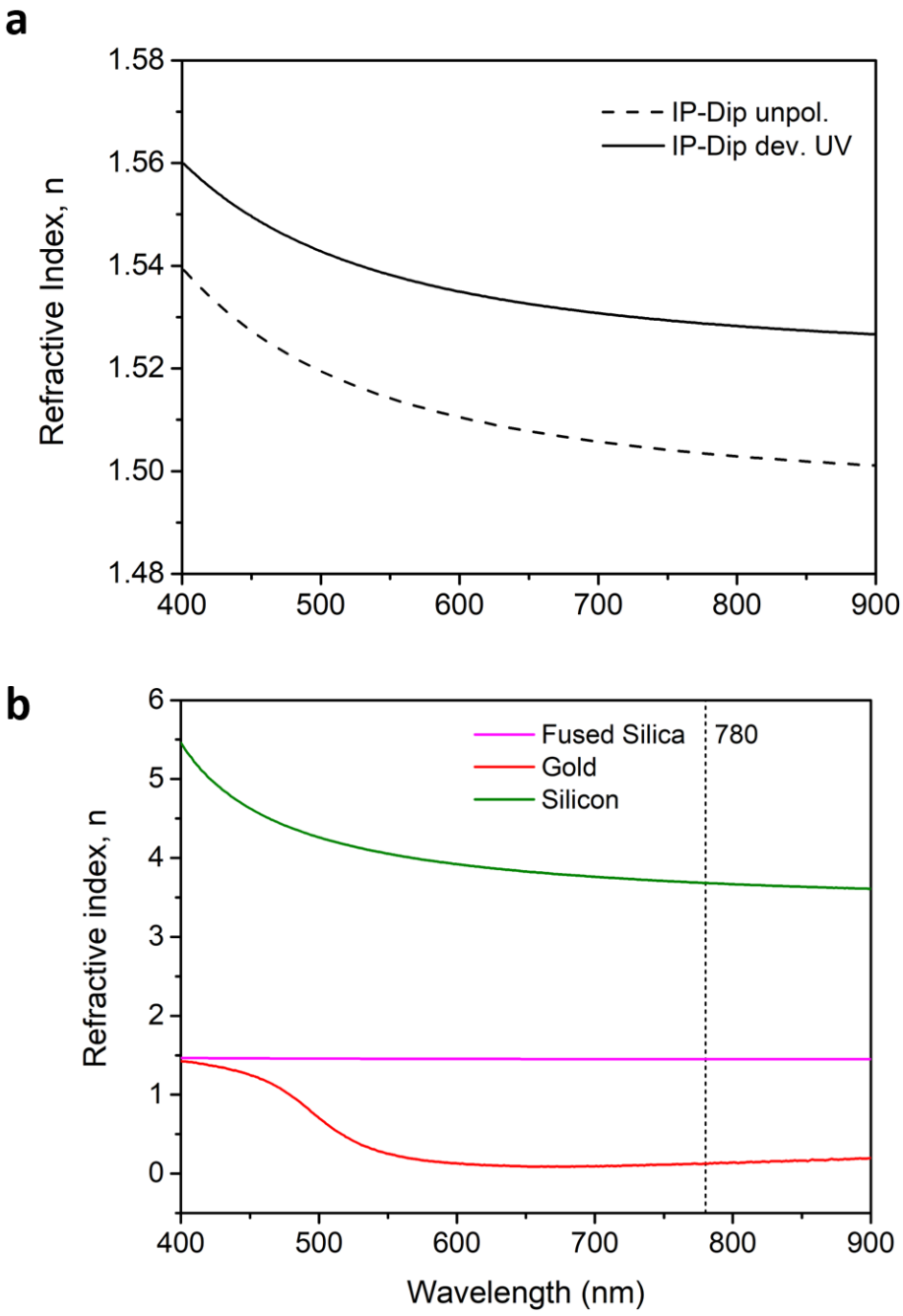

Figure S 8-1. Optical constants of the photoresist and substrate materials used

Ellipsometry results obtained (a) the photoresist (b) on the substrate materials used. The dashed and continuous lines in (a) correspond to refractive indices measured on liquid (liq.) and developed (dev.) IP-DIP photoresist, respectively. The former was used for the simulation of expected SWE-TPL structure sizes, the latter represent final values of the fabricated structures.

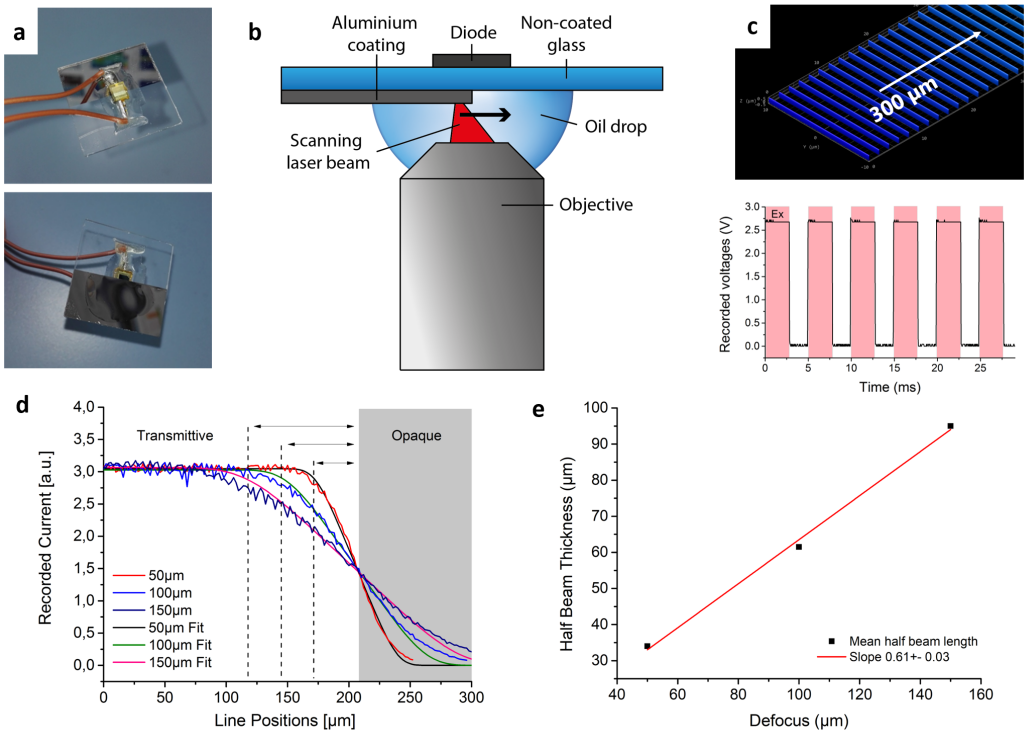

Figure S 8-2. Divergence angle characterization of the laser beam used in the TPL-system

(a) Bottom and top view of the dummy-substrate modified by a diode directly on the edge of an aluminium-coating, so that half of the diode was placed on a transparent and the other half on an opaque substrate. (b) Experimental TPL-set-up; (c) applied line pattern and an example of a recorded voltage signal. (d) Curves and their fittings of maximum voltages obtained at dree different focal planes. The half beam thickness is indicated with arrows for each focal plane, respectively. (e) Obtained half beam thickness plotted against the focal plane, the slope was obtained by a linear fit of the data points (red line).

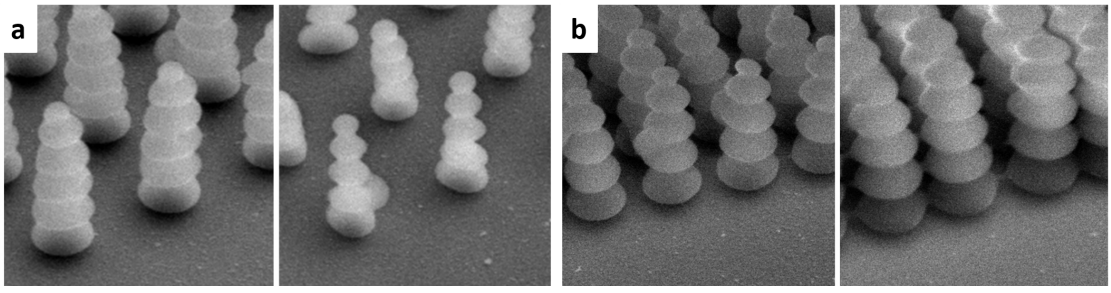

Figure S 8-3. Examples for further pillar structures fabricated via SWE-TPL

(a) Different pillar thicknesses achieved by power variation. (b) Different tip-shapes achieved by dwell time variation

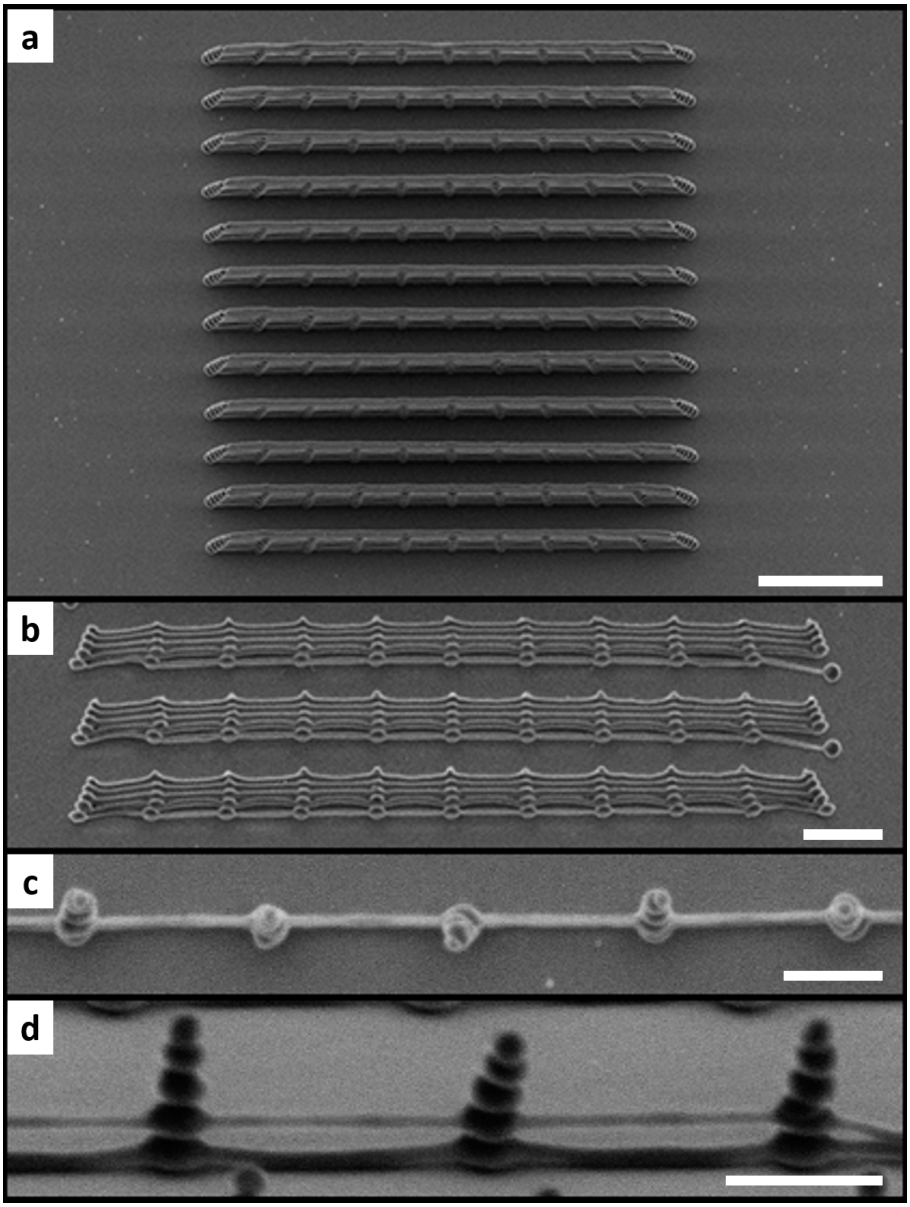

Figure S 8-4. Further SEM-images of fence-like structures

(a)Top view and side view of ‘fences’ placed with an periodic distance (b) Top view and (d) side view of ‘fence’ structures containing a fiber of a diameter of 45nm and a length of 2µm realized by singling out one intensity maximum Scale bars: (a) 5 µm, (b) 2µm and (c,d) 1 µm.

Chapter 9. Ordered and Disordered Butterfly-Inspired Photonic Structures Fabricated by Standing Wave Enhanced Two-Photon Lithography

9.1. Abstract

The wings of the Morpho butterfly appear in an iridescent blue, which is uniquely independent of the observation angle. This colouration relies mainly on the complex surface topography, which consists of periodically layered ridges of chitin and air. These structures cause multi-film interference, while an overall disorder of the periodical ridges minimizes Bragg-interference. Mimicking the air-material layering as well as introducing disorder of structures is very challenging for current fabrication techniques. Standing wave enhanced two-photon lithography (SWE-TPL), a two-photon lithography process with integrated standing wave patterning, was utilised to mimic the three-dimensional layered structure of the butterfly wings' topography and to study the effects of order and disorder on their optical properties. Disorder was deliberately introduced by locally varying the layer numbers and orientation of structure segments. The SWE-TPL structures obtained were imaged by scanning electron microscopy and analysed regarding their colouration and angle stability in perpendicular and parallel viewing direction with respect to their structure orientation using spectroscopy, microscopy, and conoscopy. The samples had similar 3D structures and optical properties as found for in the *Morpho*-butterfly wings. Besides applications in optical data management, sensors and for decorative features such SWE-TPL-structures could also lead to new security features, as presented in this publication.

9.2. Introduction

Devices capable of guiding and manipulating light are especially sought after in the fields of data management[1], sensors[2], wave control devices[3], and laser development[4]. Multi-dimensional periodic nanostructures, also known as photonic crystals (PC), are of great interest for such applications, as they allow an efficient manipulation of light. One of the most stunning examples of a natural photonic crystal is the blue surface of the *Morpho*-butterfly with its unique iridescent and angle independent structural colouration[5]. The blue colouration derives from the interaction of the incident light with freestanding periodical chitin layers connected by thin stalks[6] (**Figure 9-1**), while the angle-constancy originates mainly from different modes of disorder, such as vertical and lateral displacement, or tilting of the layer arrangements[7]. Wide application potential has been reported for such structures[8], such as building blocks for photonic integrated circuits[9], optical gas sensors[2,10] photonic band gap structures[11], stimuli-responsive photonic crystals[12], IR-detection systems[13], and as hotspots in surface-enhanced Raman spectroscopy[14].

Although the physical principle of the butterfly colouration is well understood[15,7,16-18], the direct mimicking of the topography remains still a challenge. This is mainly due to the difficulties to create freestanding structures with nanometre sized layering of air and material and to introduce disorder at the same time. Among others, multi-layer depositions with subsequent etching[19-21], focused ion beam patterning[22], common two-photon lithography[23], laser interference lithography on reflective substrates [24], and hot embossing of shape memory polymers[25] were reported. The most promising results were achieved by continuous multilayer systems applied on pre-structured substrates varying in surface heights paired with an underlying absorption layer, often referred to as disordered surfaces[26-29]. Indeed, simulations showed that the introduction of disorder could improve the angular independency of colouration inspired by butterflys[20,24,29,30]. The main disadvantage of such multi-layer films is the absence of a true 3D structure with air layers. Such 3D structures are necessary for applications such as vapour sensing, stimuli responsive photonic crystals[10,12,31], enhanced Raman scattering[14], or the double moulding for imprint technologies[32].

In the last decades micro fabrication by two-photon lithography (TPL) was developed and advanced as a universal tool for complex 3D structuring[33-36]. However, the resolution of this technique is limited to approximately 600 nm in the vertical direction. As it has been shown in Chapter 8, this resolution can be improved by using standing wave enhanced two-photon lithography (SWE-TPL). In that chapter it was also shown that this novel approach enables the fabrication of layered freestanding structures mimicking those found on iridescent *Morpho*-butterfly wings. The improved vertical resolution and the possibility to fabricate structures of well-defined geometries as well as the deliberate introduction of defects makes SWE-TPL a very suitable technique for the fabrication of 3D-photonic crystals.

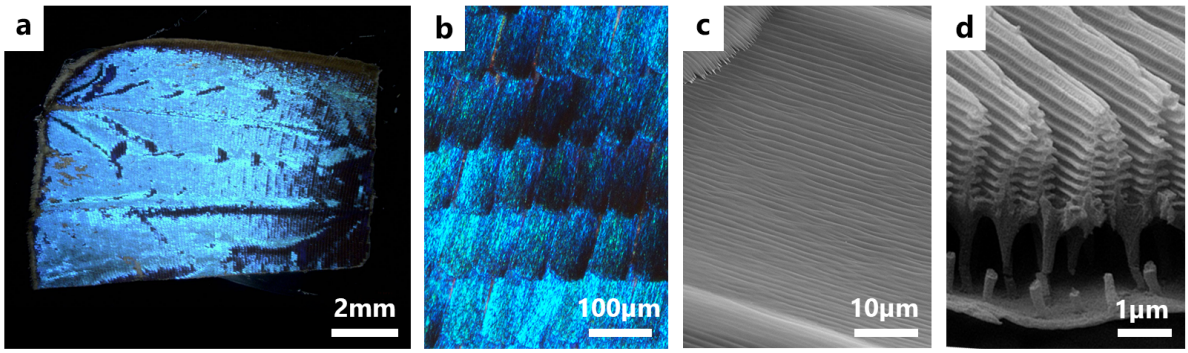

Figure 9-1. Photonic crystals of a *Morpho rethenor* butterfly

The butterfly wing recorded with (a,b) optical microscopy and (c,d) scanning electron microscopy at different magnifications: The surface of (a) a butterfly wing, is covered by (b) iridescent scales (c) possessing periodical ridges on their surfaces. (d) In cross-section each ridge reveals a complex 3D-structure exhibiting periodic, freestanding layers of chitin connected by a thin stalk.

In this study, SWE-TPL was utilised to fabricate two butterfly-inspired surfaces: a) a sample with highly ordered structures exhibiting periodically layered ridges and b) a sample with deliberately disordered structures, where layered ridges were varied in height and orientation. The topographies obtained were characterised by scanning electron microscopy, while the optical properties were investigated using light microscopy, angle resolved microscopy, angle resolved spectroscopy and conoscopy. The results were compared to the properties of original butterfly wings.

9.3. Experimental

9.3.1. *Standing Wave Enhanced Two-Photon Patterning and Simulations*

The structures were fabricated on a silicon substrate (Silicon Materials) from a polyacrylated photoresist (IP-DIP, Nanoscribe) by using a commercially available TPL-system (Nanoscribe). The laser was operated at laser powers of 15 mW (ordered sample) and 11 mW (disordered sample), respectively. The laser beam was moved over the sample with a scan velocity of 7000 µm/s. After exposure, the photoresist was developed according to the above proposed, revised development procedure, which leads to an increased mechanical stability of sub-micrometre TPL-structures[37]. Structure geometries were designed using the programming language provided by the utilised, commercially available TPL-system (DeScribe, Nanoscribe). Vertical intensity distribution simulations were conducted using a self-written programme described in detail elsewhere[38] (see also Chapter 4.8 and Chapter 8.3.3). For the simulations, a substrate reflectivity of 0.164, a laser wavelength of 780 nm, a beam divergence angle of 31.4°, and a refractive index of 1.50 (from ellipsometry data shown in **Figure S 9-1** and Chapter 4.4)) were used as parameters. The structures of the ordered samples were built by stacking 5 lines in vertical

direction separated by 300 nm in focus distance. The pitch between lines was set to 1000 and 500 nm in the experiments with ordered and disordered structures, respectively. To obtain disordered samples, the lines were randomly divided into multiple segments with lengths between 1 and 2 µm. In addition, the segments were rotated in plane by a maximum of 18° with respect to the overall writing direction of the lines. The number of vertical layers in one segment was randomly set to 4, 5, or 6 layers. The pattern of the disordered sample was implemented using a Matlab-script (MathWorks). As the structuring area is restricted by the field of view of the used objective (63x, Zeiss, Germany), areas were stitched using the stage movement of the TPL-system.

9.3.2. *Scanning Electron Microscopy*

The resulting SWE-TPL 3D-structures were examined using a scanning electron microscope (SEM) (Quanta 250 FEG, FEI) equipped with an Everhart-Thornley-detector (ETD) in high vacuum. Samples were cut and fixed with clamps on a metallic sample holder. In order to minimise charging effects, a copper tape was placed close to the samples. Different perspectives of structures were obtained by tilting and rotating the microscope stage. Images for size-analysis were recorded perpendicular to the structures using a 90°-holder. The spot size and the accelerating voltage were set to 2.0 and 2 kV, respectively. No coating was applied to retain the functionality of the samples after SEM examination.

9.3.3. *Optical and Angular Resolved Microscopy*

Optical microscopy and angular resolved microscopy were performed by using an Eclipse LV100ND microscope with a 5x air objective (NA = 0.15, Nikon) and a digital optical microscope VHX-5000 (Keyence) equipped with a tiltable objective holder and two different telecentric zoom objectives, VH-Z20W and VHZ100UW (Keyence). The optical microscopes were operated with a fully opened aperture using a white sheet of paper for white balance correction. Angular resolved images and videos were recorded under retroreflection conditions. That is, the light source and the detector had the same orientation. In the case of the VH-Z20W objective, the illumination was through the objective (bright field situation), whereas in the case of the VHZ100UW objective the light came from circularly arranged diodes around the objective lens resulting in an incidence angle of approximately 35° (dark field situation). Angular recordings were conducted at observation angles ranging from 0° to 60° in 10° steps. Videos were recorded while manually tilting the objective from 0° to 80° position.

9.3.4. *Angular Resolved Spectroscopy*

Angular resolved spectroscopy was performed by using a self-built device to detect retroreflection. This device consisted of a goniometer, a light source (DH-mini UV-Vis-NIR deuterium-Halogen light source, Ocean Optics), and a spectrometer with a detector range of 200 – 1000 nm (USB 4000 Ocean Optics) equipped with a 400 µm reflection probe fibre. The samples were attached to the sample holder using

double sided tape. The reflection spectra were determined for observation angles from 0° (normal to the sample surface) up to 55° in two different beam directions with respect to the orientation of the lines, perpendicular, θper, and parallel, θpar. The recorded spectra were used to create 2D plots showing the reflection intensity depending on the observation angle and wavelength. Each figure was created using 12 recorded spectra (5° tilting steps). Intermediate angles were interpolated. The prominent signals around 655 nm were omitted, as they arise from the deuterium light source used (the lamp spectrum is shown in **Figure S 9-2** in the Supplementary Information)

9.3.5. *Conoscopy*

Spatial scattering was analysed using the so-called conoscopic configuration (Scope.A1 with HAL 100, Zeiss). By inserting a Bertrand lens into the light path, the spatial distribution of a scattered or diffracted beam can be directly observed and recorded[39]. In the experiments, a 50x-objective with a numerical aperture of 0.95 (Zeiss, Germany) and a supercontinuum laser (SuperK EXTREME, EXU-6, 600 mW, Gaussian distribution, single mode, 78 MHz, NKT Photonics) operated at 475 nm was used. The beam diameter was 3.5 µm. Radial intensity profiles of images recorded with the same exposure time were determined using a circle with the radius of 1000 pixels (ImageJ software, radial profile angle plugin). In case of the disordered structures, the image was corrected by excluding an artefact, most likely caused by a reflection within the experimental set-up. The first 200 values of each profile were excluded, as they contained high intensity zero-order reflection not relevant for the scattering analysis. To obtain the radial intensity profile, all intensities at a certain radius $Rn + \Delta R$ from the centre were summed up and divided by the considered area. In the case of a pixelwise radius increase, this area was approximated by the circumference of the circle with the radius R_n.Typically, a reference sample with a known periodicity was used to calibrate the scattering angles on x-axis of the radial intensity plots. In the present case, the ordered SWE-TPL sample was used with a known distance between lines of d = 0.97 µm (experimentally determined by SEM, see results part). For a laser wavelength of λ = 475 nm, the corresponding scattering angle θ was calculated as 29.3° according to the grating equation $\lambda = d\,sin(\theta)$.

9.4. Results

9.4.1. *SEM Analysis of SWE-TPL-Butterfly-Inspired Structures*

For ordered and disordered butterfly-inspired topographies, the applied exposure patterns and the expected vertical intensity distributions during the SWE-TPL structuring are shown in **Figure 9-2**. The ordered sample featured periodically arranged lines with a 1000 nm pitch distance and equal heights of 1500 nm (**Figure 9-2a**). On the disordered sample, the lines were divided into segments with random heights, lengths, and rotations (with respect to the general line orientation). The pitch distance was set

to 500 nm (**Figure 9-2b**). According to the simulations structure heights of 1.31, 1.57, and 1.84 µm for 4, 5, or 6 layers, respectively, were expected. The distance between the layers was predicted to be approximately 270 nm (**Figure 9-2c**).

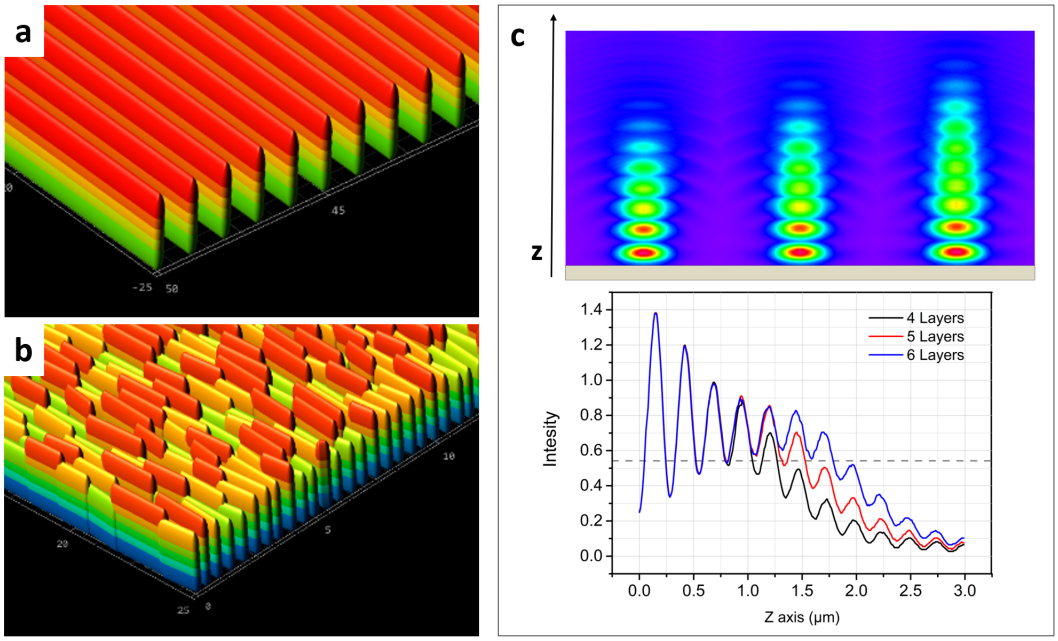

Figure 9-2. Lateral exposure patterns and vertical intensity simulations of butterfly-inspired SWE-TPL structures

Applied exposure pattern of (a) ordered and (b) disordered butterfly-inspired structures. (c) 2D-intensity maps and corresponding intensity profiles along the optical axis expected for SWE-TPL structures with 4, 5 and 6 layers. The grey dashed line in the graph indicates the presumed polymerisation threshold for the used photoresist (see Chapter 8.4.3 for details).

The resulting SWE-TPL structures are presented in **Figure 9-3** and **Figure 9-4.**On a macroscopic level, the structured surfaces of both samples exhibited a blue iridescent colour with stronger iridescence on the ordered surface. In contrast to this, the unstructured silicon substrate appeared black (due to the high reflectivity of silicon and the slightly deviant incident and reflected light path). The blue colouration also persisted at higher magnifications (**Figure 9-3b** and **Figure 9-4b**). On the ordered structures, SEM-analysis revealed 19.67 ± 0.19 µm long ridges with a lateral distance of 0.97 ± 0.04 µm, and a stitching gap of 0.91 ± 0.13 µm between the line ends (**Figure 9-4c**). The structure height, maximum thickness (measured at the structure base), and the distance between two polymeric layers (measured between the outermost points of adjacent layers) were 1140 ± 35 nm, 337 ± 17 nm and 216 ± 11 nm, respectively (**Figure 9-3d**). The lines appeared shorter at the top than at the base, which indicates anisotropic shrinkage.

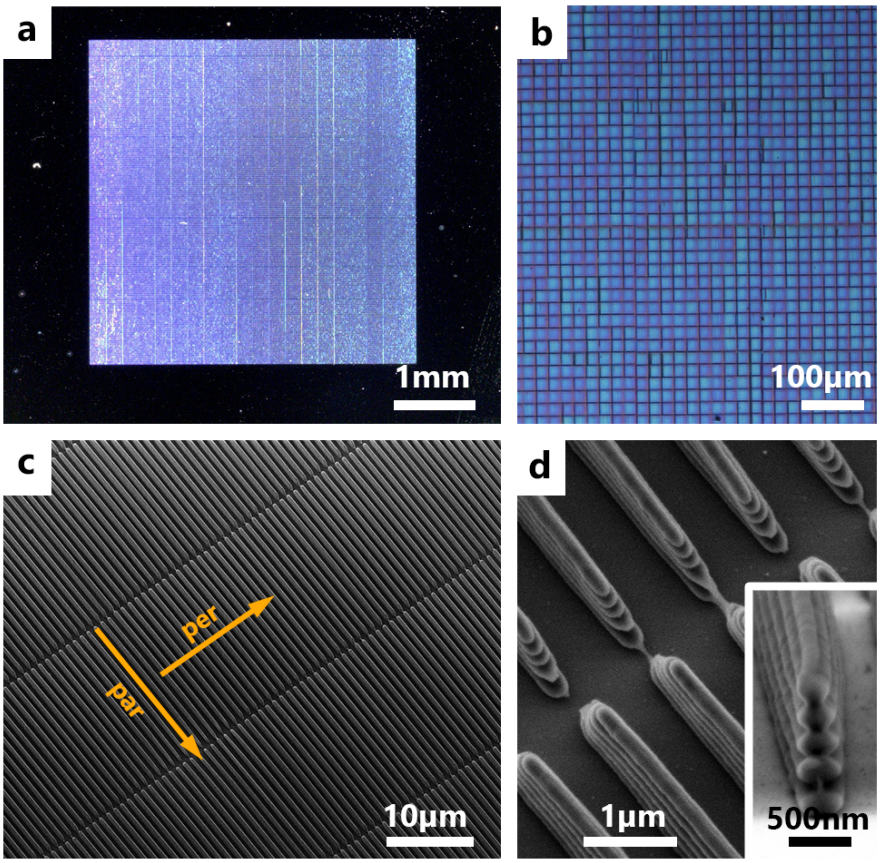

Figure 9-3. SWE-TPL fabricated ordered butterfly-inspired surfaces

Different magnifications recorded by (a.b) optical microscopy and (c,d) SEM. SEM-images were recorded at a tilt angle of ca. 20°. The yellow arrows indicate the viewing directions of the angle resolved microscopy analysis; (per) perpendicular and (par) parallel with respect to the structures. The insert shows a line tip at 90°.

As the disordered structures were fabricated with segments varying in rotation angles and heights, a precise dimensional analysis via SEM was challenging and the actual structure could differ slightly from the reported values. The stitching gap at the structure tips was 710 - 1430 nm with a mean value (MV) of 1021 ± 203 nm. The lines were divided into segments of 840 to 1880 nm length (MV = 1339 ± 280 nm, measured at the structure tips) with thicknesses of 320 to 405 nm (MV = 353 ± 20nm, measured at the structure base) and heights of 450 to 1365 nm (MV = 875 ± 290 nm). The vertical layers had a distance of 160 to 225 nm (MV = 187 ± 17 nm, measured between the outermost points of adjacent layers). In agreement with the observations on the ordered structures, the tips showed stronger shrinkage than the bases.

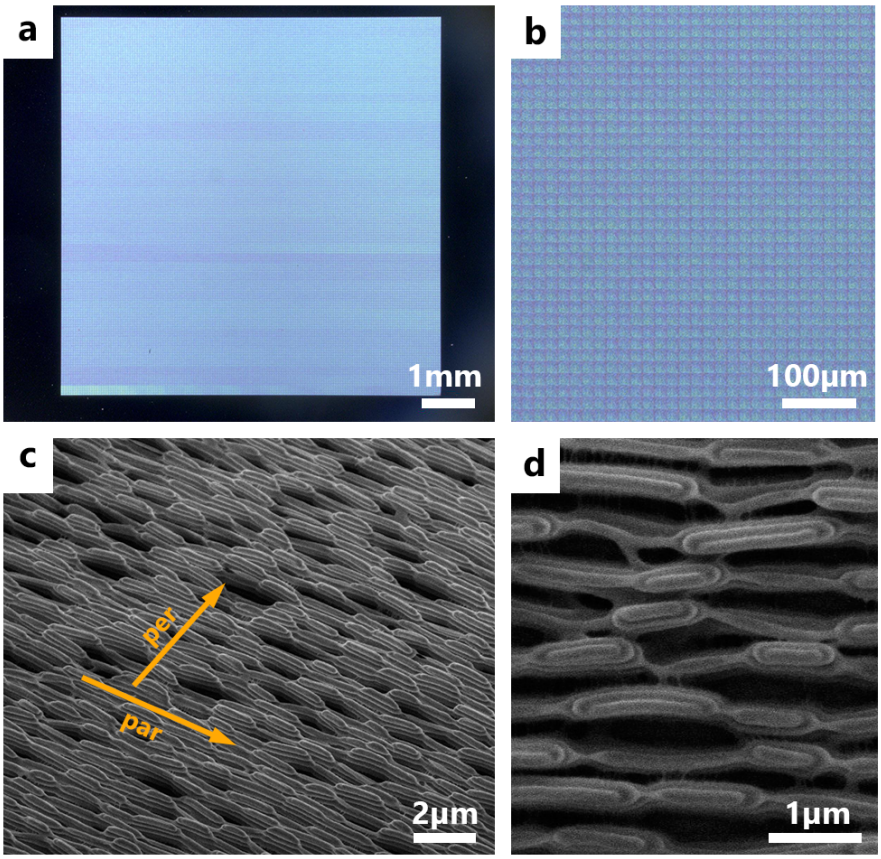

Figure 9-4. SWE-TPL fabricated disordered butterfly-inspired surfaces

Different magnifications recorded by (a.b) optical microscopy and (c,d) SEM. SEM-images were recorded at a tilt of ca. 40°. The yellow arrows indicate the viewing directions of the angle resolved microscopy analysis; (per) perpendicular and (par) parallel with respect to the structures.

9.4.2. *Angle and Orientation Dependent Optical Properties*

To obtain a full picture of the optical behaviour, angle dependent optical properties were determined by several techniques: bright field and dark field microscopy, spectroscopy and conoscopy. All samples were investigated at least in two orientations, with the objective tilted perpendicularly and parallelly to the line pattern.

Results obtained by bright and dark field microscopy are displayed in **Figure 9-5** and **Figure 9-6**, respectively. In bright field, all samples appeared blue coloured from 0° to 40° observation angle and above, when observed from a perpendicular observation direction (**Figure 9-5**). With a parallel observation direction, however, each sample behaved differently. While the blue iridescence on the disordered sample was comparable to the tilting experiment with perpendicular orientation but with minor reflectivity at larger angles > 20°. (**Figure 9-5e**), it remained solely at 0° on the ordered sample (**Figure 9-5c**) and between 5-15°on the butterfly (**Figure 9-5g**). The latter points to a tilted wing surface

with respect to the optical system. At even larger angles, these samples appeared mostly black or brown with yellowish lines originating from stitching defects or scale edges.

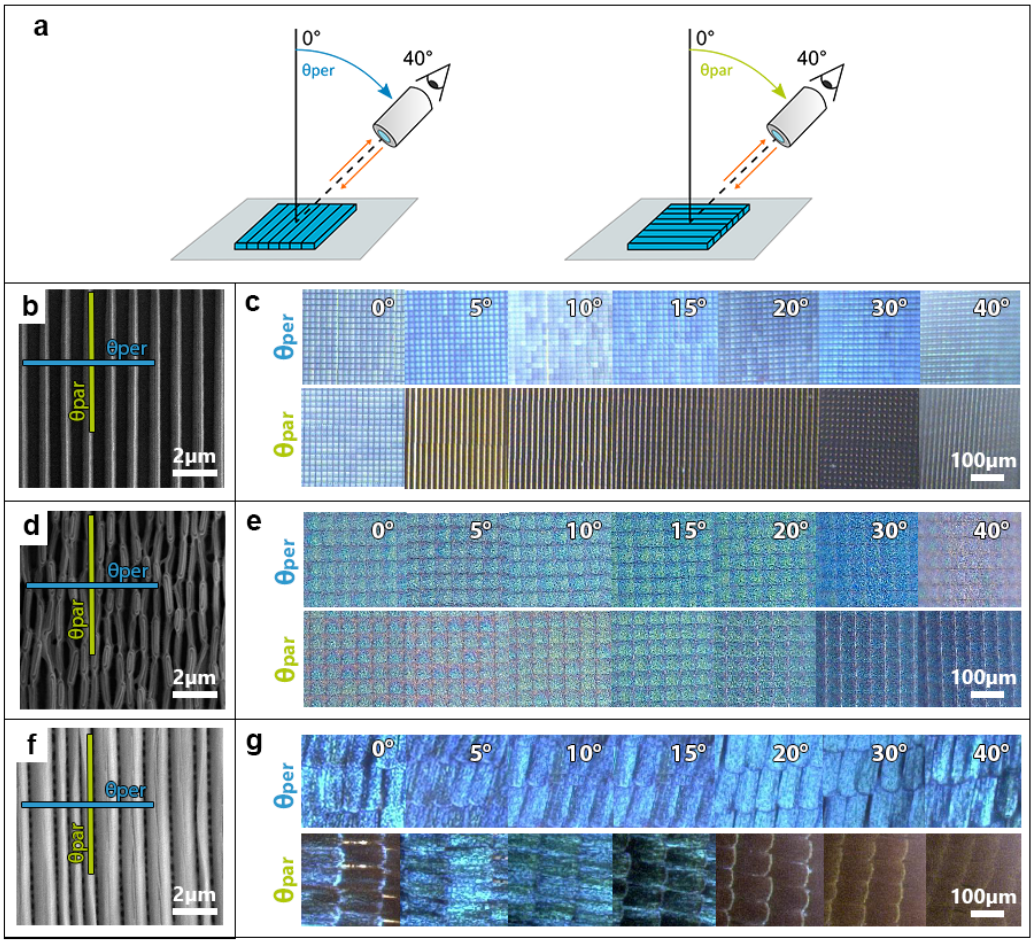

Figure 9-5. Angle dependant optical appearance of samples and the butterfly using bright field illumination

(a) Experimental set-up to measure the retroreflection of samples, i.e., light incidence and recording directions coincide (orange arrows). (c,e,g) Angular recordings obtained from two orientations perpendicular θper and parallel θpar with respect to the surface structures, as indicated in the SEM images (b,d,f). (b,c) ordered sample, (d,e) disordered sample, For comparison (f,g) show the butterfly wing.

A similar behaviour of the samples was observed while using dark field microscopy (**Figure 9-6**). Here, however, the blue reflection was superimposed by Bragg-diffraction at higher viewing angles apparent from the changes of colouration in dependence on the angle. This effect was found to be strongest on the ordered sample. (**Figure 9-6a**). On the disordered sample it was significantly reduced and mainly perceptible at the largest viewing angles close to 50° (**Figure 9-6b**). No Bragg-diffraction was noticeable on the butterfly's wing (**Figure 9-6c**).

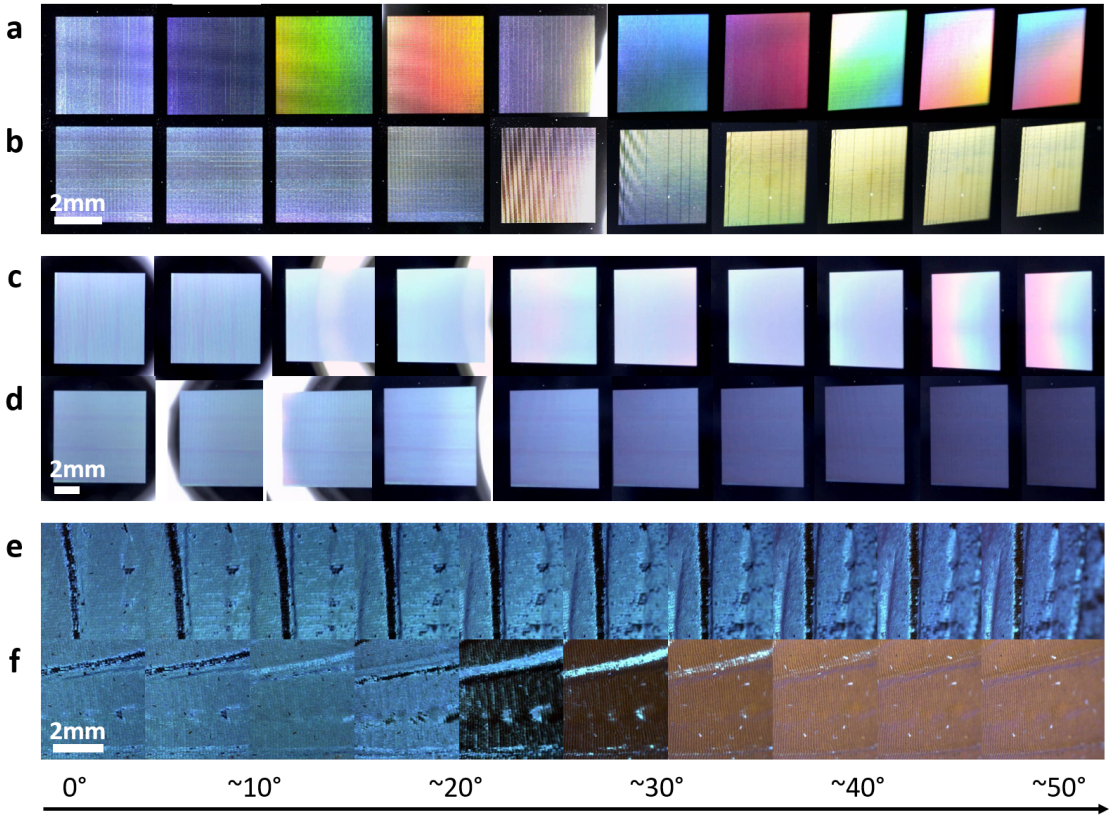

Figure 9-6. Angle dependant optical appearance of samples and the butterfly using dark field illumination

Angle dependant retroreflection obtained on (b,c) the ordered sample, (d,e) the disordered sample, and (f,g) the butterfly wing. (a,c,d) in perpendicular observation direction θper and (b,d,f) in parallel observation direction θpar. Images were taken from videos recorded during a manual tilt of the objective. The white bended line observed in some images results from the direct reflection of the light source, which is arranged annularly around the objective.

The results of the angle dependent spectroscopy (**Figure 9-7** to **Figure 9-10**) agreed well with the findings obtained by microscopy, when comparable illumination conditions were used, i.e., retroreflection in perpendicular and parallel orientation. In perpendicular orientation, all samples showed a pronounced reflection in the blue wavelength range with maxima between 450 and 500 nm (**Figure 9-8**). While already small divergences of the peak position of about 30 nm and 40 nm were found on the ordered and butterfly sample, it shifted only by 5 nm on the disordered sample.

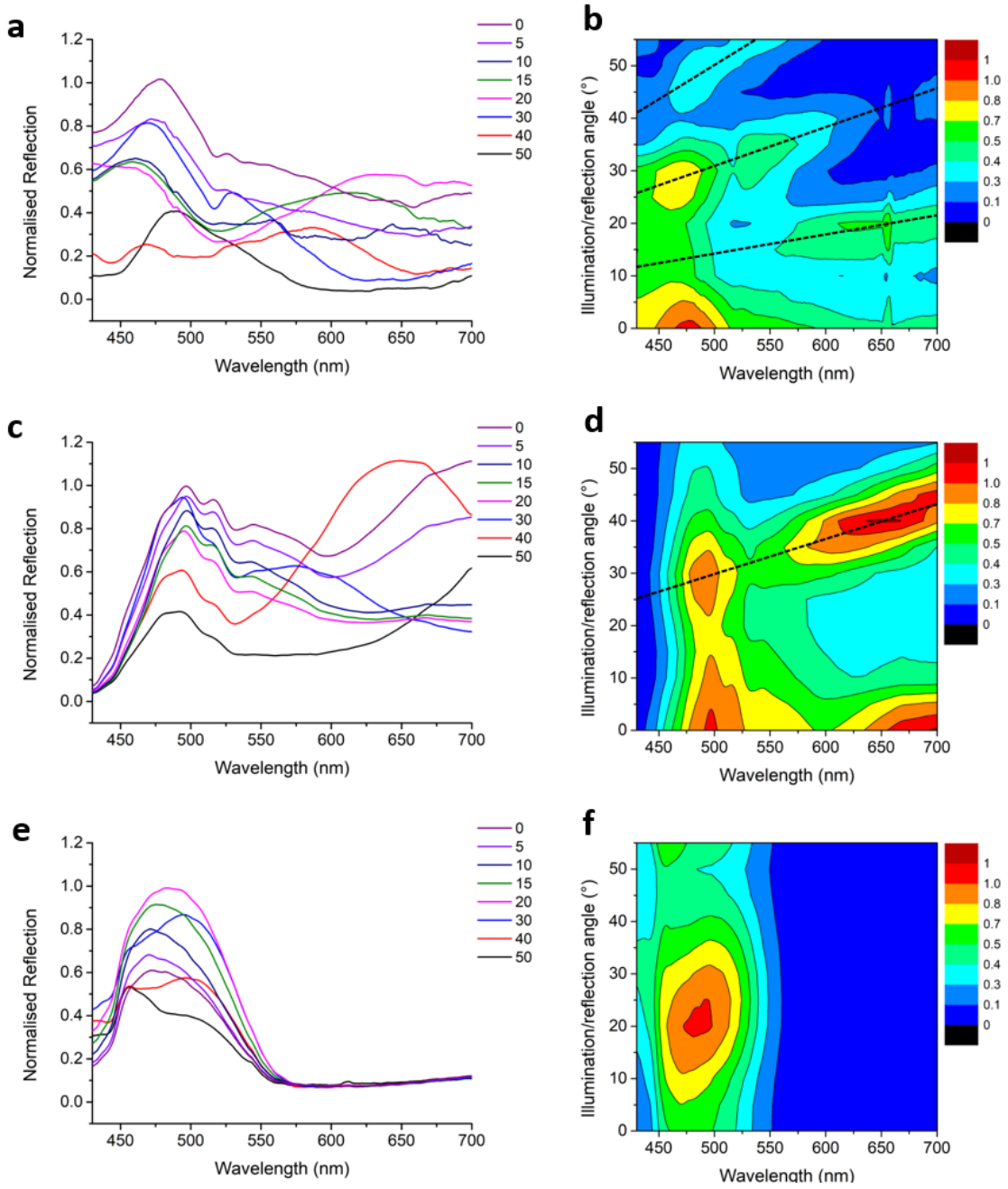

Figure 9-7. Angular resolved spectroscopy in perpendicular orientation

Angle dependent (a,c,e) reflection spectra and (b,d,f) intensity contour plots of (a,b) the ordered sample, (c,d) disordered sample, (e,f) and the butterfly. Contour plots include 12 spectra, measured between 0° and 55° every 5°. Data are normalised to the maximum intensity at wavelength below 500 nm.

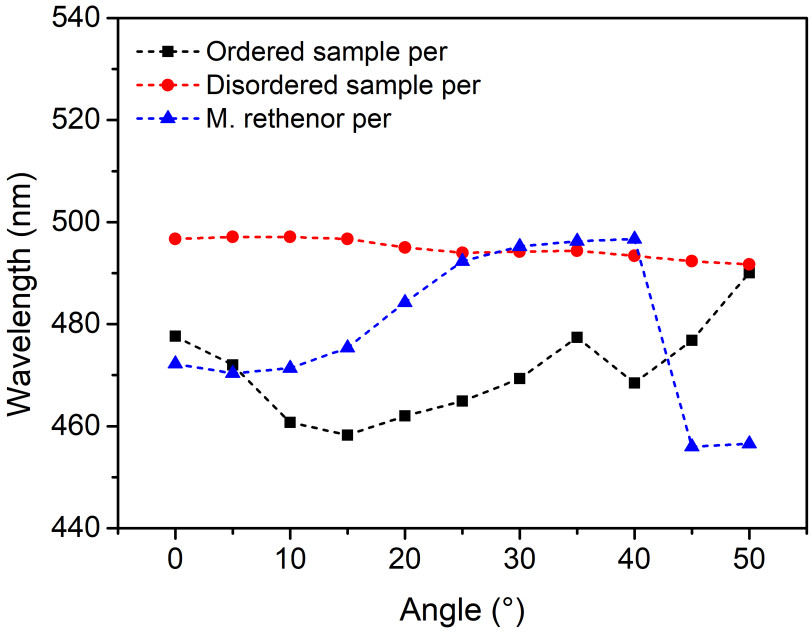

Figure 9-8. Wavelength of the blue peak of the blue peek in dependence on the recording angle measured in perpendicular direction

Blue peak wavelengths obtained on the ordered sample (black), the disordered sample (red) and the butterfly (blue), when samples were tilted in perpendicular orientation in regard to the ridged structure. Dashed lines are intended to guide the eye.

At larger angles, additional local intensity maxima occurred on the bio-inspired samples, whose wavelength strongly correlated with the observation angles (dashed lines in **Figure 9-7b,d**), and thus, are associated with the Bragg-diffraction mentioned before. Strikingly, the reflection of light with wavelength above 550 nm is almost completely suppressed on the butterfly. The most intense retroreflected signal on the butterfly was recorded at an slightly tilted observation angle of approximately 20°(**Figure 9-7e-f**) pointing again to a slightly tilted surface.

Investigations of structures in parallel orientation, confirmed the significant decrease in colouration on the ordered and butterfly sample found before (**Figure 9-9a-b,e-f**). While the blue peak shifted on the ordered sample by over 15 nm at an angle of 10° and then fully vanished, the butterfly showed a constant blue reflection up to a 20° tilt with a variation of only a few nanometres. Only then a strong wavelength shift of 15 nm occurred and the colour eventually disappeared (**Figure 9-10**). On the disordered sample, however, the blue reflection was detected up to 40° (**Figure 9-9c,d** and **Figure 9-10**) with a constant slight shift of only 10 nm in total.

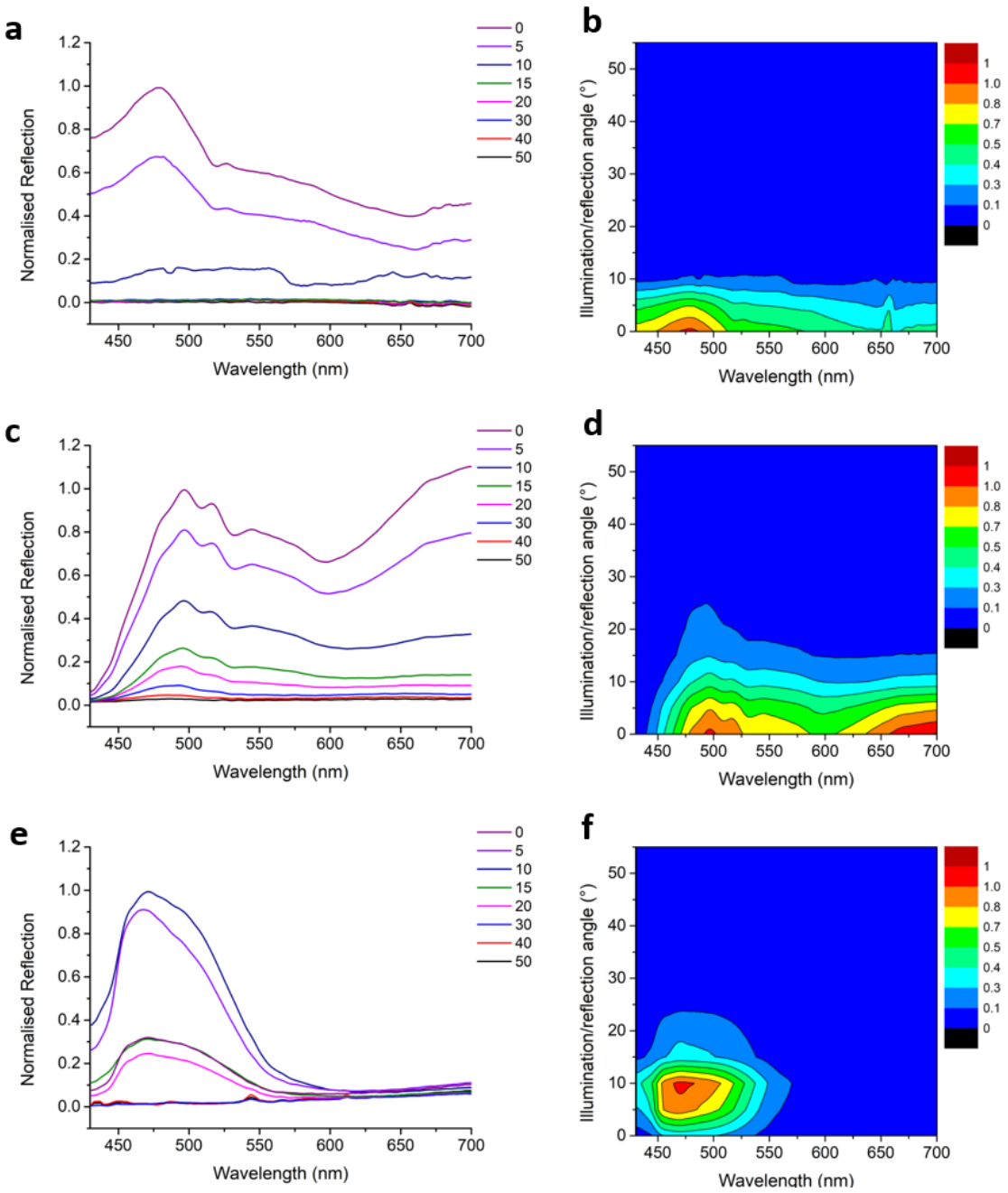

Figure 9-9. Angular resolved spectroscopy in parallel orientation

(a,c,e) Reflection spectra depending on the observation angle as well as (b,d,f) intensity contour plots of (a,b) the ordered SWE-TPL-sample, (c,d) disordered SWE-TPL-sample, (e,f) the butterfly. Contour plots include12 spectra, measured between 0° and 55° every 5°. Data are normalised to the maximum intensity at wavelength below 500 nm.

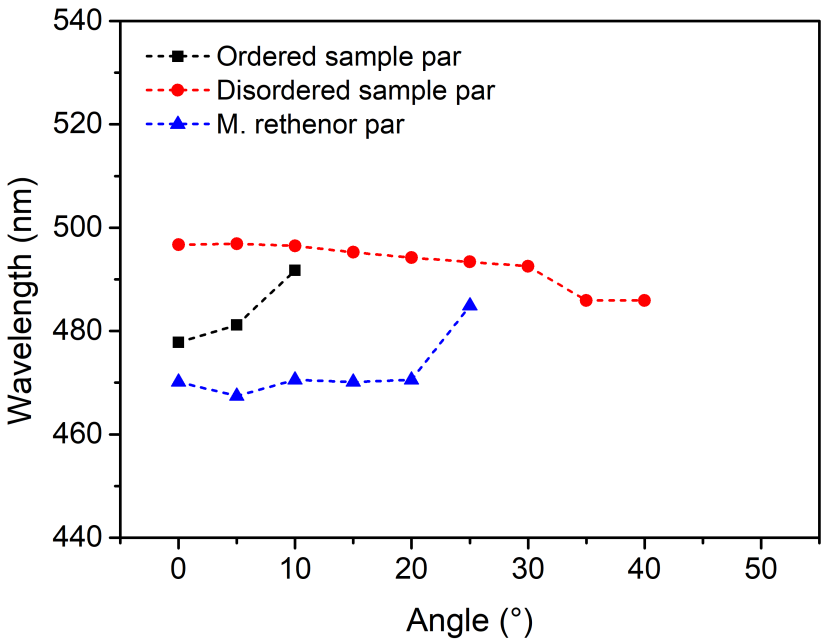

Figure 9-10. Wavelength of the blue peak in dependence on the recording angle measured in parallel direction

Blue peak wavelength obtained on the ordered sample (black), the disordered sample (red) and the butterfly (blue), when samples were tilted in parallel orientation in regard to the ridged structure. Dashed lines are intended to guide the eye. At angles without data points no reflection in the blue was detected.

The spatial scattering of samples, investigated by means of conoscopy, is shown for the laser wavelength λ = 475 nm in **Figure 9-11a-c.** On the ordered sample, the scattering pattern showed high intensity reflections positioned on one distinct line, which were accompanied by weaker spots perpendicular to this line (**Figure 9-11a**). The former originates from the periodical arrangement of the line structures (1 µm line distance), whereas the latter arise most probably from stitching inaccuracies at the edge of each 20 µm field where the stage was moved (compare **Figure 9-3c**). In contrast to that, no typical diffraction pattern was found on the disordered sample. Here, the intensity was spread over many different angles in a wide band (**Figure 9-11b**). Besides the zero-order reflection, strong reflections were not observed. Results obtained on the butterfly have to be viewed with caution as the zero order spot was shifted with respect to the point of light incidence, which indicates a tilt of substrate[40], and thus, a light incidence not perpendicular to the substrate surface. Notwithstanding this, an intensity distribution similar to that of the disordered sample was found, only in a band with a smaller width.

The radial intensity profiles, which were extracted and plotted for the pixels between the two yellow circles, are depicted in **Figure 9-11d**. The intensities of the radial profile determined on the ordered structures were low over the whole range of 10 to 50° except for the strong first order peak at 29.3°. This peak is assigned to the periodicity of 0.97 µm, the line distance measured by SEM. In contrast, the overall radial intensity on the disordered sample was comparatively high but slowly decreasing with a maximum at 0°. On the butterfly, the highest intensities occurred at angles between 15-25°. Diffraction

peaks as prominent as on the ordered sample were found neither on the butterfly nor on the disordered sample.

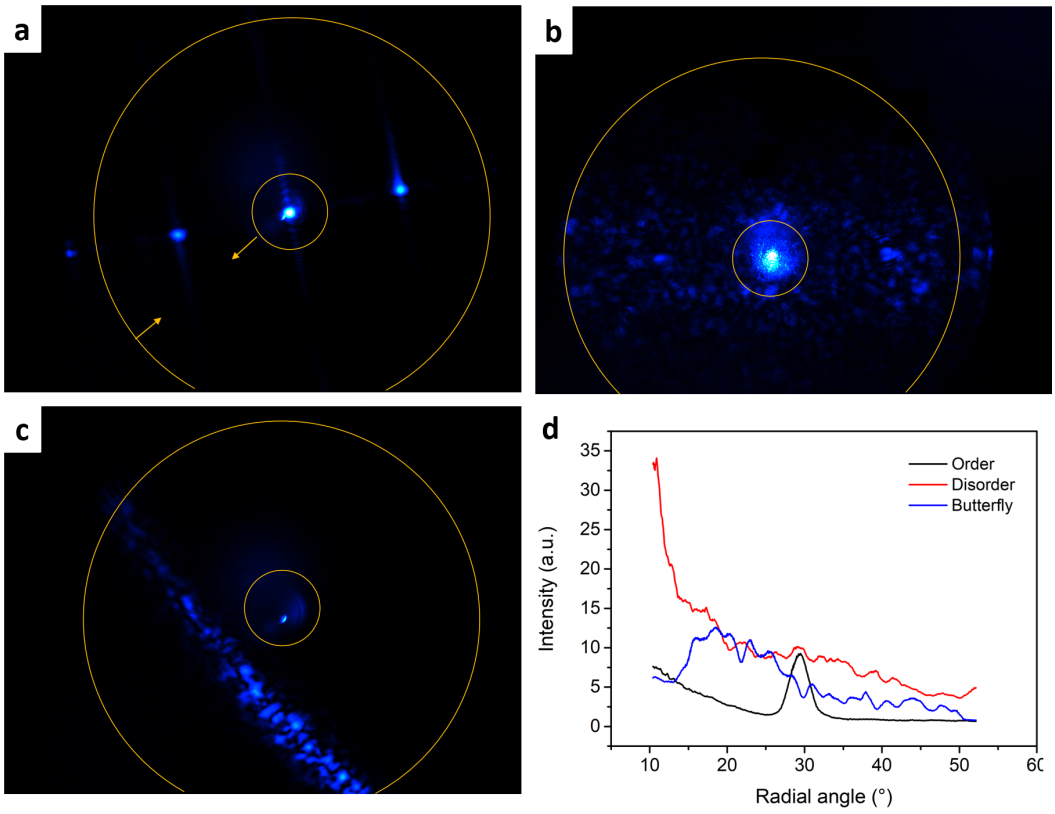

Figure 9-11. Comparison of the spatial scattering data obtained from the on SWE-TPL fabricated samples and the butterfly

(a) Ordered sample, (b) disordered sample, and (c) the butterfly. (d) Radial intensity profiles showing the collective intensities in dependence on the radial angles. The data were recorded using an incidence wavelength of 475 nm and a 50x objective with a numerical aperture of 0.95.

9.4.3. *Application example*

The structuring of butterfly-inspired structures via SWE-TPL is not limited to simple squares as it was best suited here for the investigation of the optical properties but can be precisely tailored in their shape. The example in **Figure 9-12** shows such a tailoring, aiming for the appearance and disappearance of characters depending on the viewing and rotation angle. While the characters were formed by structures with optical properties strongly depending on the viewing angle, structures evoking a rather constant appearance were used for the surrounding area. As a result, the characters do not stick out much from the background at 0° at both orientations θper and θpar. At larger angles, however, the letters become clearly discernible and appear bright or dark depending on the orientation of the surface.

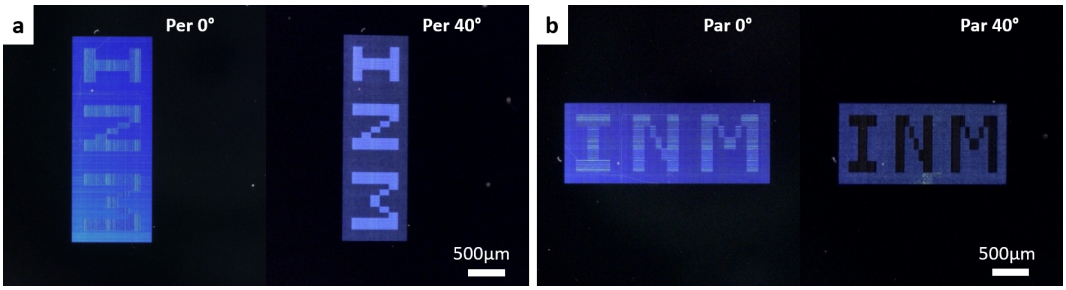

Figure 9-12. Example of a photonic surface composed of anisotropic and isotropic butterfly-inspired 3D-structures

Observation direction (a) perpendicular and (b) parallel in respect to structure lines.

9.5. Discussion

9.5.1. *Comparison of SWE-TPL Structures with the Butterfly*

The dimensions of the obtained SWE-TPL structures, such as height, width, pitch distance as well as the layer distances within individual structures agreed very well with those reported for the *Morpho rethenor* butterfly wing[6,41]. Especially, the periodicity between different layers of approximately 200 nm corresponded well with the 190 nm found in the natural blueprint[42]. Moreover, the structures did not only mimic the butterfly surface structurally, they also resembled the refractive index of the butterfly chitin $n_{500,\,chitin}$= 1.55[43], which is identical to the one of the developed photoresist $n_{500,\ resist}$= 1.55 used (from ellipsometry data shown in **Figure S 9-1** and Chapter 4.4)). A small difference, though, was apparent in the shape of the layers, where the artificial structures exhibited an ellipsoidal cross section due to the sinusoidal shape of the standing wave in the SWE-TPL process, instead of the sliced lamella of the butterfly.

Both bio-inspired surfaces and the butterfly wing showed an intense and constant blue reflection over a wide angle range in perpendicular orientation with respect to the line pattern (**Figure 9-7**). The smallest wavelength shift over the measured angle range, and thus, the best angle independency was found on the disordered sample. In contrast to the perpendicular tilting orientation, the angle range was strongly limited in the case of the ordered and butterfly sample in parallel orientation. This anisotropy is most probably caused by the structural anisotropy and thus difference in structure surface area facing the illumination direction; it is high in perpendicular orientation and low in parallel orientation. In the case of the disordered sample, this anisotropy is lowered by the rotation of the individual segments of each line leading to a more isotropic optical behaviour. The angle constancy is further improved by the different height of these segments[29,30]. In combination, both structural attributes give rise to many, additional low intensity reflections distributed in broad spatial angles, and thus a wide-angle blue reflection that even outperforms that of the *Morpho* butterfly wing. In addition to the disorder of

structural elements, the Bragg peaks of the overall line structures appear at higher angles due to the smaller line distance in comparison to the ordered sample. From the grating equation (16) and the Bragg equation (15), where the former applies to the conoscopy and the latter to the spectroscopy case, it can be calculated that structures separated by 500 nm show Bragg diffraction at angles twice as high as structures separated by 1000 nm (cp. the dashed lines in **Figure 9-7b,d**). In conoscopy, the first order peak even shifts beyond the recorded data range (**Figure 9-11d**). On the butterfly, Bragg diffraction is suppressed even further by additional structural peculiarities, e.g. the tilts of scales varying by up to 20°[41,44] or an absorbing layer for longer wavelengths[45]. The former is most likely the reason for the angle deviation of the maximum intensities from 0° observed by microscopy, spectroscopy and conoscopy.

To further improve the optical performance of SWE-TPL samples with respect to the butterfly colouration, a number of optimisations could be done: a) the blue saturation could be enhanced by increasing the numbers of vertical layers[46] as well as the refractive index of structure material; b) unwanted reflection could be reduced through a roughening of the subtrate[47] after the fabrication process or by applying an absorbing layer operating in the visible but not in the near infrared; c) the angle constancy of the colouration could be improved by increasing the disorder, e.g., by an additional substrate topography as reported by others[26,27,45].

9.5.2. *Comparison of SWE-TPL with Other Structuring Techniques*

Techniques providing vertical disorder such as multi-layer deposition on pre- structured surfaces[26-29] are applicable on large areas but have a significant drawback: they often lack the freestanding layering of material and air important for many applications. Air-material layered structures are achievable, though, by combining multifilm deposition, selective radical etching and double molding[19,20]. However, such a fabrication is very complex and struggles with the introduction of vertical and horizontal disorder.

The application of SWE-TPL allows a new way of mimicking butterfly-inspired structures. By using SWE-TPL it is not only possible to reproduce the air-material layering of the butterfly structures, but also introduce a tailored level of disorder to improve the optical behaviour. Furthermore, it could be shown that periodically layered structures with distances down to 200 nm can be achieved. This is a huge improvement to the 500 nm discussed by Fischer and co-authors[48] (related to a comparable laser wavelength, NA of the objective, and refractive index of the medium). Surfaces similar to that depicted in **Figure 9-12** could be applied, e.g., as photonic masters in moulding processes to achieve micro-imprint stamps for volume production[20]. In fact, the elliptical shape of the layers (cp. the inset in **Figure 9-3d**) should be an advantage, as distinct corners hamper the detachment of the mould and thus favour the rupture of replicated structures. Further, the comparison of fabricated structure heights and pitches with those predicted by simulations show a good correlation, if a shrinkage of 20% during the TPL-fabrication[37] is considered. The opportunity to predict structure dimensions, and thus the optical

properties, would be of great value during the design of SWE-TPL-structures, e.g. in the fields of telecommunication[49], solar-energy-harvesting, photodetectors[50-52], diffractive optical elements[53,54], random lasers[55], metamaterials[56], and many more.

9.6. Conclusions

Standing wave enhanced two-photon lithography (SWE-TPL) was successfully used to fabricate areas of ordered and disordered butterfly-inspired structures. The optical properties of these areas were investigated and compared to the original butterfly. The following conclusions can be drawn from the results:

(1) By using SWE-TPL complex freestanding butterfly-like structures with a periodic material/air layering of ~200 nm in the vertical direction were created. This was the first time, that two-photon lithography was used to fabricate bio-inspired 3D photonic crystals with a photonic bandgap in the blue range.

(2) On the artificially fabricated structures the blue iridescence was recordable up to angles of 50°, what is comparable to angles found on the butterfly. Regarding the rotation and angle constant blue iridescence, the disordered sample even excelled the natural blueprint.

(3) The contribution of Bragg diffraction to the optical appearance of the fabricated surfaces can be reduced by a closer placing of lines, through horizontal disorder by rotating line segments, and by vertical disorder by stacking varying numbers of voxels. By adjusting these or similar parameters, the optical effect of single elements to disordered materials can be investigated in detail.

(4) Resulted structured and simulations were greatly in line, if a shrinkage of 20% was considered. As this ratio is in line with other studies, it could be used in future simulations to obtain a better correlation in structure periodicity between simulations and subsequently manufactured structures.

(5) Complex photonic surfaces bearing several different butterfly-inspired structures could be designed by computer aided design. These surfaces have further potential to be used as masters for imprint technologies, and thus, to mass production.

9.7. Acknowledgements

Foremost I want to thank Silvia Vignolini and Villads Edge Johanson from Cambridge University for the opportunity to use their equipment to perform the conoscopy analysis. Further thanks go to Reza Hosseinabadi, INM, for his support in the TPL-fabrication, the optical imaging and the implementation of the INM Logo as well as to Jennifer Atchison for her introduction to experimental spectroscopy and data analysis. I acknowledge also Andreas Verch, Peter Rogin, and Elmar Kroner for the helpful discussions as well as proofreading.

9.8. References

1. Blanco A, Chomski E, Grabtchak S, Ibisate M, John S, Leonard SW, *et al.* Large-scale synthesis of a silicon photonic crystal with a complete three-dimensional bandgap near 1.5 micrometres. *Nature* 2000, **405**(6785)**:** 437-440.
2. Potyrailo RA, Ghiradella H, Vertiatchikh A, Dovidenko K, Cournoyer JR, Olson E. Morpho butterfly wing scales demonstrate highly selective vapour response. *Nat Photon* 2007, **1**(2)**:** 123-128.
3. Akahane Y, Asano T, Song B-S, Noda S. High-Q photonic nanocavity in a two-dimensional photonic crystal. *Nature* 2003, **425**(6961)**:** 944-947.
4. Russell P. Photonic Crystal Fibers. *Science* 2003, **299**(5605)**:** 358-362.
5. Vukusic P, Sambles JR, Lawrence CR, Wootton RJ. Quantified interference and diffraction in single Morpho butterfly scales. *Proceedings of the Royal Society B: Biological Sciences* 1999, **266**(1427)**:** 1403-1403.
6. Ghiradella H. Structure of Iridescent Lepidopteran Scales: Variations on Several Themes. *Annals of the Entomological Society of America* 1984, **77**(6)**:** 637-645.
7. Kinoshita S, Yoshioka S, Miyazaki J. Physics of structural colors. *Reports on Progress in Physics* 2008, **71**(7)**:** 076401.
8. Zhang W, Gu J, Liu Q, Su H, Fan T, Zhang D. Butterfly effects: novel functional materials inspired from the wings scales. *Physical Chemistry Chemical Physics* 2014, **16**(37)**:** 19767-19780.
9. Huang J, Wang X, Wang ZL. Controlled Replication of Butterfly Wings for Achieving Tunable Photonic Properties. *Nano Letters* 2006, **6**(10)**:** 2325-2331.
10. Potyrailo RA, Bonam RK, Hartley JG, Starkey TA, Vukusic P, Vasudev M, *et al.* Towards outperforming conventional sensor arrays with fabricated individual photonic vapour sensors inspired by Morpho butterflies. *Nat Commun* 2015, **6**.
11. Kertész K, Molnár G, Vértesy Z, Koós AA, Horváth ZE, Márk GI, *et al.* Photonic band gap materials in butterfly scales: A possible source of "blueprints". *Materials Science and Engineering: B* 2008, **149**(3)**:** 259-265.
12. Xu D, Yu H, Xu Q, Xu G, Wang K. Thermoresponsive Photonic Crystal: Synergistic Effect of Poly(N-isopropylacrylamide)-co-acrylic Acid and Morpho Butterfly Wing. *ACS Applied Materials & Interfaces* 2015, **7**(16)**:** 8750-8756.
13. Zhang F, Shen Q, Shi X, Li S, Wang W, Luo Z, *et al.* Infrared Detection Based on Localized Modification of Morpho Butterfly Wings. *Adv Mater* 2015, **27**(6)**:** 1077-1082.
14. Tan Y, Gu J, Xu L, Zang X, Liu D, Zhang W, *et al.* High-Density Hotspots Engineered by Naturally Piled-Up Subwavelength Structures in Three-Dimensional Copper Butterfly Wing Scales for Surface-Enhanced Raman Scattering Detection. *Adv Funct Mater* 2012, **22**(8)**:** 1578-1585.
15. Ghiradella H. Structure and development of iridescent butterfly scales: Lattices and laminae. *Journal of Morphology* 1989, **202**(1)**:** 69-88.

16. Gralak B, Tayeb G, Enoch S. Morpho butterflies wings color modeled with lamellar grating theory. *Opt Express* 2001, **9**(11)**:** 567-578.
17. Ghiradella H. Structure of butterfly scales: Patterning in an insect cuticle. *Microsc Res Tech* 1994, **27**(5)**:** 429-438.
18. Kinoshita S, Yoshioka S. Structural Colors in Nature: The Role of Regularity and Irregularity in the Structure. *ChemPhysChem* 2005, **6**(8)**:** 1442-1459.
19. Aryal M, Ko D-H, Tumbleston JR, Gadisa A, Samulski ET, Lopez R. Large area nanofabrication of butterfly wing and three dimensional ultrastructures. *Journal of Vacuum Science & Technology B* 2012, **30**(6)**:** 061802.
20. Cary AT, Yulan F, Anne-Martine J, Eugenii UD, Rene L. Reproduction and optical analysis of Morpho -inspired polymeric nanostructures. *Journal of Optics* 2016, **18**(6)**:** 065105.
21. Siddique RH, Diewald S, Leuthold J, Hölscher H. Theoretical and experimental analysis of the structural pattern responsible for the iridescence of Morpho butterflies. *Opt Express* 2013, **21**(12)**:** 14351-14361.
22. Watanabe K, Hoshino T, Kanda K, Haruyama Y, Matsui S. Brilliant Blue Observation from a Morpho -Butterfly-Scale Quasi-Structure. *Japanese Journal of Applied Physics* 2005, **44**(1L)**:** L48.
23. Zyla G, Kovalev A, Grafen M, Gurevich EL, Esen C, Ostendorf A, *et al.* Generation of bioinspired structural colors via two-photon polymerization. *Scientific Reports* 2017, **7**(1)**:** 17622.
24. Siddique RH, Hünig R, Faisal A, Lemmer U, Hölscher H. Fabrication of hierarchical photonic nanostructures inspired by Morpho butterflies utilizing laser interference lithography. *Opt Mater Express* 2015, **5**(5)**:** 996-1005.
25. Schneider N, Zeiger C, Kolew A, Schneider M, Leuthold J, Hölscher H, *et al.* Nanothermoforming of hierarchical optical components utilizing shape memory polymers as active molds. *Opt Mater Express* 2014, **4**(9)**:** 1895-1902.
26. Saito A, Yoshioka S-y, Kinoshita S. Reproduction of the Morpho butterfly's blue: arbitration of contradicting factors. 2004; 2004. p. 188-194.
27. Chung K, Yu S, Heo C-J, Shim JW, Yang S-M, Han MG, *et al.* Flexible, Angle-Independent, Structural Color Reflectors Inspired by Morpho Butterfly Wings. *Adv Mater* 2012, **24**(18)**:** 2375-2379.
28. Saito A, Murase J, Yonezawa M, Watanabe H, Shibuya T, Sasaki M, *et al.* High-throughput reproduction of the Morpho butterfly's specific high contrast blue. 2012; 2012. p. 83390C-83390C-83310.
29. Song B, Johansen VE, Sigmund O, Shin JH. Reproducing the hierarchy of disorder for Morpho-inspired, broad-angle color reflection. *Scientific Reports* 2017, **7:** 46023.
30. Johansen VE. Optical role of randomness for structured surfaces. *Appl Opt* 2014, **53**(11)**:** 2405-2415.
31. Li Q, Zeng Q, Shi L, Zhang X, Zhang K-Q. Bio-inspired sensors based on photonic structures of Morpho butterfly wings: a review. *Journal of Materials Chemistry C* 2016, **4**(9)**:** 1752-1763.
32. Kang S-H, Tai T-Y, Fang T-H. Replication of butterfly wing microstructures using molding lithography. *Current Applied Physics* 2010, **10**(2)**:** 625-630.
33. Farsari M, Chichkov BN. Materials processing: Two-photon fabrication. *Nat Photon* 2009, **3**(8)**:** 450-452.
34. Hohmann JK, Renner M, Waller EH, von Freymann G. Three-Dimensional μ-Printing: An Enabling Technology. *Adv Opt Mater* 2015, **3**(11)**:** 1488-1507.
35. Geissler M, Xia Y. Patterning: Principles and Some New Developments. *Adv Mater* 2004, **16**(15)**:** 1249-1269.
36. Alberto P, Raymond CYA, Heungsoo K, Nicholas AC, Scott AM. Laser 3D micro-manufacturing. *Journal of Physics D: Applied Physics* 2016, **49**(22)**:** 223001.
37. Purtov J, Verch A, Rogin P, Hensel R. Improved development procedure to enhance the stability of microstructures created by two-photon polymerization. *Microelectron Eng* 2018, **194:** 45-50.
38. Purtov J, Rogin P, Verch A, Johansen VE, Hensel R. Nanopillar Diffraction Gratings by Two-Photon Lithography. *Nanomaterials* 2019, **9**(10)**:** 1495.

39. Vignolini S, Moyroud E, Glover BJ, Steiner U. Analysing photonic structures in plants. *Journal of The Royal Society Interface* 2013, **10**(87).
40. Yoshioka S, Kinoshita S. Wavelength–selective and anisotropic light–diffusing scale on the wing of the Morpho butterfly. *Proceedings of the Royal Society of London B: Biological Sciences* 2004, **271**(1539)**:** 581-587.
41. Berthier S, Charron E, Boulenguez J. Morphological structure and optical properties of the wings of Morphidae. *Insect Science* 2006, **13**(2)**:** 145-158.
42. Han Z, Niu S, Yang M, Mu Z, Li B, Zhang J, *et al.* Unparalleled sensitivity of photonic structures in butterfly wings. *RSC Advances* 2014, **4**(85)**:** 45214-45219.
43. Leertouwer HL, Wilts BD, Stavenga DG. Refractive index and dispersion of butterfly chitin and bird keratin measured by polarizing interference microscopy. *Opt Express* 2011, **19**(24)**:** 24061-24066.
44. Ghiradella H, Aneshansley D, Eisner T, Silberglied RE, Hinton HE. Ultraviolet reflection of a male butterfly: interference color caused by thin-layer elaboration of wing scales. *Science* 1972, **178**(4066)**:** 1214-1217.
45. Song B, Eom SC, Shin JH. Disorder and broad-angle iridescence from Morpho-inspired structures. *Opt Express* 2014, **22**(16)**:** 19386-19400.
46. Land MF. The physics and biology of animal reflectors. *Prog Biophys Mol Biol* 1972, **24:** 75-106.
47. Koynov S, Brandt MS, Stutzmann M. Black nonreflecting silicon surfaces for solar cells. *Appl Phys Lett* 2006, **88**(20)**:** 203107.
48. Fischer J, Wegener M. Three-dimensional optical laser lithography beyond the diffraction limit. *Laser & Photonics Reviews* 2013, **7**(1)**:** 22-44.
49. Deubel M, von Freymann G, Wegener M, Pereira S, Busch K, Soukoulis CM. Direct laser writing of three-dimensional photonic-crystal templates for telecommunications. *Nat Mater* 2004, **3**(7)**:** 444-447.
50. Kelzenberg MD, Boettcher SW, Petykiewicz JA, Turner-Evans DB, Putnam MC, Warren EL, *et al.* Enhanced absorption and carrier collection in Si wire arrays for photovoltaic applications. *Nat Mater* 2010, **9:** 239.
51. Spinelli P, Verschuuren MA, Polman A. Broadband omnidirectional antireflection coating based on subwavelength surface Mie resonators. *Nat Commun* 2012, **3:** 692.
52. Rockstuhl C, Fahr S, Bittkau K, Beckers T, Carius R, Haug FJ, *et al.* Comparison and optimization of randomly textured surfaces in thin-film solar cells. *Opt Express* 2010, **18**(S3)**:** A335-A342.
53. Dholakia K, Čižmár T. Shaping the future of manipulation. *Nat Photon* 2011, **5:** 335.
54. Ligon SC, Kumpfmüller J, Pucher N, Stampfl J, Liska R. Fabrication of Waveguides and Other Optical Elements by Multiphoton Lithography. *Multiphoton Lithography*. Wiley-VCH Verlag GmbH & Co. KGaA, 2016, pp 265-296.
55. Wiersma DS. The physics and applications of random lasers. *Nature Physics* 2008, **4:** 359.
56. Gorkunov MV, Gredeskul SA, Shadrivov IV, Kivshar YS. Effect of microscopic disorder on magnetic properties of metamaterials. *Physical Review E* 2006, **73**(5)**:** 056605.

9.9. Supplementary Information

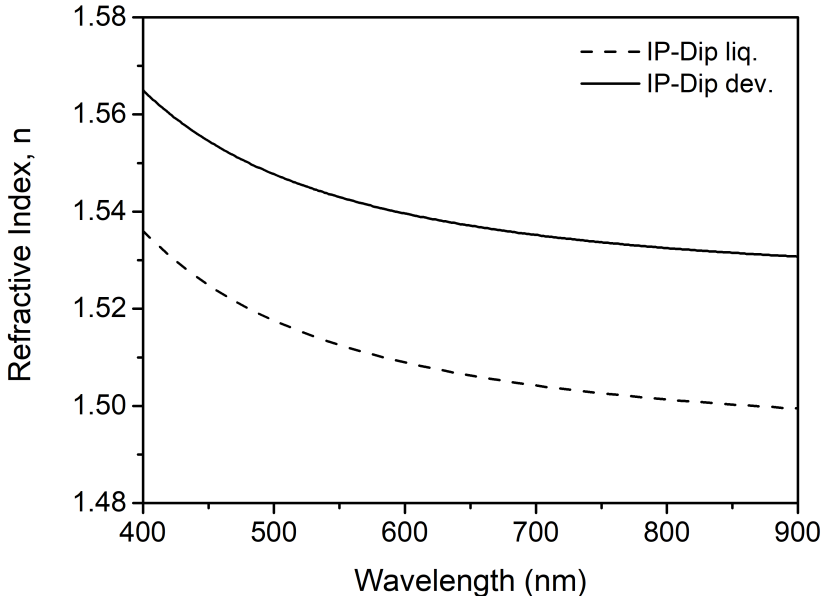

Figure S 9-1 Optical constants of the used phot resist (IP-DIP)

The dashed and continuous line corresponds to refractive indices measured on liquid (liq.) and developed (dev.) IP-DIP photoresist, respectively. The former was used for the simulation of expected SWE-TPL structure sizes, the latter represent final values of the fabricated structures.

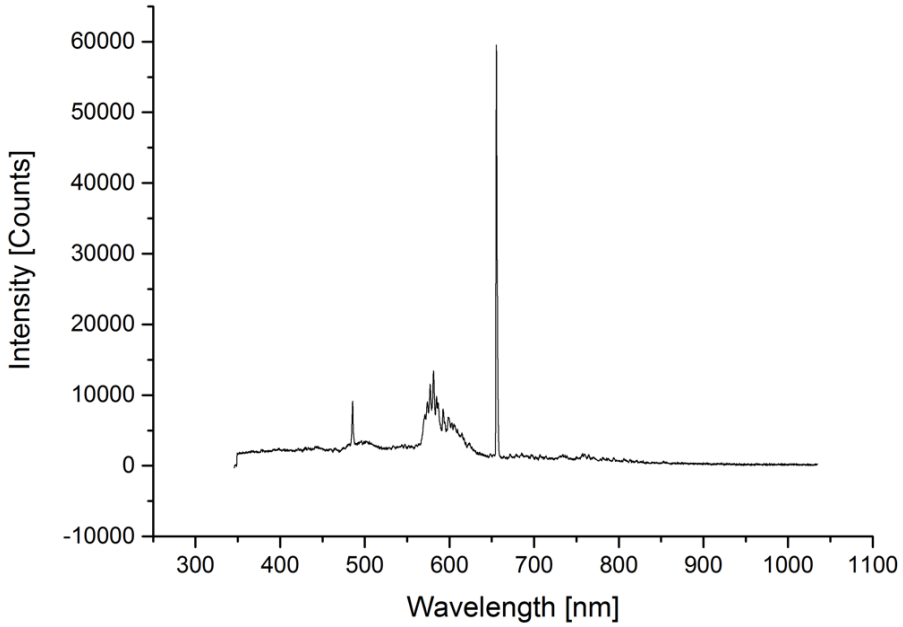

Figure S 9-2. Spectrum of the lamp used in angular spectroscopy

Chapter 10. Future Research Directions

As demonstrated in this thesis, TPL can be used to fabricate a growing variety of photonic structures, which interact with visible wave lengths down to the blue range. It was also shown that these structures differ strongly in their optical response and potential applications depending on the structure sizes, shapes, and spatial arrangement.

The knowledge gained can now be utilised to design more sophisticated photonic systems or to develop surfaces with unique optical behaviour. Some examples of structures, which could lead to further advances in the photonic field are depicted in **Figure 10-1**, **Figure 10-2**, and **Figure 10-3**. As disordered materials are promising for new lasing designs, TPL could be used to rapidly fabricate novel photonic crystal prototypes with divers orders of disorder and to investigate them regarding their optical and dialectical behaviour. Potential candidates for such a study exhibiting different lateral arrangements are shown in **Figure 10-1a-f**. Techniques, such as conoscopy (**Figure 10-1g-i**), could then be used to investigate resulting diffraction phenomena and wavelength dependencies. Such surfaces could potentially also become important for the light distribution from one beam into several sensors or glass fibres in the field of photonic computing.

Butterfly inspired structures differing in their layer-to-layer distance could find attention in the field of photonic displays (**Figure 10-2**). By tailoring structure parameters precisely, not only blue, but various other colours, such as cyan, magenta, or yellow, could be realised reproducibly (**Figure 10-2 a,c**). First comparisons of achieved colours and finite element simulations (compare **Figure 10-2d** and **Figure 10-2f**), indicate that the colour effect truly originates from the vertical periodicity. The results of this preliminary investigations are worth extending by characterising areas comprising pillars with various layer distances. One aim and great innovation would be, if a white reflection of white light could be achieved by mixing red, green, and blue reflecting pillars.

A further, important task, in order to truly establish TPL as a universal tool for the fabrication of photonic structures is to show the successful replication of the 3D-structure. This would be fundamental for a sincere commercial application, as the main disadvantage preventing the usage of TPL is the excessive processing time needed to structure larger areas. Methods for accomplishing such a replication could be, e.g., electroplating or double moulding procedures. A first double moulding attempt with PDMS as moulding material gave already a promising outcome yielding several layered structures that showed some green structural colouration (data not shown).

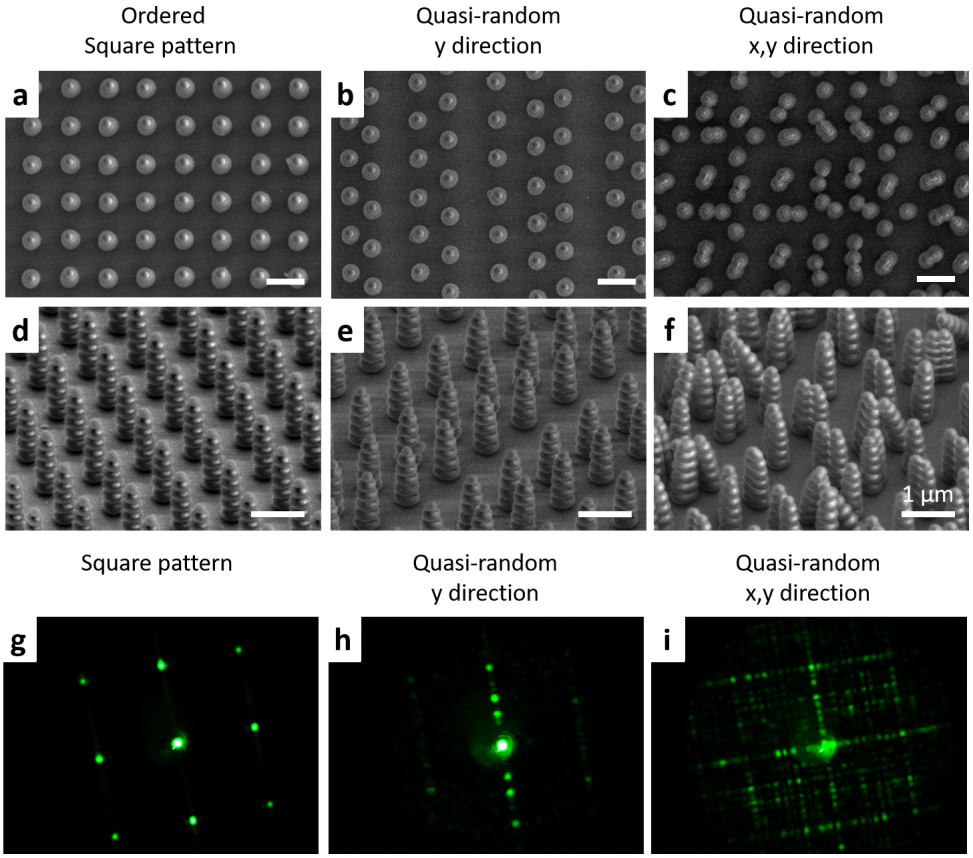

Figure 10-1. 3D-photonic crystals with different disorder ratios

SEM-images in (a-c) top view and (d-f) at ~40° tilt of butterfly-inspired structures with (a,d) ordered lateral arrangement, (b,e) lateral disorder in y-direction, and (c,f) lateral disorder in x and y-direction. (g-f) Corresponding conoscopy images showing the spatial diffraction pattern in dependence on the structure displacements. All scale bars are 1µm.

Another feasible project could be to establish SWE-TPL fabricated photonic porous films as vapor sensors (introduced in Chapter 8). In preliminary experiments (summarised in **Figure 10-3**) a clear colour change of a TPL fabricated porous film in the presence of isopropanol vapour and liquid could be observed. The experiments also indicated a high reversibility of the colour change, that could appear in a continuous or stepwise manner. It would be very interesting to repeat these experiments in a controlled environment in order to correlate the changes in the reflection spectra to the vapour concentration. In addition, a more detailed SEM-analysis of FIB-milled films as depicted in **Figure 10-3e,f** could be conducted to gain a better understanding of important parameters influencing the colour switch. Here, parameters such as hight, width, volume of cavities, thickness of connections, and number of layers could play important roles. This data would be very helpful to validate simulation models with experimental results.

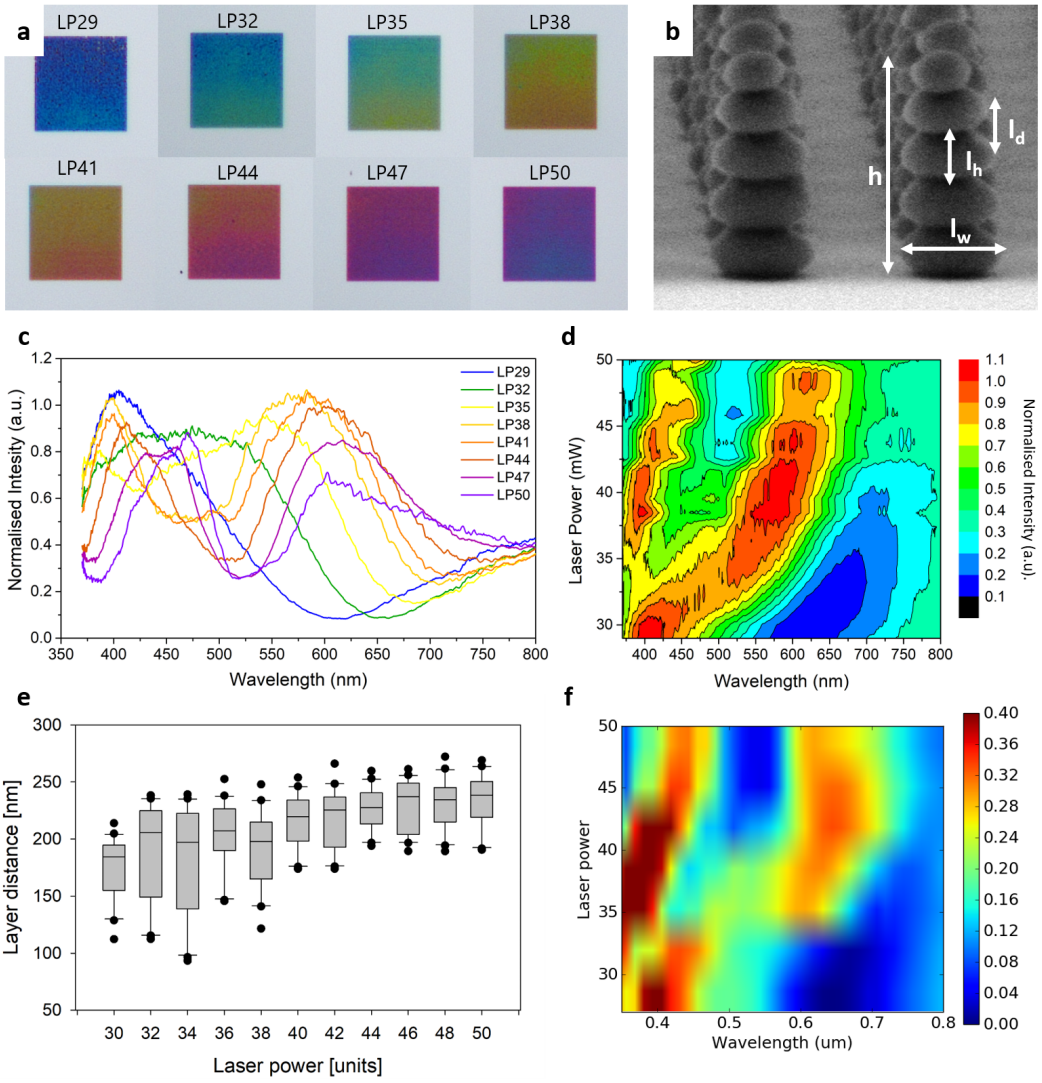

Figure 10-2. Tailored butterfly-inspired colouration

(a) Micrographs of coloured butterfly-inspired structures fabricated on one substrate using different laser powers. (b) SEM-image indicating structure parameters relevant for the observed colouration: h: height, l_w: layer width, l_h: layer height, l_d: layer distance. (c,d) Spectroscopy measurements on the structures shown in (a). (e) Layer distance in dependence on the laser power obtained from SEM-images as presented in (b). The data show an increase in layer distance as a result of laser power increase. Such an increase in layer distance should lead to a red shift of the reflection spectrum, which correlated with the spectroscopy measurement in (c,d). (f) Rigorous coupled wave analysis based on structure sizes indicated in (b) support the experimentally determined optical properties in (c,d).

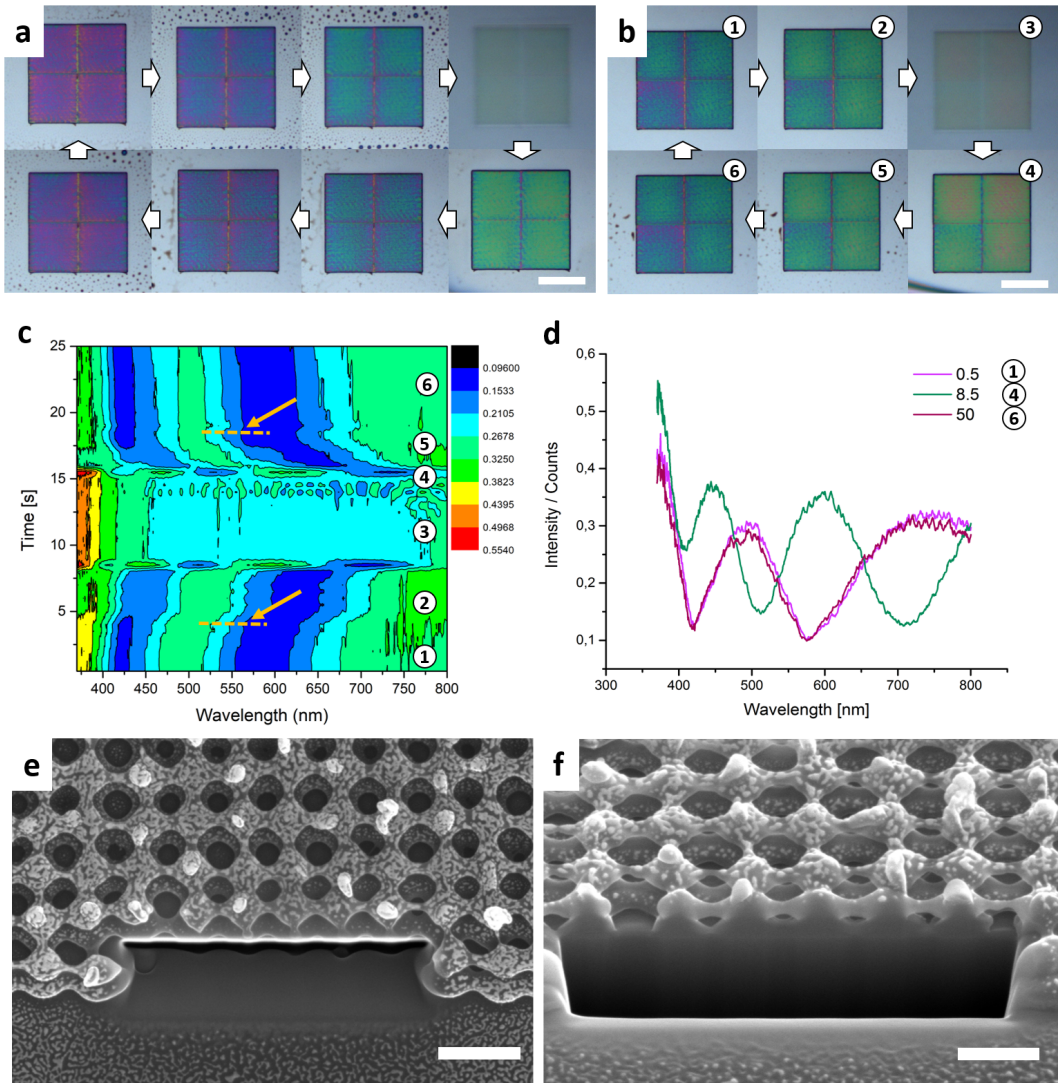

Figure 10-3. Coloured porous films as reversible gas sensors

(a,b) Two examples of colour switching porous films: Micrographs were recorded while isopropanol was approaching the layered films. It is assumed that the saturation increases with decreasing distance, until the film is completely overflown with isopropanol; images in the very right corner, first row, respectively. The Scale bar is 20µm. (b) Real time spectroscopy measurements correlating to the experiment presented in (d) and supporting the different phases (1)-(6) found by microscopy. The yellow lines and arrows indicate the points, between which one layer is most probably completely filled with liquid. (d) Spectra obtained at the phases (1), (4), (6), demonstrating the maximal colour shift and the reversible character of the system. (e,f) SEM-images of a FIB-milled SWE-TPL sample in top and tilted view. The images reveal a porous film with layered pores. The Scale bars are 500 nm

Chapter 11. General Summary and Conclusion

In the course of this thesis novel approaches allowing to create photonic structures by means of two-photon lithography (TPL) are presented. This work provides paths to master some of the major challenges of TPL with regard to the fabrication of bio-inspired 2D and 3D photonic crystals. Classically, TPL is used as deterministic structuring method for micro-structures but has limitations in the fabrication of nano-structures due to its low resolution and proneness to structural defects at this scale. In this thesis, it is shown that by using new approaches this method can be utilised for structuring of mechanically stable features as small as 120 nm in the lateral direction and 45 nm in the vertical direction, and thus, allows a greater variety of structures, which could not be manufactured by TPL before.

TPL can be described as a bottom-up approach, in which structures are fabricated layer-by-layer by moving the focus of a short-pulsed, high energy laser beam through a monomeric material. Only in the focus of the laser, the intensity of photons is sufficient to trigger a two-photon reaction of the photoinitiator, and thus, a subsequent cross-linking of the monomers. The laser intensity required to start the polymerisation of a photoresist material is called polymerisation threshold, while the smallest structured volume is typically represented by an upright standing ellipsoid is called voxel. With a voxel size of ca. 200 nm in horizontal (x,y) and 600 nm in vertical (z) direction, however, TPL is hardly feasible to be used for the fabrication of photonic crystals interacting with visible wavelengths.

The aim of the thesis was to improve and widen the typical TPL process to enable the fabrication of stable sub-micrometre structures interacting with light, and to utilise the acquired knowledge to fabricate bio-inspired photonic crystals that mimic the 2D-pillar gratings found on the moth eye or the 3D-‘christmas tree’ structures of the *Morpho*-butterflies.

The following improvements, analyses, and structure fabrications were conducted in the context of moth inspired 2D-pillar gratings:

- ***Chapter 5:*** The mechanical stability of TPL structures was increased by improving the development procedure of the TPL structuring process. This leads to significantly enhanced structure quality and defect rates, as structures resist capillary forces better during the drying.

- ***Chapter 6:*** Structures were fabricated close to the polymerisation threshold of the photoresist yielding pillars with diameters as small as 120 nm. Insights about the occurring polymer shrinkage and optical properties were gained by comparing experimentally obtained results with simulations.

- ***Chapter 7:*** An anti-reflective moth eye like film and a coloured diffraction grating were fabricated on one single surface as model for potential anti-counterfeiting applications. The optical properties of both structures were characterised and discussed in detail.

Following improvements, analysis and structure fabrication were discussed in the context of butterfly inspired 3D-structures:

- ***Chapter 8:*** The introduction of a reflective substrate enabled the modulation of the intensity distribution of the typically vertically elongated focal spot of the TPL laser beam by a standing wave formation. Crucial parameters are discussed in detail on basis of simulations and experiments. This approach enabled the fabrication of novel sub-micrometre sized, layered structures and vertical feature sizes down to 45 nm.

- ***Chapter 10:*** The influence of disorder on butterfly inspired structures was investigated on ordered and disordered line arrays and compared to the natural blueprint. The introduction of a vertical and lateral disorder into the structure topography, allows a significant increase in the rotation and angle constancy of the blue reflection.

Chapter 5: Improvement of the development strategy

The fabrication of structures via TPL typically involves three main steps: (I) designing of the exposure sequence, which defines where the resist is going to be exposed; (II) the exposure step, during which the photoresist is crosslinked; and (III) the development, in which not cross-linked residues are removed. Especially the last step a critical in regard to photonic structure fabrication, as occurring capillary forces cause structures to deform and collapse. As a result, the photonic crystal structure is disturbed, and its optical efficiency is lost.

Motivated by this, a revised development procedure was elaborated that includes an additional UV-crosslinking step prior to drying. Two different types of structures, micrometre sized mushroom structures and sub-micrometre sized 2D optical pillar gratings, were used for comparison of the new and the standard development procedure. Structures fabricated using the revised approach clearly showed enhanced structural integrity, and quality of structures (see **Figure 11-1**). The ratio of collapsed and deformed pillars among them was drastically reduced, which is caused by an improved mechanical stability and resistance against the capillary forces occurring during the final drying step. The effect of the modified development was particularly apparent on the 2D optical gratings, where defect rates were reduced from more than 95% of collapsed pillars within the grating to 0%. A low defect rate, as is now possible with the new development procedure, is essential for a high efficiency of optical interactions, and as such an essential parameter to describe the performance and quality of a photonic crystal.

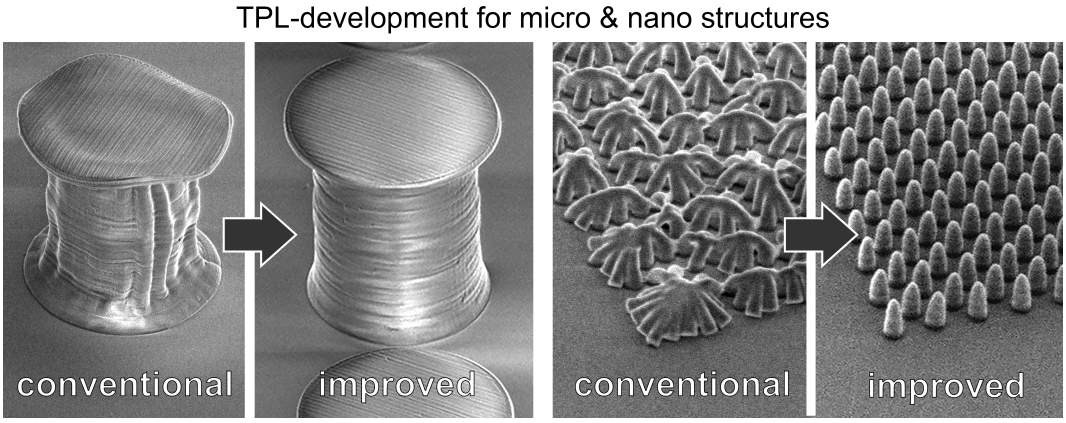

Figure 11-1. Comparison between the conventional and the new development method devised in this thesis

On the left: effect on micro mushroom pillars; on the right: effect on 2D optical nano gratings.

Chapter 6: Analyses and simulation of pillars in nanopillar gratings close to the polymerisation threshold of the photoresist

Deviations of only a few tens of nanometres in height, width, and distance between pillars within an optical pillar grating strongly influence the optical response of such a grating. For that reason, the precise fabrication of pillars is inevitable to obtain structures with a tailored optical behaviour. Until now, though, such a precise fabrication via TPL has been challenging as the structures were strongly influenced by poorly understood shrinkage effects and deformation due to capillary forces. These influences are most distinct when high aspect ratio nano pillars are fabricated close to the polymerisation threshold of the photoresist - exactly the conditions needed for photonic TPL structures.

In order to improve the predictivity of TPL fabricated structures nano pillar gratings were fabricated close to the threshold of the photoresist using differing laser powers between 10 and 23mW. Analyses of the resulting gratings via scanning electron microscopy revealed pillars with diameters of 430 down to 120 nm and heights of 1320 down to 330 nm. To obtain a quantification of the structure shrinkage during TPL-process experimentally found pillar sizes were compared to those predicted by Monte Carlo simulations based on voxel sizes (see **Figure 11-2)**. This comparison revealed an inhomogeneous shrinkage in lateral and vertical structure direction, which increased significantly with decreasing laser powers. The extend of this shrinkage in both directions also affected the resulting pillar shapes. This effect can be rationalised by differences in the cross-linking density, surface energy minimisation, and pinning at the base caused by substrate adhesion. In addition to structure analyses, the colouration of the gratings was evaluated and compared to spectra predicted by rigorous coupled-wave simulations. The findings indicated that considering diameters and heights of pillars alone is not sufficient to forecast the optical properties of the fabricated TPL gratings. Indeed, the exact shape of a pillars, and thereby

deformation and shrinkage effects, must be regarded, too, to gain reliable predictivity of the optical response. This again emphasises how important it is to investigate potential factors that influence the shapes of TPL fabricated photonic structures.

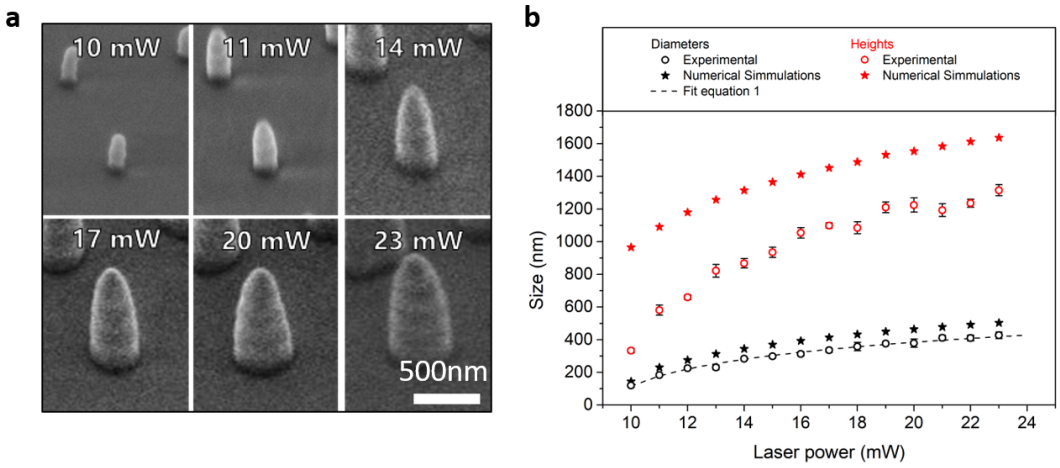

Figure 11-2. Sizes of pillars within optical pillar gratings fabricated close to the polymerisation threshold of photoresist and their comparison to expected values from simulations

(a) Scanning electron microscopy images of high aspect ratio pillars fabricated by means of TPL using different laser powers. The smallest diameter of a freestanding pillar achieved was 120 nm at 10 mW. (b)

Chapter 7: Diffraction and Anti-reflection Gratings for Anti-counterfeiting

Surfaces which can both, diffract and anti-reflect visible wavelengths, could add a particularly useful component for the design of anti-counterfeiting surfaces. To obtain such a surface, pillar gratings composed of large and well-separated pillars have to be placed close to pillar gratings, which possess much smaller and closely packed pillars. This, however, is challenging for the most structuring techniques as they either allow for only one type of grating per surface or are restricted to particular sizes of structures.

In this chapter it is demonstrated that TPL can be used to achieve the desired placement of pillars described above by precisely adjusting the experimental parameters during the fabrication process. The fabricated pillar gratings were investigated regarding their structure sizes and optical properties using scanning electron microscopy, optical microscopy, and reflective and transmissive spectroscopy (**Figure 11-3**). Depending on the pillar distance, these structures interacted with light either as classical optical lattices or exhibited anti-reflective properties similar to those known from moth eyes. The efficiency of the diffraction grating was very high over a broad wavelength range with a maximum diffraction efficiency of 95% in the green. The performance of the anti-reflection grating was also promising, showing a reduction in reflectivity of ca. 20 % and hardly affected transmission over the entire measured wave spectrum of 450-700 nm. The effect of anti-reflection is assumed to be caused by

a continuous refractive index gradient similar to that found on the moth's eye, as refractive index of the material and structure sizes are comparable to that of the nature's blue print. The general observation that two optically very distinct surfaces can, indeed, be placed in close proximity on one single substrate during one fabrication process paves the way for the development of even more sophisticated surfaces for anti-counterfeiting.

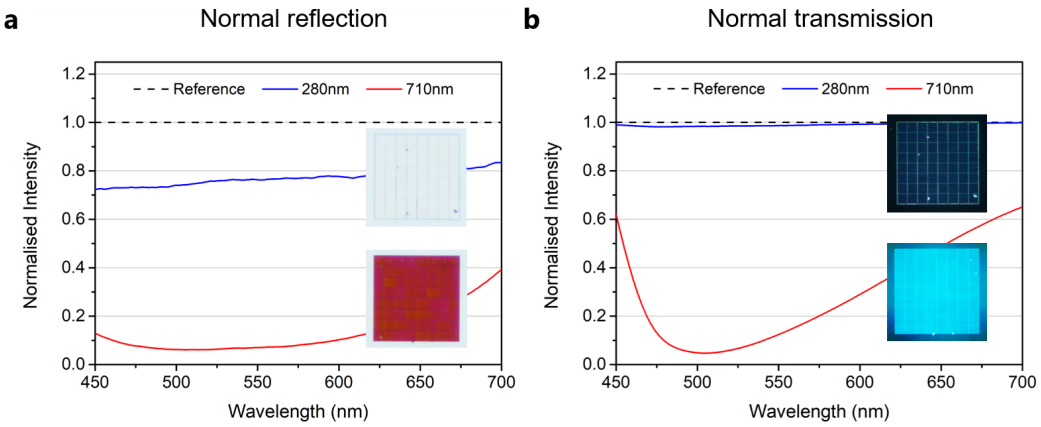

Figure 11-3. Optical properties of diffraction and anti-reflection gratings simultaneously fabricated by TPL on one single surface

(a) Appearance at bright filed microscopy and reflection spectra of both pillar gratings. (b) Appearance at dark filed microscopy and transmission spectra of both pillar gratings.

Chapter 8: Standing wave enhanced two-photon lithography (SWE-TPL)

The fabrication of 3D photonic crystals such as those of *Morpho*-butterflies by means of standard two-photon lithography is impossible, as the vertical writing resolution is insufficient to fabricate vertical periodicities that interact with visible wavelengths down to the blue range.

A solution for this limitation is proposed in Chapter 8 by a novel approach termed standing wave enhanced TPL (SWE-TPL). Here, a reflective substrate is used to introduce a standing wave around the TPL-focal point, revealing itself by a modulation of the beam intensity profile along the vertical axis (**Figure 11-4a**). Because of the light intensity sensitive photoresist, it was anticipated, that polymerisation occurred predominantly in regions with high beam intensity, which have a periodicity of $\lambda/2$ but vary in their maximum values (**Figure 11-4b**).

And indeed, pillars and lines with a vertically layered nanometre structure were obtained in experiments on reflective substrates (**Figure 11-4c** and **d**). To gain a better understanding of the impact of parameters, such as the divergence angle of the beam, the reflectivity of the substrate, and the focal distance in respect to the substrate, Monte-Carlo-simulations of intensity profiles were conducted. The results of such simulations agreed well with the experimentally found structures, e.g., the number of layers, the distances between layers of approximately 250 nm, and the overall shapes of the resulting structures. As

predicted by simulations, the individual layers of fabricated pillars became more distinct with increasing substrate reflectivity, and thus higher modulation depths, while the connections between them become narrower. Especially at lower laser powers, this effect could be so pronounced that no connection was formed between layers on top of each other. Furthermore, the modulation was strongest close to the reflective substrate and decreased with higher distance, which led to less distinct layers at the top of the structures. Yet another striking finding was that the polymerisation can be truly confined to the one intensity maximum closest to the focal point by tuning the laser power and substrate reflectivity, as it was projected by simulations. This was demonstrated by the fabricated 'fence'-like structures, where fine wires with a vertical feature size as small as 45 nm are spun between pillars (**Figure 11-4e**). Compared to the state-of-the-art value of 600 nm this is an improvement in the minimal vertical features size by a factor of 13.

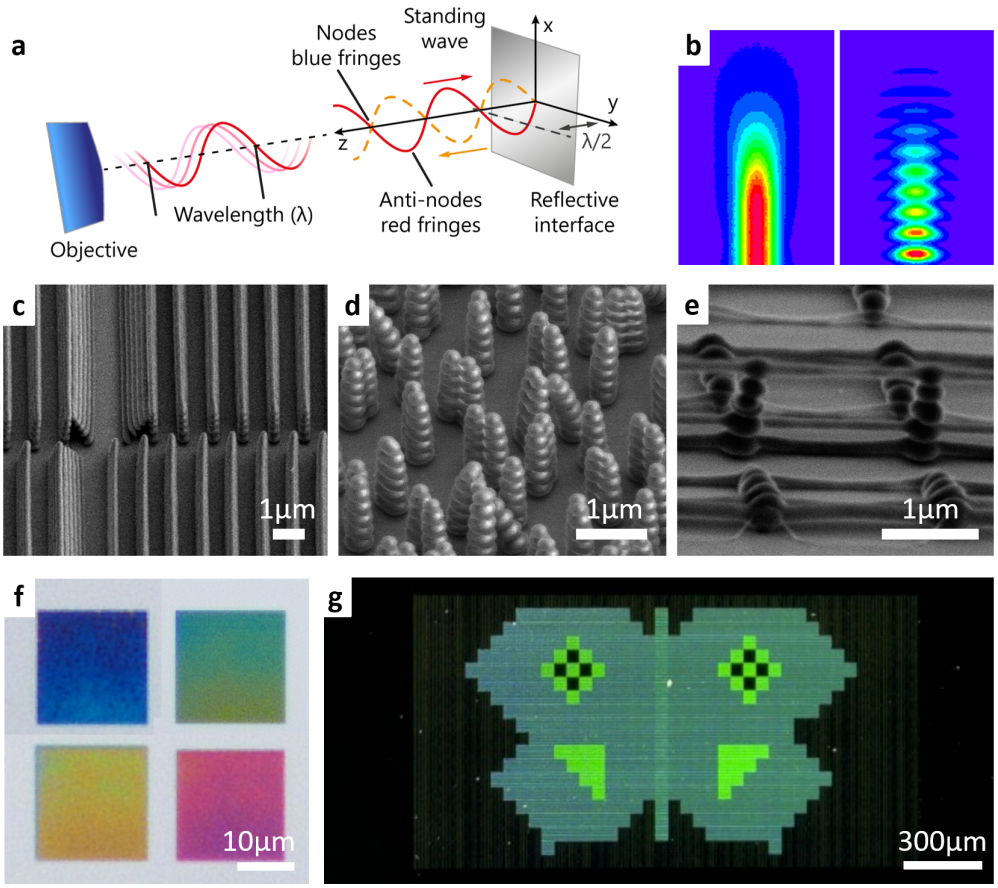

Figure 11-4 Concept and results of the novel standing wave enhanced two-photon lithography (SWE-TPL) approach

(a) Schematic of a standing wave pattern along the optical axis of the laser beam caused by a reflective substrate in the TPL-system. (b) Monte-Carlo intensity simulations showing the difference of two-photon intensity distributions for common TPL and SWE-TPL. Scanning electron microscopy images of SWE-TPL fabricated (c) *Morpho*-butterfly like free-standing layered lines, (d) freestanding segmented pillars, (e) and fence like structures. Micrographs of larger areas of freestanding layered structures fabricated with: (f) different laser powers to tune the colouration or (g) varying heights and shapes of structures to obtain differences in intensity.

The potential of SWE-TPL in the field of photonic crystal fabrication is demonstrated on larger arrays, where, e.g., the colouration was tuned by changing the applied laser power (**Figure 11-4f**), or the intensity of the reflection was manipulated by changing structures' heights and shapes (**Figure 11-4g**).

Chapter 9: Ordered and disordered butterfly-inspired structures

The *Morpho*-butterflies are famous for their distinctive iridescent and angle independent blue colouration, which is caused by a natural 3D photonic crystal covering the wings of the butterflies. From the technological point of view the manufacturing of such photonic crystals is expensive and challenging as current fabrication techniques require multiple process steps and are limited in structural flexibility. The latter becomes particularly evident when deliberate imperfections, e.g., disorder as it is found to a certain degree on the *Morpho*-butterfly wing, are to be introduced. These imperfections, though, plays a crucial role for the butterfly wing's angle-independent optical appearance.

In Chapter 9, a strictly ordered and a partially disordered, butterfly-inspired photonic surface were successfully fabricated by 'standing wave enhanced two-photon lithography' (SWE-TPL). The ordered surface was conceived to have parallel uniform ridges with a fixed distance (**Figure 11-5a**), while the ridges of the disordered structure were subdivided into segments with different heights and small, random deviation from the parallel/main line orientation (**Figure 11-5b**). The resulting arrays were analysed regarding their structure and optical properties by means of scanning electron microscopy, angular microscopy, angular spectroscopy, as well as conoscopy and compared to results obtained on the natural blueprint. The ridges in both arrays mimicked closely the geometry of the butterfly's free-standing layered ridges with an inter-layer distance around 200 nm. Both artificial structures and the butterfly showed an almost angle independent blue reflection, if they were tilted up to 50° around an axis perpendicular to the direction of the ridges (**Figure 11-5c**). When tilted parallel to the direction of the ridges, the colouration quickly disappeared on the ordered sample, as a result of its structural anisotropy (**Figure 11-5d**). Surprisingly, the artificial, disordered sample performed even better in this regard than the natural blueprint. The deliberately introduced disorder also reduced the distinctive Bragg-diffraction found on the ordered sample (**Figure 11-5e**). A possible application of such butterfly-inspired SWE-TPL-structures could be as anti-counterfeiting features, as it was demonstrated by fabricating large-scale patterns with areas of angle dependent and independent colouration (**Figure 11-5f,g**).

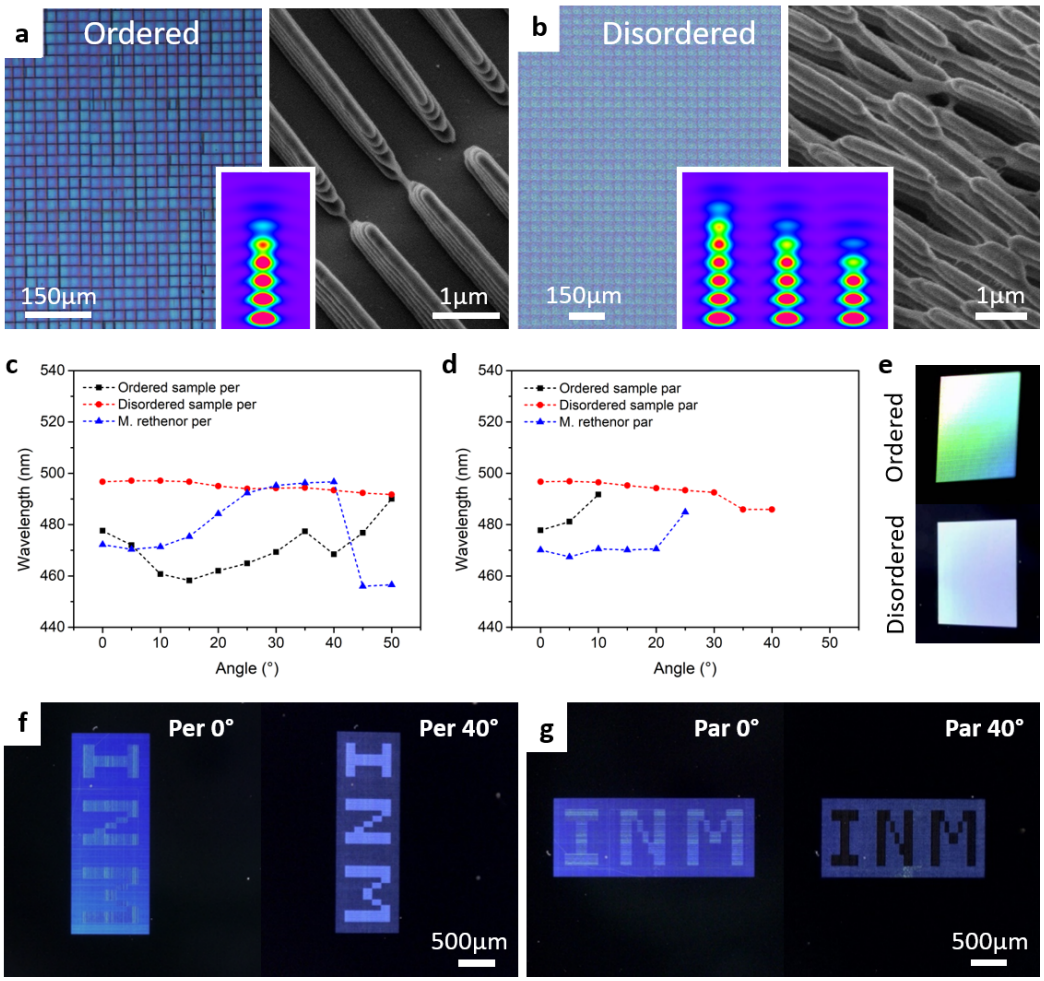

Figure 11-5. Ordered and disordered butterfly-inspired structures

Optical micrographs and scanning electron microscopy images of (a) the ordered and (b) disordered butterfly-inspired freestanding layered structures fabricated by means of SWE-TPL. The inserts show simulations of intensity distributions expected during the fabrication process. (c,d) Wavelength dependence of the blue peek on the tilting angle found on the fabricated samples and the natural butterfly blueprint in (c) perpendicular and (d) parallel direction in respect to the ridged structure. The disordered sample showed the smallest shift in both cases. (e) Macroscopic appearance of an ordered and a disordered sample at approximately 40°tilt. Optical micrographs of an example of an anti-counterfeiting feature: letters become more intense when tilted in (f) perpendicular (per) direction and disappear when tilted in (g) parallel (par) direction.

Final conclusion of the thesis

- By using novel approaches in two-photon lithography (TPL) fabrication, such as improved development procedures or standing wave enhanced two-photon lithography, the fabrication of stable sub-micrometre structures interacting with light as photonic crystals was enabled.
- These approaches allow a new size scale for defect free TPL-structuring – 120 nm in horizontal and 45 nm in vertical direction.
- On the nanoscale, the TPL structures are strongly influenced by capillary forces during development and shrinkage effects, which make the understanding of these effects quite pivotal, especially, if a precise tailoring of structures and optical behaviour is desired.
- The presented 2D-pillar gratings mimicking the gratings found on the moth's eye and the butterfly-inspired 3D-'christmas tree' structures showed a great variety of optical behaviours: effective diffraction gratings, anti-reflective surfaces, and angle independent blue colouration.
- Novel approaches are not limited to the mimicry of natural photonic crystals but can also be used to manufacture layered films applicable as sensors, fence-like structures usable as super fine resonators, and many other structures on the sub-micrometre scale.
- All these surfaces can be combined freely on one surface in only one single exposure process.
- Several photonic structures are suitable to be used as masters for microimprinting, which is important for volume production.
- The presented investigations represent only the beginning for the application of TPL in photonics. Especially, SWE-TPL supported structuring paves the way for further extensive research, such as applications in sensor and display technology, and photonic computing.

List of Figures

List of Tables